TECHNISCHE UNIVERSITÄT DRESDEN

Leibniz-Institut
für Festkörper- und
Werkstoffforschung
Dresden

Unusual electronic properties in LiFeAs probed by low temperature scanning tunneling microscopy and spectroscopy

DISSERTATION
zur Erlangung des akademischen Grades
Doctor rerum naturalium (Dr. rer. nat.)

der Fakultät Mathematik und Naturwissenschaften
der Technischen Universität Dresden
Deutschland
20.03.2017

vorgelegt von
M.Sc.-Physik **Pranab Kumar Nag**
geboren am 06. Mai 1989
in Pashchim Medinipur (Khirpai), Westbengalen, Indien

2017

Eingereicht am: 20.03.2017

1. Gutachter: Prof. Dr. Bernd Büchner
2. Gutachter: Prof. Dr. Rüdiger Klingeler

Die Dissertation wurde in der Zeit von August 2012 bis März 2017 im Institut für Festkörperphysik (IFF) des Institutes für Festkörper- und Werkstoffforschung Dresden (IFW) angefertigt.

TECHNISCHE
UNIVERSITÄT
DRESDEN

Leibniz Institute
for Solid State and
Materials Research
Dresden

Unusual electronic properties in LiFeAs probed by low temperature scanning tunneling microscopy and spectroscopy

Dissertation
for obtaining academic degree
Doctor of Philosophy (Dr. rer. nat.)

The Faculty of Mathematics and Natural Sciences
Technical University Dresden
Germany
20th March, 2017

presented by
M.Sc.-Physics **Pranab Kumar Nag**
born on 6th May, 1989
at West Midnapur (Khirpai), West Bengal, India

2017

Submitted on: 20^{th} March, 2017

1. Referee: Prof. Dr. Bernd Büchner
2. Referee: Prof. Dr. Rüdiger Klingeler

This dissertation was done from August 2012 to March 2017, i.e. within 4 years and 8 months, at the Institute for Solid State Research (IFF) at the Institute for Solid State and Materials Research Dresden (IFW Dresden).

Dedicated to my parents and elder sister...

Abstract

In this thesis, the electronic properties in superconducting LiFeAs single crystal are investigated using low temperature scanning tunneling microscopy and spectroscopy (STM/S) at various temperatures. For this purpose, the differential conductance ($\mathrm{d}I/\mathrm{d}V$) measured by STS which is directly proportional to the local density of states (LDOS) of the sample to the sub-atomic precision, is used together with the topography information.

The $\mathrm{d}I/\mathrm{d}V$ spectra within the ±1 V energy range reveal a characteristic feature at around -350 mV to -400 mV in stoichiometric LiFeAs. This feature seems to be a universal property among all the Fe-based high temperature superconductors, because it is also found in $\mathrm{Fe_{0.965}Se_{1.035}}$ and $\mathrm{NaFe_{0.975}Co_{0.025}As}$ single crystals at the energy of -210 mV and -200 mV, respectively.

The temperature dependent spectroscopy data averaged over a spatially fixed clean area of 2 nm × 2 nm are successfully executed between 5 K and 20 K. The two distinct superconducting phases with critical temperatures $T_c = 16$ K and 18 K are observed. In addition, the distance between the dip position outside the superconducting gap and the superconducting coherence peak in the spectra remains temperature independent which confirms that it is not connected to an antiferromagnetic (AFM) spin resonance. The temperature dependent spectra have been measured between 5 K and 61 K within the energy range of ±100 mV as well. The hump structure at 42 mV tends to disappear around 60 K from unknown origin.

The temperature dependent quasiparticle interference (QPI) has been studied within the temperature range between 6.7 K and 25 K and analyzed by the Fourier transformation of the measured spectroscopic maps. The dispersion plots in momentum space as a function of temperature show an enhancement of QPI intensity (±5.5 mV) within the superconducting gap at the Fermi level at 6.7 K near $q \approx 0$. This is interpreted on the basis of Andreev bound state. In both polarities outside of this, a depletion of QPI intensity is noticed between 5.5 mV and around 9 mV. At positive energies, the QPI intensity becomes very rich above 9 mV. The size of the enhanced QPI intensity near the Fermi level, and the edge of the rich QPI intensity beyond 9 mV are found to behave like superconducting order parameter with rising of temperature. Furthermore, an energy mode peaked at around 14 mV appears in the integrated QPI intensity below superconducting T_c (6.7 K). This is consistent with the observed peak at 1st derivative of the $\mathrm{d}I/\mathrm{d}V$ spectra. In both of these cases, such 14 mV peak is suppressed at normal state (25 K). This mode is therefore directly related to superconductivity in LiFeAs.

The off-stoichiometric LiFeAs single crystal with superconducting T_c of 6.5 K has a 10 mV rigid band shift of the Fermi level towards electron doping. The absence of the rich QPI intensity between 9 mV and 17 mV is found compared to the stoichiometric LiFeAs, and hence the 14 mV mode is absent here. This brings us to conclude once more time that such 14 mV energy mode is relevant for superconductivity in LiFeAs.

Contents

1. Introduction

Superconductivity in high temperature superconductors (HTSC) is widely believed to appear in the proximity of an antiferromagnetic (AFM) ground state [1–4]. However, LiFeAs, which belongs to the family of Fe-based HTSC, does not seem to follow such canonical phase diagram [5]. Unlike the other Fe-based HTSC where superconductivity emerges from a Fermi-surface nested AFM ground state [6–9], LiFeAs superconducts without any doping [10]. To elaborate its unusual electronic properties in details, the experimental band structure measured by photoemission spectroscopy reports a poorly nested Fermi surface between electron and hole pockets [11, 12]. Furthermore, on the one hand the introduction of doping suppresses superconductivity [5, 13], whereas on the other hand, it does not show any structural transition in its whole phase diagram [5] unlike the other Fe-based HTSC [2, 7]. The inelastic neutron scattering (INS) experiment [14] has reported a static magnetic ordering at the incommensurate wave vector $(0.5 \pm \delta,\ 0.5 \mp \delta,\ 0)$ with $\delta \sim 0.07$ instead of a commensurate peak which is commonly observed in other Fe-based HTSC [4, 15]. In fact, no specific mode has been found in INS experiments in this compound in both energy and temperature scan [16]. Thus, in a nut shell, LiFeAs is one of the most debated Fe-based HTSC and therefore, puts a special attraction among all the Fe-based HTSC in the field of research to investigate its superconducting nature. This is the main motivation of this work in which the focus of interest is to study the electronic properties in LiFeAs using low temperature scanning tunneling microscopy.

Currently, the only available experimental tool which has the ability to study the real space electronic information with sub-atomic spatial resolution is known as scanning tunneling microscopy (STM) and scanning tunneling spectroscopy (STS). Apart from the investigation of sample's electronic properties combined with its topography information, an STM/S has the potential to study the atomic scale defect, spatial inhomogeneity, magnetic structure [1] and their electronic properties [17–21]. This technique can also be used to study experimental band structure of any unknown material in scattering space which is also known as the Fourier transformed spectroscopic imaging STM technique. The local density of states (LDOS) of the sample can be measured in STM/S via the differential conductance ($\mathrm{d}I/\mathrm{d}V$) measurement at the sub-atomic perfection. By a combination of topography (STM) and spectroscopy (STS) measurements, we explore this technique to study the superconducting as well as normal state electronic properties in LiFeAs between 5 K and 61 K. Quasiparticle interference (QPI) studied by transforming spectroscopic maps to Fourier space in STM/S has also been

---

[1] Spin-polarized STM [17] tool can even measured the magnetic structure of individual atomic spin.

used to study the band structure close to the Γ point as a function of temperature to disentangle the normal and superconducting state in LiFeAs.

In the topography section of the result chapter, we use an STM as a nano-scale microscope to image the two types of different representative atomically resolved topography images on stoichiometric LiFeAs. The main difference between those two images is the types of defects representing the respective surfaces. In both cases, defects are statistically distributed over the surface. The commonly observed defects have also been studied and discussed in detail. Besides those topography measurements, dI/dV spectra have been recorded in both a wide energy and a wide temperature range which is discussed in spectroscopic section. This section is split into two subsections. In the first subsection, the uncommon and challenging measurement of dI/dV spectra between ±1 eV far away from the Fermi level within the temperature range of 5 K and 20 K are shown and discussed. Such wide energy range spectroscopic data show a temperature independent (between 5 K and 20 K) feature around -350 mV to -400 mV. This, in comparison with the measurement on $Fe_{0.965}Se_{1.035}$ and $NaFe_{0.975}Co_{0.025}As$ single crystals where such feature appears at -210 mV and -200 mV, respectively, allows us to suggest that it is a universal property among all the Fe-based superconductors. This is supported by a recent photoemission measurement in Ref. [22] where a characteristic mode peaked at -500 mV in case of NaFeAs parent compound was considered to couple with the low energy fermions to explain the low energy anomalies. In the second subsection, we focus on the spectroscopic features near the Fermi level, e.g. the temperature evolution of superconducting gap and the dip-hump structure located just outside the superconducting coherence peaks. A very thorough dI/dV measurement of superconductivity near the Fermi level within the temperature range of 5 K and 20 K on a spatially fixed area over the cleaned surface reveals two distinct superconducting phases in LiFeAs with the characteristic superconducting T_c values of 16 K and 18 K. In addition, the dip-hump structure outside the superconducting coherence peak is very distinct in the dI/dV spectra. Strikingly, the experimentally observed almost temperature independent distance between the dip position and the superconducting coherence peak rules out its relation with the strong coupling bosonic mode [23]. The possibility of a larger superconducting gap (around 15 mV to 17 mV energy gap) has been considered to capture the dip-hump structure using extended Dyne's formula which gives only a qualitative agreement with the experimental data. Therefore, it is not originated from such a large superconducting gap. The other important result is the 42 mV hump in the dI/dV spectra which approaches to disappear around 61 K. This is most likely to be related to the spin-density wave gap in LiFeAs.

An STM/S can measure a full spectroscopic data set where atomic level dI/dV value on each sample location can be recorded as a function of temperature. Such spectroscopic maps are useful to study the QPI information which, in fact, provide the electronic band structure information of the sample. In the third section of the result chapter, the dispersion plots of the QPI measurements at various temperatures reveal Andreev bound states near the Fermi level around $q = 0$. It has similar size of the superconducting energy gap and behaves like a superconducting order parameter with increasing temperature. The depletion of QPI intensity beyond the Andreev bound state between 5.5 mV to 9 mV in both polarities has also been noticed and remains temperature independent. The edge (9 mV) of the rich QPI intensities at positive energies track the superconducting order parameter but it remains at 3.7 mV above the Fermi level in the normal state. Furthermore, the difference of the integrated QPI intensity between 6.7 K and 25 K has a characteristic peak at 14 mV. Such 14 mV peak is very similar to the observed peak at the 1st derivative of the bare surface $\mathrm{d}I/\mathrm{d}V$ spectra. This is a striking result which explains a direct relation of this 14 mV energy mode with superconductivity in stoichiometric LiFeAs.

The last section of the result chapter deals with the QPI and defects studies on off-stoichiometric LiFeAs which has superconducting T_c of 6.5 K. The QPI data show a rigid band shift of 10 mV of the Fermi level towards unoccupied side to make it electronically doped LiFeAs sample. The interband scattering is observed between the γ and α_2 hole like bands which can be well describe with similar scattering from the calculated band structure of the tight binding fit to the ARPES data. The rich QPI intensity between 9 mV and 17 mV in the unoccupied side is absent here, and thus the peak in the integrated QPI intensity at 14 mV does not appear in this compound. Therefore, this boosts us to state that the 14 mV peak is a characteristic energy mode which has a direct relation with superconductivity in stoichiometric LiFeAs.

This thesis is structured as follows. Chapter 2 contains the basic principles and different measurement modes in STM/S. The basic of the QPI measurements in STM/S experiment is described in chapter 3. The experimental setup of the low temperature STM/S measurements and the data analysis of the measured QPI are discussed in detail in chapter 4. Chapter 5 deals with the basic of the Fe-based HTSC and the introduction to the LiFeAs superconductor. The results are presented in chapter 6 which is divided into four sections. The first two sections are about the topography and spectroscopic results including temperature dependent spectroscopic features. The third section describes the temperature dependent QPI results whereas the fourth section contains the defects and QPI study on off-stoichiometric LiFeAs. The summary of the thesis is done in chapter 7.

2. Scanning tunneling microscopy and spectroscopy (STM/STS)

Gerd Binnig and Heinrich Rohrer, scientists from IBM Zürich (Rüschlikon, Switzerland) were awarded the 1986 Nobel Prize in physics for their invention of scanning tunneling microscopy and spectroscopy in 1981 [24], one of the powerful microscopic techniques in recent era to investigate electronic properties of materials down to atomic precision [18, 25]. Later, the technological advancement allowed to investigate properties (both magnetic as well as electronic) of materials with high spatial and energy resolution using this tool. In this chapter, I will discuss the basic principles of the STM setup and the basic theoretical interpretation of electron tunneling.

2.1. Principles of STM

A pictorial diagram of the STM setup is illustrated in Fig. 2.1 where a sharp metallic conducting tip[1] is brought close to the surface of a conducting sample using three dimensional piezoelectric actuators which allow the tip to move along the x, y, z directions with sub-Ångström precision to scan over the surface of the sample. When the separation between the lower-most atom on the sharp edge of the tip and the top-most atomic layer of the sample becomes in the range of a few Ångströms ($\sim$ 5Å), a finite tunneling current in the order of pico-ampere to nano-ampere is achieved due to the overlap of the electrons wavefunctions in the presence of an applied bias voltage between the tip and the sample. This applied bias voltage is usually within the range of a few milli-volts up to some volts. The tunneling current I_T depends on the tip-sample separation, d as

$$I_T \propto e^{-2kd} \int_{-eV}^{0} \rho_s(\epsilon) d\epsilon \tag{2.1}$$

Here, k is proportional to the square root of the effective barrier height (Φ') and $\rho_s(\epsilon)$ is the density of states of the sample at energy ϵ. Thus, the tunneling current is highly sensitive to the tip-sample separation, which in fact, becomes helpful to gain high spatial resolution down to sub-atomic level. It also depends qualitatively on the integrated density of states of the sample. Here, I will discuss the basic concept of electron tunneling as well as different measurement modes in STM experiments.

---

[1] Generally, a STM tip is made of Tungsten (W) or Platinum (Pt)/Iridium (Ir) or Gold (Au) due to their flat density of states within the interested energy range [26].

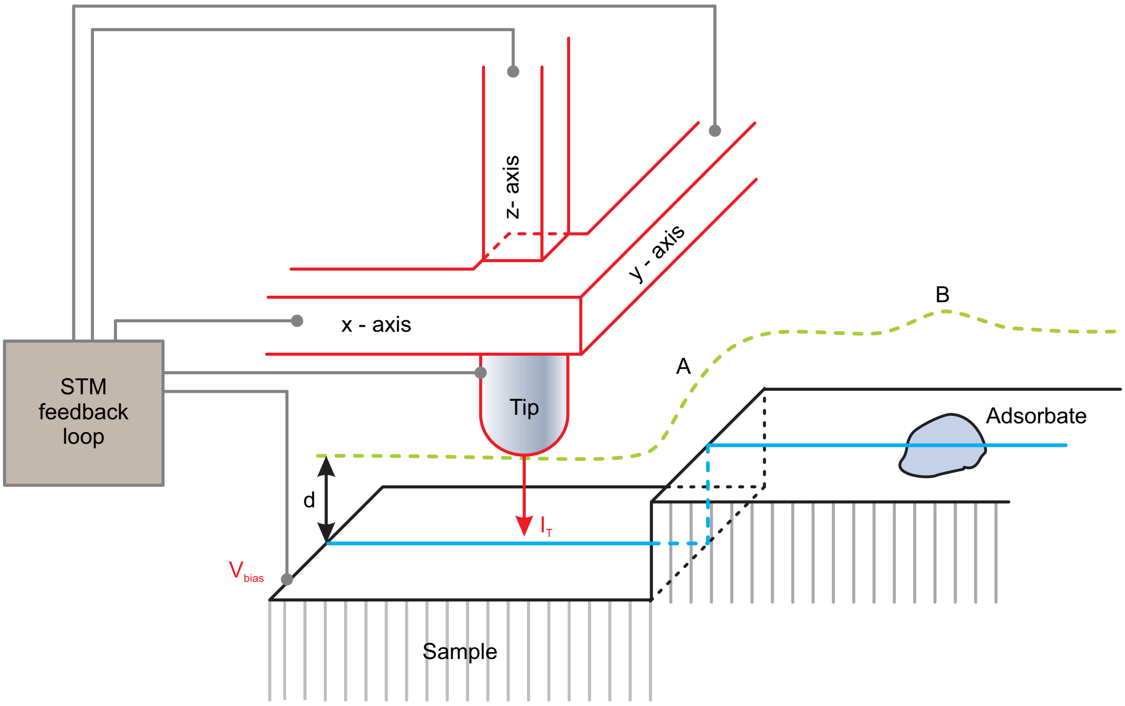

Figure 2.1.: The schematic diagram of the STM setup operating at constant current mode while it is scanning along one dimension (x-axis). The tip is attached to piezo-electric actuators for movement along the x-, y-, z-axes. The tunneling current I_T is achieved when the bias voltage, V_{bias} is applied between the tip and sample. In constant current mode topography scan, the corresponding tip-sample separation, d remains constant. In this situation, the tip follows the green path while moving along the x-axis, indicated by the blue line over the sample to keep the tunneling current constant. For similar reason, it follows path A and B over the sample at the step edge and adsorbate, respectively.

2.2. Quantum tunneling of electrons in one dimension

In this section, I will discuss quantum tunneling of electron through a vacuum barrier potential as described in Ref. [25,27]. Let us consider a simple model of an electron with energy E in one-dimension (1D) moving towards a constant energy barrier Φ of width d as depicted in Fig. 2.2. We choose this simple problem as the similar situation occurs during electron tunneling in STM/S where two sides of the barrier represent electrons in the STM tip and the metallic sample. So, the electron needs to overcome the work functions of the tip (ϕ_t) and sample (ϕ_s) to tunnel from one side of the barrier to the other side. For simplicity, we assume that the considered barrier high Φ is the linear combination of ϕ_t and ϕ_s. Classically, the electron will reach to the other side of the barrier, only if $E > \Phi$. But if we consider electron as a quantum particle having its wave nature, it will have a non-zero probability to tunnel across the barrier even though $E < \Phi$, as shown in Fig. 2.2. The time-independent Schrödinger equation in 1D which describes the wavefunction of the electron is

$$\left(-\frac{\hbar^2}{2m}\frac{\mathrm{d}^2}{\mathrm{d}x^2}+\Phi(x)\right)\psi(x)=E\psi(x) \tag{2.2}$$

Where, $\hbar$ is the reduced Planck constant, m is the mass and x is the position of the electron, respectively. The solution of the equation for the above 1D problem is given below:

$$\psi(x)=\begin{cases} e^{ik_1x}+Ae^{-ik_1x}, & \text{in the region-1 where } \Phi=0 \text{ for } x<0 \\ Be^{k_2x}+Ce^{-k_2x}, & \text{in the region-2 where } \Phi(x)=\Phi \text{ for } 0<x<d \\ De^{ik_1x}, & \text{in the region-3 where } \Phi=0 \text{ for } x>d \end{cases} \tag{2.3}$$

Where, $k_1=\sqrt{2mE/\hbar^2}$ and $k_2=\sqrt{2m(\Phi-E)/\hbar^2}$, both have the form of de Broglie relation $p=\hbar k$. The two components of the wave function in region-1 correspond to the incident and reflected waves while the wavefunction in region-3 describes the transmitted wave. The wavefunction of region-2 decays exponentially inside the barrier. Using the continuity condition at each boundaries ($x=0$ and $x=d$) of the wavefunction $\psi(x)$ and its derivative $\mathrm{d}\psi/\mathrm{d}x$, the coefficients A, B, C, D and its relation can be determined [27]. If $P(E)$ is the probability to transmit an electron from region-1 to region-3 through the barrier (region-2), this can be expressed as the ratio between transmitted (j_t=$|D|^2$) to incident (j_i=$|A|^2$) current density and has the following form:

$$P(E)=\begin{cases} \dfrac{1}{1+\dfrac{\Phi^2\sinh^2(k_2d)}{4E(\Phi-E)}}, & \text{for } E<\Phi \\ \\ \dfrac{1}{1+\dfrac{md^2\Phi}{2\hbar}}, & \text{for } E=\Phi \\ \\ \dfrac{1}{1+\dfrac{\Phi^2\sin^2(k_2d)}{4E(E-\Phi)}}, & \text{for } E>\Phi \end{cases} \tag{2.4}$$

This transmission probability, $P(E)$ is neither zero for $E<\Phi$ nor becomes equal to one for $E>\Phi$ in contrast to the classical situation. In case of a strongly attenuating barrier, when the decay constant $k_2d\gg1$, one can approximate the tunneling expression for $E<\Phi$ as:

$$P(E) \approx \frac{16E(\Phi - E)}{\Phi^2} e^{-2d\sqrt{2m(\Phi - E)/\hbar^2}} \tag{2.5}$$

This implies that the transmission probability depends exponentially on the square root of an effective potential barrier height $\sqrt{(\Phi - E)}$ and the width d of the potential barrier through which it tunnels. This elementary model covers the basic principle of electron tunneling in STM where region-1,-2 and -3 represent the conducting sample, the vacuum barrier (distance between the tip and sample) and the STM-tip, respectively. Thus, on the one hand the tunneling current I_T in STM is extremely sensitive to the distance (d) between the tip and sample, which on the other hand is an advantage to have high spatial resolution in STM. However, this model does not capture the information of the density of states (DOS) explicitly.

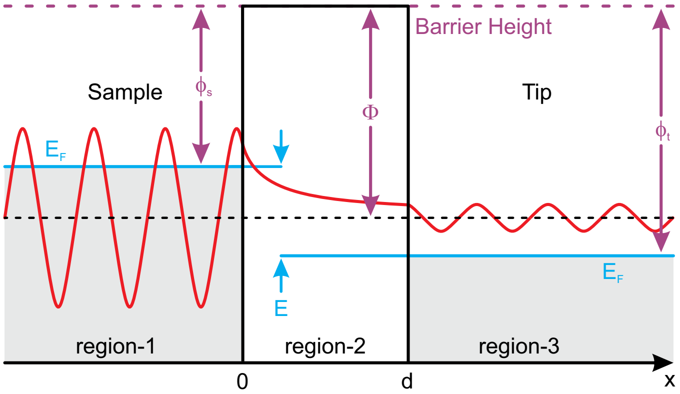

Figure 2.2.: Pictorial diagram of electron tunneling through a resultant energy barrier, Φ ($\approx (\phi_s + \phi_t)/2$). The width of the barrier, d is assumed in the order of a few Å for quantum tunneling where the energy of electron, $E(eV)$ is much lower than the resultant barrier height, Φ. Region-1 describes the incident electron and region-3 represents the transmitted electron after tunneling through the barrier, Φ (region-2).

2.3. Many particle tunneling concept

J. Bardeen treated the electron tunneling process using time dependent perturbation Hamiltonian (H') for a planer metal-oxide-metal tunnel junction for the first time in 1961 [28]. Later, J. Tersoff and D. R. Hamann extended this approach for the case of tunneling in STM by considering spherical tip states as one of the electrode in 1983 [29]. In their approach, it is assumed that the electron orbitals of the outer-most tip atom have s-wave orbital character and its amplitude decays exponentially within the barrier as discussed by Bardeen [28]. “*Fermi’s golden rule*” which provides the rate of transition probability from one energy eigenstate to another, gives the qualitative tunneling current for a weakly interacting system. According to this, the probability p for an electron to tunnel from a tip-eigenstate ψ_t with energy E_t to a sample-eigenstate ψ_s with energy E_s has the following form:

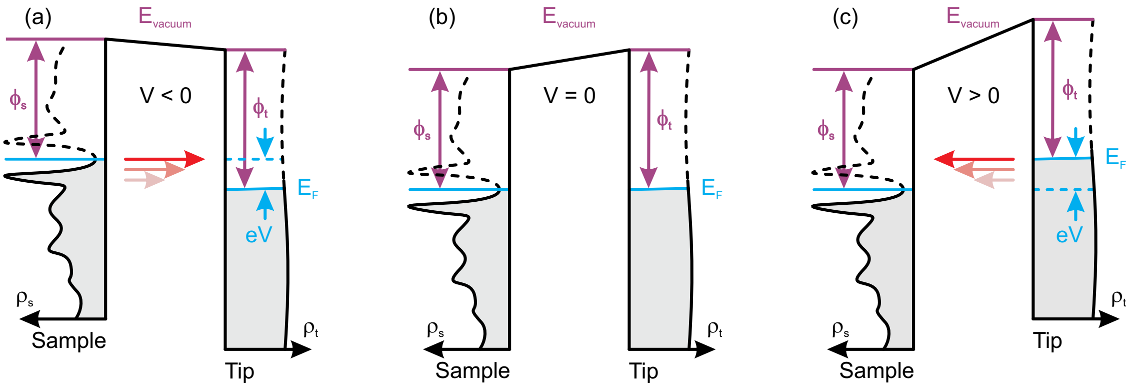

Figure 2.3.: A diagram of energy dependent tunneling where the left and right side of each diagram represent the sample and tip DOS, respectively. (a)-(c) are the tunneling conditions while the applied sample voltages are negative, zero and positive, respectively. The horizontal solid blue lines indicate the Fermi levels. The grey areas are pointing the occupied side while the areas under the dashed black curve are the DOS in the unoccupied side of the sample. We consider elastic tunneling which is shown by red arrows. ϕ_s and ϕ_t are the work function of the sample and tip, respectively. The LDOS of the occupied (unoccupied) side of the sample are measured when negative (positive) voltage is applied to the sample with respect to the tip, shown in (a) ((c)).

$$p = \frac{2\pi}{\hbar} \cdot |M|^2 \cdot \delta(E_{\psi_s} - E_{\psi_t}) \tag{2.6}$$

Where, the factor $2\pi/\hbar$ comes from the time dependent perturbation theory and $\delta(E_{\psi_s} - E_{\psi_t})$ has taken care the tunneling through only the same energy level. M is called tunneling matrix element which is integrated over the surface (dS) of the barrier region between the tip and sample. If we consider low energy tunneling associated with the overlap of electron wavefunctions of the tip and sample, M will have the following expression:

$$M = \frac{\hbar}{2\pi} \cdot \int_{x=x_0} \left(\psi_s^* \frac{\partial \psi_t}{\partial x} - \psi_t^* \frac{\partial \psi_s}{\partial x} \right) dS \tag{2.7}$$

Consider the scenario of a negative voltage ($V = -|V|$) applied to the sample. The relative changes of the Fermi level between the tip and sample is shown in Fig. 2.3(a). The tunneling current from the occupied states of the sample to the empty states of the tip (say ϵ with respect to the Fermi level, E_F) will be:

$$I_{sample \to tip} = -2e \cdot \frac{2\pi}{\hbar} \cdot \int_{-\infty}^{+\infty} |M|^2 \cdot \rho_s(\epsilon) f(\epsilon) \cdot \rho_t(\epsilon - eV)[1 - f(\epsilon - eV)] d\epsilon \tag{2.8}$$

Where, the factor 2 in front comes from electron's spin degeneracy; $\rho_s(\epsilon)$ and $\rho_t(\epsilon)$ are the DOS at energy ϵ with respect to the Fermi level E$_F$ of the sample and the tip, respectively. Here, $f(\epsilon)$ is known as the Fermi function which has the following expression:

$$f(\epsilon) = \frac{1}{1 + e^{\epsilon / k_B T}} \tag{2.9}$$

Similarly, there will be a tunneling current from the tip to the sample even though it's small. We can write down the expression of electron tunneling from the occupied states of the tip to the empty states of the sample as follows:

$$I_{tip \to sample} = -2e \cdot \frac{2\pi}{\hbar} \cdot \int_{-\infty}^{+\infty} |M|^2 \cdot \rho_s(\epsilon)[1 - f(\epsilon)] \cdot \rho_t(\epsilon - eV) f(\epsilon - eV) d\epsilon \tag{2.10}$$

The net tunneling current from the sample to the tip will be the sum of Eqn. 2.8 and Eqn. 2.10 integrated over all the possible energy states as:

$$I_T = -\frac{4\pi e}{\hbar} \cdot \int_{-\infty}^{\infty} |M|^2 \cdot \rho_s(\epsilon) \cdot \rho_t(\epsilon - eV) \cdot [f(\epsilon) - f(\epsilon - eV)] d\epsilon \tag{2.11}$$

The two main scenarios which depend on the applied bias voltage between the tip and the sample, are discussed below.

1) Low energy tunneling when $\epsilon \ll \Phi$

Let us assume that we have the situation at very low temperature ($T \approx 0$). Due to the very sharp step like behaviour of the Fermi function at low temperature, we could assume the value of the part $[f(\epsilon)$-$f(\epsilon - eV)]$ in 2.11 to be equal to 1 ($\approx$ the value at $T = 0$) within the energy range between -eV to 0. It becomes zero for the other values of ϵ. In addition to that, we chose a metallic tip e.g. tungsten (W) or Pt-Ir or gold (Au) because of its flat DOS [26] within the interested energy range[2]. Thus, we can take the tip DOS ($\rho_t(\epsilon)$) out from the integration. Furthermore, according to Bardeen's approach [28] the applied bias voltage is relatively tiny in compare to the vacuum barrier. So, the tip and sample wavefunctions fall exponentially within the barrier and their tails are overlapping, keeping the fact that they are not influencing each other. By considering the above assumptions, it can be either shown using WKB approximation or calculated explicitly from one step ahead of Bardeen's matrix element expression (see Ref. [25]) that the expression of the matrix element $|M|$ is

$$|M|^2 \propto e^{-2\frac{d}{\hbar}\sqrt{2m(\Phi-\epsilon)}} \tag{2.12}$$

Here, d, Φ, ϵ are the distance between the tip and sample, the vacuum potential barrier and the energy of the electron from the Fermi level, respectively. Usually, the vacuum potential barrier Φ can be approximated as a linear combination of the work function of the tip (ϕ_t) and the sample (ϕ_s). Typical values of ϕ_t or ϕ_s are of the order of a few electron volts. For example, the work function of tungsten metal is 4.8 eV [25]. Therefore, the approximated vacuum potential barrier Φ for low energy tunneling is sufficiently high so that the provided energy ϵ for electron tunneling can be considered to be negligibly small. Additionally, if the distance d between the tip and sample remains constant, we can take the matrix element M out from the integration as a constant. The final approximated expression of the low energy tunneling current will therefore be:

$$I_T \approx -\frac{4\pi e}{\hbar} \cdot \rho_t(0) \cdot |M|^2 \cdot \int_{-eV}^{0} \rho_s(\epsilon) d\epsilon, \quad \text{when } \Phi \gg \epsilon \tag{2.13}$$

Here, the $\rho_t(0)$ is the tip DOS at the Fermi level which can also be written down as $\rho_t(E_F)$. The situation of tunneling at a finite temperature is slightly different as the significant thermal broadening of the Fermi function has to be taken into account and

---

[2] This is roughly few hundred meV in our experiment.

thus, it needs to consider inside the integral instead of replacing by unity in the case of low temperature tunneling. Therefore, the correct expression for low energy tunneling at elevated temperature would be

$$I_T \approx -\frac{4\pi e}{\hbar} \cdot \rho_t(0) \cdot |M|^2 \cdot \int_{-eV}^{0} \rho_s(\epsilon) \cdot [f(\epsilon) - f(\epsilon - eV)] d\epsilon, \quad \text{when } \Phi \gg \epsilon \tag{2.14}$$

2) High energy tunneling when $\epsilon \approx \Phi$

In case of tunneling with energy of the order of eV, Bardeen's approximation will be invalid as there will be a significant influence of the tails of the tip and sample wavefunctions [25,26]. In this instance, the matrix element M cannot be energy independent and therefore, it needs to be considered inside the integration. The Tungsten (W) tip-state has an almost constant DOS within the energy range of ±3 eV as it was shown experimentally by Feenstra *et al.* [26]. Therefore, we can take the tip DOS out of the integral in this treatment, too. Thus, the modified tunneling current expression for high energy tunneling will have the following form:

$$I_T \approx -\frac{4\pi e}{\hbar} \cdot \rho_t(0) \cdot \int_{-eV}^{0} |M|^2 \cdot \rho_s(\epsilon) d\epsilon, \quad \text{when } \epsilon \approx \Phi \tag{2.15}$$

Here, we consider $[f(\epsilon) - f(\epsilon - eV)]$ to be constant and it has been taken out from the integration. Let us assume that the distance between the tip and the sample remains unchanged and redefine the energy dependent matrix element $|M|^2$ as $T(\epsilon,eV)$ for the next treatment when $\epsilon \approx \Phi$. We can write down the Eqn. 2.15 as follows:

$$I_T \propto \int_{-eV}^{0} T(\epsilon,eV). \rho_s(\epsilon) d\epsilon \tag{2.16}$$

The derivative of Eqn. 2.16 with respect to energy will be

$$\frac{\partial I_T}{\partial V} \propto e \cdot \rho_s(eV) \cdot T(eV,eV)\Big|_{V=-|V|} + e \cdot \int_{-eV}^{0} \rho_s(\epsilon). \frac{\mathrm{d}}{\mathrm{d}(eV)}[T(\epsilon,eV)] d\epsilon \tag{2.17}$$

Therefore dividing the Eqn. 2.17 by I_T/V, we end up with

$$\left.\frac{\partial I_T/\partial V}{I_T/V}\right|_{-eV} = \frac{\left.\rho_s(eV)\right|_{V=-|V|} + \int_{-eV}^{0} \frac{\rho_s(\epsilon)}{T(eV,eV)} \cdot \frac{d[T(\epsilon,eV)]}{d(eV)} d\epsilon}{\frac{1}{eV} \int_{-eV}^{0} \rho_s(\epsilon) \cdot \frac{T(\epsilon,eV)}{T(eV,eV)} d\epsilon} \tag{2.18}$$

Here, $T(\epsilon,eV)$ and $T(eV,eV)$ appear in the above expression as a ratio in the denominator which will cancel out as both of them have similar exponential dependency. As it was explained by Feenstra *et al.* in Ref. [26], the first term in the numerator is the DOS of the measured sample at energy $V = -|V|$. The second term in the numerator is the extra contribution arising from the fact that the tails of the tip and sample wavefunctions are affected significantly by the applied electric field in the junction, and with changing the applied voltage it changes. Now, during the sweeping of the energy of the sample with respect to the tip, two situations will arise. When the sample bias $V > 0$, the matrix element $T(eV,eV) \geqslant T(\epsilon,eV)$ provides the maximum transmission for $\epsilon = eV$. In this case, all the term of right hand side of Eqn. 2.18 will have the same order of magnitude. So, we end up with so called 'normalized' DOS together with slowly varying background. But, on the other hand for $V \leq 0$, $T(\epsilon,eV) \geqslant T(eV,eV)$ gives maximum probability at $\epsilon = 0$. In this situation, the background term in numerator will have the similar weightage like the denominator. But, both of them are larger than the sample DOS by a factor of $T(0,eV)/T(eV,eV)$ near the Fermi level. This implies that the measured spectra will be reduced by this amount as the transmission probability has a strongly peaked DOS near the Fermi level for negative energies. Therefore, one has to keep in mind that by this kind of normalization, we lose information close to the Fermi level.

2.4. Measurement modes

In STM, subatomic images use to capture in topography mode combined with their electronic information which is measured in spectroscopic mode. In this section, we will discuss different types of measurement modes based on Eqn. 2.14. As already mentioned before, the constant tip state of the used metallic tip (which is made of Tungsten (W) or Platinum (Pt)/Iridium (Ir) or Gold (Au)) does not influence the experiments (see Ref. [26]), and is therefore kept constant in the following expression. The bias voltage is applied to the sample with respect to the tip so that negative (positive) voltage probes the occupied (unoccupied) states of the sample. The typical energy applied to the sample, ϵ is in the range of milli-electron volts with respect to the Fermi level, comparatively lower than the vacuum barrier, Φ. Therefore, we can bring the matrix element out from the integration. Now, using the explicit expression of the matrix element from Eqn. 2.12 in Eqn. 2.14, the tunneling current expression will be

$$I_T \propto e^{-\frac{d}{\hbar}\sqrt{8m(\Phi-\epsilon)}} \cdot \int_{-eV}^{0} \rho_s(\epsilon) \cdot [f(\epsilon) - f(\epsilon - eV)] d\epsilon \tag{2.19}$$

So the tunneling current has mainly two dependencies. It is directly proportional to the integrated DOS of the sample, and it depends exponentially on the distance between the tip and sample. Note that, we have the Fermi function within the integration, too.

2.4.1. Topography

Measurement of an atomically resolved high precision electronic structure is one of the most powerful and common investigations in STM. There are two types of topography operations: i) constant current topography, ii) constant height topography. In this work, topography is mainly recorded in constant current mode which is discussed below.

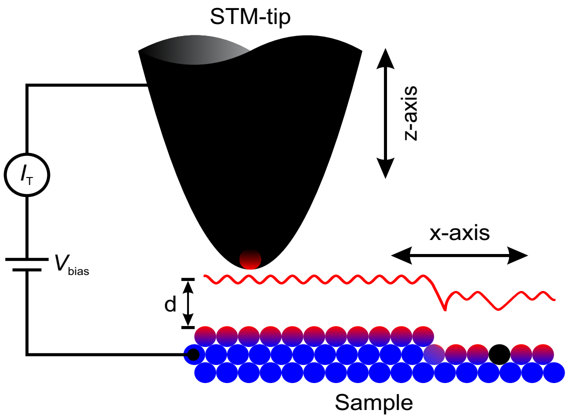

Figure 2.4.: Picture of a constant current mode topography measurement. In presence of applied bias voltage to the sample (say V_{bias}), when the tip is moving along x-axis, it follows the red oscillating path along the z-axis depending on the position of atoms, atomic edge or atomic defect to keep the tunneling current, I_T constant. The plot of the relative change of the tip-sample distance (δd) provides the topography information of the sample surface for each x-axis location. In fact for real STM measurement, the surface topography is recorded similarly for each (x, y) tip location over the sample surface.

Constant current topography:

According to Eqn. 2.19, if the integrated DOS remain constant during the measurement, the tunneling current I_T will be proportional to the exponential of the distance d between the tip and sample as follows:

$$I_T \propto e^{-\frac{d}{\hbar}\sqrt{8m\Phi'}} \tag{2.20}$$

Here, Φ' is equal to $\Phi - \epsilon$, known as the effective potential barrier. In this mode of operation, the tunneling current is kept constant during scanning over the sample surface as depicted in Fig. 2.4 in the presence of a constant bias voltage applied between the tip and sample. Depending on the position of atom, atomic step or adsorbate on the surface, the tip-sample separation d needs to be adjusted for each (x, y) location to keep I_T constant. Note that, in Fig. 2.4 the fast scanning direction along x-axis is only shown for the sake of simplicity. However, the colour plot of the change of the tip-sample separation, δd as a function of x and y position over the sample will provide the surface topography image of the sample. Additional information of the integrated DOS of the sample also use to record in the topography image in case of any inhomogeneous place of the sample e.g. on top of adsorbate or impurities/defects, adatom on the surface, etc. Thus, δd has only the information of the atomic corrugation over the surface in case of scanning over a homogeneous LDOS. Moreover, the change of the LDOS information for a chemically inhomogeneous sample affects the constant current mode topography image which can be seen in the image, too.

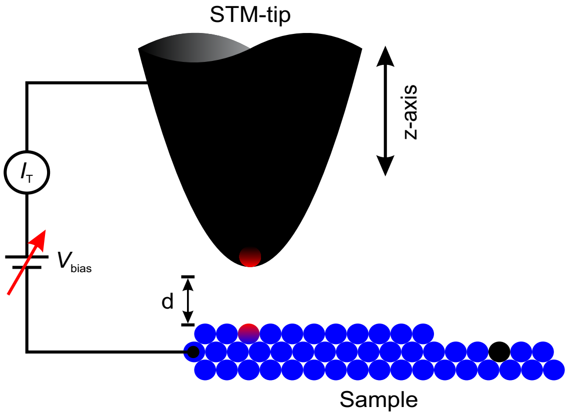

Figure 2.5.: Sketch of a spectroscopic measurement in STM. In this mode, the sweeping of the applied bias voltage is performed to record corresponding tunneling current while the tip is fixed on a particular position over the surface of the sample. The distance (d) between the tip and sample keeps constant during the measurement, too. The derivative of the I-V sweep is then directly proportional and corresponds to the LDOS of the sample.

2.4.2. Spectroscopy

Spectroscopy in STM/S provides differential conductance ($\mathrm{d}I/\mathrm{d}V$) which is directly proportional to the DOS of the sample at atomic precision, incomparable to other complementary technique e.g. ARPES, photoemission, etc. where such measurement is possible but average over a relatively larger surface area. The derivative of the tunneling current from Eqn. 2.19 for a constant tip-sample separation d is

$$\frac{dI_T}{dV}\bigg|_{V=-|V_{bias}|} \propto \int_{-\infty}^{\infty} \rho_s(\epsilon)\cdot\left[-\frac{\partial f(\epsilon-eV)}{\partial(eV)}\right]d\epsilon\bigg|_{V=-|V_{bias}|} \tag{2.21}$$

Where, the $\frac{dI_T}{dV}$ is directly proportional to the sample's LDOS at $V = -|V_{bias}|$ if we consider $\partial f(\epsilon - eV)/\partial(eV)$ as a sharp delta function ($T = 0$). Otherwise, it depends on LDOS of the sample convoluted with $\partial f(\epsilon - eV)/\partial(eV)$ which is a bell-shaped function for $T > 0$. The latter smears the LDOS features due to the finite temperature broadening of the Fermi function.

Technical details to measure LDOS:

The schematic picture is shown in Fig. 2.5 where the tunneling current I_T is recorded during the sweep of the bias voltage V_{bias} for a constant tip-sample separation at a particular (x, y) location on the sample. Eqn. 2.21 implies that the derivative of the tunneling current gives direct access to the LDOS of the sample at every energy to the occupied side for the energy range of $-|eV| < \epsilon < 0$. Similarly, we have access to the unoccupied LDOS of the sample within the energy range of $0 < \epsilon < |eV|$ while a positive voltage, V is applied to the sample relative to the tip. In principle, one can execute the numerical derivation of the recorded I-V sweep to access the LDOS of the sample. However, smoothing of the curve is often required in such procedure. But, the alternative as well as reliable method will be the use of the lock-in technique. In this case, instead of the numerical derivation, the slope ($\frac{dI_T}{dV}$) can be recorded at each point during the I-V sweep. For this purpose, a lock-in amplifier is used to modulate the bias voltage with an AC signal of a particular frequency. This modulation voltage is typically of the order of a few meV. The response AC signal will then be recorded in current channel depending on the slope of the I-V curve. The demodulated response signal from the current channel will be directly proportional to the LDOS of the sample. This is depicted in Fig. 2.6.

Energy resolution:

The energy resolution in STM is limited by the broadening of the Fermi function. The derivative of the Fermi function in Eqn. 2.21 is a bell-shaped function centred at $-|V_{bias}|$ with the full width half maxima (FWHM) of about $3.5k_BT$. The finite temperature therefore limits the energy resolution (ΔE) of the spectroscopic data in STS by this factor. For example in Fig. 2.7, the schematic representation depicts the band dispersion of a single band superconductor, the tunneling current and the differential conductance in STM/S study for various temperatures. Here, the thermal broadening causes a smearing of superconducting coherence peaks at $0 < T < T_c$ (see Fig. 2.7(c)). In Fig. 2.8, the temperature dependent pictorial plots of the derivative of the Fermi function show how the finite temperature limits the energy resolution in STM. Here, the two delta peaks separated by 1.7 mV smear out and barely distinguishable due to the thermal broadening of the Fermi function at 6 K. Therefore, to get better resolu-

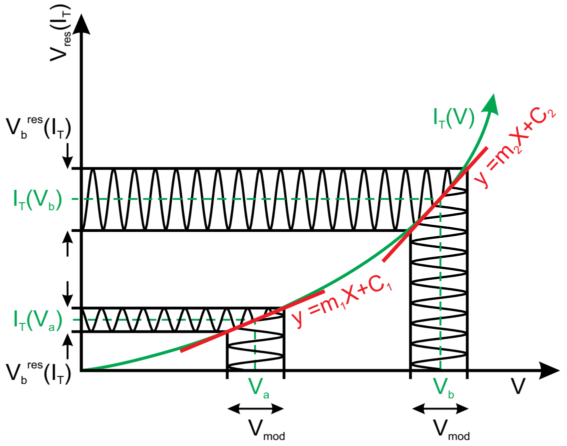

Figure 2.6.: The schematic diagram of the lock-in technique to measure directly the LDOS of the sample during the spectroscopic (I-V) sweep. The green curve is the exemplary tunneling current I_T as a function of applied bias voltage (V). Let us consider that we are interested to know the slope i.e. dI/dV at V_a and V_b point on the curve. The red straight lines are the slope of the curve at those points. While modulation voltage (V_{mod}) modulates the voltage in the horizontal axis, the response signals (V_{res}) in vertical axis have different amplitudes depending on the slope at V_a and V_b.

tion, low temperature spectroscopic measurements in STM are required. The typical energy resolution at base temperature (4.8 K) of our system is around 1.4 meV. The expression of such energy resolution in presence of a modulation signal (V_{mod}) at a finite temperature (T) is the following:

$$\Delta E \approx \sqrt{(\Delta E_{thermal})^2 + (\Delta E_{mod})^2} \approx \sqrt{(3.5k_B T)^2 + (2.5eV_{mod})^2} \tag{2.22}$$

The first term on the right hand side is the contribution of finite temperature broadening whereas the second term takes care the broadening caused by the applied modulation voltage during spectroscopic measurement.

2.4.3. Spectroscopic map

The measurement of the spectroscopic map in STM/S contains informations about spatially as well as energy resolved spectroscopic data with topography. In this case, the tip is moved over every pixel i.e. (x, y) position of the sample and performs the I-V sweep and simultaneously records the dI/dV for a certain area. Such a spectroscopic map provides a handful of informations [21,30] which are shown in Fig. 2.9. The energy resolved dI/dV informations are recorded for every x-y location on the sample. A few selected energy slices from a spectroscopic map on a off-stoichiometric LiFeAs are shown

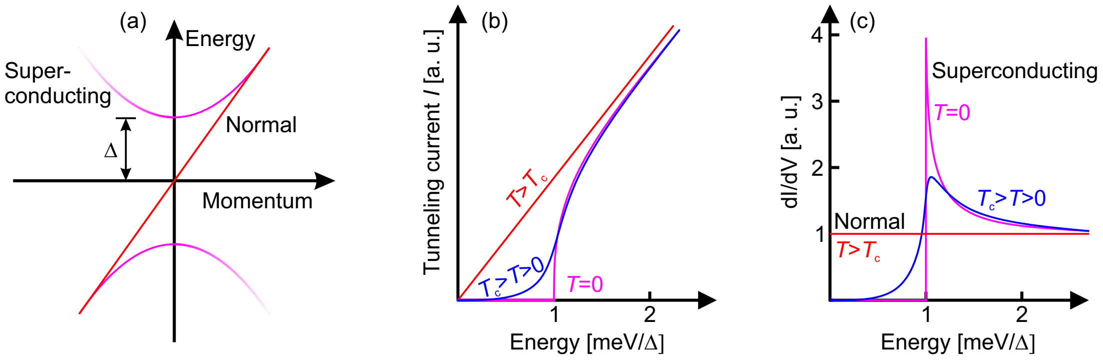

Figure 2.7.: A pictorial representation of band dispersion and spectroscopic measurements in STM at various temperatures. These finite temperatures effect on energy resolution due to thermal broadening of Fermi function. (a) A single band dispersion plot of a superconductor for its superconducting ($T < T_c$) and normal state ($T > T_c$). (b) The I-V data from tunneling measurement for three different temperatures on such superconductor. (c) The corresponding differential conductance ($\mathrm{d}I/\mathrm{d}V$) shows δ-peak like superconducting gap (pink curve) for T $\simeq$ 0, while it becomes broadened (blue curve) in case of $0 < T < T_c$ due to the Fermi function broadening at finite temperature and disappears above $T > T_c$ as one would expect in normal state.

in Fig. 2.9(b) in the normal state. In Fig. 2.9(a), the spectroscopic data are shown on a particular location on the surface of the sample, indicated by the green dashed vertical line. The $\mathrm{d}I/\mathrm{d}V$ map at a fixed energy is plotted in Fig. 2.9(c). Nevertheless, the topography information i.e. the integrated $\mathrm{d}I/\mathrm{d}V$ informations can also be achieved from such measurement as it is shown in Fig. 2.9(d). One can analyse these data to know further electronic informations as discussed below. The spectra on top of defects or impurities can be compared with the bare surface spectra to find their electronic origin [31–33]. The transformation of those energy slices in Fourier space is also useful to search for dominant quasiparticle scattering, and hence to learn about the electronic informations e.g. band dispersion. Nevertheless, some technical difficulties are present to measure such maps. Most of the time, these spectroscopic maps take measurement time from a few hours to a few days. Therefore, low temperature very stable STM is required to avoid thermal drift effect during the data acquisitions. Our system "Dip-Stick STM" (see chapter 4) is a unique, very stable system where the study of long term spectroscopic maps at base temperature as well as at elevated temperatures are being carried out successfully due to the high thermal stability of the system even at elevated temperature (see 6.2.2 and 6.3 in result section). One example of such spectroscopic maps can be found in section 6.3 where systematic temperature dependent spectroscopic map measurements have been studied for the first time to disentangle the normal state and superconducting state in stoichiometric LiFeAs.

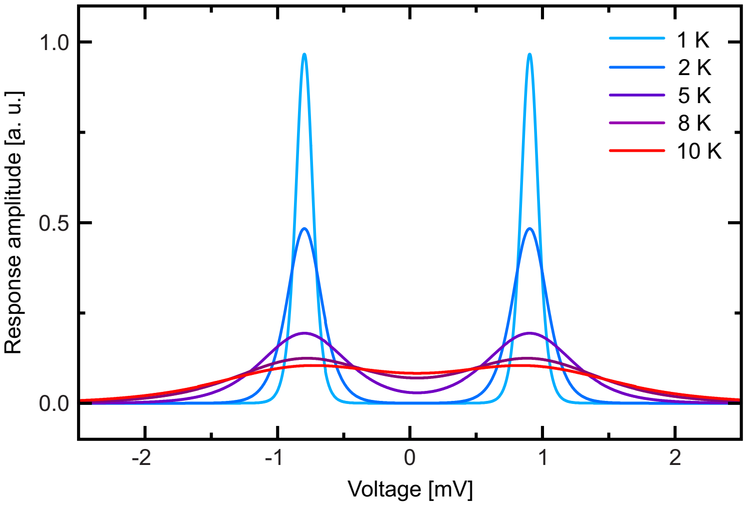

Figure 2.8.: An example of smearing of spectral feature at finite temperature due to thermal broadening. Here, two δ peaks are separated by 1.7 mV which is thermally broadened by bell-shaped $\partial f(\epsilon - eV, T)/\partial(eV)|_{V=\pm 0.85\ mV}$ at several temperatures. The sharp peaks gradually smear out with increasing temperature and at around 6 K they are barely distinguishable. The energy resolution, ΔE at 6 K is thus 1.7 meV. *Courtesy: Danny Baumann.*

2.4.4. dI/dV map

Instead of time consuming full spectroscopic measurement, the dI/dV informations on the sample at a specific energy during the topography scan can be measured, which is known as dI/dV map. Usually, it can be recorded very fast and with much higher lateral resolution. Technically, a small modulation voltage from a lock-in amplifier is used during the topography scan to get a response signal which is directly proportional to the LDOS of the sample at the scanned (stabilized) energy. The typical time required for the tip to spend for every pixel during a dI/dV map, must be sufficient enough to get the reasonable response signal from the system. In addition, the feed-back loop needs to be carefully adjusted to minimize the effect of the inhomogeneous LDOS of the sample on the tip-sample distance d which is known as z-point effect (see [18]). The drawbacks of this mode of operation are the following. One cannot compare two dI/dV maps measured at different energies as there will be the z-point effect due to the variation of the LDOS of the sample [18]. Another important drawback comes from the possibility of dI/dV map measurement only at stabilized energy (V_{bias}) of topography scan e.g. dI/dV map at zero bias is not possible as topography cannot be measured with zero applied bias voltage.

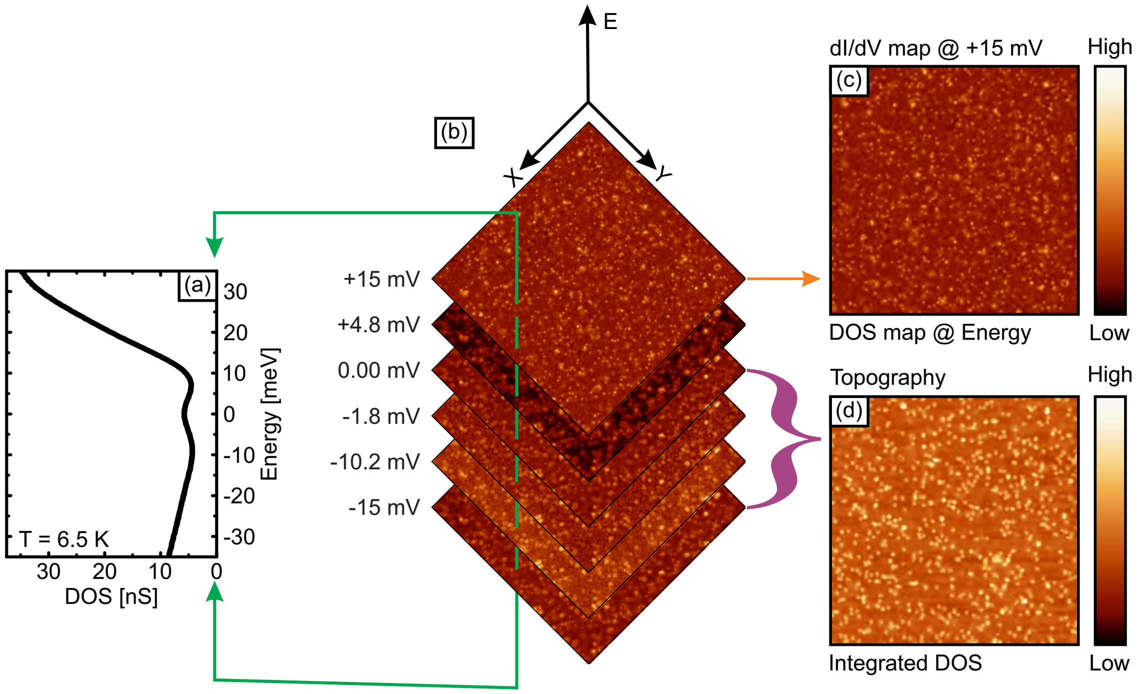

Figure 2.9.: The example of a four dimensional data set in spectroscopic map to measure LDOS(x, y, Energy) of the sample. (a) Point spectra on the surface marked by the vertical dotted green line. (b) A few exemplary energy slices where LDOS have been recorded as a function of x-y lateral positions on the sample on (b). Here, the z-axis represents the energy slices. (c) Each representative energy slice from (b) is sometime called as dI/dV map, i.e. the LDOS at a particular energy. (d) Corresponding topography i.e. the integrated LDOS information of the sample.

3. Quasiparticle interference

3.1. Friedel oscillation

When electrons are scattered off around the point-like impurities in a metal, they create oscillating charge density patterns around the impurities, known as Friedel oscillation [34, 35]. The origin of such standing wave modulation on the surface is the interference of the incoming electron with the outgoing back-scattered-electron (assuming Born approximation to be valid which I will discuss later in this chapter) by point-like impurity or at the step-edge. Roughly two decades back, STM/S had provided the striking experimental evidence of such two dimensional electronic standing waves on Cu(111) [36] and Au(111) [37] surfaces. They are so called "Friedel oscillation". It is worthwhile to take a look at these early results as they on the one hand illustrate the phenomenon, and on the other hand, already point out, how the method may be used for exploring unknown electronic structure of exotic materials. Fig. 3.1(a) shows the charge density modulation over step edges and around point-like defects measured on Cu(111) surface. The electron density modulations $\rho_s(E,x)$ from step-edge at several selected energies (E) are shown in Fig. 3.1(b) as solid lines. The dashed lines are the fitted curves using the formula [36, 37]

$$\rho_s(E,x) \propto \{1 - J_0(2q(E)x)\}, \tag{3.1}$$

Where, E, x, q, J_0 are the energy, the distance from the step-edge, the wave vector corresponding to the energy E and the zeroth order Bessel function, respectively. The energy dependent wave modulations are distinctly visible from such plot which can be fitted well with the dispersive energy dependent DOS Eqn. 3.1. A similar analysis of the electronic modulation has also been done for point-like impurities. Latter, the radial distance (r) from the centre of those impurity has been considered using the following equation

$$\rho_s(E,x) \propto 1 + \frac{2}{\pi q r}\Big[cos^2\Big(qr - \frac{\pi}{4} + \eta_0\Big) - cos^2\Big(qr - \frac{\pi}{4}\Big)\Big], \tag{3.2}$$

Where, r, η_0 represent the radial distance from the centre of an impurity and a phase shift, respectively. The wave vector (q) corresponding to every energy (E) can be extracted using both of the above fitting equations related to the electron density modulation $\rho_s(E,x)$. An example of those wave vectors at various energies for density wave modulation from step edge is plotted in the inset of Fig. 3.1(b) where the band dispersion can be found with a band minima occurred at about -0.44±0.01 eV. Later, Petersen *et al.* [38] (see Fig. 3.2) has shown the Fourier transformation of such 2-dimensional wave modulation pattern on Cu(111). Main observation was a ring like dominant scattering of scattering wave vector $q = 2\vec{k}_F$. This is called constant energy contour (CEC) which is directly connected to the band dispersion in the range of the stabilized energy (see Fig. 3.2(b)) due to the elastically scattering of electron. These studies are not only a text book like examples for the experimental proof of standing wave oscillation, but these are also useful to study those electronic properties which are directly connected to the band dispersion of the material.

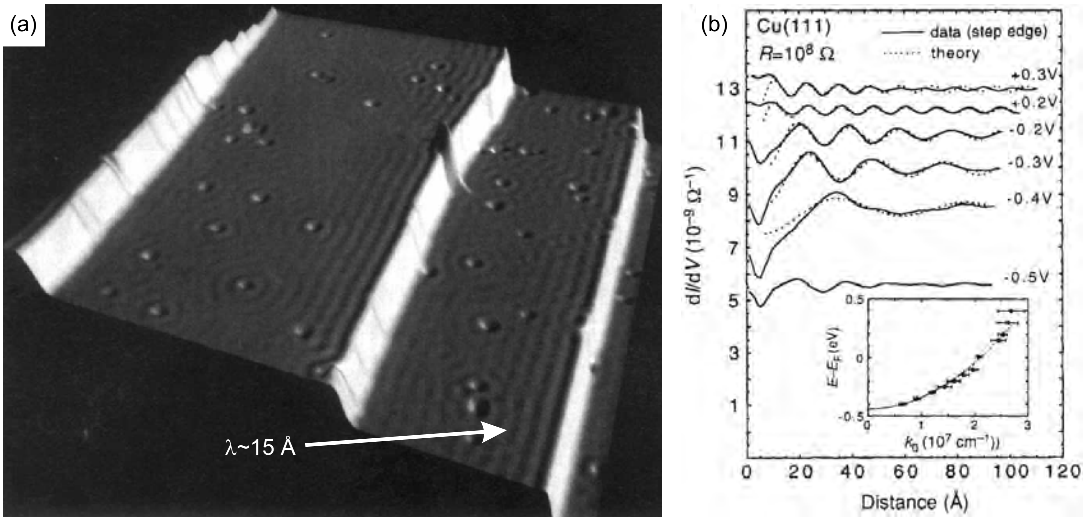

Figure 3.1.: (a) An example of Friedel oscillation in Constant current STM image of 50×50 nm^2 area at V_{bias}=100 mV and I_T = 1 nA measured at a temperature of 4 K on Cu(111) which is taken from Ref. [36]. Three mono atomic steps and 50 point defects are clearly visible over the surface. The spatial oscillations close to step edge and around point defects with a periodicity of ≈ 15 Å are clearly visible, too. (b) The solid lines are the dI/dV signal measured at different energies at a distance from the step edge. The dashed lines are the fits by Eqn. 3.1. Inset: The dispersion relation extracted from fitted data shows electronic band dispersion, and its minima which has occurred at -0.44 eV.

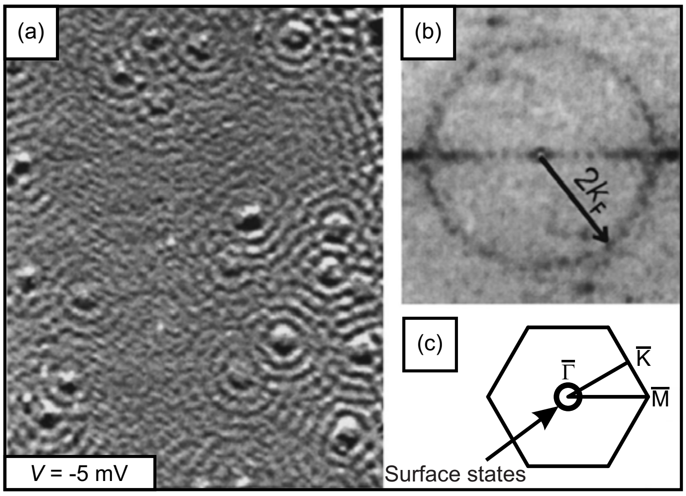

Figure 3.2.: An example of a constant energy contour extracted from Friedel oscillation in STM measurement as shown in Ref. [38]. (a) Constant current STM image of 42.5×55 nm^2 area at -5 mV energy taken at a temperature of 150 K on Cu(111). The ring like pattern around point defects can be seen clearly. (b) The 2D Fourier transform of image in (a). (c) The picture of the 2-dimensional surface Brillouin zone of Cu(111) with the Fermi contour.

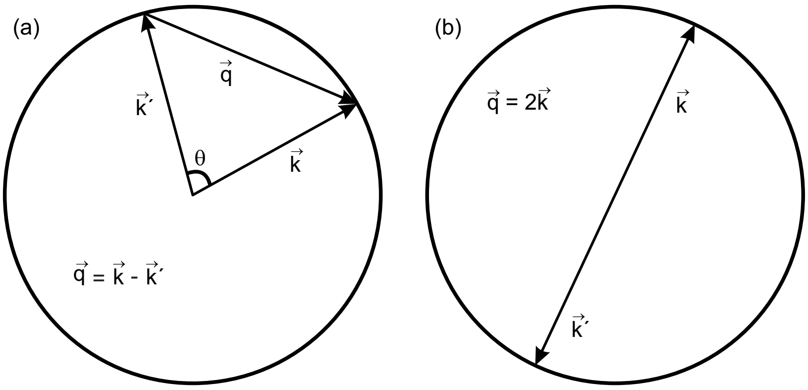

Figure 3.3.: (a) Constant energy contour where incident wave vector $\vec{k}$ of the quasiparticle is transferred to wave vector $\vec{k'}$ after being scattered by an angle of θ. (b) Most probable scattering happens for back scattering where $q = 2\vec{k}$.

3.2. Born Approximation

Fig. 3.3(a) shows the schematic plot of scattering of an electron's incident wave vector $\vec{k}$ which goes to final wave vector $\vec{k'}$ after being scattered by an angle θ. Neglecting the interaction between different scattering centres, one can calculate the scattering differential cross section for a low energy soft scattering event according to first order Born approximation [27] as

$$\frac{d\sigma}{d\Omega} \propto \frac{1}{sin^4(\theta/2)} \tag{3.3}$$

Where, $\frac{d\sigma}{d\Omega}$ and θ are the differential scattering cross section and angle between the initial and the final wave vectors $\vec{k}$ and $\vec{k}'$, respectively. According to Eqn. 3.3, the maximum scattering probability happens in case of back-scattering for $\theta = \pi$ when $\vec{q}$ becomes equal to $2\vec{k}$. This is illustrated in Fig. 3.3(b). Such back-scattering phenomenon described by the model of first order Born approximation has been observed experimentally on single band Cu(111) surface [36,38,39]. In the case of a strongly correlated electron system, the situation is more complicated and higher order scattering processes beyond Born approximation must be taken into account for an interpretation of experimental results. The corresponding theoretical approach is the self-consistent T-matrix calculation [40].

4. Experimental setup and data analysis

All the STM/S measurements which will be presented in this thesis, are measured using a custom built STM [31, 41] also called "Dip-Stick STM" which is shown in Fig. 4.1. It is working from room temperature down to liquid ^{4}He temperature ($\approx$ 4.8 K). The tremendous stabilities at base temperature as well as at elevated temperatures allow us to investigate the electronic properties of exotic materials with very high accuracy. The temperature dependent spectroscopic measurement in the result section is a clear proof of the stability of the system. In Fig. 4.1(a), a sketch of the full Dip-Stick STM setup together with a 200 liters liquid ^{4}He dewar is shown. The whole system is lifted by a damping frame, mainly to counteract the surrounding acoustic noise. The standard design of the system even allows to measure on commercially available bath cryostat e.g. Oxford low loss bath cryostat for measurements at various temperatures. Sketch of the Dip-Stick STM is shown in Fig. 4.1(b). Details of the important parts of it are listed in the caption of the image. The cold spot of the system is at the copper disk marked by 4 in Fig. 4.1(b) which is connected to the liquid Helium bath by brass part of the outer cylinder. The connection of the pump and the *in situ* cleaving mechanism control are marked by 2 and 1. The usual time required to cool down the system from room temperature to base temperature is around 12 hrs.

Measurement time:

The standard design of STM gives the possibility to measure at different cryostat. The commercially available bath cryostat e.g. Oxford ^{4}He cryostat can be used to measure at low temperature where the measurement time of the system is around 10 days at base temperature. But the measurement time can be increased up to 8 weeks using home made 220 liters liquid ^{4}He dewar for long term measurements at elevated temperatures.

STM Head:

The design of our home built Dip-Stick STM head is based on the Pan style [45] which is modified for *in situ* cleaving. The body of the STM head together with the sample holder section and the top plate where the heating cup and the stainless steel capillary tubes are attached, is made of gold-plated phosphor bronze. All parts of the STM head

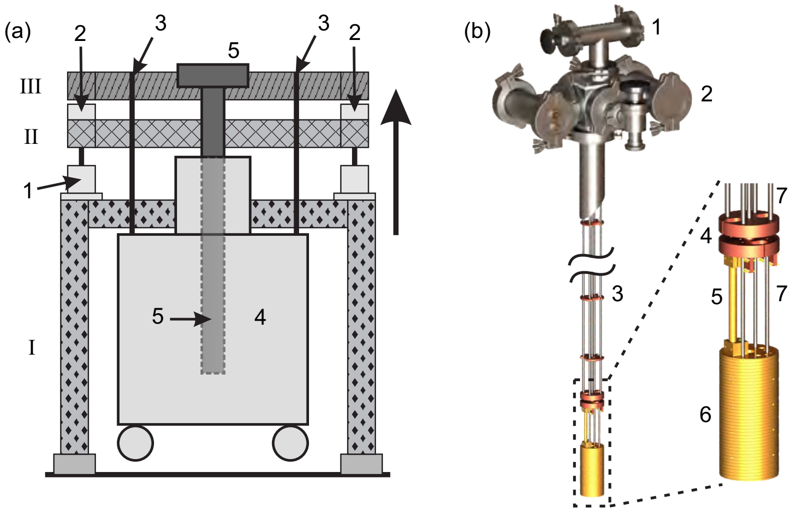

Figure 4.1.: (a) Schematic diagram of the full Dip-Stick STM cooled down in a liquid ^4He dewar. The whole setup is lifted by a damping frame. The frame is divided in three sub frames for the purpose of supporting (I, diamonds), lifting (II, crossed lines), and damping (III, diagonal lines): (1) air compact cylinders for lifting, (2) air springs, (3) heavy duty straps, (4) ^{4}He-dewar, and (5) STM system. (b) Design of the Dip-Stick STM system with a section through the stainless steel tube. The middle part has been cut out for better visualization. The image magnification shows the cold section with the heater cup attached to the STM head. (1) Cleaving mechanism control, (2) connections for electrical wiring and pumping, (3) stainless steel capillary tubes with heat radiation baffles, (4) copper disks for thermal coupling to the helium reservoir, (5) thermal connection to the STM head, (6) STM head with heating cup, and (7) stainless steel capillary tubes. This is taken from Ref. [42].

are made out of non-magnetic materials to minimize magnetic stray fields at the sample position. This will also help for external magnetic field measurements without any additional modification of the field at the sample position.

The major part of the STM head (see Fig. 4.2) is the scanner unit which consists of three parts namely, the sapphire prism (11), the scanner tube holder (10), and the scanner tube (15). The scanner tube is mounted inside the prism. The most important part of the STM head, the scanner tube has five piezoelectric connections. Four segments on the outside of the tube are the x/y-electrodes for scanning along lateral directions and one inside of the tube is for the z-electrode for expansion/contraction along depth direction. At a temperature of 300 K (4.8 K), the range of the scanner tube is 2.0 μm (800 nm) and 1.4 μm (260 nm) along the x/y and z-directions, respectively. A Macor socket with a molybdenum spring is installed on the end of the scanner tube to allow an easy exchange of the tip holder (16).

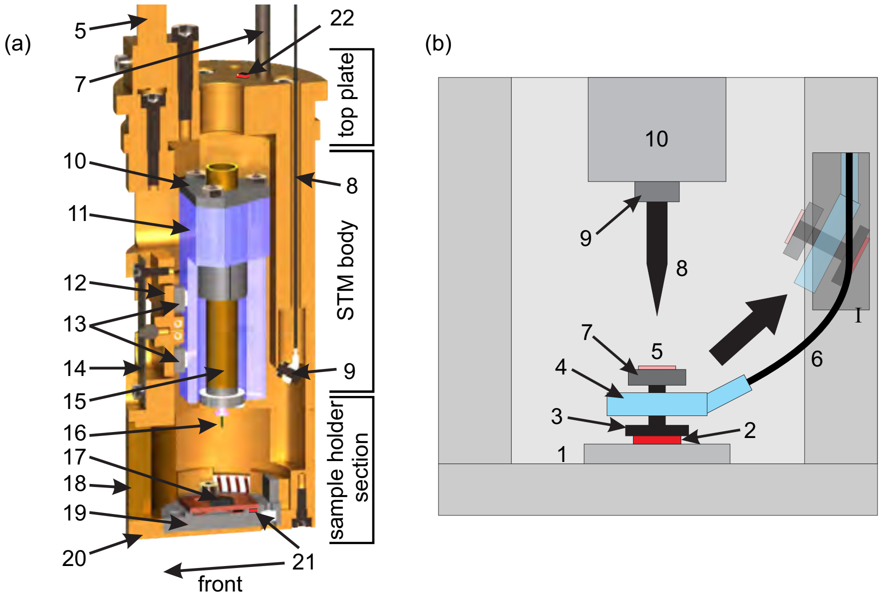

Figure 4.2.: (a) Schematic section of the STM head which can be divided into three sections: top plate, STM body, and sample holder section: (5) thermal connection, (7) stainless steel capillary tube, (8) cleaving wire, (9) cleaving stamp, (10) tube scanner holder (Macor) [43] (11) sapphire prism, (12) counterpart plate, (13) shear-piezo stacks, (14) molybdenum leaf spring, (15) tube scanner, (16) tip holder with tip, (17) sample, (18) front panel, (19) Macor part for bias insulation, (20) bottom plate, (21) Cernox [44] sample temperature sensor, and (22) Cernox STM body temperature sensor. (b) Scheme of a prepared and mounted sample. The movement of the cleaving stamp during the cleaving procedure is indicated by the broad arrow. (1) Sample holder, (2) sample, (3) cleaving post with a screw thread on one end, (4) insulating eye, (5) test sample (e.g., gold on mica), (6) cleaving wire, (7) screw nut, (8) tip, (9) tip holder, (10) scanner unit, (I) parking position of the cleaving stamp. The insulating eye is made of copper and soldered to the cleaving wire. A coating of Epotek H70E25 insulating glue prevents short-circuiting V_{bias} and ground. This is taken from Ref. [42].

The coarse approach movement of the scanner tube is done by six piezoelectric walker stacks (13). These walker stacks have been assembled using conductive glue. A polished Al_2O_3 plate at the interface between the piezoelectric stacks and the sapphire prism allows the coarse approach movement by slip-stick operating mode [46]. Four of those stacks are directly attached to the STM body where the remaining two are attached to the counter plate of the body which is pressed against the sapphire prism by a molybdenum spring (14). By changing the spring force, the friction between the sapphire prism and the Al_2O_3 plates can be adjusted. At the optimum condition, the coarse approach step width is approximately 250 nm (75 nm) at a temperature of 300 K (4.8 K).

Figure 4.3.: The picture of Ar glove box. The attached 2 meters long neck allows us to mount sample to the Dip-Stick STM inside the glove box without sample exposed to the air. The NQR spectra (e.g. Fig. 6.9) have been measured at ambient condition inside this glove to check the sample quality prior to mounting it to the STM.

Sample cleaving:

An atomically cleaned surface is usually required for high-resolution STM studies. The possibility of sample cleaving at any temperature between room temperature and base temperature (around liquid ^{4}He temperature) is the one major advantage of the system compared to available low temperature STM systems to produce cleaned surface for STM measurements until now. For example, the cleaving of stoichiometric LiFeAs at base temperature of 4.8 K creates an atomically flat non-polar surface [47–49]. Nevertheless, if there is any crystal which cleaves better at some certain temperature between 5 K and room temperature, it can be performed in this STM setup.

A sketch of the sample cleaving mechanism is shown in Fig. 4.2(b) where the red part (labelled by (2)) is the sample on top of which a cleaving stamp (3) is glued. The cleaving wire is fastened to the cleaving stamp by using a screw to the other end (4, 6, 7). The top of the screw holds the Au-on-Mica (5) on top. After cooling down the system, the tip can be characterized by scanning on the reference sample (for example Au-on-Mica) before the sample cleaving is executed. Once, proper characterization of the tip is done, the maximum retract is being conducted to have around 20 mm of space between the tip and sample. Now the cleaving is executed by pulling the cleaving wire from outside. The cleaving stamp together with Au-on-Mica and the cleaved part of the sample will go to the shaded position (I) as shown in Fig. 4.2(b). In this situation, the characterized STM tip has access to the freshly cleaved surface of the sample for measurements.

Sample handling:

Our Dip-Stick system works at cryogenic (liquid ^{4}He temperature) vacuum condition. The pressure at the STM head during experiment is below 10^{-10} mbar. Therefore, the measurement on air sensitive samples does not show any degradation with time during continuous experiments, conducted over 5-6 months. But, the difficulties come from the sample mounting in STM head. For this purpose, a long neck (2 meters long) glove box is used for sample mounting in ambient condition at Argon atmosphere as shown in Fig. 4.3. The whole Dip-Stick STM is transferred to the Argon glove box where mounting of the sample, the cleaving stamp and the STM-tip are carried out. Air-sensitive samples like LiFeAs, NaFeAs, FeSe have also been handled with great care to protect any sample being exposed to air during the sample transfer to the glove box. This procedure leaves the sample quality unaffected during handling of the sample. Once the sample mounting is done inside the glove box, a turbo pump is connected immediately to the pumping port of the STM to pump out the Argon gas and reach a pressure of 10^{-6} mbar prior to cooling down the whole system to liquid ^{4}He temperature.

Preparation of tungsten tip:

The electrochemically etched tungsten (W) wire of 0.5 mm diameter by 8% NaOH solution at ambient condition is used as STM-tip for measurements. Usually, the surface of the tip is covered with 100-200 nm layers of tungsten oxide during the etching process. Therefore, tip treatment to remove such oxide layers before the measurement of the sample, is required. Such tip preparation can be done by fast scanning and pulsing on Au-on-Mica several times at around 5 K and cryogenic vacuum which in principle is possible in our system before the sample is being cleaved (see label (5) in Fig. 4.2(b)). The other possibility is the flashing of the electrochemically etched W-tip at 10^{-7} mbar pressure at the temperature of around 2000°C to melt the tungsten oxide layer which is shown in Fig. 4.4. Later, the flashed W-tip can also be characterized on Au-on-Mica to check the quality of it before measurement on the sample.

4.1. Technical aspects of discrete Fourier transform of spectroscopic maps

In this section, I will discuss the technical aspect of First Fourier Transform (FFT) of the measured energy resolved $\mathrm{d}I/\mathrm{d}V$ slices to extract the energy dependence scattering vectors [50]. To be very specific, two-dimensional discrete Fourier transform is necessary to perform on the measured data. Let us consider that we have a simple situation where we are interested to know the discrete Fourier transform of a real-space wave pattern of

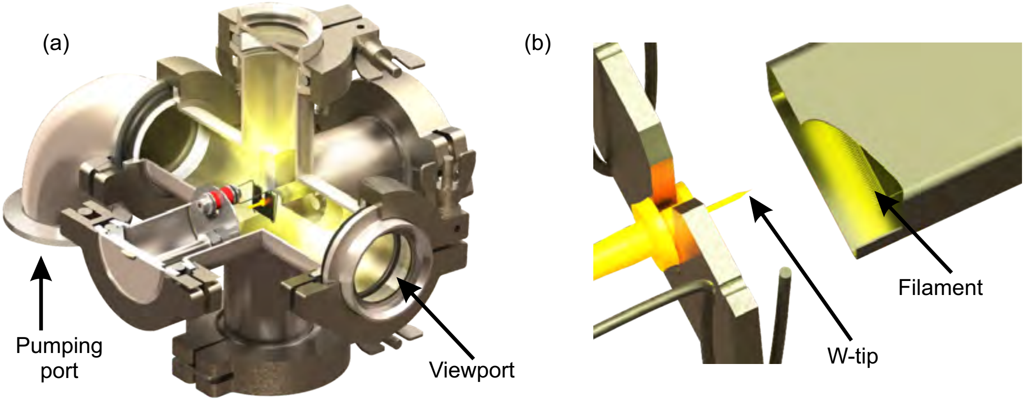

Figure 4.4.: (a) The sketch of a flash box for W-tip flashing. (b) Enlarged picture close to the centre of the flash box to show the W-tip with the tip holder and the filament. During flashing, this filament heats up the end part of the tip more than the temperature of 2000°C at a pressure of about 10^{-7} mbar to melt and remove tungsten oxide layers from the tip.

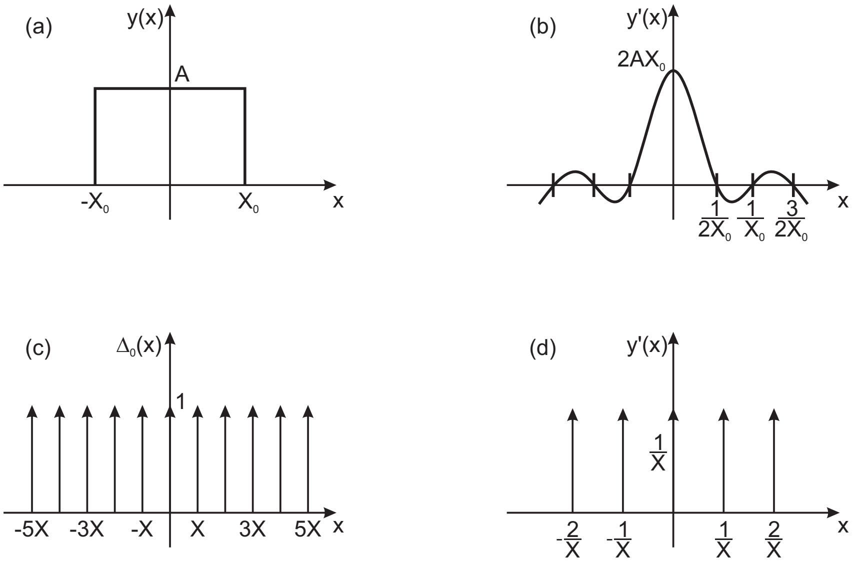

Figure 4.5.: Plots of rectangular and delta functions are shown in (a) and (c), respectively. (b) and (d) are the corresponding Fourier transformations of those functions.

a continuous function, $h(x)$ in one-dimension. Unlike continuous Fourier transform, we have discrete measurement point of $h(x)$ in real space. Impulse or delta function (say $\Delta_0(x)$) with measurement interval (δx) therefore needs to be multiplied to the $h(x)$ to describe the measurement data. Lastly, the finite length of the measurement data (say X_0) is also necessary to incorporate into the final expression. Let us consider a rectangular wave form (say $y(x)$) that describes the finite measurement length. An example of both the rectangular and impulse functions with their Fourier transformed function is described in Fig. 4.5. Thus, the final expression which needs to be Fourier transformed in discrete Fourier transform, is as follows:

$$f(x) = h(x).\,\Delta_0(x).\,y(x) \; = h(x).\sum_{n=0}^{N}\delta(x - n\cdot\delta x)\cdot y(x) \tag{4.1}$$

Where, N is the total number of pixels and δx is the spacing between two consecutive measurement points, and thus $N \cdot \delta x = X_0$. The expression of the rectangular wave form, $y(x)$ is

$$y(x) = \begin{cases} 1, & \text{when } |x| < X_0 \\ 1/2, & \text{when } |x| = X_0 \\ 0, & \text{when } |x| > X_0 \end{cases} \tag{4.2}$$

If $f'(\lambda)$, $h'(\lambda)$, $\Delta_0'(\lambda)$ and $y'(\lambda)$ (here $\lambda = 1/x$) are the individual Fourier transformation of the functions $f(x)$, $h(x)$, $\Delta_0(x)$ and $y(x)$, respectively, according to the rules of Fourier transformation [50], the expression of $f'(\lambda)$ will be:

$$f'(\lambda) = h'(\lambda).\,\Delta_0'(\lambda).\,y'(\lambda) \tag{4.3}$$

One can calculate the exact expression of $\Delta_0'(\lambda)$ as $\frac{1}{\delta x}\sum_{n=0}^{N}\delta(\lambda - \frac{n}{\delta x})$ and $y'(\lambda)$ as $X_0\frac{sin(\pi X_0\lambda)}{\pi X_0\lambda}$. The expression $\frac{sin(\pi X_0\lambda)}{\pi X_0\lambda}$ has a maximum value, X_0 at $\lambda = 0$ and first minimum occurs at $\lambda = 1/X_0$. Therefore, the intensity in the Fourier transformation of the signal $f'(\lambda)$ is the Fourier transformed intensity of $h'(\lambda)$ multiplied by $X_0/(\delta x)$ i.e. N. Thus, the actual intensity of a signal (in this case $h'(\lambda)$) in FFT needs to factor down by the number of pixels (N) to get real amplitude of the signal $h'(\lambda)$.

Sampling theorem:

According to sampling theory, if the Fourier transform of a function $h(x)$, $h'(\lambda)$ has finite value only for certain λ less than λ_c, then the continuous function, $h(x)$ can be uniquely determined from a knowledge of its sample values as

$$h(x) = \sum_{n=-\infty}^{+\infty} h'(n\cdot\delta x)\cdot\delta(x - n\cdot\delta x) \tag{4.4}$$

where $\delta x = 1/2\lambda_c$ and $\lambda = 1/x$. To observe the frequency of any periodic pattern (say λ_c) the relation $1/x = 2\lambda_c$ requires to fulfil which is known as Nyquist sampling rate [50]. This means in real space at least two sampling points are required within a period of a signal to observe the corresponding frequency in the Fourier transform.

5. Superconductivity in Fe-based high temperature superconductors

5.1. Introduction

In 1911, Heike Kamerlingh Onnes had found zero electrical resistance in Mercury (Hg) below 4.2 K which was the discovery of a new phase in matter known as superconductivity (see Fig. 5.1). Around 50 years later in 1957, the first microscopic theory of superconductivity was given by J. Bardeen, L. Cooper and J.R. Schrieffer[1] which is known as BCS theory [51]. According to this theory, phonon[2] mediated attractive electron-electron interactions (see Fig. 5.2(a)) act as the pairing glue for the formation of Cooper pairs (Pair of electrons with opposite momenta and integer spin[3]) near the Fermi level, which are the key ingredients for superconductivity. The BCS theory which is based on such weak electron-phonon interactions, is consistent to explain the superconductivity in almost all the conventional (elementary) superconductors. Later, the discovery of Cu-based high-T_c superconductors (Cu-HTSC) in 1986 by two IBM researchers J. G. Bednorz and K. A. Müller was the beginning of a new era in superconductivity where the weak electron-phonon coupling BCS theory turns out to be insufficient to explain the physical origin of superconductivity in these unconventional superconductors. They first observed superconductivity below 30 K in $\mathrm{Ba}_x\mathrm{La}_{5-x}\mathrm{Cu}_5\mathrm{O}_{5(3-y)}$ [52]. Later, the increase of superconducting T_c was found in other subclasses of this class of compounds above liquid nitrogen temperature e.g. Y-123 T_c=92 K [53], Hg-1223 with T_c=140 K [54], etc. However, the nature of superconductivity here is very different than the conventional superconductivity, e.g. superconductivity and magnetism are observed to compete with each other, electron-boson coupling is found to be relatively high, etc. But, no established microscopic theory can explain these features up to now. It therefore still remains a hot research area in the field of superconductivity.

In 2008, another new class of Fe-based high-T_c unconventional superconductors (Fe-HTSC) [2–4, 63–65] was discovered when Kamihara *et al.* [6] found $\mathrm{LaO}_{1-x}\mathrm{F}_x\mathrm{FeAs}$

---

[1] They were awarded the 1962 Nobel prize for the discovery of BCS theory.

[2] The more general concept is to use the term "boson" which originates from phonon, spin-fluctuation, magnon, etc.

[3] The total Cooper pair spin will be 0 or 1 for the case of singlet or triplet, respectively because Cooper pairs are bosonic excitation near the Fermi level.

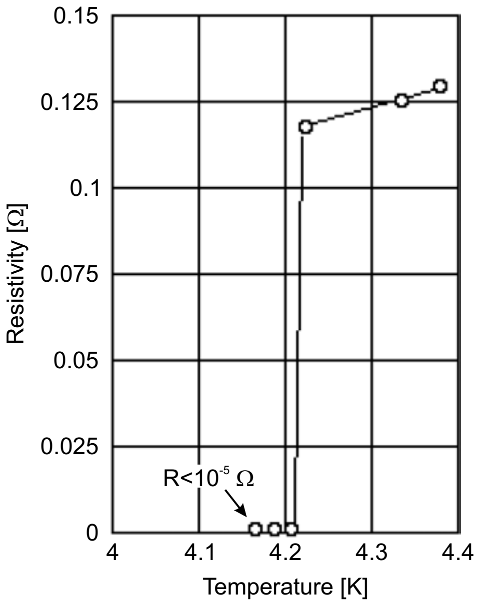

Figure 5.1.: Zero electrical resistance in Hg wire below 4.2 K (liquid He temperature) as it was observed by Heike Kamerlingh Onnes in 1911 for the first time [55].

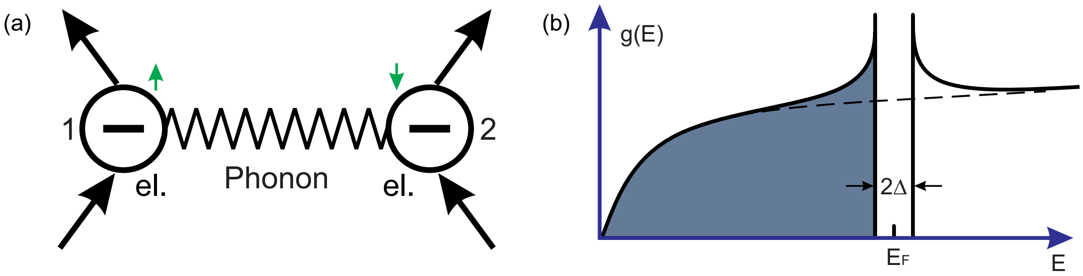

Figure 5.2.: (a) Schematic picture of bound state of electrons with opposite momentum vectors and spins (known as Cooper pair) via exchange of phonons, taken from Ref. [56]. The green arrows show the electron's spins. (b) Qualitative behavior of the DOS in superconducting state. Note, the superconducting gap close to the Fermi level characterized by sharp peak just below and above the superconducting gap due to the formation of Cooper pairs. The superconducting energy gap Δ is very small (of the order of a few meV) compared to the Fermi energy (E_F) which is in the order of eV. Therefore, the picture is exaggerated near the Fermi level roughly 10^4 times. This is taken from Ref. [57].

(x = 0.05–0.12) superconducting below T_c of 26 K. The important features among Fe-HTSC are as follows. Firstly, a tetrahedron formed by pnictogen (chalcogen)-iron-pnictogen (chalcogen) is the common building block (see Fig 5.3) among all subclasses in Fe-HTSC. Such Fe-As tetrahedron blocks which deal with Fe-atoms[4], are expected to play an important role for superconductivity [6]. Secondly, the superconducting pairing

---

[4] The experimental band structure shows mostly Fe-3d bands near the Fermi level. Therefore, Fe atoms plays an important role for superconductivity in all Fe-HTSC.

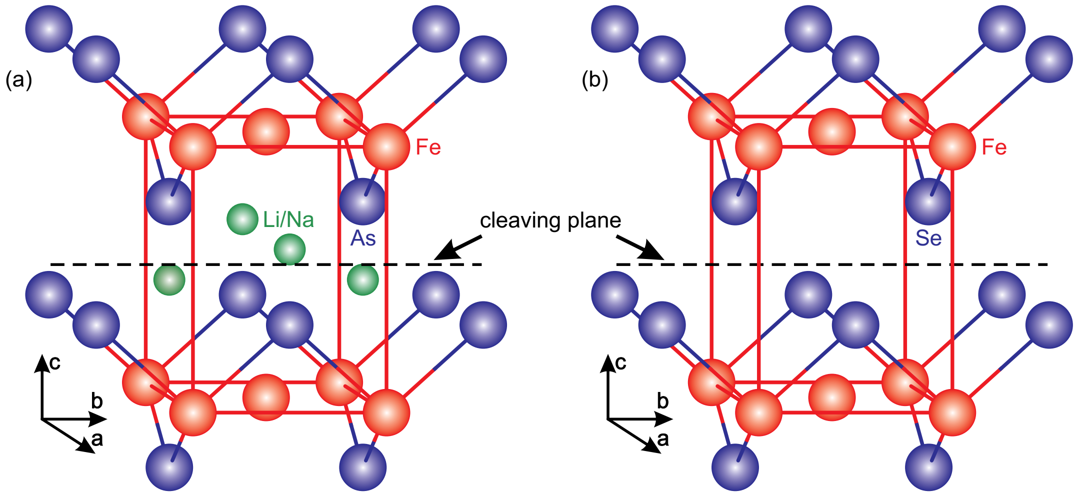

Figure 5.3.: Crystal structures of LiFeAs, NaFeAs and FeSe. The common pnictogen (chalcogen)-iron-pnictogen (chalcogen) building blocks describe the crystal structure for all cases of Fe-HTSC. (a) The crystal structure of LiFeAs and NaFeAs. (b) The crystal structure of FeSe. The unit cell and cleaving plane is shown in both cases. Similar crystal structures are shown in Ref. [58–60].

mechanism is widely believed to occur via the exchange of virtual spin fluctuations[5] as it is often observed in these compounds in the vicinity of an AFM spin-density-wave (SDW) ground state (see Fig. 5.4). In fact, such generic SDW ordered state suppresses upon electron or hole doping, and superconductivity emerges in the proximity of such magnetically ordered states [6–9,66]. Thirdly, the excellent nesting of electron- and hole-like Fermi surface pockets apparently drives superconductivity in most of the Fe-HTSC, and therefore the most likely pairing mechanism among these compounds are $s_{\pm}$-wave or s_{++}-wave order parameters [66, 67]. AFM spin fluctuations favor sign-changing $s_{\pm}$- or d-wave states due to the change of the sign of superconducting energy gap between electron- and hole-like Fermi surfaces, whereas charge or orbital fluctuations lead to sign-preserving (s_{++}-wave) state.

5.2. Fe-based high temperature superconductors

A schematic phase diagram of Fe-HTSC is shown in Fig. 5.4 where parent compounds among most of the Fe-HTSC undergo structural transitions from tetragonal to orthorhombic phase below some characteristic temperature, say T_N [6–9]. Very similar phase diagrams are observed experimentally in compounds of 1111 and 122 subclasses of Fe-HTSC which is shown in Fig. 5.5. Electron or hole doping leads to the suppression

---

[5] Such spin fluctuations could be originated from ferromagnetic or antiferromagnetic fluctuations. But in most of the Fe-HTSC, AFM spin-fluctuations are only observed in the proximity of superconducting phase except of LiFeAs superconductor.

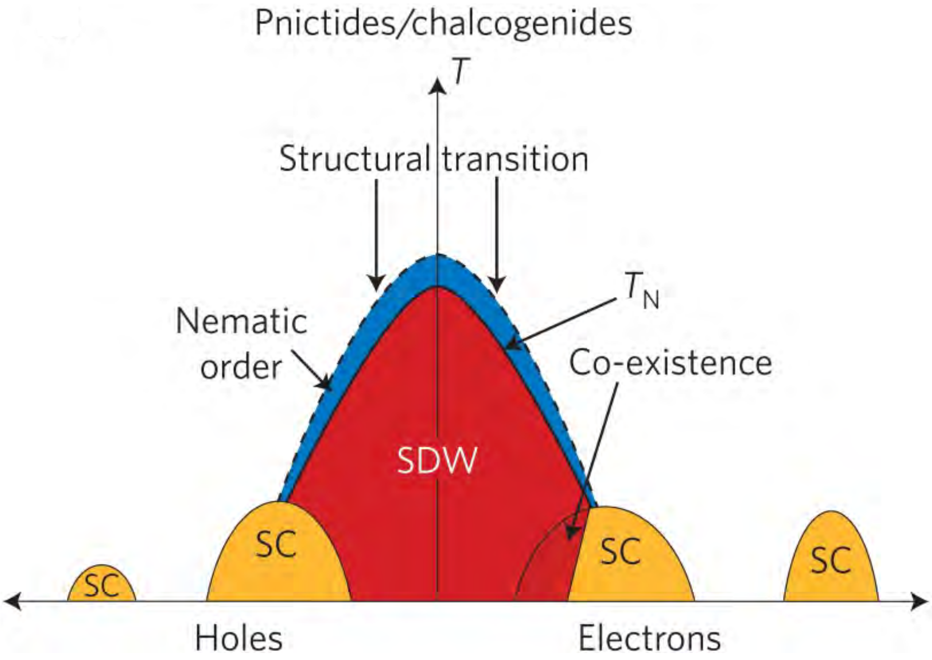

Figure 5.4.: Schematic phase diagram of Fe-HTSC. Electron or hole doping drives the system from SDW parent state towards superconductivity. The co-existence of superconducting and SDW state is present upon electron doping. Blue region indicates the nematic order below the structural transition. This is taken from [1].

of magnetic ordering, and superconductivity may set in at particularly high doping. Recently, an electronic nematic phase is predicted theoretically [68] and has been experimentally observed in several sub-classes of Fe-HTSC [69–71]. The origin of nematicity is because of either the breaking of lattice rotational symmetry due to the structural transition or charge-driven, spin-driven and orbital-driven instabilities [71–78]. The charge-driven, spin-driven and orbital-driven instabilities [71–78] are the most likely origin of it as the electronic mechanism of nematicity could induce the nematic order in the class of correlation-driven instabilities e.g. superconductivity, SDW transitions, etc [68]. The structural transition which occurs near to the ordered temperature of the nematic phase, is therefore indirectly related to electronic nematic phase where four-fold rotational symmetry of the system is spontaneously broken.

Besides the structural transition, the undoped compounds among Fe-HTSC exhibit commensurate AFM or SDW transitions (see the Fig. 5.5) which result to the change of magnetic, thermal as well as electrical properties [79–81]. An AFM parent state which was predicted theoretically earlier based on first principles electronic structure calculations [66, 82–84], was also supported experimentally by nesting between electron- and hole-pockets. Inelastic neutron scattering (INS) founds (π, π) ordering, whereas additional information about the similar size of electron- and hole-pockets for parent compounds to hold the nesting condition was given by photoemission data (see Fig. 5.13(a) and Fig. 5.6(a)) [15, 62, 85]. The nesting instabilities have also been observed in pho-

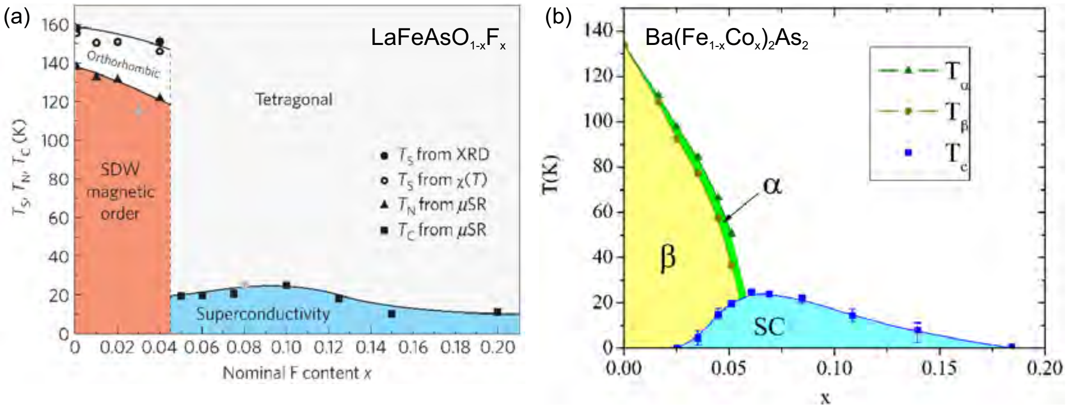

Figure 5.5.: Phase diagrams of LaOFeAs with F-doping (a) and $BaFe_2As_2$ with Co-doping (b). (a) The structural transition (T_S) from tetragonal-to-orthorhombic phase has been measured by X-ray diffraction (XRD) and from susceptibility measurements (ξ(T)). The doping dependence of the magnetic and superconducting transition temperatures were determined from the μSR experiments. (b) The magnetic/structural transition is observed below 134 K which splits into two distinct phase transitions, and they suppress rapidly with increasing of Co-doping and superconductivity emerges. Data point of T_α and T_β were obtained from heatcapacity, resistivity, Hall-coefficient, and susceptibility data for x=0, 0.016, 0.025 and 0.036, and from resistivity data alone for x=0.045 and 0.051. The superconducting T_c values are obtained from resistivity data. These are taken from Ref. [7, 61].

toemission (see Fig. 5.6(b)). One exemplary model out of several theoretical works to explain the leading instabilities is discussed in the following for LaFeAsO which is shown in Fig. 5.7 [84]. This model is based on the calculated band structure of two electron-like pockets (called as $\beta_{1,2}$) around the M-point[6] and two hole-like pockets $\alpha_{1,2}$ around the Γ point which represent the Brillouin zone. Fig. 5.7(a) shows the calculated Fermi surface in the folded Brillouin Zone where $\alpha_{1,2}$ and $\beta_{1,2}$ pockets represent the Fermi surfaces of the material. The calculated partial dynamic spin susceptibility for the states connected to various intra- and inter-band scattering wave vectors is shown in Fig. 5.7(b) as dashed and dotted lines. The total dynamic spin susceptibility is plotted as black curve where the leading instability is found for the filled dots of states connected to inter-band scattering wave vectors between $\alpha_{1,2}$ and $\beta_{1,2}$ pockets (shown by blue arrow and labelled by Q_{AFM}), sharply peaked at M-point (commensurate position). The open dots in panel (a) refer to the states connected to intra- and inter-band scattering wave vectors either within α pocket, β pocket, between α_1 and α_2 pockets, or between β_1 and β_2 pockets (shown by green arrow and labelled by Q_{SDW}) which give relatively broader peak in the incommensurate positions between $\Gamma - X$, and between $M - \Gamma$ point. The leading instability in the AFM spin-fluctuations at M-point gradually decreases with increasing doping and the system undergoes to the formation of superconducting phase [66, 84].

---

[6] The electron-like pockets are at M-point if we consider 2-Fe unit cell. On the other hand, they are at X-point for 1-Fe unit cell [2].

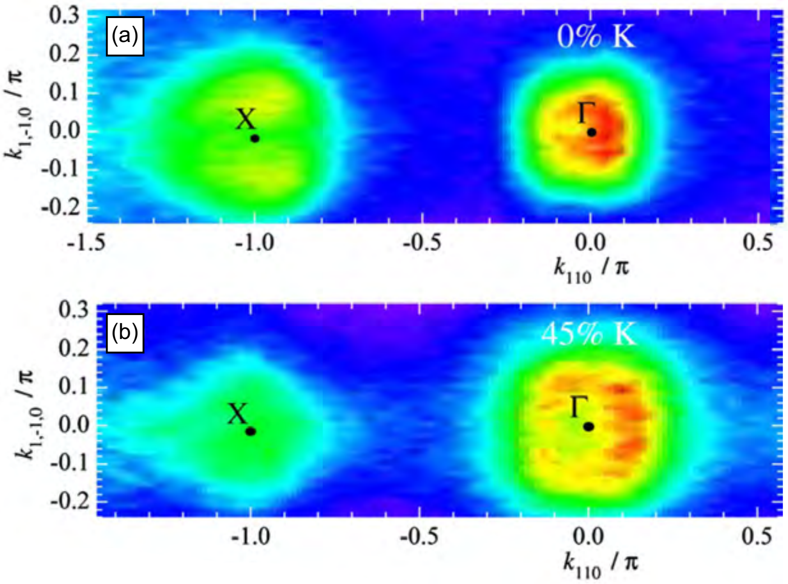

Figure 5.6.: (a) The Fermi surface map of $BaFe_2As_2$ which is the intensity of the photoelectrons integrated over 20 mV about the chemical potential obtained with 40.8 eV photons at a temperature of 100 K. Areas of bright color mark the locations of the Fermi surfaces. (b) The Fermi surface map of $Ba_{1-x}K_xFe_2As_2$ with nominal x=0.45 measured under same condition of (a). This is taken from Ref. [62]

The superconducting order parameter in Fe-HTSC is much under debate and still remains an unresolved question [64, 68]. The above discussed AFM spin-fluctuations will lead to mostly two kinds of superconducting order parameters: triplet (p-wave) or singlet (s-wave or d-wave). The triplet order parameter is characterized by different amplitudes or signs among the Fermi surfaces. As it is shown in Fig. 5.7(b), a large part of scattering between states in the electron and hole pockets is used for AFM spin-fluctuations with wave vectors exactly equal to (π, π). Therefore, the attractive spin-fluctuations in triplet channel will be lost or relatively lower due to the large scattering towards (π, π) direction. Instead, the possibility of singlet order parameter is preferred. Theoretically, it has been suggested to be $s_{\pm}$-wave (see fig. 5.8) as it has the lowest superconducting energy states [66, 67] namely $(cosk_x + cosk_y)$. If the orbital or charge fluctuations are responsible for the Cooper pair formation, this implies attractive and enhanced inter-pocket interactions. Once, these interactions overcome the intra-pocket repulsion, a superconducting instability towards an s_{++}-wave state is developed. This is a conventional pairing state where the gap functions in all the pockets have the same sign.

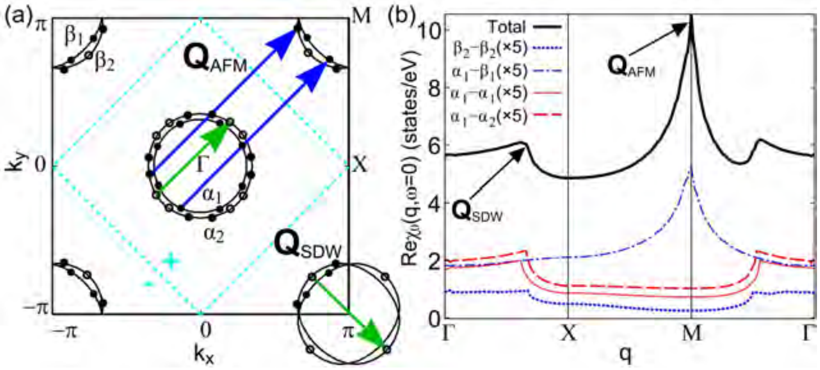

Figure 5.7.: (a) The calculated Fermi surface in folded Brillouin zone (BZ) for LaFeAsO. The dominant scattering vectors are indicated by blue and green arrows. Filled dots refer to the interband scattering with AFM wave vector Q_{AFM} whereas open dots present the incommensurate SDW wave vectors Q_{SDW} due to intra- and inter- band scattering. The dashed cyan square indicates the position of nodes while positive and negative sign corresponds to $s_{\pm}$ superconducting order parameter. (b) The calculated one loop-spin susceptibility (real part) along high symmetry direction in the first folded BZ. The thick black curve represents the total spin susceptibility where dashed blue and red curves are the partial spin-susceptibility exaggerated by a factor of 5 times for the sake of presentation. The main scattering wave vectors which can be found in (a) are also indicated in (b). This is taken from Ref. [84]

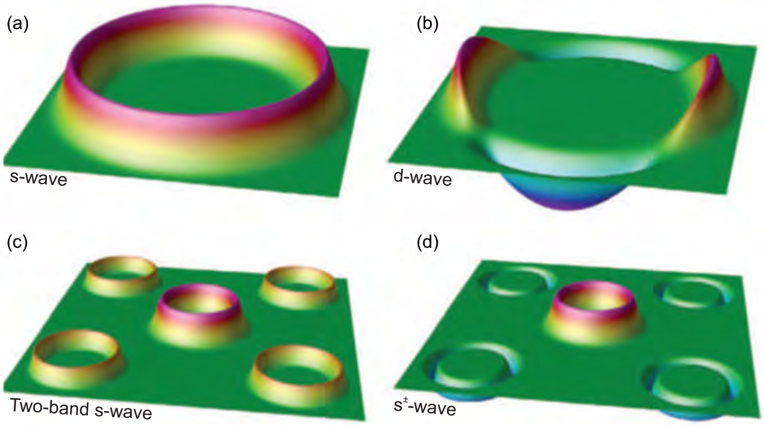

Figure 5.8.: The sketch of different possible order parameters as shown in Ref. [67]. (a) and (b) represent the s- and d- wave single band superconducting order parameter while (c) and (d) are the multi-band s-wave superconducting order parameters.

5.3. LiFeAs

Although LiFeAs is a multiband superconductor like other Fe-HTSC, the physics of it differs in many aspects from the canonical Fe-HTSC. Despite the fact that it belongs to the 111 subclass like NaFeAs, the electronic band structure reveals to be rather peculiar and different as has been reported in ARPES data [11, 12, 86, 87] (see Fig. 5.9(a)). Superconductivity usually emerges from a Fermi-surface nested SDW or AFM spin-fluctuations in Fe-HTSC [67] which had been discussed before. In most of these parent compounds, superconductivity emerges into the system upon electron or hole doping or by external pressure [6–9]. Such generic phase diagram seems to violate for LiFeAs. It is a stoichiometric superconductor i.e. superconductivity emerges without doping or external pressure into this compound [58]. Moreover, with doping or external pressure, suppression of superconductivity has been noticed [90, 91]. Strikingly, stoichiometric LiFeAs does not have any structural phase transition which implies that the theory of nematic order probably is not relevant in case of LiFeAs [70]. Its Fermi surface is also quite different compared to other Fe-HTSC. The measured Fermi surface in ARPES study and the calculated electronic band structure using ten-orbital tight-binding fit to the ARPES data are shown in Fig. 5.9(a) and (d), respectively where three hole pockets (say $\alpha_{1,2}$ and γ) at the Γ point and two electron pockets ($\beta_{1,2}$) at the M point represent the Fermi surface. The Fermi surface has strong k_z dependency (see Fig. 5.9(d)). For

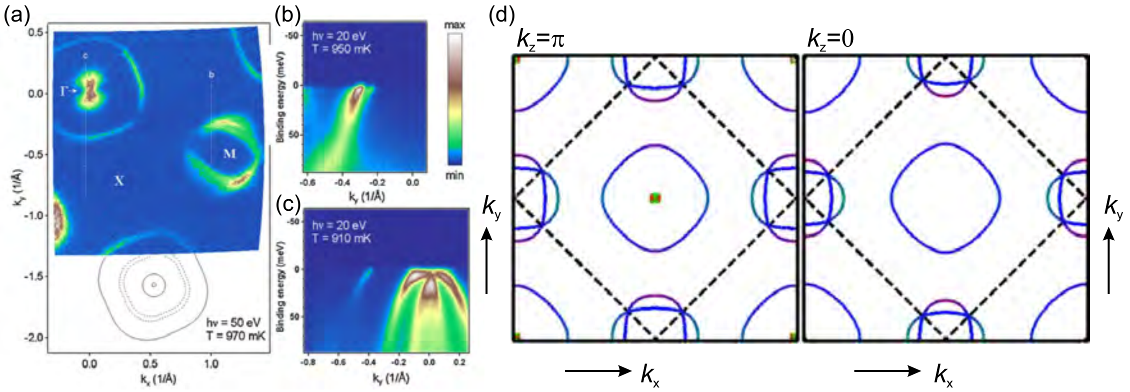

Figure 5.9.: (a)-(c): ARPES data on stoichiometric LiFeAs taken from Ref. [11]. (a) Different size of the hole-like Fermi surfaces at the Γ point and the electron-like Fermi surfaces at the M-point are indicating a lack of Fermi surface nesting. This is also sketched by solid and dashed lines, respectively. (b) and (c) are the line cut along M-point and Γ-point as shown by vertical white dashed line in (a). (d) The Fermi surface at $k_z = 0$ and $k_z = \pi$ are quite different as depicted in schematic diagram of its first Brillouin zone (one-Fe unit cell) based on ARPES data [88]. This is taken from Ref. [89]. The indicated γ- and β- pockets possess only a weak k_z-dispersion while the α_1- and α_2-pockets are located only close to $k_z = \pi$.

instant at $k_z = \pi$, all five bands cross the Fermi level whereas only γ and $\beta_{1,2}$ appear at $k_z = 0$. Earlier de Haas-van Alphan (dHvA) study together with density functional theory (DFT) calculation by Putzke *et al.* [92] suggested a nested Fermi surface between electron and hole pockets in this compound. This is found to be inconsistent with the ARPES band structure [11,12,86]. Later, a dHvA study by Zeng *et al.* [93] has detected

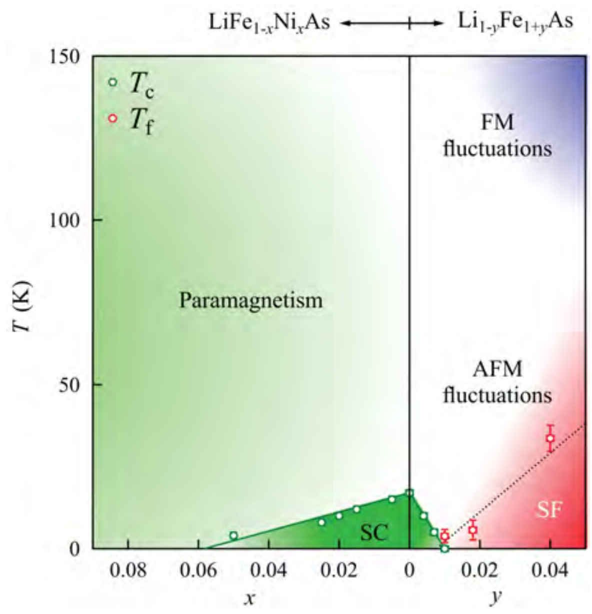

Figure 5.10.: Phase diagram of LiFeAs in case of Ni-doping and access Fe into the system. In both cases, superconductivity is suppressed significantly by doping. In case of Fe-access, ferromagnetic fluctuation is observed at 150 K while spin-fluctuation becomes dominant at low temperature, and upon further cooling down, system enters into spin-freezing state. This is taken from [5].

the appearance of a small isotropic hole like Fermi surface at the Γ point which becomes consistent with the experimental band structure. Such a feature of rich DOS at Γ point rules out the possibility towards AFM or SDW instability in LiFeAs. The phase diagram in this compound is still not well established. In its stoichiometric composition, the appearance of isotropic α-pockets at the Γ point might fulfill the stoner criterion towards ferromagnetism where the dominant scattering wave vectors are at or near $q \approx 0$ [94,95]. However, Wright *et al.* [5] based on their magnetometry and muon-spin rotation (μSR) data (see Fig. 5.10), have reported its phase diagram upon Ni doping and Fe excess samples. They found suppression of superconductivity up to 6% electron doping[7]. Further doping drives the system towards paramagnetic phase. The situation for Fe excess samples is even more complicated. Similar to Ni-doping, the superconductivity

---

[7] Ni is doped to the Fe site.

is destroyed until 1% Fe excess samples. The doping of around 4% Fe-access creates three different phases at various temperatures. The evidence of ferromagnetic fluctuations is found at higher temperature of around 150 K. While with lowering the temperature, it is reported that AFM spin-fluctuations become dominant into the system. By lowering the temperature even further, spin freezing states are claimed to develop into the system. Their findings of the suppression of superconductivity duo to Ni-doping or Fe excess samples are consistent with Co-doped LiFeAs data reported by Aswartham *et al.* [13].

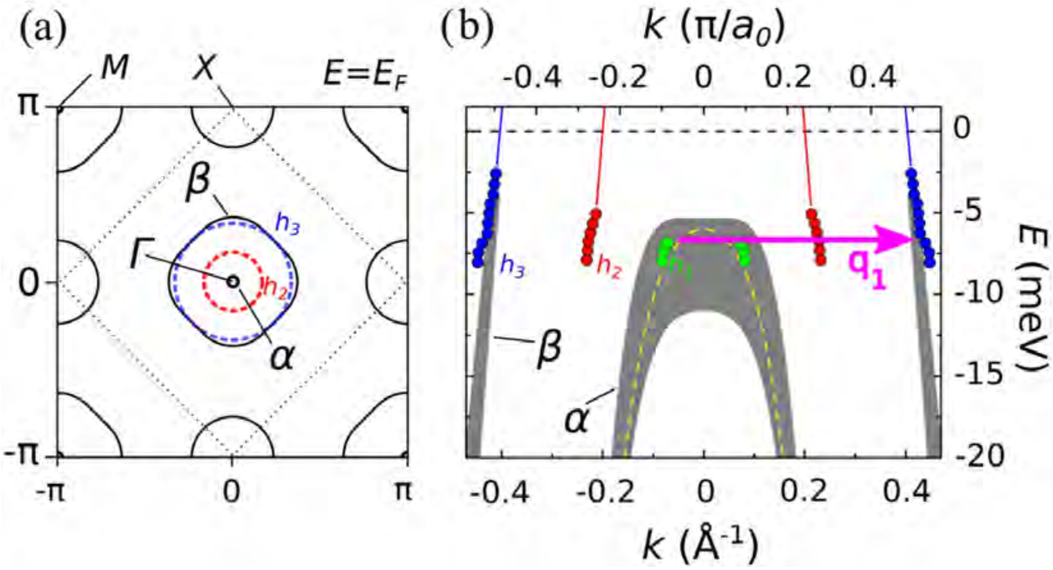

Figure 5.11.: (a) Schematic Fermi surface of an unfolded Brillouin Zone (BZ) in LiFeAs which refers to 1Fe-unit cell as shown in Ref. [48]. The red and blue marked h_2 and h_3 bands are taken from Ref. [96]. The rest of the bands are the data taken from Ref. [47]. (b) The broad dark contours represents the α band and β (in our notation it is γ) band compared with band structure data in ARPES measurement [11]. The extended width of α band indicates its k_z dependency which has obtained from different photon energy measurements [86].

A further possibility to visualize the electronic band structure of LiFeAs is a QPI study in Fourier transformed spectroscopic imaging scanning tunneling microscopy (FT-SI-STM). Earlier reported data have shown several aspects which are inconsistent with the picture of the band structure reported in ARPES [11, 12, 86] measurement and de Haas-van Alphan (dHvA) [93] experiments. The QPI study by Allan *et al.* [96] suggests that the superconductivity in LiFeAs originats from intraband scattering within the three hole-like pockets at the Γ-high symmetry point. However, their discussed h_2 band is absent in the ARPES data [11, 12, 86]. Later, in combination with theoretical calculation Hess *et al.* [48] formed a consistent description of the QPI data with ARPES band structure. They suggest that the interband scattering between h_1 (in our notation α_2 band) and h_3 (in our notation γ band) is responsible for the QPI intensity that has led to the misleading h_2 band discussed by Allan *et al.* (see Fig. 5.11). Another very recent QPI study by Allan *et al.* [97] suggests that superconductivity in LiFeAs is mediated by AFM spin-fluctuations between γ-pocket and β-pockets (see Fig. 5.12). However, such AFM spin-fluctuation is absent in INS experiments [4,14,16,98] (see Fig. 5.13). These experiments only found broad excitations at $(\pi \pm \delta,\ \pi \mp \delta)$ which later have been referred to ordinary scattering processes between the γ-pocket and the β-pockets by Knolle *et al.* [99]. Allan *et al.* [97] considered a sharp resonance peak at $(\pi,\ \pi)$ in their model, inconsistent with available experimental data [14,16]. In fact, Qureshi *et al.* [14,16] did not find any resonance mode, neither in energy nor in temperature scans. Thus, from the existing data in literature, one can conclude that the existence of usual generic AFM ordering which mediates superconductivity in most of the Fe-HTSC, violates in case of LiFeAs.

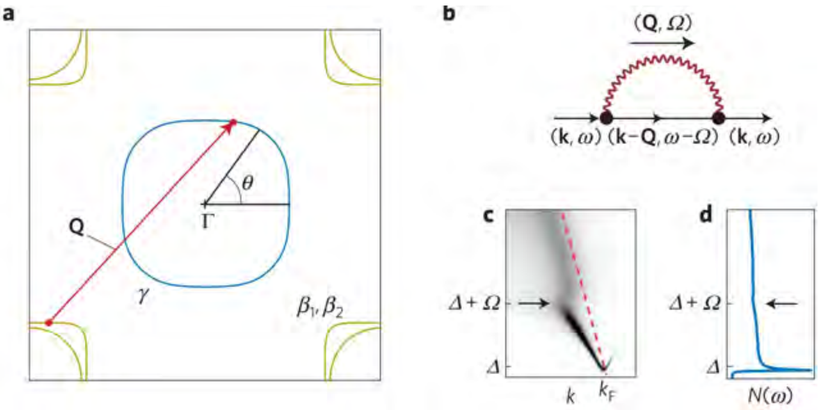

Figure 5.12.: (a) AFM spin-fluctuations between γ and $\beta_{1,2}$ bands as shown in Ref. [97]. They claim such spin-fluctuations as the origin for the tempted bosonic mode which drives superconductivity in LiFeAs. (b) Feynman diagram of the bosonic mode and its coupling to quasiparticle. (c) The kink in band dispersion and (d) dip in the DOS are the hints of bosonic mode coupling as discussed by them.

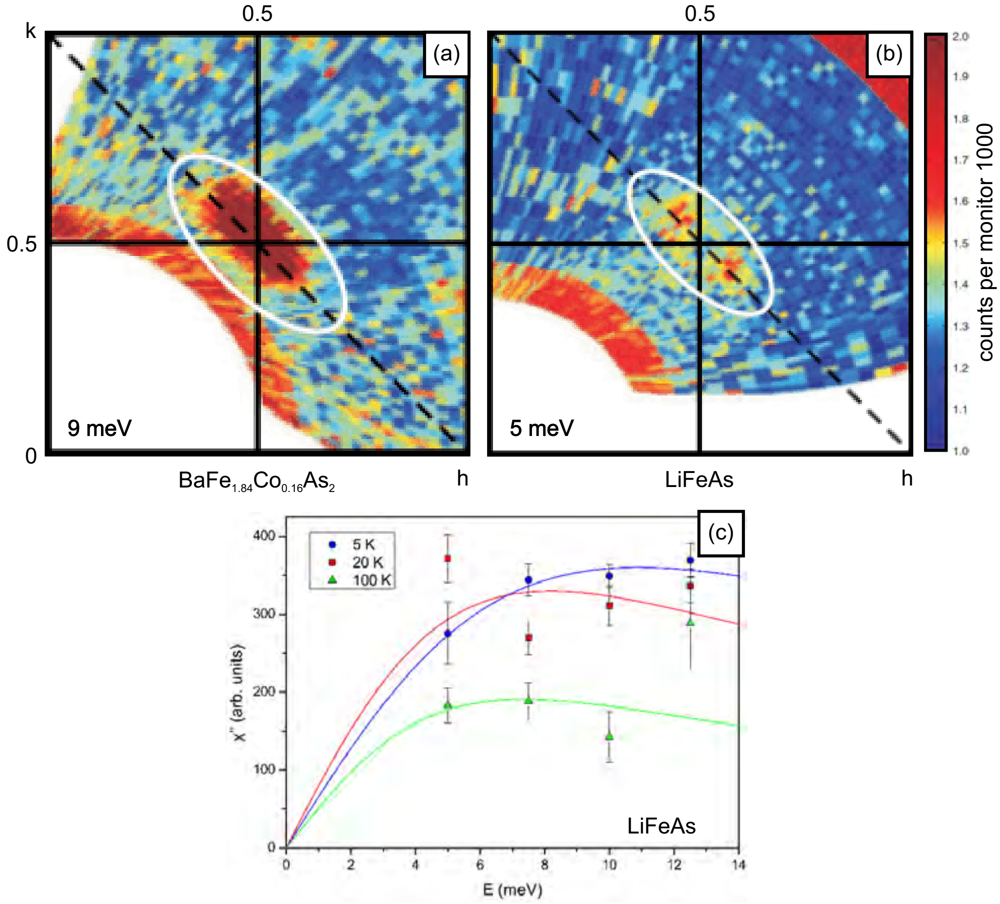

Figure 5.13.: Inelastic neutron scattering data on 8% optimally Co-doped BaFe$_2$As$_2$ and stoichiometric LiFeAs which are measured on 9 meV and 5 meV energy scan shown in figure (a) and (b), respectively for l=0 plane. Distinct (π, π) ordering is present in case of BaFe$_2$As$_2$ consistent with Ref. [100] whereas it is absent in case of LiFeAs. Instead of (π, π) ordering, incommensurate spin-fluctuations have been noticed at ($\pi \pm \delta$,$\pi \mp \delta$) positions in LiFeAs. (c) The energy scan at different temperatures has been plotted where no distinct AFM spin-fluctuations have been found in both temperature and energy scan. This is taken from Ref. [14, 16] respectively.

Strong controversy still remains regarding its superconducting order parameter [47, 86, 88, 89, 95, 101–104]. The presence of small isotropic α pockets at the Γ point which possesses a high DOS near the Γ point, might be a big difference with other Fe-HTSC so that the ferromagnetic fluctuations might play the dominant role in this system. In this thesis, I consider this aspect from the viewpoint of searching for small q scattering by probing the temperature dependent QPI studies in FT-SI-STM techniques.

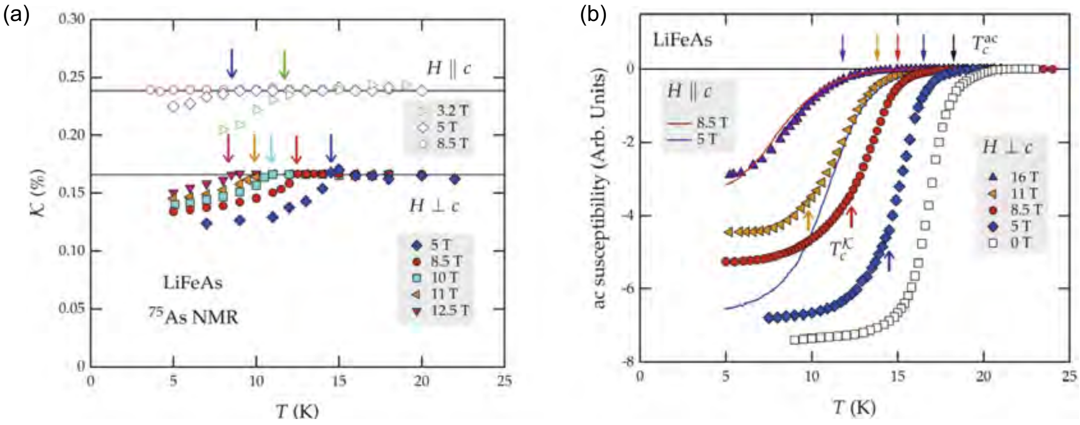

Figure 5.14.: The successive NMR Knight shift (a) and AC-susceptibility (b) data on superconducting LiFeAs at different magnetic fields as reported in Ref. [105]. The onset of superconductivity in Knight shift indicated by down-arrows in (a) is also marked in (b) as up-arrows at each field which in comparison with down-arrows in (b) taken from AC susceptibility measurements describe different T_c for each particular magnetic field.

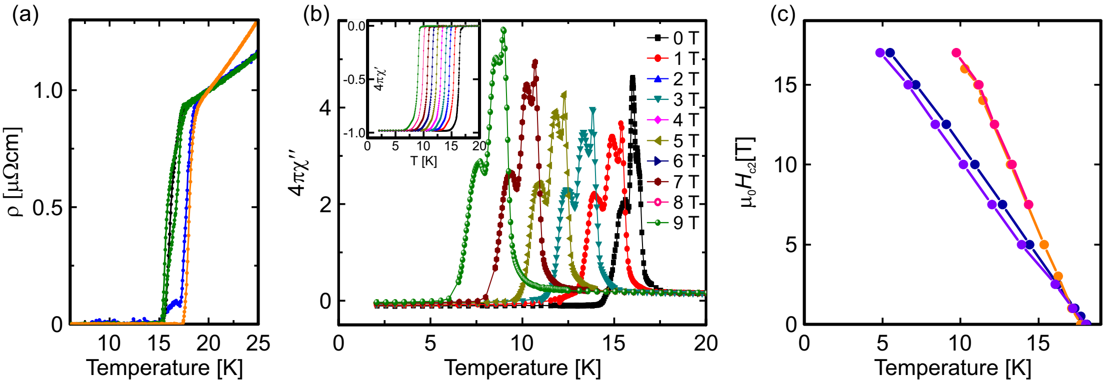

Figure 5.15.: (a) Measured resistivity data on several samples in LiFeAs follow two superconducting T_c with different slopes of the normal state above T_c. Sometimes during the superconducting transition, it jumps from 18 K to 16 K (see the blue curve). (b) Multiple peaks between 0 T to 9 T appear during AC susceptibility measurement on LiFeAs single crystal. (c) The H_{c2} measurements on several samples follow two distinct slopes. Fig. (a) is taken from D. Bombor, PhD thesis and Fig. (b) has been measured by M. Abdel-Hafiez, IFW Dresden while Fig. (c) is measured in IFW Dresden and University of Köln.

Earlier works have reported an unusual temperature evolution of the critical temperature T_c in stoichiometric LiFeAs. This is partially supported by previous experimental works of reported T_c^* with values that scatter between about 15 K and 18 K [58,90,92,106–113]. Furthermore, the occurrence of multiple critical temperatures has previously been reported from successive Knight shift measurement in nuclear magnetic resonance (NMR) study and AC susceptibility measurements of one LiFeAs single crystal [105] (see Fig. 5.14) as a function of magnetic fields. In Fig. 5.15, such unusual behaviour has also been noticed in transport measurements e.g. resistivity and upper-critical field (H_{c2}) study. The bulk transport e.g. resistivity shown in Fig. 5.15(a), has mostly two specific paths, either T_c of 15 K or 18 K. This feature might be understood from the fact that the sample follows the least superconducting path during cooling down if the origin lays into the inhomogeneity of the sample. Additionally, even during lowering the temperature in resistivity (see blue curve in Fig. 5.15(a)) sometimes the jump of T_c occurs from 18 K to 15 K which is not explainable by the afore discussed origin. Such unconventional behaviour has also been observed in AC susceptibility measurement shown in Fig. 5.15(b) where multiple peaks have been observed near T_c at various magnetic fields. Two different slope among different samples have been noticed in H_{c2} measurements, too, as shown in Fig. 5.15(c). The origin of this peculiar behaviour, however, is unclear. Because in all of the above mentioned experiments, the bulk or the global properties of a superconductor is typically probed. Thus, it is difficult to rule out the possibility of sample inhomogeneity which in principle could allow the mentioned probes to respond from different parts of the sample, each with a potentially different critical temperature. It is therefore necessary to probe carefully on a microscopic level to show whether the origin is from intrinsic electronic property or due to the inhomogeneity of the sample. In this case, scanning tunneling microscopy/spectroscopy (STM/S) is probably the only powerful tool where such temperature evolution of superconductivity can be registered with atomic precision in real space.

5.4. Strong coupling superconductivity

It has already been mentioned that superconductivity in most of the elementary superconductors is originated from a weak electron-phonon coupling[8]. The strong electron-boson coupling becomes important to describe spectral features in type-II superconductors, e.g. in Pb and other unconventional superconductors, etc. [6, 23, 114, 115]. This was first explained in 1966 by Scalapino [23] and the idea is discussed in the following (see Fig. 5.16). For simplicity, let us consider that we have a phononic[9] mode with its natural frequency ω_0 as shown in Fig. 5.16(a). For excitation energy $\omega \leq \omega_0$, the frequency of the bulk phonon (ω_0) has higher energy than ω. Thus, the lattice vibration can provide energy to have a positive effective electron-electron interaction. But for $\omega \geq \omega_0$, the

---

[8] More general statement would be the use of the term “electron-boson coupling” where the bosons represent other degrees of freedom like phonons, spin-fluctuations, magnons, etc.

[9] The Scalapino’s description was based on phonons [23]. But later, the term “boson” is used to generalize it from any integer elementary excitations.

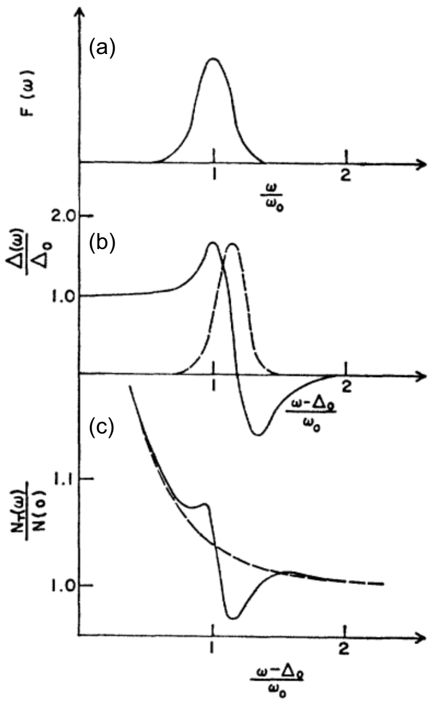

Figure 5.16.: The picture of strong electron-boson coupling as described in Ref. [23]. (a) The excitation energy, ω_0 of bosonic spectral function $F(\omega)$. (b) The real (solid) and imaginary (dashed) parts of gap $\Delta(\omega)$ for the case of zero Coulomb pseudo-potential. (c) The normalized tunneling DOS in the presence of such bosonic mode (solid line) out side the superconducting gap while the dashed line is for BCS like gap.

natural frequency of the bulk phonon has relatively lower energy than ω. In this case, lattice needs to be driven above the natural bosonic frequencies. This produces therefore a repulsive effective electron-electron interaction. As it is discussed in Ref. [23], the real part of superconducting gap (Δ) describes the strength of the electron-electron interaction. Therefore, one would expect a similar structure as described in Fig. 5.16(c) due to such strong electron-boson interaction. There will be an enhancement of DOS below ω_0 and a reduction of DOS above the ω_0, and for larger energy, it goes to zero for zero Coulomb pseudo-potential (see Fig. 5.16(b)) but remains negative in the presence of Coulomb pseudo-potential [23,116].

5.5. High energy spectral features in Fe-based HTSC

The high energy spectral features in the order of eV are challenging to study due to technical difficulties as well as the lack of theoretical data interpretation. Very rare techniques are available to experimentally probe such high energy spectral features. In this regard, ARPES study provides a handful experimental works only [22,115,117–124] among different strongly correlated electron systems. Among Fe-based HTSC, recently Evtushinsky *et al.* [22] has reported first experimental ARPES data measured on NaFeAs parent compound and other Fe-based HTSC as shown in Fig. 5.17. They considered a bosonic spectrum sharply peaked at -0.5 eV which together with the Eliashberg function and the electron self energy, coupled to the low energy fermions to produce all low energy anomalies, which can interpret the spectral features in NaFeAs. From additional measurements on other Fe-based HTSC and other strongly correlated materials, they claim that such high energy bosonic mode is relevant for any low energy anomalies including superconductivity or SDW/AFM ordering. In fact in their ARPES measurement, such -0.5 eV energy mode is very distinctly visible for NaFeAs parent compound. Other experimental evidence or theoretical interpretation is still missing on this regard. Thus, we would like to measure such high energy dI/dV spectra on different Fe-based HTSC which will inform us about integrated LDOS of the sample, and hence might be comparable with the ARPES data.

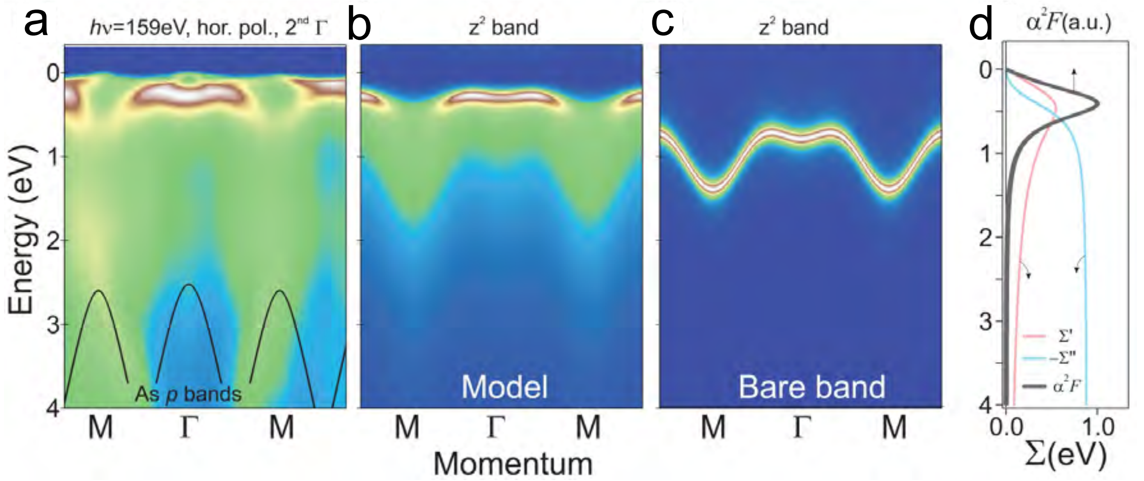

Figure 5.17.: (a) Experimental data, recorded at photon energy of 159 eV with horizontal light polarization in the second Mahan's photoemission cone. (b)-(c) Spectral function, obtained for the z^2 band and $\lambda = 1.6$ (d) Considered bosonic spectrum, $\alpha^2\mathrm{F}(\omega)$ and self energy in the model. This is taken from Ref. [22].

6. Results

6.1. Topography

In this section, two types of topography images of stoichiometric LiFeAs, and various types of defects related to them will be discussed. A representative topography scan of a freshly cleaved atomically flat non-polar LiFeAs surface representing Li-terminated surface states is displayed in Fig. 6.1 which is consistent with recently reported data in literature [31, 32, 47–49, 96, 112]. The atomic corrugation on the surface attributes to the Li atoms if the cleaving occurs between two adjacent Li layers due to weak van der Waals force. Commonly observed defects on such a surface (say surface-A), which are discussed in details by Schlegel *et al.* [31], are shown in Fig. 6.2 (see Ref. [31, 32, 113]). Fig. 6.2(a) and (b) show a missing Li atom and an additional Li atom on the surface which are labelled by Li-D_4-1 and Li-D_4-2, accordingly. So, these four-fold rotation-reflections symmetric (D_4) missing or additional atoms on the surface must be related to the Li lattice. Therefore, we call them Li defects. The height profiles along the grey arrow are shown at the right side of every image. Such height profiles are around 1.5-2 Å lower and higher, respectively at the place of these defects than the background atomic corrugation. Fig. 6.2(c) and (d) represent the dumbbell-like defects labelled Fe-D_2-1 and Fe-D_2-2, respectively. The c-axis projection of the LiFeAs crystal structure in Fig. 6.2(h) affirms that only Fe atoms in the lattice possess D_2 symmetry. Therefore, Fe-site is most likely to be their origin. Both of these Fe defects have two-fold rotation-reflection symmetry (D_2). The height profiles show strong depletion of the intensity more than the background atomic contrast at the center of the Fe-D_2-2 defect, in stark contrast to the Fe-D_2-1 defect. The donut defect in Fig. 6.2(e) which has a four-fold rotation-reflections symmetry (D_4), originates from As-site. Fig. 6.2(f) describes one fold rotation-reflection symmetric (D_1) defect which is rotated 45° to the Li-atomic corrugation on the surface. The crystal lattice symmetry does not corroborate to its origin in the lattice site. Therefore, this defect might consist of dimer or trimer configuration of defects. However, its origin cannot be clarified with the existing data till now. Similar argument holds for chiral defect in Fig. 6.2(g). It has two fold rotational symmetry (C_2). The last two types of defects are rarely found on the surface.

So far, the topography of surface-A is only reported in literature by STM study on stoichiometric LiFeAs. However, sometimes a different type of surface (say Surface-B shown in Fig. 6.3) has also been seen where donut (As-D_4) defects, the additional Li atom (Li-D_4-1) defects and the missing Li atom (Li-D_4-2) defects are predominantly visible. This type of surface is not reported in literature but has been observed frequently and mentioned earlier in Ref. [125]. A very similar LDOS with respect to the surface-A

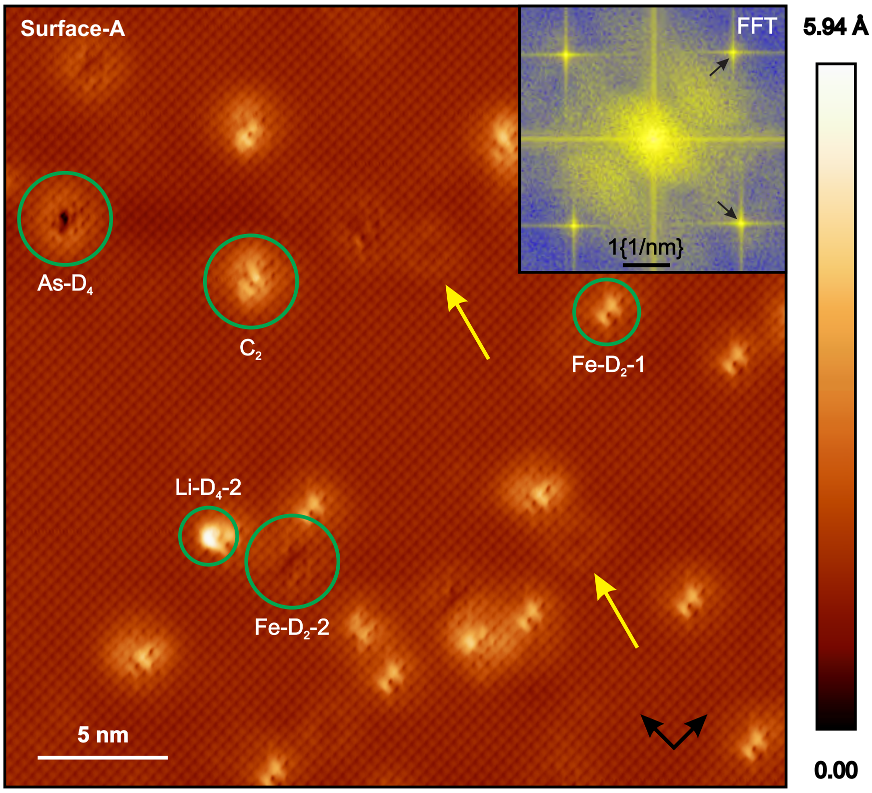

Figure 6.1.: A representative surface-A type topography image on LiFeAs (I_T = 300 pA, V_{bias} = +35 mV). Clear atomic corrugation on the surface attributes to Li-Li lattice constant (0.38 nm). Black arrows indicate atomic corrugation directions. Different types of defects on the sample surface are marked by green circles. Possible origin of those defects from their symmetry is also mentioned accordingly. The yellow arrows indicate the shaded defects. Inset: The FFT image is shown where Bragg peaks due to Li lattice constant are pointed by black arrows.

at this surface, both in the superconducting state (5 K) and in the normal state (20 K), have been noticed. Defects on surface-B are distributed statistically over the surface with a concentration of 0.35% ± 0.05%, consistent with the reported data on surface-A by previous STM studies [31, 32]. Therefore, we assign this surface (surface-B) to be related to the stoichiometric LiFeAs surface, too. The first Bragg peaks, indicated by black arrows in Fig. 6.3(b), refer to the Li-lattice constant which arise in the FFT of Fig. 6.3(a). The microscopic superconducting T_c is found to be 16 K from our measurement. Depending on the defect symmetry, their origin is assigned and labelled, accordingly. These defects show similar electronic properties like surface-A. Remarkably, both of the Fe-defects which have major defect concentration in surface-A, do not appear in surface-B.

Grothe *et al.* [32] and Schlegel *et al.* [31] have recently reported the spectroscopic study on these defects. According to them, Li-defects in Fig. 6.2(a) and (b) show a

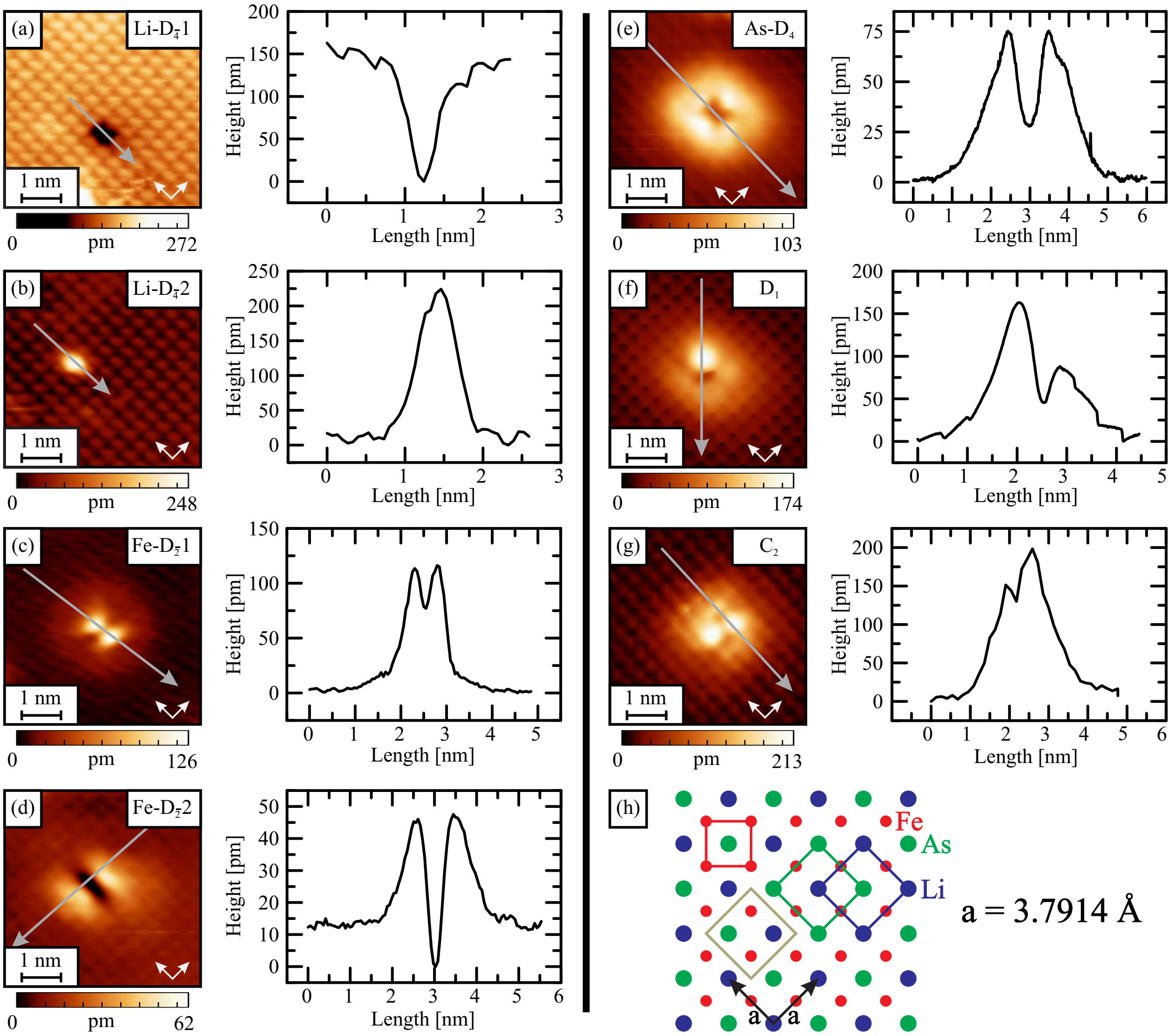

Figure 6.2.: Topography images and line profiles on the different observed defects in LiFeAs at 5 K. (a, b) Li vacancy and excess Li, Li-D$_4$-1 and Li-D$_4$-2 (V_{bias} = -35 mV, I_T = 500 pA), (c, d) defects at Fe-sites, Fe-D$_2$-1 and Fe-D$_2$-2 (V_{bias} = -35 mV, I_T = 400 pA), (e) As-defects, As-D$_4$ (V_{bias} = -35 mV, I_T = 800 pA), (f, g) low-symmetry defects, D$_1$ (V_{bias} = -35 mV, I_T = 300 pA) and C$_2$ (V_{bias} = -35 mV, I_T = 300 pA). (h) Sketch of the c-axis projection of the LiFeAs crystal structure. This is taken from Ref. [31].

very similar spectroscopic data to the bare surface, and they do not influence superconductivity significantly in comparison to other defects. Fe defects in Fig. 6.2(c) and (d) affect superconductivity stronger than all the other observed defects. A significant defect-induced bound state at positive energy with pronounced peaks in the on-site dI/dV spectral value between 4 mV and 12 mV has been observed at these Fe-defects. The enhancement of dI/dV spectral value at donut defect (see Fig. 6.2(e)) at both positive and negative bias voltages has been noticed [31]. Nevertheless in surface-A, second layer defects which are marked by yellow arrows in Fig. 6.1, appear as a shaded defects and are only possible to observe at positive energies. These shaded defects are

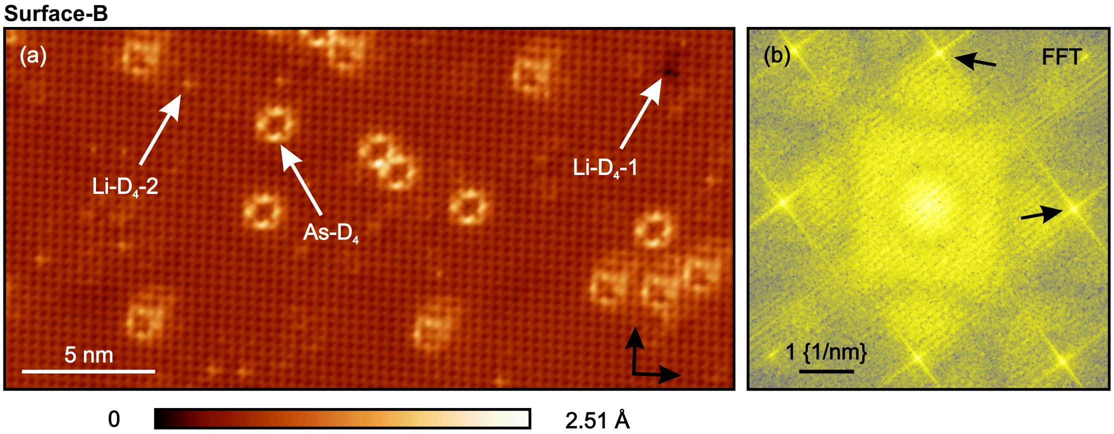

Figure 6.3.: (a) Constant current mode surface-B type topography image of 13 nm× 27 nm on LiFeAs single crystal measured at 5 K. Stabilization condition: I_T=300 pA V_{bias}=-50 mV. The donut- (As-D$_4$) and point- (Li-D$_4$-1 and Li-D$_4$-2) like defects on the surface are pointed by white arrows. The black arrows indicate the Li-Li lattice direction. (b) The FFT image of (a). The black arrows are pointing to the first Bragg peaks due to Li-lattice constant.

also mentioned recently by Schlegel *et al.* [31] and Nag *et al.* [49]. In the following, I will discuss two dumbbell shaped Fe defects in detail as they have the major defect concentration over the surface.

Fe-D$_2$-1 defect: A topography image which captures a Fe-D$_2$-1 defect with a lateral size of 5 × 5 nm^2, is depicted in Fig. 6.4(a) (see also Ref. [31]). A full spectroscopic map between ±15 mV has been taken in this place. The averaged dI/dV spectra over the shaded square in the lower right corner of the image is used as a reference dI/dV (dI/dV_{ref}) spectra for further data analysis below. The raw dI/dV spectra after subtracting the dI/dV_{ref} spectra along the long black arrow are shown in Fig. 6.4(b) in false-color plot. Here, the enhanced spectral feature between zero and 8 mV has a lateral width of 2 nm which occurs at the defect center. Such extension becomes even larger above 12 mV where the lateral width is of the order of 5 nm. The five representative dI/dV spectrum are marked by different symbols on the black arrow in Fig. 6.4(a). Raw dI/dV spectrum on those symbol positions are shown in Fig. 6.4(c) whereas Fig. 6.4(d) describes them after subtracting the dI/dV_{ref} spectra. The dI/dV spectra on the defect are strongly influenced at positive energies in comparison to its value at negative energies. In Fig. 6.4(d), this is almost energy independent at negative energies except of a depletion at -6 mV and slight increase at below -10 mV. On the other hand, two peaks appear at 4 mV and 12 mV at or near the center of the defect with an enhancement of background intensity. In Fig. 6.4(e)-(f), the dI/dV energy slices are shown for four selected energies where the features discussed above have strong impact on the measured constant energy dI/dV maps. The selected energy slices are -15, -6, 4, 12 mV. Here, the strong enhanced intensity around the defect at 4 mV has again lateral size of 2 nm which is in good agreement with the similarly observed feature Fig. 6.4(b).

The two fold symmetries at 4 mV in this defect structure remain present at 4 mV. At the energy of -6 mV, a depletion of dI/dV signal relatively lower than the 4 mV energy slice is noticed which is also consistent with Fig. 6.4(b) and (d). The feature at 12 mV in Fig. 6.4(b) has a lateral extension of 5 nm which can be seen in Fig. 6.4(h). Most importantly, the observed 4 mV peak within the superconducting gap is very likely the defect bound state associated with Fe-D$_2$-1 defect which is consistent with the reported data by Grothe *et al.* [32] where they found similar feature at 3 mV.

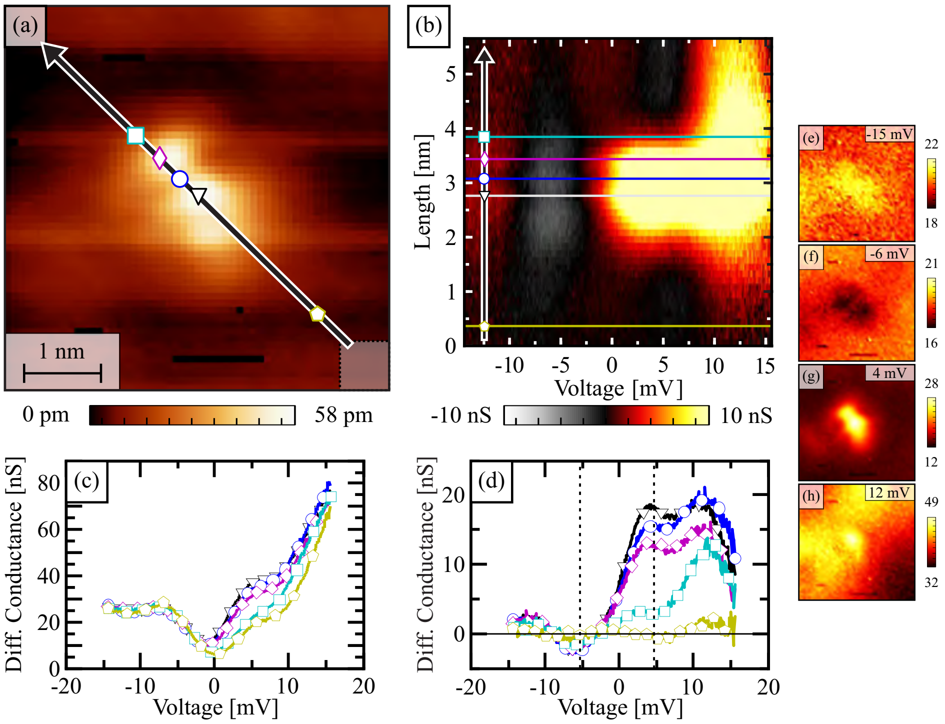

Figure 6.4.: Spectroscopy map on a Fe-D$_2$-1 defect with a field of view of 5 nm × 5 nm at 5 K. (a) Topography image (V_{bias}= -15 mV; I_T= 300 pA). A full spectroscopy map has been taken at the same time with 56 × 56 pixels^2 lateral resolution where each dI/dV spectrum has been taken between ±15 mV with a resolution of 0.1 mV for each pixel. The shaded square box at the lower right corner indicates the area where dI/dV_{ref} has been determined. (b) Spectra along the arrow in (a) after subtracting dI/dV_{ref} as a function of distance. (c) Single-point spectra according to symbols along the arrow in (a). (d) Point spectra of (c) after subtracting dI/dV_{ref}. (e-h) dI/dV energy slices at -15, -6, 4, and 12 mV. This is taken from Ref. [31]

Fe-D$_2$-2 defect: A Fe-D$_2$-2 defect has been investigated by measuring spectroscopic map where the topography image of Fig. 6.5(a) was taken. In the lower part of the image, a change of the tip is noticed but does not influence the spectroscopic data as will be discussed in the following[1]. The shaded square area close to the upper right corner in Fig. 6.5(a) is used for reference dI/dV (dI/dV_{ref}) spectra which will be needed for further analysis later. The data are analysed similar like the case of Fe-D_2-1 defect. The false-color plot in Fig. 6.5(b) describes the spectral features along the black arrow in Fig. 6.5(a) after subtracting the dI/dV_{ref} spectra. The depletion and enhancement of the dI/dV spectra at -6 mV and 4 mV are seen here and their lateral extensions are about 2 nm at or near the center of the defect. But at 4 mV, it has relatively lower intensity in comparison to Fe-D_2-1 defect. The dI/dV value is depleted from the center of the defect around width of 2 nm above 20 mV energy (see Fig. 6.5(b)). The raw dI/dV spectra in Fig. 6.5(c) depicts that the spectra on different positions of the symbols on the defect have changed comparably less than the Fe-D_2-1 defect. The subtracted spectra plotted in Fig. 6.5(d) confirms similar spectral features as shown in Fig. 6.5(b). An enhanced intensity peaked around 20 mV is also present here just outside the defect. The selected dI/dV slices are plotted in Fig. 6.5(e)-(h) at -15, -6, 4, and 20 mV energy values, respectively. The change of tip mentioned above does not find to affect the entire analysed data. A bound state has also been noticed at 4 mV in Fig. 6.5(g). Such similar feature is shown in Fig. 6.5(b), (d), too.

---

[1] For example, the dI/dV energy slices shown in Fig. 6.5(b)-(h) have confirmed that the change of the tip-state does not affect the results.

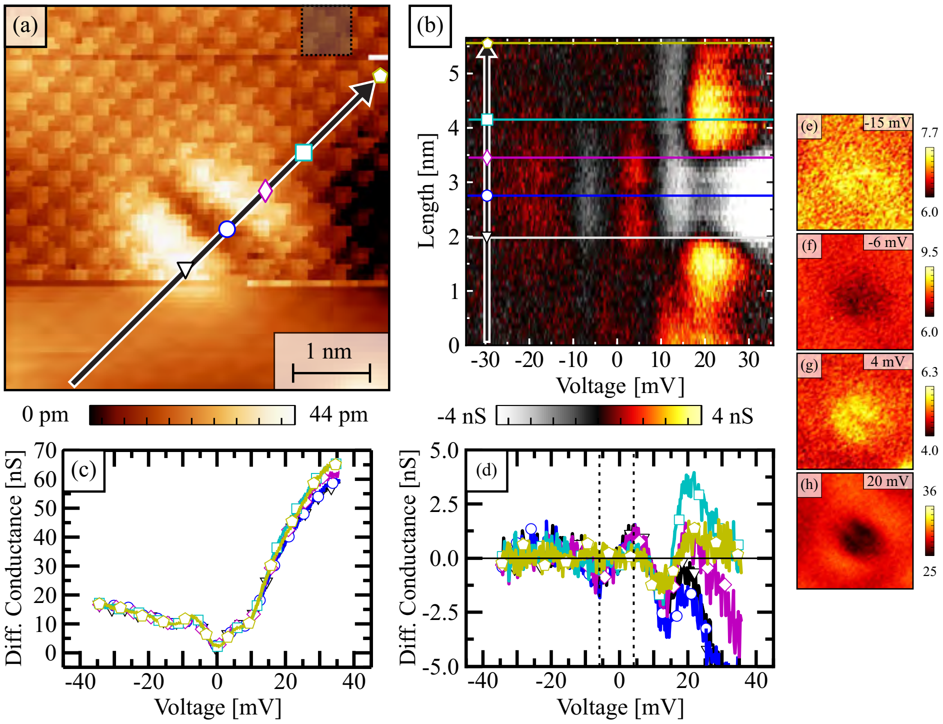

Figure 6.5.: Spectroscopy map on a Fe-D$_2$-2 defect with a field of view of 5 nm × 5 nm at 5 K. (a) Topography image (V_{bias}= -35 mV; I_T= 400 pA). A full spectroscopy map has been taken at the same time with 70 × 70 pixels^2 lateral resolution where each dI/dV spectrum has been taken between ±25 mV with a resolution of 0.25 mV for each pixel. The shaded square box at the right upper corner indicates the area where dI/dV_{ref} has been determined. (b) Spectra along the arrow in (a) after subtracting dI/dV_{ref} as a function of distance. (c) Single-point spectra according to symbols along the arrow in (a). (d) Point spectra of (c) after subtracting the dI/dV_{ref}. (e-h) dI/dV energy slices at -15, -6, 4, and 20 mV. This is taken from Ref. [31]

6.2. Spectroscopy

This section is divided into two subsections. The first subsection contains spectral features in dI/dV spectra over the energy range of a few hundred millielectron volts. The focus of the second subsection is to investigate spectroscopic features near the Fermi level. In both cases, the temperature dependent measurements are performed. To study the pristine properties of the material, all the shown spectra in the following subsections are averaged over several single point spectra on bare surface of the sample so that defects do not influence the spectral features.

6.2.1. High energy spectral features

The exemplary spectra within the energy range of ±1 V at a temperature of 5 K on a clean surface of stoichiometric LiFeAs are shown in Fig. 6.6(a). Such high energy spectroscopic features become consistent in both of the above discussed LiFeAs surfaces (surface-A and surface-B) in section 6.1. The overall structure of such wide energy range spectroscopic features is V-shaped with some additional modifications. To know the energy of the additional features, the derivative of the dI/dV curve is plotted in Fig. 6.6(b) where the change of the curvature of the dI/dV spectra shown in Fig. 6.6(a) are clearly distinguishable. A dip and a peak in the Fig. 6.6(b) is found at -350 mV and 70 mV, respectively. The hump energy at -500 mV can also be noticed. The spectra at other temperatures of 10 K, 15 K and 20 K are also shown in the same plot in Fig. 6.6(a) to clarify that all the features are temperature independent at energy range higher than ±0.1 V.

In section 2.3, it is shown that typical dI/dV spectra, taken very far away from the Fermi level, have a strong influence of the matrix element. A test to normalize the high energy spectra (dI/dV) by dividing the corresponding I/V curve to exclude the additional effect due to the influence of the matrix element is therefore performed and shown in Fig. 6.7[2]. Here, a sharp peak at -390 mV is present with two additional peaks at 85 mV and 920 mV. All the features are temperature independent except of the superconducting gap at the Fermi level. The normalized spectra at normal state (20 K) is quite comparable to the raw spectra (dI/dV) near the Fermi level, indicating that such normalization is not required if the focus of interest lies close to the Fermi level. The 920 mV peak is very broad in shape compared to the other peaks. Due to the singularity problem at zero bias during such normalization, we have taken out zero and near zero energy points from the shown spectra (see inset of Fig. 6.6). All these features are well consistent with the features observed from the derivation of the dI/dV. Most importantly, the observed feature in the range of -350 mV to -390 mV is very distinct in both cases.

Discussion

The origin of all these high energy features observed by us, in principle is difficult to interpret based on our data themselves, as we are probing the integrated DOS in real space. A few experimental studies[3] have been published within the last decade on several strongly correlated electron systems [22, 115, 117–124] as has already been mentioned in section 5.4. Most recently, the reported data by Evtushinsky *et al.* [22] on NaFeAs parent compound have argued that a bosonic excitation mode sharply peaked at -0.5 eV exists in this compound. The coupling of such an excitation mode together with the

---

[2] Its raw dI/dV spectra have already been shown in the Fig. 6.6(a)

[3] These are mostly band structure studies by ARPES and some times together with theoretical calculations.

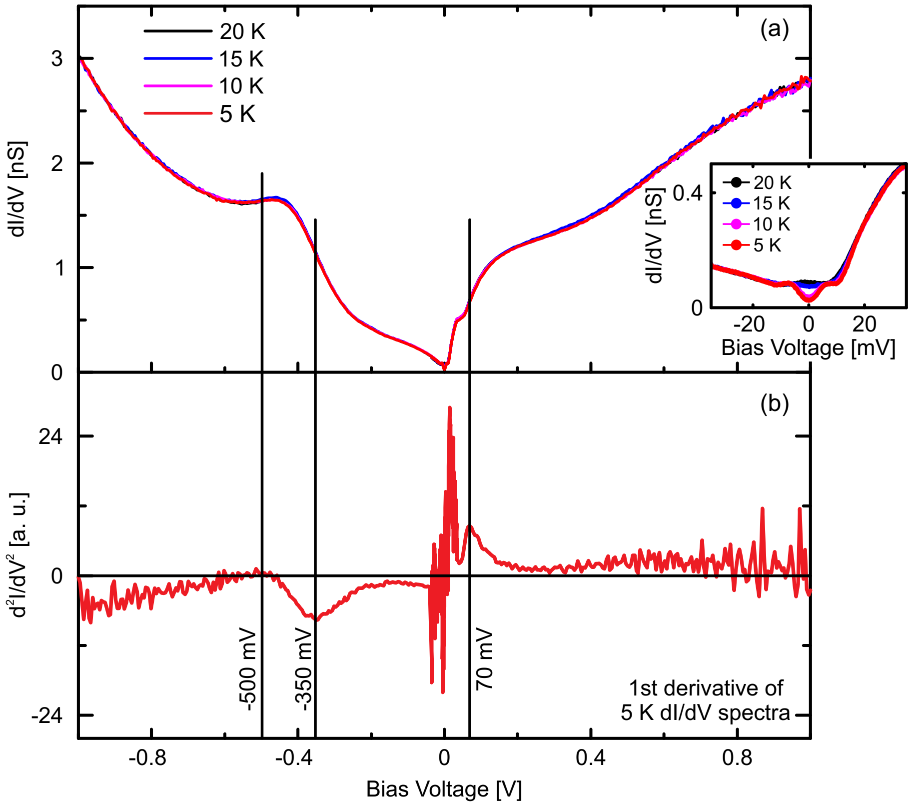

Figure 6.6.: (a) Exemplary spectra within ±1 V on a clean area of surface-B type stoichiometric LiFeAs at 5 K, 10 K, 15 K and 20 K. Inset of (a): Zoom in of the temperature dependent spectra within ±25 mV to show clear opening of superconducting gap at 5 K and 10 K. (b) The 1st derivative of the 5 K dI/dV spectra shown in (a). The peaks at -350 mV and 70 mV correspond to the change of the curvature of dI/dV spectra at those points. The zero value of the 1st derivative of the 5 K dI/dV spectra at -500 mV relates to the position of hump in the 5 K dI/dV spectra.

Eliashberg function and the electron self energy help them to explain all the low energy features (see Fig. 5.17). Considering the existence of such a mode to be the realistic situation, the observed high energy peaks at around -350 mV to -400 mV (LiFeAs), -200 mV ($NaFe_{0.975}Co_{0.025}As$) and -210 mV ($Fe_{0.965}Se_{1.035}$)[4] in three different Fe-HTSC compounds, might have the same origin. However, we propose the direct experimental observation of these high energy features from the integrated band structure studied in ARPES experiment and to compare it with our data to make a strong argument.

---

[4] The data on $NaFe_{0.975}Co_{0.025}As$ and $Fe_{0.965}Se_{1.035}$ are shown in appendix section A.

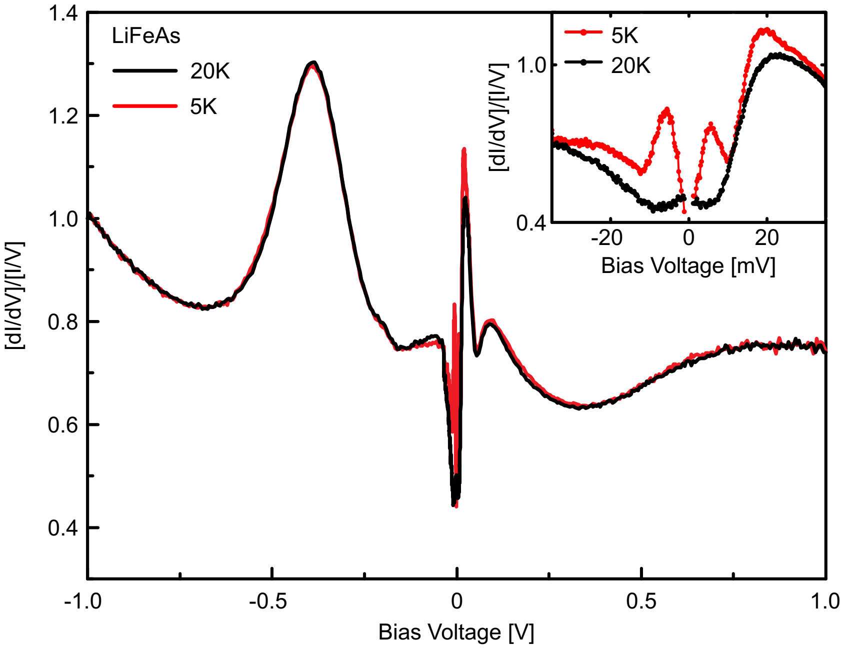

Figure 6.7.: Normalized high energy spectra on LiFeAs which are shown in Fig. 6.6: a peak in the LDOS at -400 mV appears at 5 K as well as at 20 K. At unoccupied side, there are two peak at +85 mV and +920 mV. Inset: Such normalization also reproduce superconducting gap near the Fermi level at 5 K spectra and hump like feature at the Fermi level at 20 K. The data points very close to zero bias (Fermi level) have been taken out intentionally as such normalization diverges very close to the Fermi level.

6.2.2. Low energy spectral features

1) Superconductivity: Temperature dependent spectroscopy:

In the previous subsection, we have mostly discussed the high energy spectral features in LiFeAs. In this subsection, we will focus on a very careful investigation of temperature dependent spectroscopy close to the Fermi level to probe superconducting properties in LiFeAs. More specifically, in order to clarify the temperature evolution of superconductivity, a temperature dependent STM/S on a spatially fixed cleaned surface of LiFeAs single crystal has been performed. The earlier experimental probes which are mentioned in Chapter 5, mostly measured the bulk superconductivity [105]. Therefore, to probe microscopically the superconductivity of the material, we chose with great care of a lateral area of about 2 nm × 2 nm on a pristine surface. Such an area is not only of the order of the superconducting coherence length (ξ) of this material [126, 127], but also becomes uninfluenced by any defects on the surface (see Fig. 6.8) [31]. The possibility of spatial inhomogeneity of stoichiometry or superconductivity therefore will not be affected in the following study. Additional awareness was also taken in sample selection prior to the STM/S experiment e.g. great care was taken to choose a sample piece by a Nuclear Quadrupole Resonance (NQR) spectroscopic study. Such NQR spectra is measured at room temperature inside an Argon glove box (see Fig. 6.9) to avoid any degradation of the air sensitive sample. The measured NQR spectra is fitted using a Lorentzian function (see the red curve in Fig. 6.9). The extracted NQR frequency and the line width of the signal from the fit are 21.54 MHz and 0.024 MHz, respectively. Such unprecedented sharpness of the ^{75}As line in the NQR spectra gives a very good account of the global distribution of the electrical field gradient at the As sites; stating that the sample is globally homogeneous in comparison to all the previously reported data [101, 128, 129]. This very air-sensitive sample has also been handled inside Ar-atmosphere prior to mounting to the STM without any expose of sample to air (see the Chapter 4). Therefore, any thinkable complication can be ruled out about handling as well as quality of the studied sample.

A typical representative topography scan of 30 nm × 30 nm field of view is shown in Fig. 6.8(a), measured at $T = 4.8$ K. The clear atomically resolved corrugation reveals the position of about 6300 surface Li-atoms [47] with a lattice spacing of roughly 3.77 Å, consistent with the reported lattice constant in literature [10]. Isolated bright spots represent defect states of the first layer of this material. These defects could influence superconductivity significantly as has already been discussed in Ref. [31, 32]. Apart from these, faint structures are present in the image, presumably arising from the second layer defect states, as highlighted in Fig. 6.8(c). This has been reported recently by Schlegel et al. [31] and has also been pointed in the section 6.1. These might modify the electronic properties locally. Therefore, in order to spectroscopically investigate the pristine electronic properties of the material, the area of 2 nm × 2 nm was chosen far away from any defect as indicated by a black square area in Fig. 6.8(a) and (b) so that the influence of first and second layer defect states can be neglected. The temperature dependent STM/S measurements have been performed in this area to investigate the superconductivity of the pristine material.

Before we discuss the results, some additional aspects are presented to confirm that in the experiment, we probe the intrinsic electronic properties of the crystal. i) The topography data measured before (4.8 K) and after (20 K) the temperature dependent spectroscopy which are shown in Fig. C.1, confirm that the tip-state remains unchanged during the whole temperature dependent spectroscopic measurement[5]. Additional measurements i.e. topography data taken at stabilized energy of ±35 mV at each temperature (see Fig. C.2), guarantee that the same tip-state is always probing the LDOS of the sample. This implies that the tip-state does not influence our measurement. ii) The thermal stability at elevated temperature is shown in Fig. C.3. The topography data taken at 20 K within 4 hours interval, ensure that the thermal drift of the system is less than 1 atom/hour even at elevated temperature. In addition to that, the topography images, i.e. the LDOS information integrated from stabilized energy up to the Fermi level at ±35 mV show a different atomic contrast, presumably, due to the asymmetric

---

[5] The effect of different tip-states on topgraphy scan is discussed in appendix D explicitly.

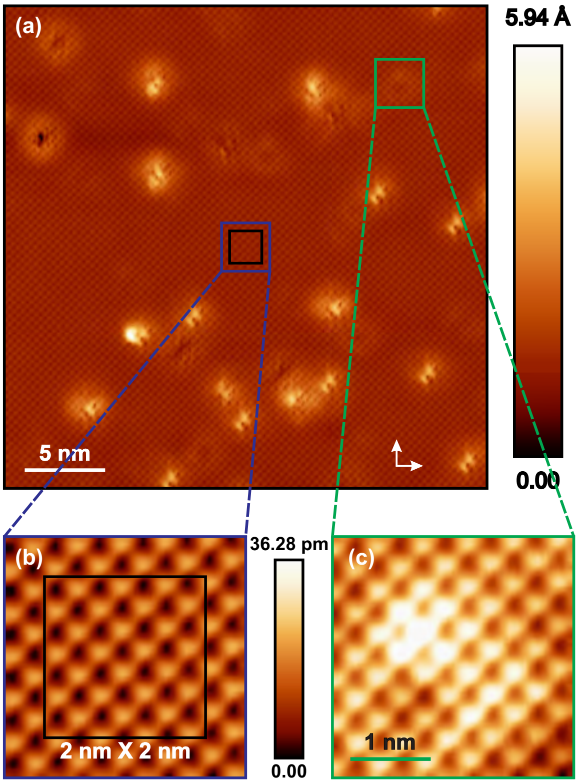

Figure 6.8.: (a) 30 nm × 30 nm area of atomically resolved constant current mode topography image of LiFeAs (I_T = 300 pA, V_{bias} = +35 mV) measured at $T = 4.8$ K. White arrows indicate the in-plane shortest Fe-Fe directions. The atomic corrugation on the surface corresponds to the Li-Li (As-As) lattice spacing of 3.77 Å. 22 bright defects from the first layer appear within the scan area. Faint signatures of defects presumably of the second layer of the material are also visible (green square). Temperature dependent spectroscopy has been measured within the black square of 2 nm × 2 nm area. (b) Zoom-in into the blue square in (a) to show atomic contrast in absence of defects. (c) Zoom-in into the green square in (a) to show the influence of a defect in the second layer.

LDOS background but it is not due to a different tip-state (see Fig. C.4).

Fig. 6.10 shows the averaged differential conductance (dI/dV) within the black area in Fig. 6.8 as a function of applied bias voltage V_{bias} for various temperatures. Two aspects are readily recognised in this data: i) in the normal state (20 K), the dI/dV curve exhibits a strong asymmetry between the occupied and unoccupied states with a hump-like enhancement around the Fermi level (zero bias), which is in good agreement with previous findings [112, 113]. ii) At the base temperature of our system (4.8 K), a pronounced signature of the superconducting state is superimposed on the normal state dI/dV background, where the depletion of the dI/dV at zero bias and the appearance of the coherence peaks at finite bias voltages are the most prominent indicators of the superconducting gap consistent with literature [97, 112, 113]. With increasing

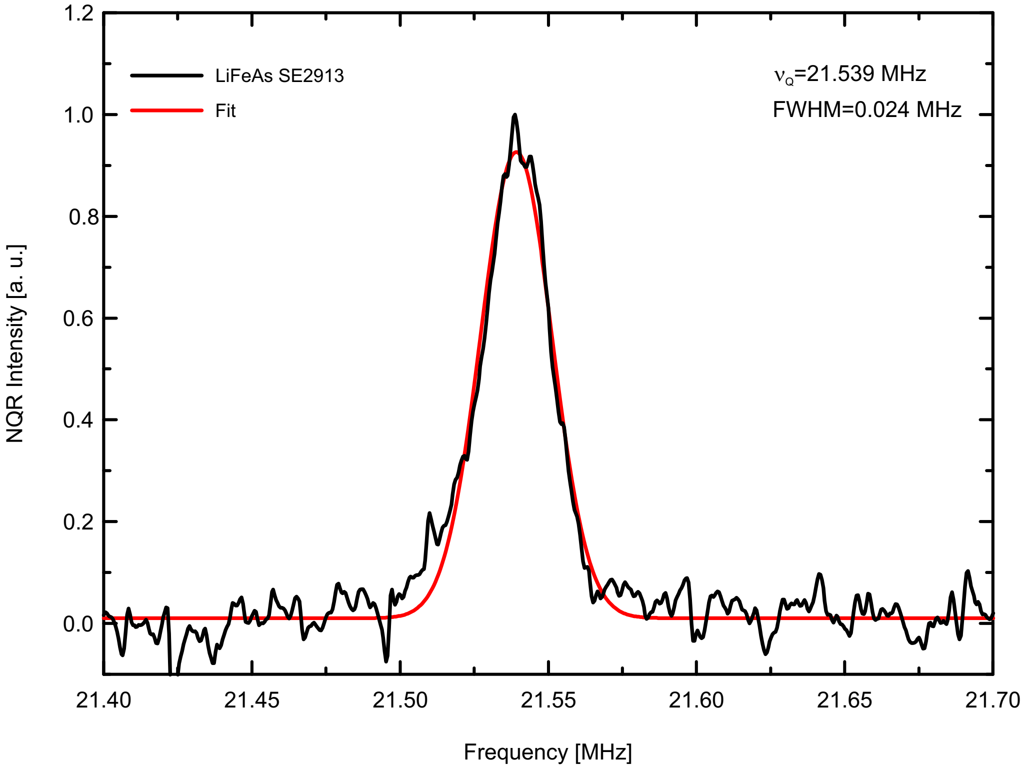

Figure 6.9.: Room temperature ^{75}As NQR data (black curve) on LiFeAs single crystal measured at ambient condition inside glove box at Ar atmosphere. The red curve is the Lorentzian fit to the data. The extracted NQR frequency (ν_Q) and line width signal (FWHM) from the fitted curve are 21.54 MHz and 0.024 MHz, respectively.

temperature, the data reveal a systematic closing of the gap as one would expect with an apparent T_c of about 16 K. For the illustration of the gap closing, we have plotted dI/dV data at the energy of strongest depletion, i.e. at zero bias in the inset of Fig. 6.10 as a function of temperature. The onset of a strong decrease of the dI/dV data below 16 K is clearly visible. However, a close inspection of the data (see inset of Fig. 6.10) reveals that the closing of the gap is incomplete even at temperatures $T > 16$ K.

In order to obtain further insight into the feature close to T_c, we have normalized all tunneling spectra with respect to the normal state spectrum at 20 K, see Fig. 6.11(b). This type of normalization allows us to disentangle superconducting LDOS states from normal LDOS states. All the features of the superconducting state are pronounced more after such normalization, as one can see in Fig. 6.11. The superconducting coherence peaks have been indicated by vertical solid lines. The feature within the marked coherence peak at small energies is particle-hole symmetric. Remarkably, this symmetry does not hold at larger energies. In particular, at positive V_{bias}, a pronounced dip and a hump appear at all temperatures (see Fig. 6.11). On the other hand, at negative V_{bias}, the dip is hardly below the normal state dI/dV value, but the hump structure is more

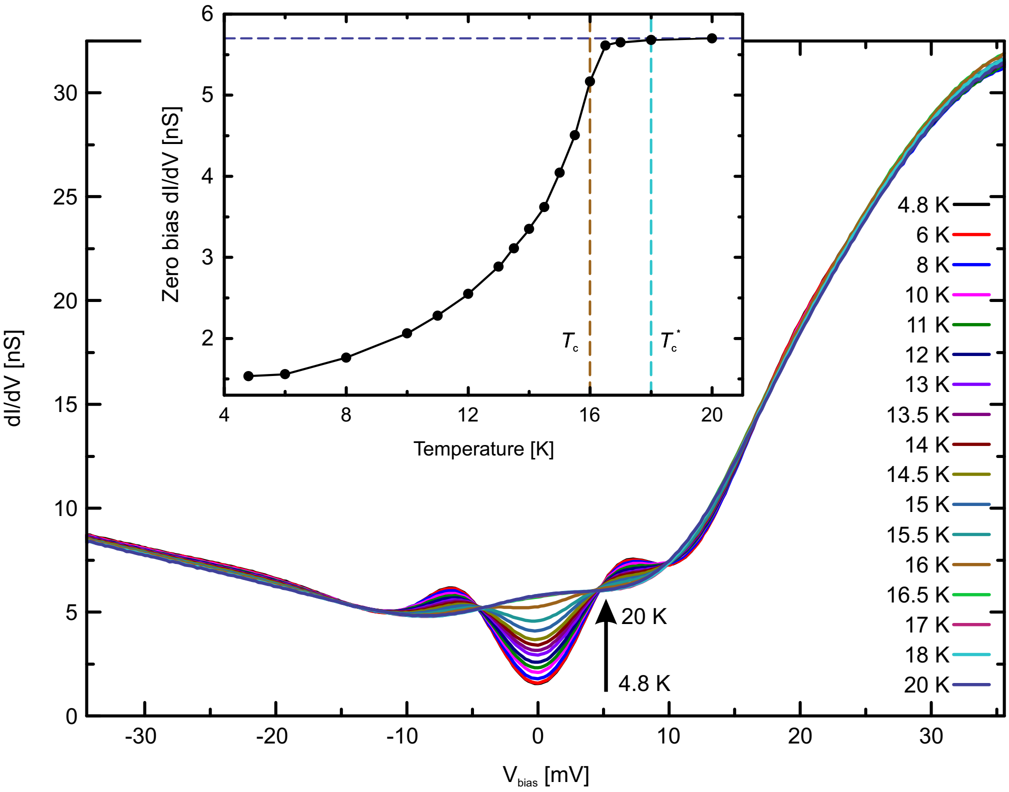

Figure 6.10.: Temperature dependent tunneling spectra measured within the black square of Fig. 6.8 between 4.8 K and 20 K. The up-arrow indicates the order of the curves at $V_{bias} = 0$ with increasing temperature. Inset: Zero bias differential conductance as a function of temperature. The horizontal dashed line is a guide to the eye. Vertical dashed lines indicate T_c and T_c^*, see text.

pronounced. Such dip-hump features are a good example of well-established theory of strong electron-boson coupling in high T_c superconductors which was introduced first by Scalapino *et al.* [23] around 50 years back in 1966[6]. These features are observed very frequently in Fe-based as well as in Cu-based high T_c superconductors where these are often interpreted as the fingerprints of a bosonic mode, mostly originating from spin-fluctuations. Surprisingly, the canonical spectral signatures of superconductivity, i.e. the coherence peaks, and the dip-hump structures are also clearly present in the normalized tunneling data at temperatures above the afore-inferred T_c of 16 K. This has become unambiguously clear in Fig. 6.11(c) which focuses on the temperature range between 16 K to 18 K. Thus, in addition to the onset of pronounced superconductivity at $T_c = 16$ K, our LiFeAs sample shows a superconducting state that is characterized by faint particle-hole symmetric spectral features already below $T_c^* = 18$ K.

After having established the main experimental observation, we now turn to analyse

---

[6] This is also discussed in chapter 5.

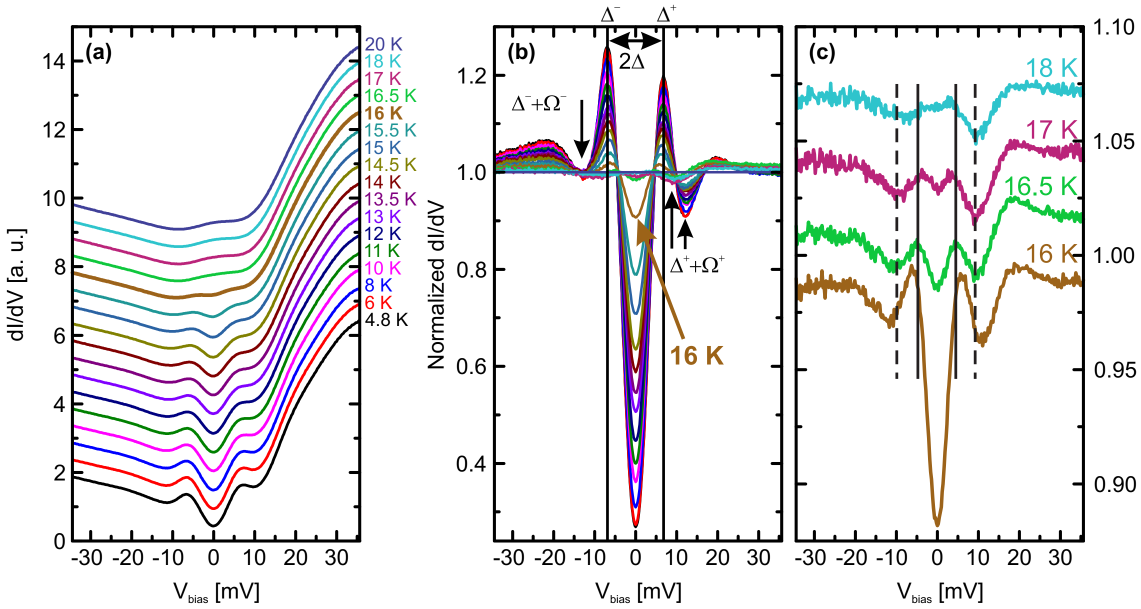

Figure 6.11.: (a) Waterfall representation of the differential conductance for various temperatures. The spectrum at 16 K is highlighted in bold. (b) Differential conductance at various temperatures normalised to that at 20 K. Black up-arrows indicate the shift of the position of the positive energy dip at $\Delta^+ + \Omega^+$ towards lower energy upon raising the temperature through $T_c = 16$ K. The down-arrow indicates the coarse position of the negative energy dip at $-\Delta^- - \Omega^-$. (c) Waterfall representation of normalised spectra in (b) at 16 K to 18 K. Superconducting coherence peaks and dip positions at 17 K are indicated by solid and dashed vertical lines, respectively.

thoroughly the observed spectral features as a function of temperature. In Fig. 6.11(b) we assign the distance between the coherence peaks at positive (negative) energy $\Delta^+(\Delta^-)$ to the double gap value 2Δ, and at each polarity the distance between the coherence peak and the dip position to the energy of a tentative bosonic mode $\Omega^+(\Omega^-)$ at positive (negative) energy. At base temperature (4.8 K), we find $\Delta \approx 6.9$ meV and a practically particle-hole symmetric $|\Omega^+| \approx |\Omega^-| = (5.4 \pm 0.1)$ meV, consistent with previous findings [112, 113]. The temperature evolution of the coherence peaks $(\Delta^+, -\Delta^-)$, the dip positions $(\Delta^+ + \Omega^+, -\Delta^- - \Omega^-)$, and the mode energies (Ω^+, Ω^-) are summarised in Fig. 6.12. The peak positions which provide an estimation for the temperature dependence of the superconducting gap $\Delta(T)$, interestingly, remain almost constant up to almost T_c. To be specific, $\Delta(T = 16K)/\Delta(T = 4.8K) \approx 0.87$. Upon increasing the temperature further, $\Delta(T)$ drops abruptly to about 50% of its low-temperature value at 17 K and becomes barely resolvable at $T_c^* = 18$ K. This unusual behaviour is in clear contrast to any BCS-like weak coupling scenario [130] as has previously been suggested by Chi *et al.* [112]. Concerning the positions of the dips, a very similar temperature dependence is found in our data. These remain almost constant at a value of about ±12 mV up to $T_c = 16$ K, and a jump-like decrease to about ±9 mV at higher temper-

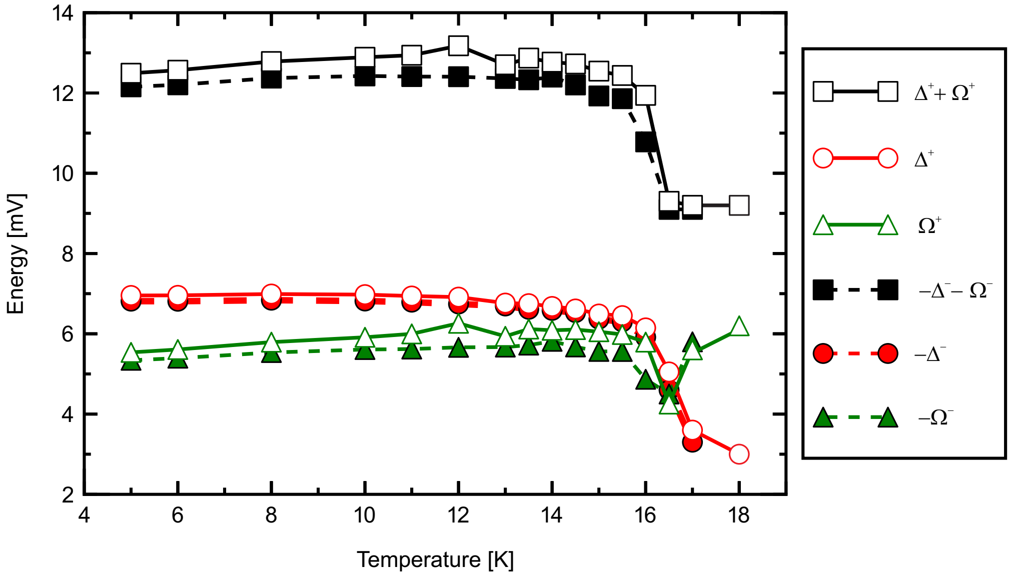

Figure 6.12.: Temperature evolution of superconducting coherence peaks (Δ^+, $-\Delta^-$), the dip positions ($\Delta^+ + \Omega^+$, $-\Delta^- - \Omega^-$) and the resulting Ω^+, $-\Omega^-$.

ature up to $T_c^* = 18$ K. Remarkably, the energy of the tentative bosonic mode (Ω^+,Ω^-) exhibits only a small dip around T_c but stays practically uninfluenced at lower and higher temperature.

Discussion

i) Two superconducting transition temperatures:

In general, a spatial homogenic behavior of the superconducting order parameter is expected within the coherence length of a superconductor. Thus, the observation of two transition temperatures T_c and T_c^* at an atomically fixed well-defined microscopic area of the order of ξ^2 reveals this feature to be an intrinsic property of the material. Therefore, it corroborates earlier findings where the measured critical temperature on the very same sample depends on the probing method and provides a reconciliation of the spread of reported T_c values [58,90,105–113].

The two transition temperatures might originate from a multiband electronic structure which can in principle be pictured as a possible source for a complicated superconducting state with multiple order parameters [64,131]. In LiFeAs, according to the ARPES-derived electronic band structure [88], the Fermi surface consists of quasi two-dimensional hole-like (labelled γ) and electron-like pockets (labelled β) centered around the Γ- and M-points, respectively (see the Chapter. 5). Two further hole-like Fermi surface pockets (labelled α_1 and α_2) are centered around the Z-point. The latter are tiny, yet have been reported to possess the largest superconducting gap of about 6 meV as compared to about 3.5-4 meV gap at the γ and β-pockets [12,86]. Recent theoretical work focuses on analysing possible pairing scenarios on the basis of this band structure [89]. They suggest a complicated multigap order parameter which allows for peculiar temperature dependency. In particular, it has been proposed that the α-Fermi surface pockets at $k_z \approx \pi$ may cause Cooper pairing prior to that of the Fermi surface pockets at $k_z \approx 0$, where the α-bands remain below the Fermi level (see Fig. 6.13). As a consequence, at temperatures just below the onset of superconductivity, the superconducting state may be very different than at lower temperature, where all the Fermi surface pockets contribute to the superconductivity. Considering such scenario, the observed $T_c^* = 18$ K might be interpreted as the onset of superconductivity at $k_z \approx \pi$, whereas the critical temperature $T_c = 16$ K can be related to the onset of full superconductivity emerging from the complete Fermi surface at all k_z.

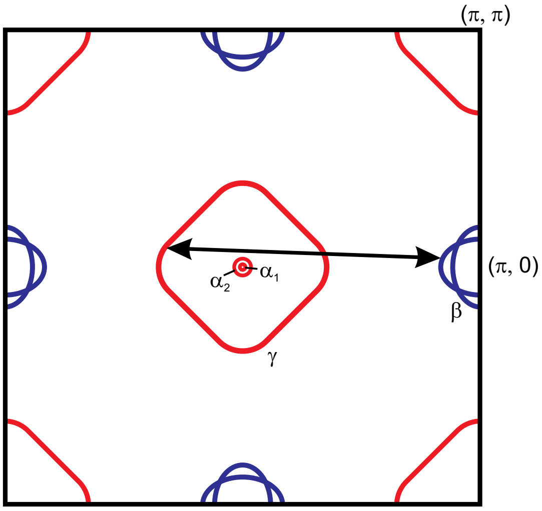

Figure 6.13.: Schematic diagram of the first Brillouin zone (one-Fe unit cell) in LiFeAs based on ARPES data [11]. The γ pocket at Γ-point and β pockets at M-point are present at all k_z value while the small isotropic α bands only cross the Fermi level for $k_z = \pi$.

Similar temperature dependent measurement has been done previously by Chi *et al.* [112] but the exact location of their temperature dependent measurement was not mentioned. Our very careful temperature dependent spectroscopic measurement on a spatially fixed area therefore allows us to study and compare all the different low energy features as a function of temperature with better accuracy. Moreover, Chi *et al.* have tried to fit the low temperature 6 mV superconducting gap and small-gap structures using modified Dyne's formula [132, 133] (see also Eqn. 6.1) where neither the considered gap anisotropy nor linear damping in their model could fit the zero DOS structure within the small-gap[7] states for non-zero bias values, which are now well established phenomena and seen by other groups in their low temperature data [97, 113]. They could even fit the spectra only until 6.8 mV, beyond which the spectra deviate significantly. Furthermore, their used spectra for extended Dyne's formula fitting are not normalized where one needs to consider the normal states DOS as a background. Therefore, from such analysis even a qualitative estimation is difficult if the focus of interest is either within the small-gap states or outside the large gap structure. In our data, we do not see the small-gap structure due to the thermal broadening of the system. But the overall structure is very similar to what has been observed by other groups [96, 112, 113].

ii) Origin of the dip-hump structure:

a) Connection of dip with an AFM resonance:

Besides the two transition temperatures, the second unusual observation in our data is the almost temperature independent energy of the tentative bosonic mode Ω. In previous works, the dip indeed has been refereed to a strongly coupled bosonic mode connected to an AFM spin resonance [97, 112]. However, this interpretation can be clearly ruled out due to following reasons. Firstly, in case of a connection of the dip to an AFM resonance, one would expect that the mode energy Ω tracks the order parameter as a function of temperature. This is contradictory in our data. Secondly, an AFM resonance at $(\pi, 0)$ is, in fact, absent in LiFeAs [14, 16] (also discussed in chapter. 5). Instead, INS only reports weak intensity response at incommensurate positions away from $(\pi, 0)$, which has been assigned later to ordinary interband excitations connected between poorly nested states in the γ- and the β-bands (see Fig. 5.9(d) in chapter. 5) [99]. This incommensurate feature in the dynamic spin susceptibility is too weak and too broad in energy to cause a very pronounce and sharp dip feature at the superconducting state tunneling spectra. Furthermore, in all high temperature superconductors, the peak related to peak-dip-hump structure of the tentative bosonic mode is rarely experimentally observed. This also boosts us to suggest that the interpretation of AFM resonance connected with the dip-hump structure is unlikely the realistic scenario. We will provide further discussion on this in the next chapter from temperature dependent QPI measurements.

b) Larger superconducting gap:

One can interpret the dip-hump structure as the signature of a larger superconducting gap. A test has been done by considering an additional superconducting gap of around 15 mV-17 mV with the other two known superconducting gaps in Dynes' formula [133] to catch the measured spectral features (see Fig. 6.1). A linear damping ($\Gamma = \alpha E$) with energy (E) is introduced in Dynes' formula to take care of inelastic processes [112, 132]. The proportionality constant α captures either the usual life-time broadening of the Cooper pairs or the anisotropy of the superconducting gap. The larger gap of around

---

[7] The highly resolved small-gap low temperature (0.5 K) data are reported by Hanaguri *et al.* [113] until now.

15 mV-17 mV must have high life-time broadening of Cooper pairs as they are far from the Fermi level. Therefore, it will probably produce very broad superconducting coherence peak. The Dynes' formula for three gap model for the superconducting DOS is the following:

$$\left.\frac{dI}{dV}\right|_{norm} = \int Re\Big[\sum_{i=1}^{3} \frac{w_i.\,(E - j\Gamma_i).\,\frac{\partial f(E-eV)}{\partial(eV)}}{\sqrt{((E - j\Gamma_i)^2 - |\Delta_i|^2)}}\Big]dE \tag{6.1}$$

Where, $f(E-eV)$ is the Fermi-Dirac distribution, linear damping $\Gamma_i = \alpha_i \times E$ and w_i is the weight factor for the each superconducting gap with the constraint $w_1+w_2+w_3 = 1$. However, these weight factors for different superconducting gap should depend on tunneling matrix elements between the tip and the sample. Therefore, a qualitative agreement is only possible between experimental spectra and Eqn. 6.1. In Fig. 6.14, the plot of the Eqn. 6.1 with the 6 K Fermi function broadening is shown in the red curve, where the considered superconducting gaps (Δ_i) are 2.7 mV, 6 mV and 17 mV and the corresponding weight factors (ω_i) are 0.05, 0.70, 0.25, respectively. The used life-time broadening of the Cooper pairs (α_i) are 0.25, 0.08, 0.40, respectively. The comparison of this model with the measured spectra which is shown in the black curve in Fig. 6.14, only provides a qualitative agreement between them. Mostly, the agreement holds better outside the superconducting coherence peak but the asymmetric shape of the dip-hump structure is still not possible to capture using such a model. Therefore, only the consideration of larger gap is not sufficient to explain fine details of the spectral features. Further possibility is to consider tip DOS and convolute it with such three gap Dynes' formula to fit the experimental data. However, this is even more complicated and the interpretation of the model is rather ambiguous. Anyway, in the section 6.3 we will enlighten the 15 mV to 17 mV feature better from the temperature dependent QPI data.

c) Inelastic tunneling processes:

Another possible origin of such dip-hump structure has been discussed very recently based on the inelastic tunneling in Ref. [134] (see Fig. 6.15). This is shown in Fig. 6.15. In their study, they have shown the strong-coupling scenario by Scalapino [23] where only elastic contributions are considered in red curve in Fig. 6.15(a) and yellow curve in the lower panel of (c)when a bosonic mode is present in the superconducting state at the energy of $\Delta+\Omega_{res}$. As below T_c, both the electronic DOS and the bosonic spectrum obtain a gap by Δ and Ω_{res}, respectively, the inelastic differential conductance is also gapped by $\Delta + \Omega_{res}$ (red curve in Fig. 6.15(b)). This increases sharply from $\Delta + \Omega_{res}$ with its significant influence to the LDOS for $eV > \Delta + \Omega_{res}$ but does not cross the normal state inelastic conductance value (blue curve in Fig. 6.15(b)) at high energies. They also argued that the inelastic contribution could be tuned by changing the tunneling amplitudes cutoffs D from the dip-hump structure (large inelastic contribution) to Scalapino's elastic strong-coupling scenario (i.e. zero inelastic contribution). This is shown in Fig. 6.15(d). To show such difference distinctly, the second derivative is

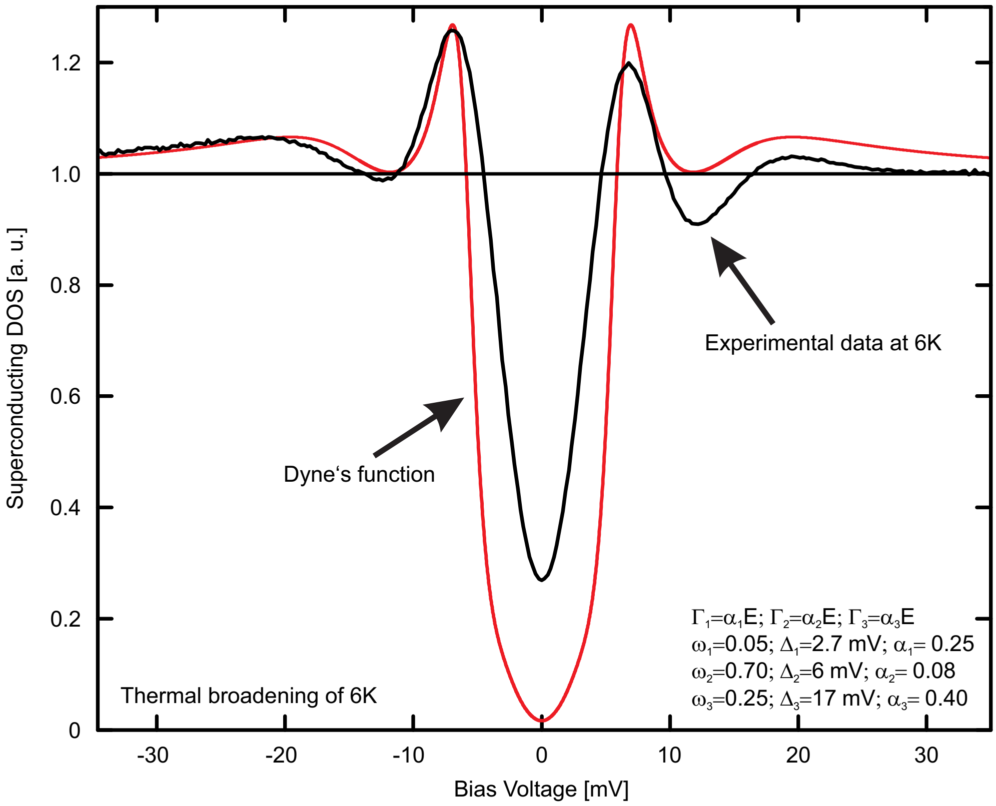

Figure 6.14.: The extended Dynes' function for three gap model which is described in Eqn. 6.1 is plotted in the red curve. The superconducting coherence peak and dip-hump structure have been tried to capture using such model. The details of the fit values are shown in the plot and mentioned in the text as well. The Fermi function broadening of 6 K temperature has been incorporate, too. The black curve is the normalized $\mathrm{d}I/\mathrm{d}V$ spectra of 6 K which is shown in Fig. 6.11(a).

plotted in Fig. 6.15(e) where the changes from a pure elastic to a strong inelastic scattering processes have different $\mathrm{d}\sigma_{norm}/\mathrm{d}U$ values at $\Delta + \Omega_{res}$. From the observation discussed above in Ref. [134] and based on another recent inelastic tunneling work on the superconducting Pb-films [135], they claim that such high energy electron scatters inelastically through the absorption or emission of a bosonic mode to a state near the Fermi level and coupled to low-energy states e.g. Cooper pairs. Further, their claim about the bosonic mode for such inelastic processes is originating from a spin-fluctuation which is mediating an unconventional sign-changing pairing state for LiFeAs. However, the dip position in our experiment does not behave like an order parameter, and INS did not observe any $(\pi, 0)$ resonance. So, the inelastic tunneling does not explain the spectral features and its temperature dependent response, too.

Thus, two important conclusions can be made from the results above: i) The data reveal two distinct superconducting phases in LiFeAs, which underpins the unconventional

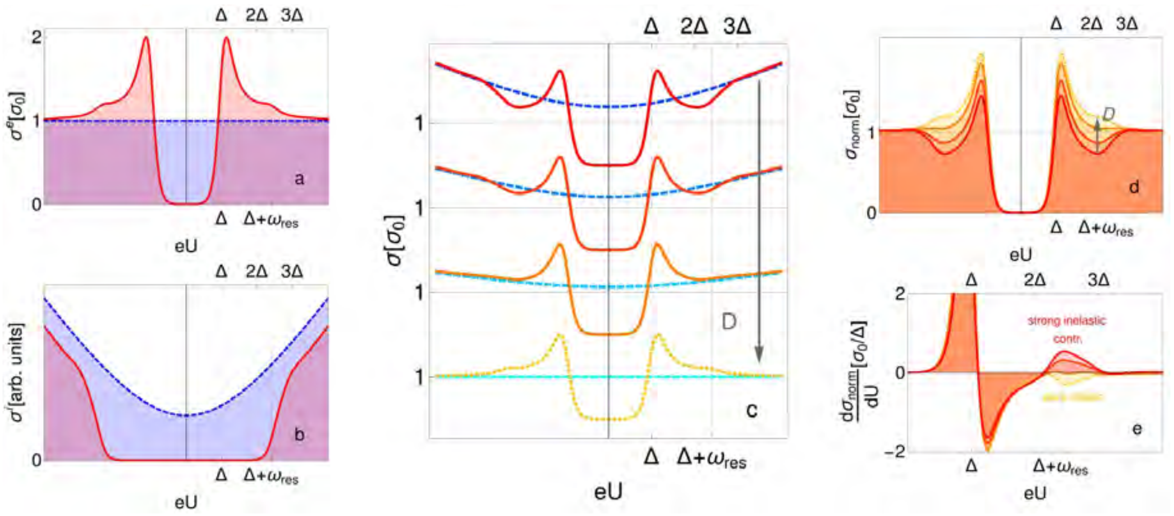

Figure 6.15.: The elastic (a) and inelastic (b) contribution to the differential conductance both in the superconducting (red, orange) and normal state (blue) tunneling spectra for different inelastic tunneling amplitudes energy cutoffs D (c) (increasing D lowers inelastic contributions), normalized conductance $\sigma_{norm}(U) = \sigma_{sc}(U)/\sigma_{nc}(\sqrt{U^2 - (\Delta/e)^2})$ (d) and derivative of the normalized conductance (e). The tunneling parameters are set such that the current I at $eU = 10\Delta$ is the same for the normal and superconducting state. This is taken from Ref. [134].

nature of superconductivity in this compound. This calls for further investigations of its superconducting order parameter to verify other predicted unconventional properties such as breaking of time-reversal symmetry [89, 136]. ii) Practically, the temperature independent distance between the dip positions from the superconducting coherence peaks in the tunneling spectra rule out its relation to an AFM resonance. In fact, this observation supports the INS data [14, 16] where no AFM resonance at $(\pi, 0)$ is found. Three following scenarios are also discussed as the possible origin of this but, however none of them could explain its origin entirely. Firstly, we will discuss the bosonic mode which Scalapino considered in strong coupling limit (see section 5.4). This can produce such a strong dip-hump structure [23], but the peak related to its peak-dip-hump is absent in the LiFeAs spectra. Therefore, Scalapino's strong coupling theory might not be a good explanation of the dip-hump structure. Another possibility is to consider inelastic scattering to explain this feature as it provides a very good qualitative agreement with the experimental results. The complex phenomenon of inelastic tunneling in Ref. [134] claims that high energy electrons (for $eV > \Delta + \Omega_{res}$) couple to bosonic mode[8] and produce the low-energy superconducting state (Copper pairs). But, the strong signature of such spin-fluctuation was not observed from other experiment like INS till now [14, 98]. Thirdly, a much simpler as well as effective approach is to consider a superconducting gap of energy around 15 mV-17 mV of linearly damped life-time broadened Cooper pairs in extended Dynes' formula. One might expect that such larger gap is probably origi-

---

[8] They claim such bosonic mode to be the collective mode mediating an unconventional sign-changing pairing state.

nated from the shallow α_1 band which crosses the Fermi level at the Z high symmetry point. In addition, such high DOS at $q \approx 0$ due to the top of the α_1 band at the Fermi level could lead to ferromagnetic spin-fluctuation to fulfil Stoner criterion. However, it is not supported by any other data yet. This means that in this regard, more thorough investigations are necessary for LiFeAs, and previous according interpretations for other iron-based superconductors [88,112,137,138] should be carefully reconsidered.

2) Spectral features beyond superconducting gap:

In this part, the focus of interest will be the spectroscopic features outside the superconducting gap within the energy range of ±0.1 V. The typical spectra[9] within ±0.1 V are shown in Fig. 6.16(a) where the clear particle-hole symmetric superconducting gap ($\Delta = 6.4$ mV) is noticeable close to the Fermi level at $T = 5$ K. An asymmetric dI/dV signal is visible outside the superconducting gap in both polarities. A rich dI/dV signal at unoccupied side from outside the superconducting gap is observed at 5 K in stark contrast to the occupied side, where any feature is hardly distinguishable from the dI/dV signal itself. The normal state dI/dV signal at temperature of 20 K has also been plotted to find temperature dependent features. To know the exact position of the change of the curvature i.e. inflection point in the dI/dV signal, its 1st derivative is shown in Fig. 6.16(b). Two peaks have been identified at ±15 mV which are the inflection points between the hump and dip positions in Fig. 6.11(b) and (c). The peak at +15 mV is relatively sharper than the peak at -15 mV. Interestingly, the 15 mV peak intensity at 20 K reduces significantly in comparison to its intensity at superconducting state at 5 K. Therefore, it might be connected to the superconductivity. The presence of a hump at 42 mV is found at both of these temperatures. Strikingly, the slope of the dI/dV signal beyond the 42 mV hump, in case of the 20 K spectra, is lower than that of the 5 K spectra. In contrast, the value of the dI/dV signal at the hump energy (42 mV) is relatively larger at the 20 K spectra with respect to the 5 K spectra. In Fig. 6.16(b), the 1st derivative of the dI/dV signal is used to find the energy of the hump position.

We have also studied the effect of temperature on the 42 mV hump by measuring the temperature dependent point spectra on the bare part of surface-A of LiFeAs until 61 K. The measured spectra at 6 K, 20 K, 50 K and 61 K are shown in Fig. 6.17(a)-(d), respectively. Like previous reult at Fig. 6.16(a), similar features at the superconducting state (6 K) and above the superconducting T_c (20 K) have been noticed, e.g. a superconducting gap opens at the Fermi level at 6 K, an appearance of a hump near the Fermi level at 20 K. However, the hump at the Fermi level which is distinct at 20 K, disappears at 50 K and 61 K. The 42 mV hump, which remains at the same position until 20 K, seems to reduce its intensity at 50 K and 61 K. As thermal broadening might be a possible origin of this, we therefore try to analyse the 20 K spectra convoluted with the 50 K and 61 K thermally smeared Fermi function to look for the finite temperature broadening effect. Data are shown in the inset of Fig. 6.17(b) and are also plotted separately in Fig. 6.17(f) and (g). After the convolution, the hump near the

---

[9] This is taken on surface-B. However, surface-A also shows very similar behavior.

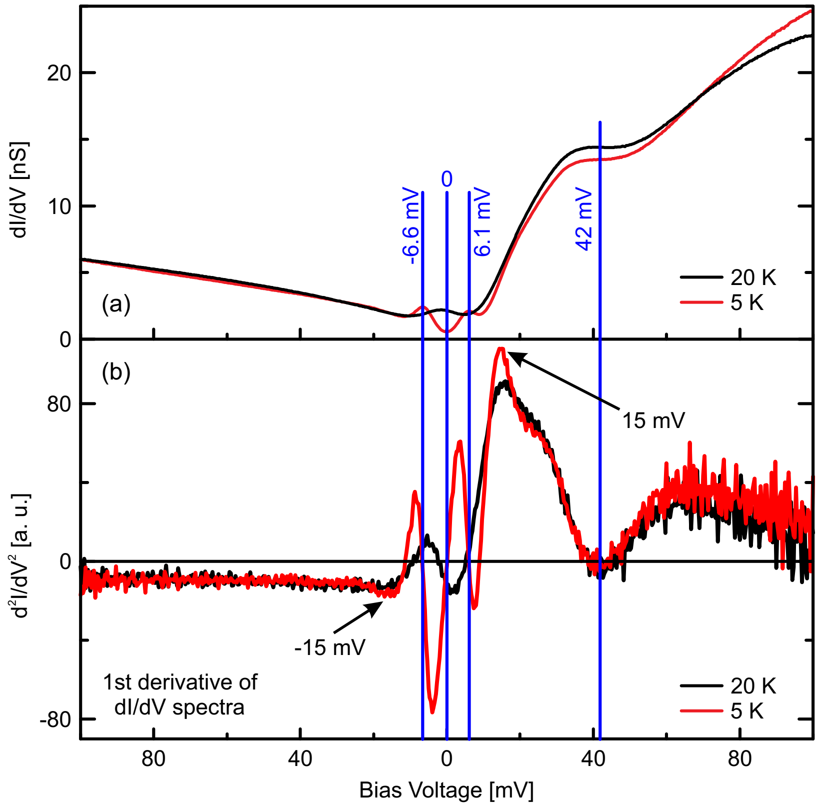

Figure 6.16.: (a) Spectra on stoichiometric LiFeAs (this data is taken on surface-B) within ±0.1 V taken at 5 K and 20 K. The 1st derivatives of (a) are shown in (b). Peaks at ±15 mV have observed in the lower panel where the change of the curvature of the dI/dV spectra is maximum. Interestingly, 15 mV peak at positive energy is distinctly lower at 20 K than the 5 K spectra at superconducting state.

Fermi level at 20 K has disappeared at 50 K and 61 K due to the thermal broadening effect. But, the 42 mV hump remains intact in the convoluted spectra (see Fig. 6.17(f) and (g)), indicating that the temperature dependent reduction of intensity of the 42 mV feature is an intrinsic electronic property of the material. The strong enhancement of the asymmetric dI/dV signal at 50 K and 61 K also cannot be explained by the thermal broadening effect. The derivative of the dI/dV spectra at 50 K and 61 K are plotted in the inset of Fig. 6.17(c) and (d), respectively. This indicates that the 42 mV hump is close to disappear at 61 K.

Discussion

The comparison of measured spectra between 5 K and 20 K in Fig. 6.16(a) provides the following interesting features. The peak intensity at the 1st derivative in the dI/dV signal at 15 mV is found to reduce while the system changes from superconducting state to normal state. This reflects a direct connection to this peak with the superconductiv-

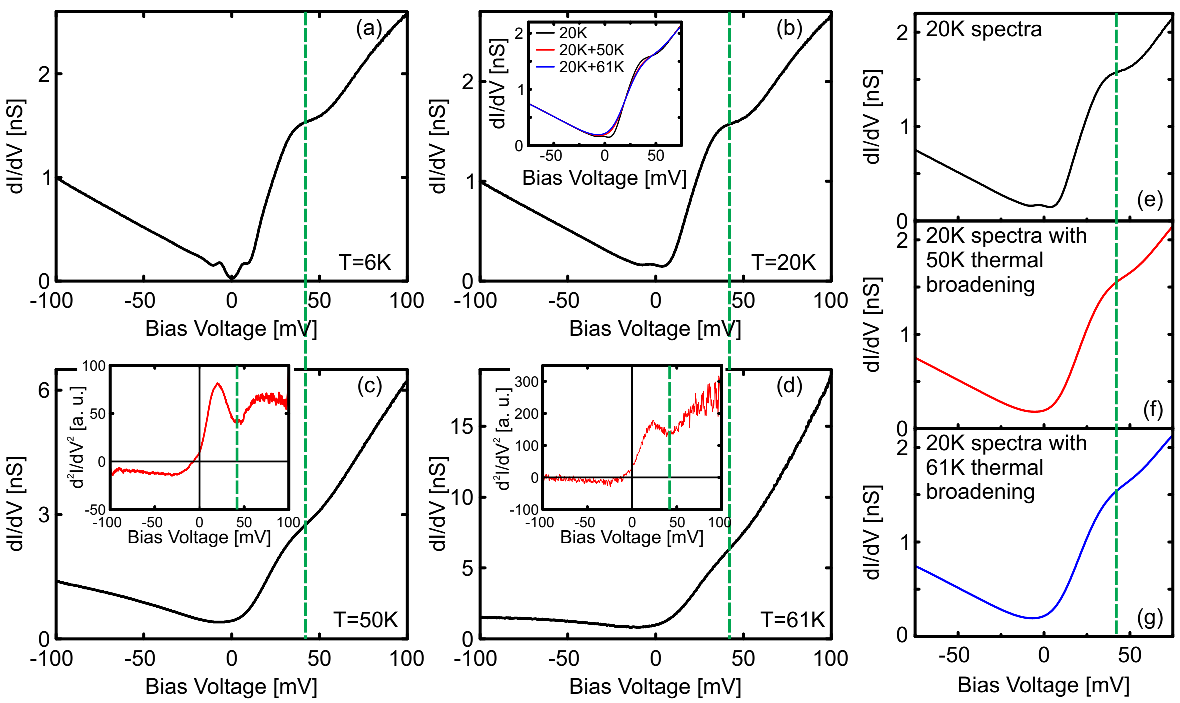

Figure 6.17.: Spectra of ±0.1 V on LiFeAs bare surface are shown within the temperature range of 6 K and 61 K. (a)-(d) The measured spectra at 6 K, 20 K, 50 K and 61 K are plotted, respectively. Inset of (b): The convoluted spectra of 20 K measurement with 50 K and 61 K thermal broadening of the Fermi function are plotted. The inset of (c) and (d): The respective 1st derivative of the spectra show the relative decrease of the +43 mV dip intensity with increasing temperature. (e)-(g) The inset of (b) is shown separately to show how the 50 K and 61 K thermal broadening affect the 20 K LiFeAs spectra.

ity. I will illustrate further details about this in the QPI section (section 6.3). The dip positions in the 1st derivative in Fig. 6.16(b) which indicates the 42 mV hump energy, keep in the same place at both 5 K and 20 K temperatures. But the intensity of the dI/dV signal at 42 mV becomes higher at 20 K than 5 K spectra which is not only unusual, but its origin also cannot be explained. This still remains an open question.

The other observation of the temperature dependent hump features, both near the Fermi level and at the energy of 42 mV in Fig. 6.17(a)-(d) in comparison with thermal smearing of the 20 K spectra in Fig. 6.17(f) and (g) confirms that the disappearance of the hump near the Fermi level is due to the thermal broadening effect. On the other hand, the 42 mV hump does not seem to be affected by such thermal broadening in the convoluted data. But remarkably, their intensities in the 1st derivatives of the measured spectra shown in the insets of Fig.6.17(c) and (d) go to non zero higher value in both cases in comparison to 5 K data (for example in Fig. 6.16(b)) where the dip touches the zero value at 42 mV. This observation allows us to suggest that the hump gradually disappears around 61 K. Its origin is still unknown to us. A recent optical spectroscopy data have reported the signature of spin density wave gap [139]. This might be the possible origin of such 42 mV feature which persists relatively higher temperature of around 60 K, similar to NaFeAs [70].

6.3. Visualizing the electronic band structure in LiFeAs by temperature dependent quasiparticle interference

6.3.1. Topography

In this section, we will explore the method of so called Fourier transformed quasiparticle interference by using STM/S tool in order to visualize the band structure in stoichiometric LiFeAs close to the Γ point (for scattering vector, $q \approx 0$). A representative topography on surface-A of stoichiometric LiFeAs is shown in Fig. 6.18. It has a relatively larger scan area of 110 nm × 110 nm which has been used for such spectroscopic map measurements. Six different types of frequently observed defects can be identified on the surface with defect concentration that is consistent with previously reported data [31, 32, 47, 97]. Surface-A was chosen for spectroscopic measurements as the previously studied QPI measurements were only performed on this type of surface [47,48,96,97,103]. It is therefore worthwhile to compare our result with the existing data in literature if any similarities are found. The Li-D_4-1 (missing Li atom) and Li-D_4-2 (additional Li atom) defects are not seen within the field of view. Previously, defects study in Ref. [31] have reported that the bound states associated with Fe-D_2-1 and Fe-D_2-2 (shown by number 4 and 6 in Fig. 6.18) defects[10] have energy width of ±4 mV. These Fe-defects together have the major concentration of about 38% among all types of defects on the surface. Therefore, the scattering of quasiparticles by these Fe-defects have the major contribution to the QPI signal. Each spectroscopic map is taken within the energy range of ±30 mV with 91 energy points resolution as a function of temperature from 6.7 K to 25 K. To avoid the z-point effect i.e. the effect due to the variation of LDOS on the tip-sample separation, the tip was stabilized relatively far from the sample surface using a larger bias voltage (V_{bias}=-50 mV) for each spectroscopic map. The corresponding set-point, I_T was 0.6 nA. Before start with results, the used orientation of the QPI maps are plotted as a schematic diagram in Fig. 6.19(a) for all temperature measurements. Here, both 1Fe and 2Fe unit cells are shown but we consider only 2Fe unit cell in case of QPI data analysis. The Brilloiun zone of the LiFeAs crystal is shown in Fig. 6.19(b). The k_z values from 0 to π correspond to the $\Gamma - Z$ high symmetry direction where its 0 and π values are pointing to the Γ and Z high symmetry point, respectively.

6.3.2. Quasiparticle interference

Real space and its FFT information

A few selective energy slices from one representative spectroscopic map[11] which are measured at the temperature of 6.7 K are shown in Fig. 6.20 while their FFT images are

---

[10] Both of these defects are discussed in section 6.1.

[11] The full real space spectroscopic data and their corresponding QPI signals are shown in appendix section E for three selective energies 6.7 K, 14 K and 25 K.

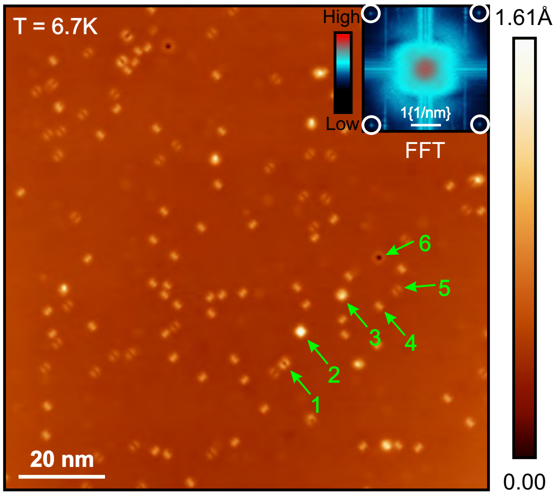

Figure 6.18.: One representative high resolution (2048 × 2048 pixels^2) topography image (Set point: I_T=0.6 nA, V_{bias}=-50 mV) where spectroscopic map with 256 × 256 pixels^2 lateral resolution within ±30 mV energy with 91 energy points has been taken over an area of 110 nm × 110 nm at 6.7 K. Six different types of defects which typically observed as well as reported in literature [31, 32] in case of stoichiometric LiFeAs, are visible and have been marked by green arrows. According to the number, the marked defects are C_2 symmetric with unknown origin, As-D_4 defect, D_1 symmetric defect with unknown origin, Fe-D_2-1 defect, Fe-D_2-2 defect, As-D_4 defect, respectively. The two types of Fe-defects are mostly seen on the surface. Inset: FFT image corresponds to the topography image, where first order Bragg peaks due to the Li-lattice constant are marked by white circles along the diagonal directions.

plotted in Fig. 6.21. The energy dependent structures around the defects are already visible in Fig. 6.20 whereas the rich QPI intensity patterns near $q = 0$ are noticed in all FFT images in Fig. 6.21. Such energy dependent QPI patterns, according to their size, relate to the oscillating structure around the defects in the respective $\mathrm{d}I/\mathrm{d}V$ energy slices. To elaborate on it in detail, let us compare energy slice at energy 26 mV in Fig. 6.20(t) with its QPI signal in FFT image of Fig. 6.21(t). This is separately enlarged and analysed which is shown in Fig.6.22. One defect is zoomed in the lower inset of Fig. 6.22(a). The line profiles along the arrows in the zoomed image as well as in the inset FFT image are plotted in Fig. 6.22(b) and (c). The size of the biggest ring marked by the dark brown color in the inset FFT image has a radius of (0.152/3.8) Å^{-1}, or 0.04 Å^{-1}, which corresponds to the real space value of 2.5 nm. The dark ring like contrast at the center of defect in the energy slice in Fig. 6.22(b)(also see Fig. 6.20(t)) has the similar size of 2.5 nm. Another example is the edge of the reddish contrast shown by the green arrow in the same inset FFT image which has a radius of (0.086/3.8) Å^{-1} or 0.0226 Å^{-1}. It is related to the real space width of 4.4 nm which corresponds to the strong white intensity around the defect in Fig.6.22(b)(also see Fig. 6.20(t)). Both of these examples are marked by a pair of dark brown and green vertical lines, respectively

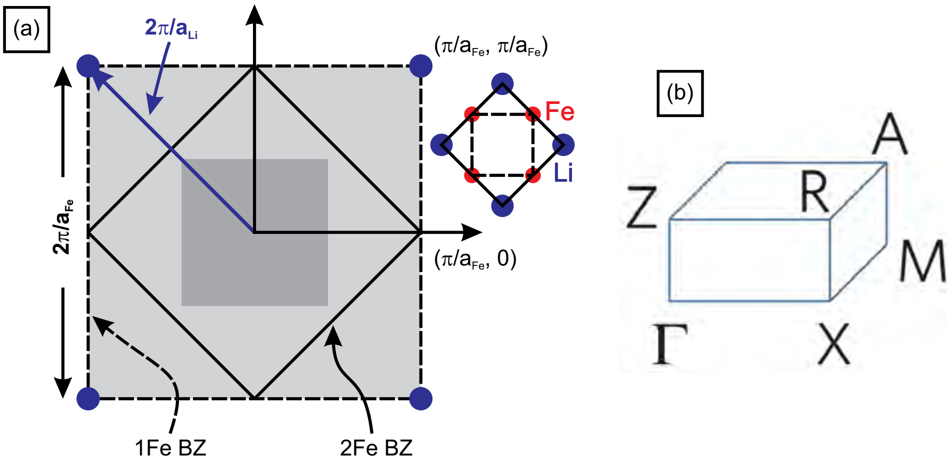

Figure 6.19.: (a) The spectroscopic map measurement is performed with such orientation. The grey area close to the Γ point is the total size that covers using such large area (110 nm × 110 nm) spectroscopic map study. The same orientation is used for all temperature study. Here, the shortest Fe-Fe direction is along the horizontal direction. However, the measured orientation was rotated by 45° for the case of spectroscopic measurement in off-stoichiometric LiFeAs which will be discussed in section 6.4. In the upper right side of the image, the Li and Fe atoms orientations in real space related to the FFT pattern of (a) are shown. (b) The Brillouin zone of LiFeAs where the high symmetry points are pointed. It is taken from Ref. [87].

in both of the Fig. 6.22(b) and (c)[12]. Similarly, it can be shown that all the QPI features are related to the real space modulations of the corresponding dI/dV energy slices. However, to visualize the detailed QPI structure, the line cuts along the high symmetry directions is plotted to look at the dispersion like behavior in q space.

Line profile of the QPI image

The QPI signals at a few selective energies which are plotted in Fig. 6.23, illustrate the main results of this chapter that are discussed in detail later. The corresponding line cuts of them along two high symmetry directions (Fe-Fe and Fe-As directions) are also plotted in the right hand side of each image. In all QPI images, the high intensity at $q = 0$ due to the DC part of the signal are present as an indicator of the Fourier trans-

---

[12] Note that, in the line profile of Fig. 6.22(c), the distance of one of the line from either side of zero is equivalent to the distance of pair of the lines in Fig. 6.22(b).

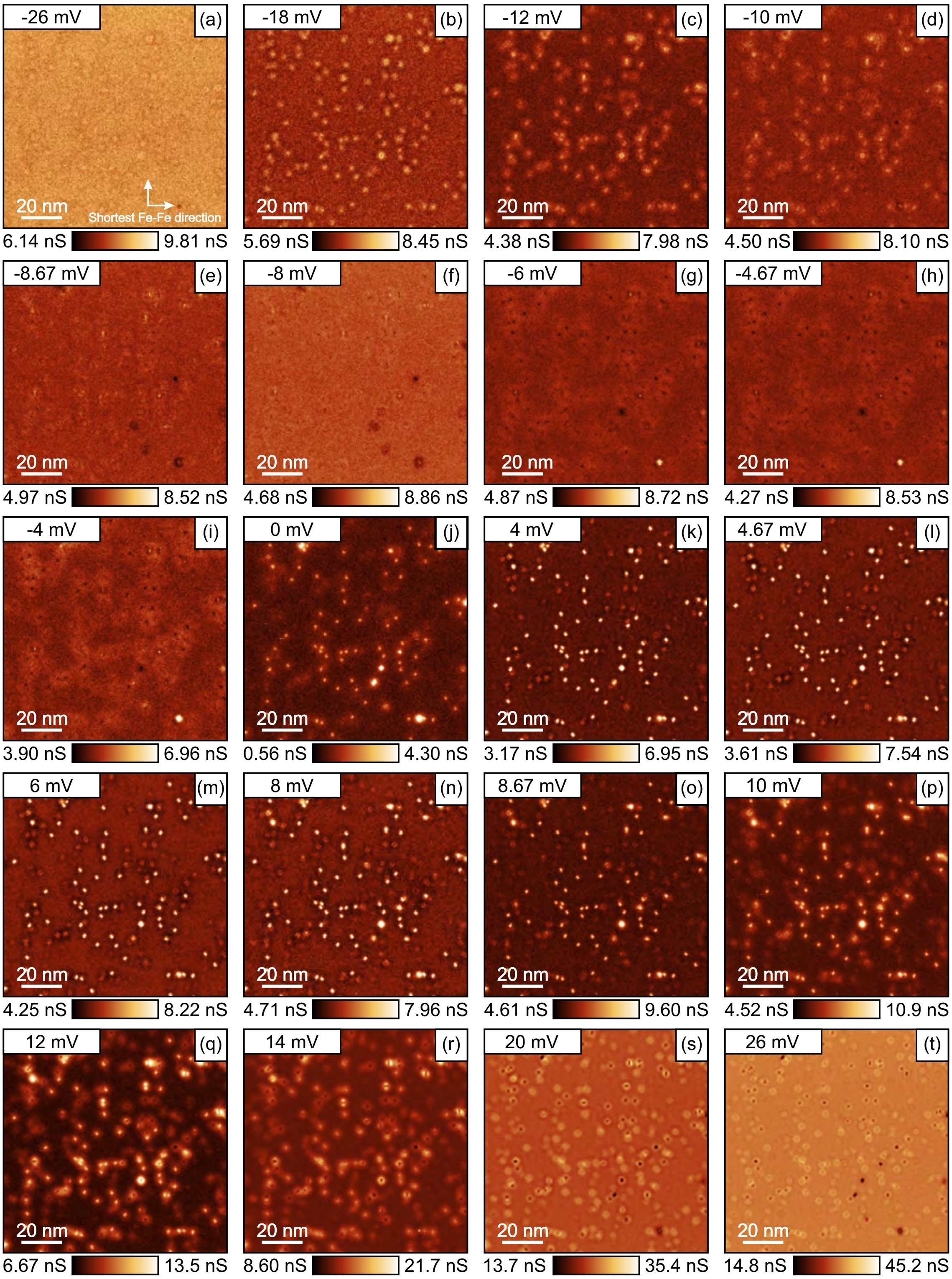

Figure 6.20.: A few selected constant energy $\mathrm{d}I/\mathrm{d}V$ slices from a spectroscopic map taken at the same place of Fig. 6.18 at 6.7 K. The corresponding energies of those images ((a)-(t)) are shown in the left upper corner of each image. The energy dependent structure is visible around defects.

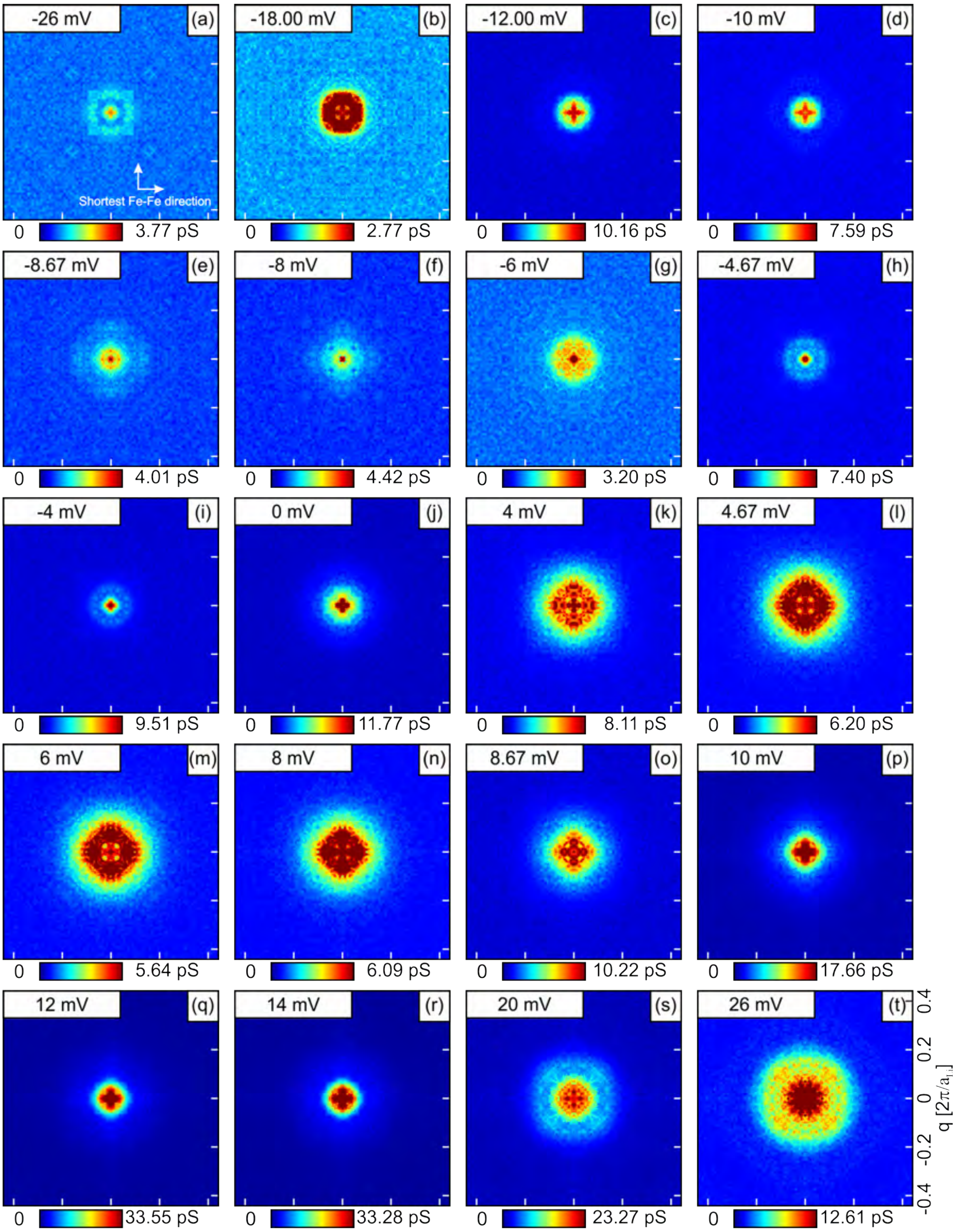

Figure 6.21.: The QPI signals related to the constant dI/dV energy slices of the spectroscopic map shown in Fig. 6.20. The Γ point is at the center of each image. Total size of each image is $0.44\times 2\pi/\mathrm{a}_{Li}$. The QPI intensity is found to be strongly energy dependent. This is measured at 6.7 K.

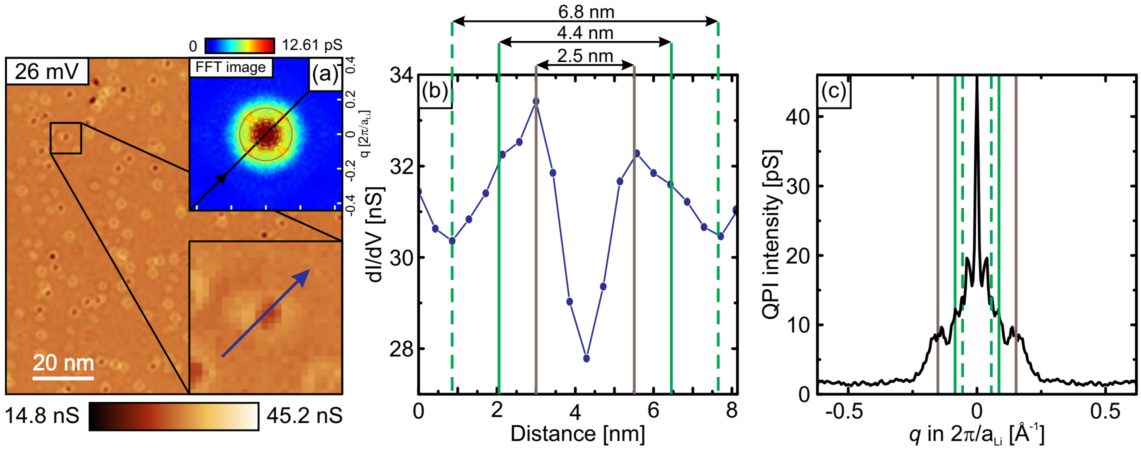

Figure 6.22.: (a) The 26 mV dI/dV energy slice from the spectroscopic map shown in Fig. 6.20. Oscillations around one dumbbell (Fe-defect) defect with an area of 10 nm × 10 nm marked by the black square is zoomed in and shown in the lower inset of the image. The QPI intensity corresponding to the 26 mV energy slice is shown in the upper inset. The dark brown and green arrows in the QPI image are indicating dominating ring like QPI intensities. (b) The line profile along the blue arrow on the zoomed image in (a) is plotted, whereas the line profile over the QPI intensity along black line is shown in (c). The oscillations around the zoomed in image in (a) are compared to the corresponding dominant QPI scattering which are shown using dark brown, green solid lines and green dashed line. They are also pointed by dark brown and green rings in FFT image.

-formation of the real space energy slices. Apart from that, all the other structures are observed as QPI patterns which are related to the electronic properties of LiFeAs sample. For example, the very strong enhanced intensity at 15.33 mV energy can be identified easily as a distinct feature compared to QPI patterns at other selected energies. The comparison of its intensity even shows its asymmetric behavior with QPI signal at -15.33 mV energy where the QPI intensity is five times smaller than at 15.33 mV energy. The QPI signals at 8 mV and -8 mV energies have very low intensities with respect to all the other QPI signals. A very particular structure at q value of $0.04{\times}2\pi/\mathrm{a}_{Li}$ has been found for the QPI signals at 4 mV, 0 mV and -4 mV energies. These are marked by up arrows in those line cuts. Overall, the QPI signal intensities at the occupied side are relatively weaker than the unoccupied side. In the following, the structures of enhanced intensity near q = 0 at 4 mV, 0 mV and -4 mV energies; the reduced QPI intensities at 8 mV and -8 mV and the rich QPI signal at 15.33 mV have been analysed and are discussed in detail.

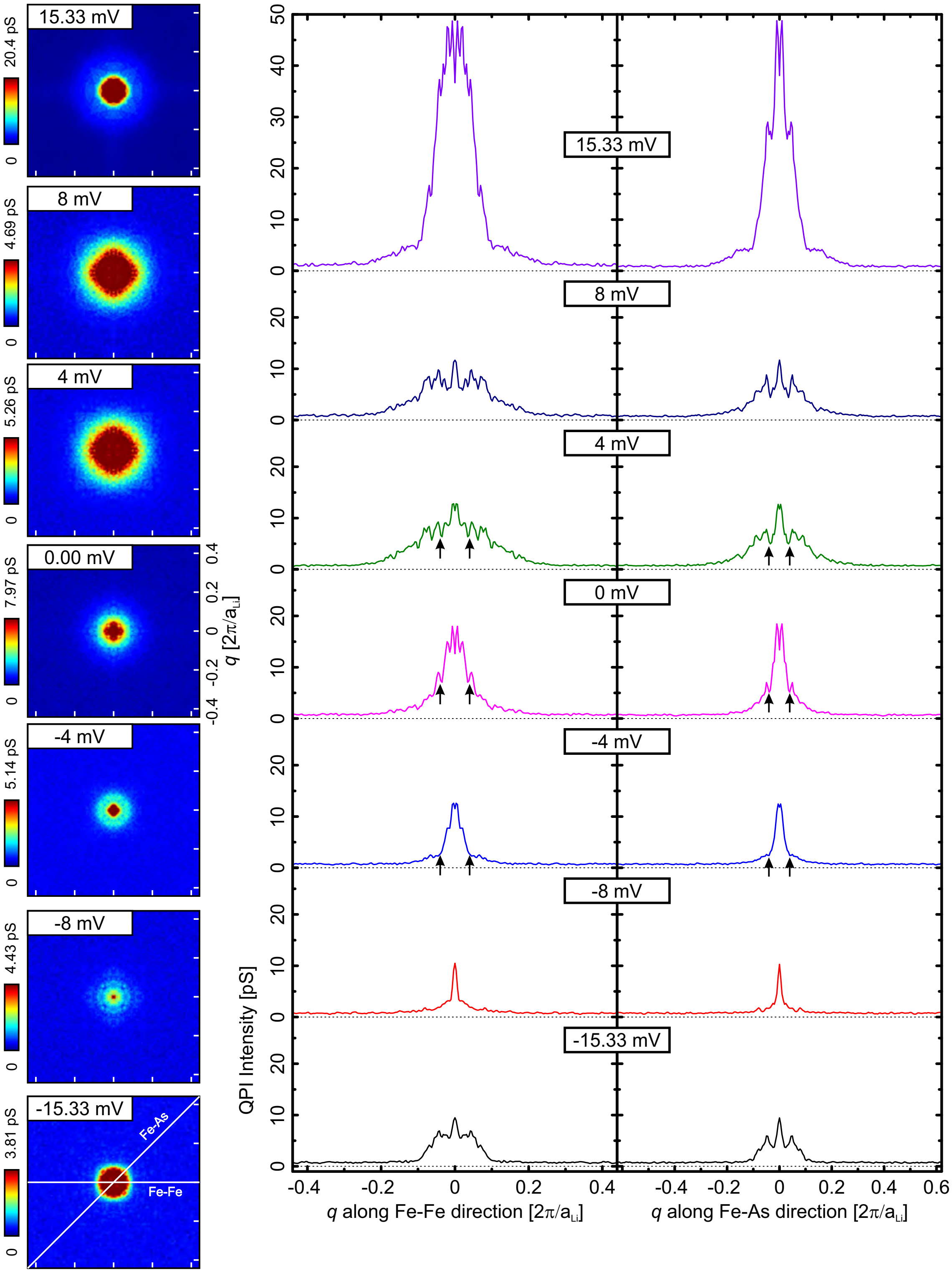

Figure 6.23.: The selected energies of QPI signal where the interesting changes have occurred in QPI pattern, are shown in the left column. The line cuts along Fe-Fe and Fe-As directions are plotted in the right side of each images.The black arrows are indicating the width of the enhanced QPI intensities between ±5.5 mV in q direction.

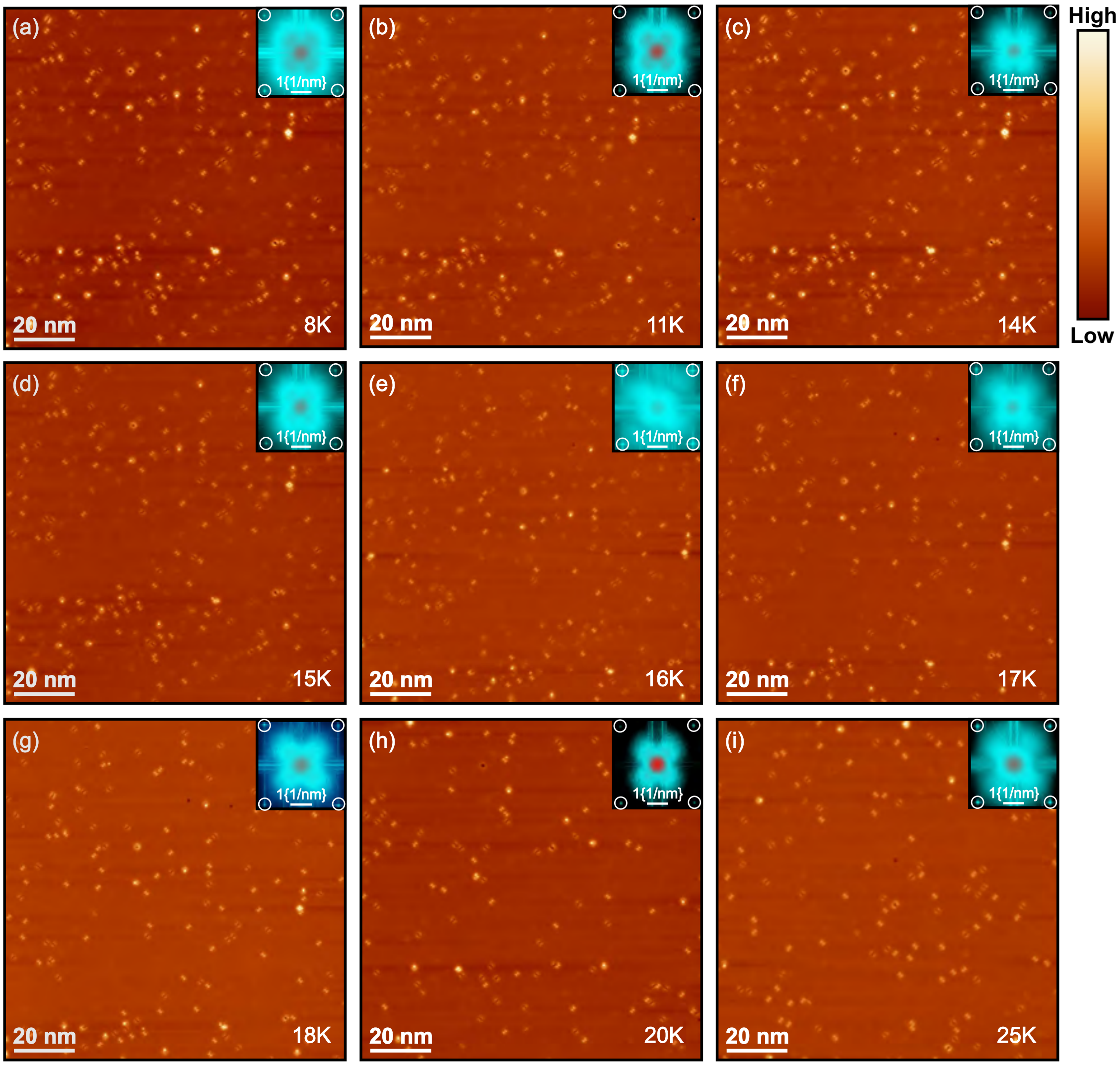

Figure 6.24.: The topography data are shown at each temperature of measured spectroscopic maps. The stabilization conditions of each image are V_{bias}=-50 mV and I_T=0.6 nA.

dI/dV spectra

Before going to the detailed analysis of the results, we would like to have a look at the topography images as well as the corresponding spectroscopic data on bare surface at the measured QPI maps for all temperatures. The high resolution (2048×2048 pixels^2) topography images where the respective spectroscopic maps have been measured in the temperature range between 8 K and 25 K[13] are shown in Fig. 6.24. The Bragg points marked by white circles in the inset of each diagram, correspond to the Li-Li lattice constant. All spectroscopic data of three selective temperatures of 6.7 K, 14 K

---

[13] The topography at 6.7 K, has already been shown before in Fig. 6.18.

and 25 K are shown in appendix E and all the rest of the QPI data are shown in the electronic version of this thesis. The representative bare surface dI/dV spectra[14] at each spectroscopic map are shown in Fig. 6.25 for all the measured temperatures between 6.7 K and 25 K. Here, a systematic closing of the superconducting gap with rising temperature and the strong particle-hole asymmetric background spectral feature are observed, consistent with previously discussed spectroscopic features in subsection 6.2.2. All the 1st derivatives of those representative dI/dV spectra are shown in Fig 6.26. The 1st derivative of the 25 K spectrum is plotted with 6.7 K data in Fig.6.26(a), too, where besides closing of the superconducting gap, the suppression of intensity at 15 mV is observed at 25 K. At low temperatures, these 15 mV peaks are very pronounced while the reduction of their intensities occurs with increasing temperatures. Similar observation has also been mentioned in the subsection 6.2.2 in Fig. 6.16 where the comparison was between 5 K and 20 K dI/dV spectra.

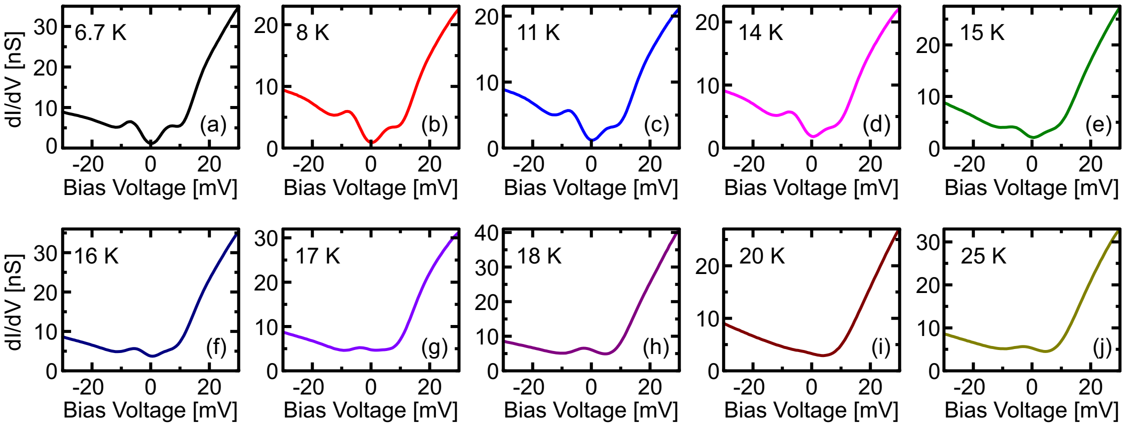

Figure 6.25.: Average dI/dV spectra over the clean surface on every spectroscopic map taken between 6.7 K and 25 K. The stabilization conditions for each spectra are V_{bias}=-50 mV and I_T=0.6 nA.

$E(q)$ dispersion

The dispersion $E(q)$ of the QPI signal for each measured temperature along Fe-Fe and Fe-As directions are plotted as upper and lower panels, respectively in Fig. 6.27. In each plot, the vertical axis represents the energy of the quasiparticles and the horizontal axis represents the scattering wave vector q of them, while the false colors are indicating quasiparticle intensities. The vertical and horizontal distances of the red rectangle in the line cut along Fe-As direction at 6.7 K indicate the size of the enhancement of the QPI intensity near $q = 0$ in both energy and q directions, respectively. The dashed red lines at the center of every image are indicating the Fermi level for each plot. The solid

---

[14] All the shown spectra are averaged over several single point spectrum on the bare surface.

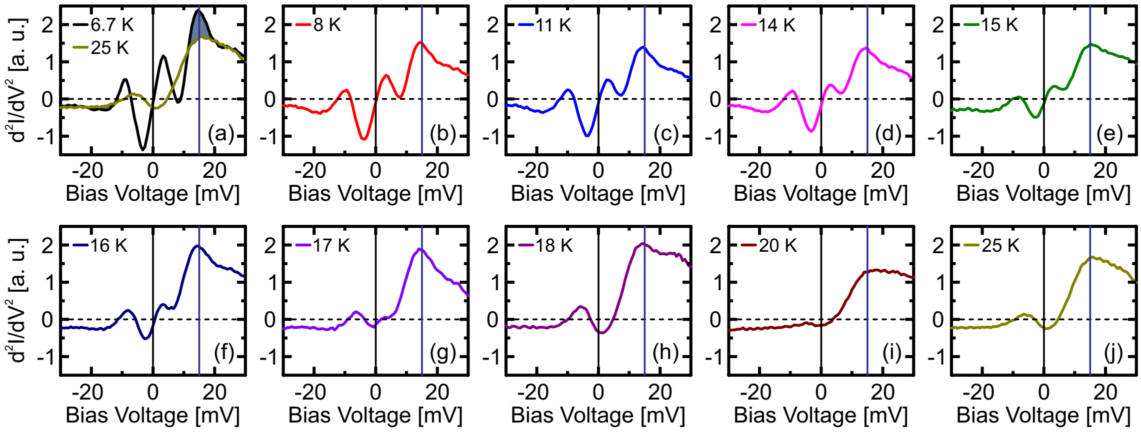

Figure 6.26.: The derivative of the respective clean surface spectra which are shown at Fig. 6.25. The dashed horizontal lines and the black vertical lines are indicating the zero $\mathrm{d}^2I/\mathrm{d}V^2$ value and the Fermi level for each plot. The vertical blue lines are pointing the peak position (15 mV) of the shaded area for every plot which reduces with rising temperature. The 25 K spectra are plotted in (a) with 6.7 K spectra, too.

red lines are pointing the upper (lower) energy edge of the depletion of the QPI intensity (at around ±9 mV) at temperature of 6.7 K, above (below) which, a sharp enhancement of the QPI intensity has started. It helps to observe how this feature moves towards the Fermi level with increasing temperature. The particle-hole symmetric enhancement of QPI intensity within ±5.5 mV disappears with rising temperature and the top of the α_2 band possibly appear in the same position above superconducting T_c. However, a strong enhancement of the QPI intensity above 9 mV at unoccupied side remains unchanged, indicating that this is directly related to the enhanced bare surface $\mathrm{d}I/\mathrm{d}V$ spectra (shown in Fig. 6.28).

Comparison between $E(q)$ dispersion and dI/dV spectra

One of such line cut measured at a temperature of 6.7 K along Fe-As direction (also shown in Fig. 6.27), is enlarged and shown in Fig. 6.28. The $\mathrm{d}I/\mathrm{d}V$ spectrum measured on bare surface has been plotted on top of it to compare them together, and hence is to find the corresponding origin of different features in such $E(q)$ dispersion plot. The energy dependent rich structure is visible mostly in the positive energies above 9 mV, which is consistent with the enhanced $\mathrm{d}I/\mathrm{d}V$ spectrum. Below 9 mV (above -9 mV), the particle-hole symmetric depletion of QPI intensities until 5.5 mV (-5.5 mV) is observed. The same energy locations of such depletion are marked by the black areas at $\mathrm{d}I/\mathrm{d}V$ spectrum. In addition, an enhancement of almost particle-hole symmetric[15] QPI intensity within the energy width of ±5.5 mV is distinctly visible. Its extension

---

[15] It is almost particle-hole symmetry in QPI intensity because a faint additional QPI intensity at unoccupied side within 0 to 5.5 mV appears due to defect bound state related to Fe-defects [31] which will be discussed later in this chapter from integrated QPI intensity data. But, in the following, I only will call this as a ”particle-hole symmetricÂťÂť feature so that the language becomes easy for the audience to follow.

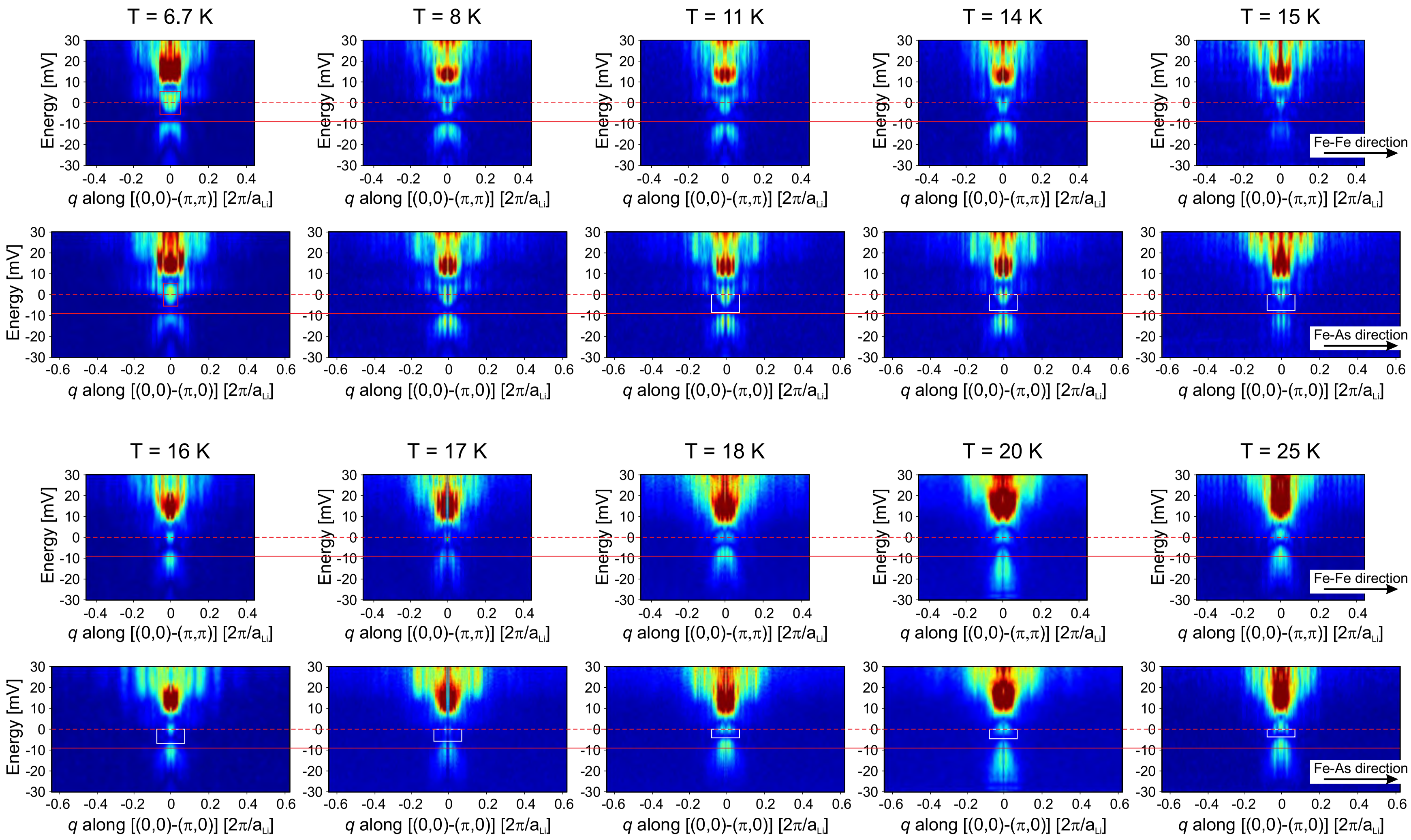

Figure 6.27.: The $E(q)$ dispersion plots at various temperatures. Upper panel (a-e and k-o) and lower panel (f-j and p-t) at each temperature are the line cuts along Fe-Fe and Fe-As directions, respectively. The vertical lengths of the white rectangles provide the distance of the top of the α_1 band from the Fermi level. The vertical distance of the red rectangles are the distance of the edge of the enhanced QPI intensity beyond 9 mV from the Fermi level at base temperature (6.7 K). It is clear that this reduces with increasing temperature and stops at around 3 meV below the Fermi level (see images (o) and (t) of 25 K data). The dashed line at the center of each image indicating the Fermi level whereas the solid lines pointing the starting of enhanced QPI intensities below (above) 9 mV(-9 mV).

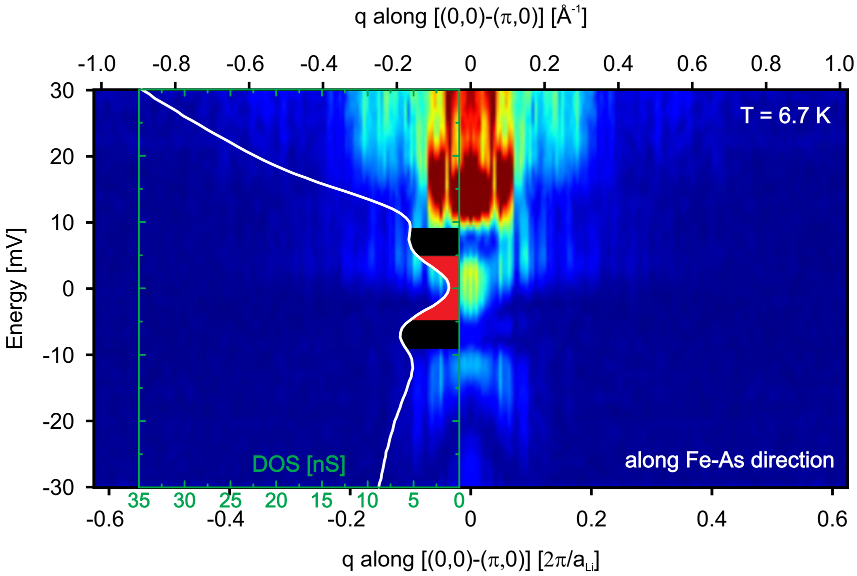

Figure 6.28.: The comparison of dispersion of the QPI signal at 6.7 K with the dI/dV spectra taken on bare surface. The vertical energy scales are the same for both cases. At the center of the plot, a strong intensity of $q \approx \pm 0.01$ Å^{-1} is indicated as the red area in the spectra while the black area on both sides is showing the absence of QPI intensity until ±9 mV. Above 9 mV at unoccupied side, the stronger QPI intensity is corresponding to the rich differential conductance.

along q direction is about $q \approx \pm 0.01$ Å^{-1}. And there is a strong depletion of QPI intensities between 5.5 mV and 9 mV (also -5.5 mV and -9 mV) in both polarities. All this features are already consistent with the mentioned QPI informations in Fig. 6.23.

Tracking of α_1 band

In order to further analysis, the line cuts of the 6.7 K spectroscopic map along Fe-Fe direction[16] are plotted in a waterfall representation in Fig. 6.29(a) where the energy dependent structure close to $q = 0$ can be noticed clearly with an enhancement of intensities at positive energies above 9 mV. A zoom-in of it between $\pm 0.105 \times 2\pi/\mathrm{a}_{Li}$ is shown in Fig. 6.29(b) which focuses the energy range between ±10 mV. The size of the enhanced particle-hole symmetric QPI intensity along q direction within the energy width of ±5.5 mV close to $q = 0$ are indicated by the two vertical lines in the plot. The pink lines are pointing the edge of the same QPI intensity along energy direction. The QPI signal at the Fermi level is marked by the red line. The blue lines are pointing to the edge of the depletion of QPI intensities which starts at 5.5 mV (-5.5 mV) until 9 mV (-9 mV) approximately. In the occupied side of Fig. 6.29(a), a dispersive QPI pattern has been found from -10 mV to -24.67 mV energy range at q close to zero. The energy and q values of this are extracted by Gaussian fit to the line cuts and plotted separately in Fig. 6.30(a). The details of the extracted data points from QPI line cuts are discussed in the appendix E. It is also compared with the intraband scattering to the

---

[16] The line cuts along Fe-As direction for 6.7 K map are shown in the appendix E.

measured α_1 band dispersion (see left column of Fig. 6.31) by ARPES [86] for $k_z = \pi/2$ along the $\Gamma - Z$ high symmetry direction[17]. The normal state $E(q)$ dispersion[18] (25 K) has also been tried to compare with tight binding fit [140] to the ARPES data with 10.5 mV spin-orbit coupling parameter[19]. It is shown in Fig. 6.30(b). It gives both a qualitative and a quantitative agreement with the intraband scattering within the α_1 band for $k_z = \pi/2$ along the $\Gamma - Z$ high symmetry direction[20].

Comparison with ARPES

The observed QPI features have been tried to compare with the experimental photoemission band structure. This is shown in Fig. 6.31. We use Eqn. 6.2

$$E = \pm\sqrt{\left(\frac{\hbar^2 k^2}{2m_e^*} - \mu\right)^2 + \Delta^2} \tag{6.2}$$

to fit qualitatively the ARPES bands [86] which were measured at 1 K (superconducting state) and 22 K (normal state), respectively (see the first column of Fig. 6.31). Using the plot, we compare the base temperature (superconducting) and 25 K (normal state) QPI data, which are shown in second and forth columns of Fig. 6.31, respectively. Similar plot is done in the third column at 17 K data in Fig. 6.31 to compare how the gap disappears close to T_c. By such fitting, it seems that the $\alpha_{1,2}$ band dispersions might be related to the observed features near the Fermi level for $q \approx 0$. More specifically, the inner enhanced QPI intensity might be related to the α_2 band. On the other hand, the larger superconducting gap like structure might be fitted with the α_1 band dispersion. The effective mass (m_e^*), the chemical potential (μ) and the superconducting energy gap (Δ) values related to the α_1 (α_2) band are $0.6256\times m_e$ ($3.0147\times m_e$), -3 meV (2 meV) and 8.18 meV (5.4 meV), respectively. However, such fitting does not provide a very good match between the QPI and ARPES data for the case of α_2 band dispersion. The enhanced QPI intensity in the positive energy does not look like a very distinct band like dispersion. Instead, it only seems a strong enhanced QPI intensity above 9 mV.

---

[17] We look at the normal state band dispersion (top of the band is at $\approx$-3 mV) for $k_z = \pi/2$ along the $\Gamma - Z$ high symmetry direction where the superconducting gap of 9 mV is introduced to the respective band (α_1) to get the dispersion relation in superconducting state using Eqn. 6.2.

[18] The line cuts in waterfall representation at 25 K is shown in Fig. E.33 in appendix E

[19] The 10.5 mV spin-orbit coupling parameter is used for the model calculation as it gives the very similar band structure with the photoemission data [87, 140].

[20] The QPI study by real space spectroscopic imaging technique in STM does not provide any k_z resolution. However, one might argue that QPI results are sensitive to the integrated k_z value between 0 to π. It implies that naively, average k_z value i.e. $k_z = \pi/2$ will dominate in QPI results. This is, in fact, supporting from our QPI results in case of both stoichiometric and off-stoichiometric LiFeAs.

Integrated QPI intensity

In this paragraph we will focus on the enhanced QPI intensities at positive energies. The observed very strong enhanced QPI intensities above 9 mV energy can be related to the enhancement of the derivative of the $\mathrm{d}I/\mathrm{d}V$ spectra at positive energies. It is mostly temperature independent as it can be seen in Fig. 6.27 and Fig. 6.26 for QPI and derivative of the bare surface spectra at various temperatures. The maximum of this strong signal between about 9 mV to 30 mV is difficult to predict from the QPI plot. Therefore, the integrated QPI intensity within ± 0.1 Å^{-1} is plotted in Fig. 6.32 for the energy range between ±30 mV. A peak around 16 mV at 6.7 K is observed which suppresses in normal state at 25 K. The difference in intensity between 6.7 K and 25 K, which is also shown in lower panel of Fig. 6.32, has a peak around 14 mV. The peak in the negative energy (-13.5 mV) has been observed in the same energy range, too. Apart from this, a peak at around 4 mV arises in the 6.7 K data which after subtracting the 25 K data, gives also a very pronounced peak at the same energy of 4 mV. Although the particle-hole symmetric QPI intensities within ± 5.5 mV energy seem from the $E(q)$ dispersion plot (see Fig. 6.28), an asymmetric integrated QPI intensity appears here which is due to a faint additional intensity contribution at 4 mV related to defect bound state. It is very likely to be related to the Fe-defect bound states reported in the same energy value [31] in defect study.

Temperature dependent QPI features

In Fig. 6.33, the $\mathrm{d}I/\mathrm{d}V$ spectra on the bare surface have been plotted together with the line cuts of the QPI dispersion plot along Fe-As directions at various temperatures within the $q = \pm 0.1$ $(2\pi/a_{Li})$ and the energy width of ±10 meV. This is the same feature which is shown in Fig. 6.28 and in the line profiles of the QPI intensities in Fig. 6.29(b). The red marked area indicates the width of the enhanced intensity at base temperature. The black areas in both polarities are indicating the absence of QPI intensity from the both edge of the red area before the appearance of QPI intensity above (below) the energy of 9 mV (-9 mV). Remarkably, we have found that the particle-hole symmetric enhanced QPI intensities gradually disappear with increasing temperature at superconducting T_c (18 K) of the material like a superconducting order parameter. At the same time, the larger energy edge of the depletion of the QPI intensities also reduces in energy direction similarly. The depletion of QPI intensities within 5.5 mV and 9 mV (-5.5 mV and -9 mV) remain unchanged with increasing temperature.

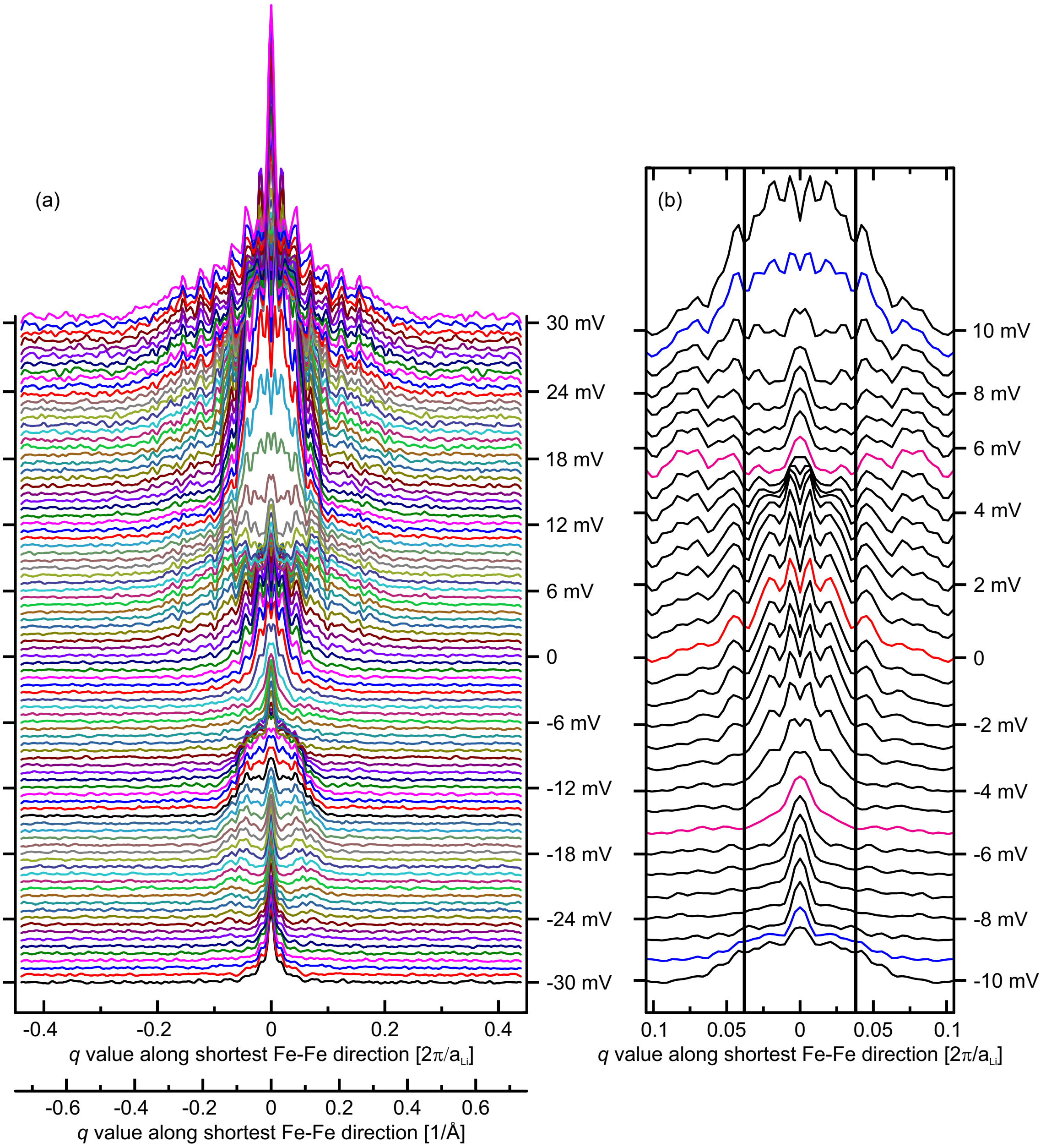

Figure 6.29.: (a) A waterfall representation of the line profiles of the line cut of the QPI signal along Fe-Fe direction at 6.7 K. The colors of the lines are randomly chosen to distinct them from one another. (b) The zoom-in of (a) between $\pm 0.105 \times (2\pi/a_{Li})$ in q direction and within the energy range of ±10 mV. The red line indicates the QPI intensity at the Fermi level. The width between pink lines are pointing to the energy extension of the enhanced QPI intensities which is ±5.5 mV. Its extension along q direction is indicated using the vertical black lines. The QPI intensity between the pink and the blue lines in both polarities is showing the reduction of QPI intensity between 5.5 mV and 9 mV (-5.5 mV and -9 mV) energies.

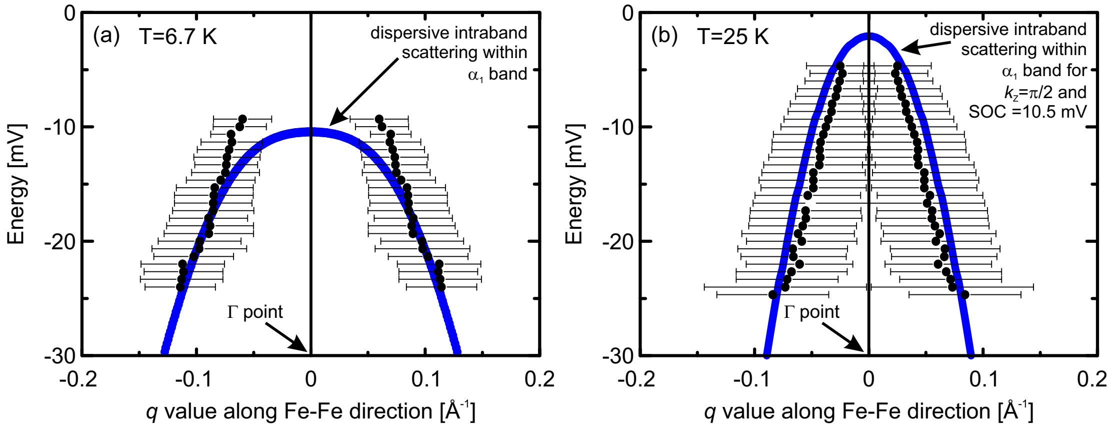

Figure 6.30.: (a) The extracted q values from Fig. 6.29(a) is plotted here at 6.7 K. This is compared with the used dispersion of α_1 band by fitting ARPES data in Ref. [11]. The data points from QPI line cuts are extracted using a Gaussian function fit[21]. The details of the fits are discussed in appendix E. (b) The 25 K data points are extracted from QPI study using similar Gaussian fit[22] to the QPI data. The tight binding model [140] for $k_z = \pi/2$ along the $\Gamma - Z$ high symmetry direction are well matching with such normal state QPI data for the α_1 band.

6.3.3. Discussion

We have successfully performed the temperature dependent QPI study on stoichiometric LiFeAs. We have observed very interesting QPI signals for q value very close to zero. The band dispersions in QPI signal close to the Γ-point ($q \approx 0$) have been tried to fit with the $\alpha_{1,2}$ dispersion from ARPES measurement [11]. In addition, we have found the temperature dependent superconducting gaps induced to the respective bands, suggesting that the $\alpha_{1,2}$ bands are relevant for superconductivity. However, no hint of the α_2 band dispersion is found in our QPI data. The used superconducting gap size in the α_1 band is around 9 mV (Δ) which helps to qualitatively fit the ARPES dispersion(see Fig. 6.31) and hence allows us to compare with QPI data for intraband scattering to the α_1 band for 6.7 K (see Fig. 6.30(a)). The significant QPI intensity surprisingly has not been found between 5.5 mV and 9 mV in both polarities. However, within ±5.5 mV, we do observe the particle-hole symmetric enhancement of QPI intensity, which with increasing temperature gradually disappears at 18 K (superconducting T_c). Such enhancement of the QPI intensity is very likely to be related to Andreev bound state [130] where the defect centers act as normal state while outside the defect, sample surface shows usual superconducting properties so that the superconducting-normal-superconducting states appear around defects on the sample surface. Such Andreev scattering related to the superconducting-normal-superconducting state in QPI study has been considered earlier to interpret the QPI results from HTSC [40]. According to such Andreev bound state for superconductor-metal-superconductor junction, a quasiparticle with a certain energy E when reaches from the normal state to one of the interface of superconducting-normal

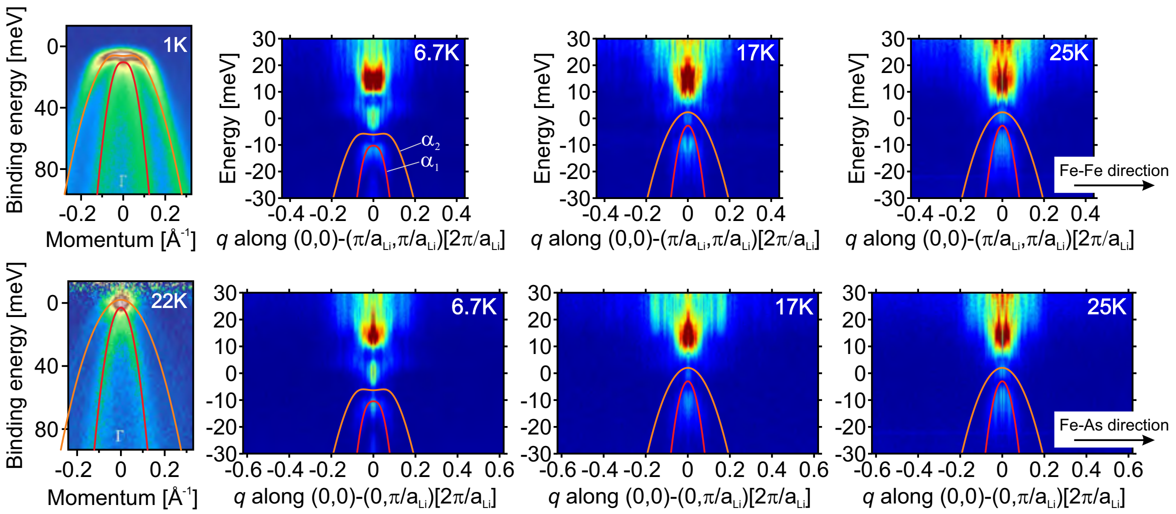

Figure 6.31.: The left column is the data at the Γ point from ARPES measurement from Ref. [86]. The red and orange colors are the fitted dispersion of the α_1 and α_2 bands. The right three columns are the QPI signals at 6.7 K (superconducting phase), 17 K (near the T_c) and 25 K (normal states) while upper and lower rows are the line cut along the Fe-Fe and Fe-As directions. The same parameters are used to fit the dispersion of α_1 and α_2 bands in QPI signal.

state, it creates an Copper pair in the superconducting part of the interface. Therefore, for elastic case to keep the energy and momentum conservation valid, the now quasiparticle will be created with opposite energy (-E) in normal state which will move towards opposite direction of the incident one[23]. The new quasiparticle then reaches to the other interface and similar situation happens there as well and it keeps continuing. Therefore, such multi-reflection processes within the superconducting energy gap (energy of the order of Copper pair) could lead to an enhancement of the DOS. Usually, such enhancement of zero bias intensity of the order of superconducting gap is experimentally observed. In our experimental QPI data, the real space modulation of this enhanced intensity signal is around 10 nm (inverse of 0.01 Å^{-1}) which is larger than the distance between defects. Therefore, such Andreev bound state could be explained in our QPI data in the following two ways. In first case, it might be due to the higher order scattering processes which are relevant because of high defect concentration. In fact, if the decay length of the first order scattering intensity is higher than the inter-defect distance, one would expect that such higher order scattering processes are important. In such case, those multiple scattering processes could interfere between themselves constructively as well as destructively and produce such pattern. Another possibility comes from the fact that the center of the defects on the surface could act as a source of normal state of the quasiparticle[24]. In this case, the Andreev bound state associated with our QPI data is very similar to the conventional Andreev bound state for superconductor-

---

[23] The new quasiparticle reflects back from the interface to the normal state with opposite energy and momentum with respect to the incident quasiparticle.

[24] We already know that superconductivity is strongly suppressed to the center of the dumbbell shaped Fe-defects. In fact, these defects have a major contribution to the QPI signal.

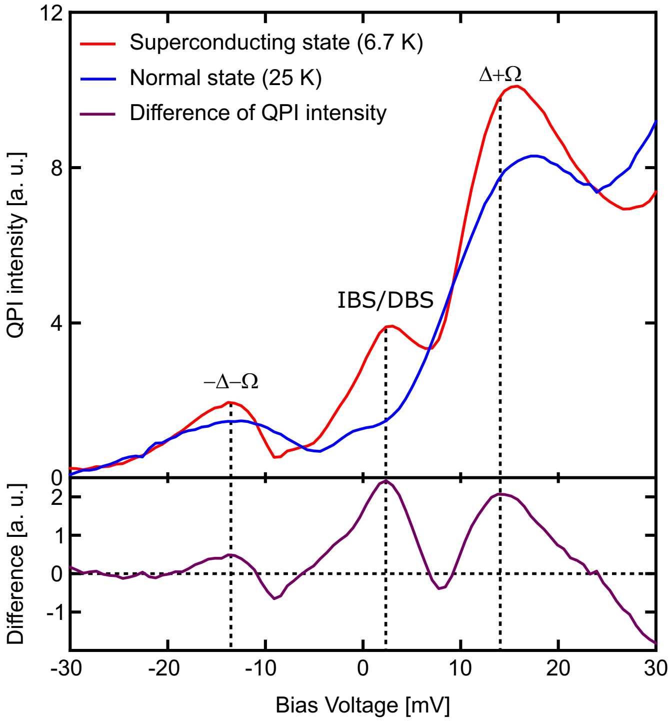

Figure 6.32.: The integrated QPI intensities over q values within $\pm 0.1\text{Å}^{-1}$ between ±30 mV energy range at superconducting state (6.7 K) and normal state (25 K). The lower panel shows their difference. The 4 mV impurity/defect bound state (IBS/DBS) are pointed by the vertical dashed line. The energy mode at ±14 mV is also observed and marked by vertical dashed lines at $-\Delta - \Omega$ and $\Delta + \Omega$.

metal-superconductor junction which is discussed above in this paragraph.

The enhanced QPI intensity at positive energy above 9 mV turns out as a very interesting feature related to superconductivity in stoichiometric LiFeAs due to the following reason. First of all, this is well consistent with the bared surface spectra where a rich integrated DOS appear at positive energies (see Fig. 6.28 and Fig. 6.25). The integrated QPI signal in Fig. 6.32 shows that a peak in the QPI intensity appears at 16 mV, which remains nearly unchanged with the increase of temperature until 25 K. The difference of those integrated QPI intensities at 6.7 K and 25 K are plotted in the lower panel of Fig. 6.32, where peaks are clearly noticed at the energy of ±14 mV. Peaks at very similar energies in the first derivative of $\mathrm{d}I/\mathrm{d}V$ in Fig. 6.26 for temperatures below 18 K have been observed. In the latter case, the peak is mostly pronounced at positive energy. In both cases, the intensity of this is reduced with rising temperature. This 14 mV feature therefore might be the signature of a mode which is directly connected to the superconductivity in stoichiometric LiFeAs. More experimental evidence will been done from the QPI study on off-stoichiometric LiFeAs, and will be discussed in the summary chapter, too (see chapter 7). Additionally, in the lower panel of Fig. 6.32, the defect bound state at 4 mV is observed which refers to the bound state associated with Fe-defects. This is comparable with the observed defect bound state with Fe-defects discussed in section 6.1.

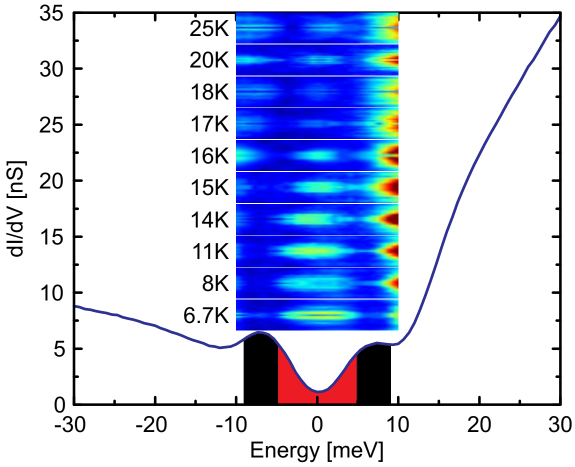

Figure 6.33.: The representative dI/dV spectra on bare surface at 6.7 K. Inset: The Zoom in of ±0. 1 Å^{-1} and ±10 mV for each temperature of the QPI dispersion indicates the strong enhanced particle-hole symmetric intensity within ±5.5 mV at 6.7 K which disappears above 18 K.

Furthermore, the edges of the rich QPI intensities can be fitted very well using the BCS mean field equation as a function of temperature (see Fig. 6.33). This also insists us to suggest that such enhanced QPI intensity is originating from an existing mode in stoichiometric LiFeAs which is coupled to the superconducting state. The edge of the enhanced QPI intensity within the gap (±5.5 mV) which is related to the Andreev bound state and hence is directly related to superconductivity. However, in our measurement, the focus of interest of the temperature dependent QPI study is near the Γ point. The interband scattering between the α bands and the γ band which is reported previously in literature [47, 48] and found also in the next section on off-stoichiometric LiFeAs, does not observe here.

6.4. Defects and electronic band structure study in off-stoichiometric LiFeAs

6.4.1. Sample characterization

It is well established that the stoichiometric LiFeAs already superconducts without doping, in stark contrast to other Fe-based superconductors where optimally doping is required. But due to the slight variation of the physical conditions during crystal growth, the off-stoichiometric LiFeAs single crystal of good quality is possible to grow. Real chemical composition is always hard to state from EDAX (Energy Dispersive Analysis of X-rays) measurement. Mostly, the composition of the light element like Li atom is always difficult to detect using such technique. Therefore, we have performed ^{75}As NQR spectroscopic study[25] at room temperature inside an Argon glove box on the same sample piece prior to mounting to the STM to check the sample quality. We have found NQR frequency of 21.589 MHz which is 50 KHz higher than that of the stoichiometric LiFeAs (see Fig. 6.34(a) and Fig. 6.9). This confirms that the sample has off-stoichiometric composition. According to the phase diagram of off-stoichiometric LiFeAs samples in Uwe Gräfe's thesis [141], the frequency shift of the NQR frequency towards high frequency in compare to the stoichiometric LiFeAs leads to Fe excess LiFeAs composition[26] and superconductivity becomes suppressed gradually with increasing of such electron doping. Even at higher electron doping, a ferromagnetic phase has been found. However, the bulk susceptibility data from the same batch of the our studied sample shows very broad superconducting transition which starts below 18 K (see Fig. 6.34(b)) unlike stoichiometric LiFeAs where a sharp superconducting transition below 18 K appears[27]. Such broad superconducting transition suggests that the bulk sample is not fully superconducting, and therefore it corroborates that such sample has off-stoichiometric composition. The asymmetric line shape and larger line width (FWHM) of NQR spectra than that of the stoichiometric composition which provide the electric field gradient of surrounding chemical environment of As positions, informs that the sample is chemically doped, too. The chemical composition[28] of a sample can be studied by counting the number of defects microscopically in STM measurement. We use STM/S results to get the composition of the sample which provides a direct connection to the local electronic properties as well as the stoichiometry of a place where the electronic information is recorded in our measurements.

---

[25] Similar ^{75}As NQR spectra were taken on stoichiometric LiFeAs to check sample quality which is shown in Fig. 6.9.

[26] As we go on in this chapter, we will find similar results of Fe access LiFeAs composition in this sample from our STM measurements.

[27] An example of sharp transition in stoichiometric LiFeAs below 18 K is shown by Morozov *et al.* [128].

[28] An exact percentage of the each element in the composition is difficult to state as an STM is blind to detect different elements. However, it is possible to state how much the studied sample is off from the stoichiometric one.

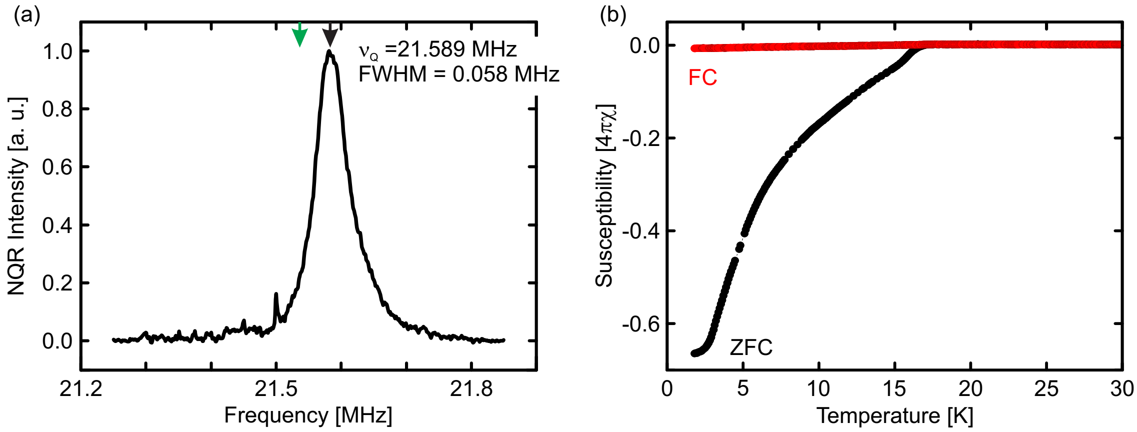

Figure 6.34.: (a) NQR data taken at ambient condition inside an Argon glove box on the very same sample which was used for STM measurements. The green arrow is pointing the NQR frequency (21.54 MHz) for stoichiometric LiFeAs. The NQR frequency and the line width of the signal (FWHM) are 21.589 MHz and 58 KHz, respectively. (b) Poor superconducting state is ensured by the susceptibility data, indicating that the sample is off-stoichiometric. See Ref. [142] for the origin of the data.

6.4.2. Topography

A representative topography in Fig. 6.35 over a freshly cleaved surface of off-stoichiometric LiFeAs single crystal appears atomically flat with the presence of different types of defects on the surface. The atomic corrugation of about 21,000 atoms on the surface indicates the Li lattice positions. The typical defects observed on such surfaces are the donut defect (see in chapter 6.3), missing Li atom and the bright dot defect which are quite different from the reported defects on stoichiometric LiFeAs [31, 32] which will be discussed later in this paragraph. All these three types of defects are statistically distributed over the surface with defect concentration of $1.1 \pm 0.1\%$, relatively higher than the stoichiometric LiFeAs [49, 112]. The underlying 2nd layer defects which have negligible influence on the electronic properties of the surface in comparison to 1st layer defects, are only visible at positive energies, similar to stoichiometric LiFeAs [31, 49]. We do not take those 2nd layer defects into account in case of analysis of defect concentration. Such high defect concentration affirms that the sample is far away from stoichiometric LiFeAs. According to the symmetry of the defects, the four fold symmetric donut defects are originated at As sites [31]. The atomic corrugation over those donut defect rules out its origin from Li position[29]. The bright dot defect which also has four fold symmetry, has lateral extension of 1 × 1 Li-Li lattice constant[30]. This is

---

[29] The cleaving most likely occurs between two adjacent Li layers due to weak van der Waals force.

[30] Here, the lattice constant refers to a_{Li} of 0.38 nm.

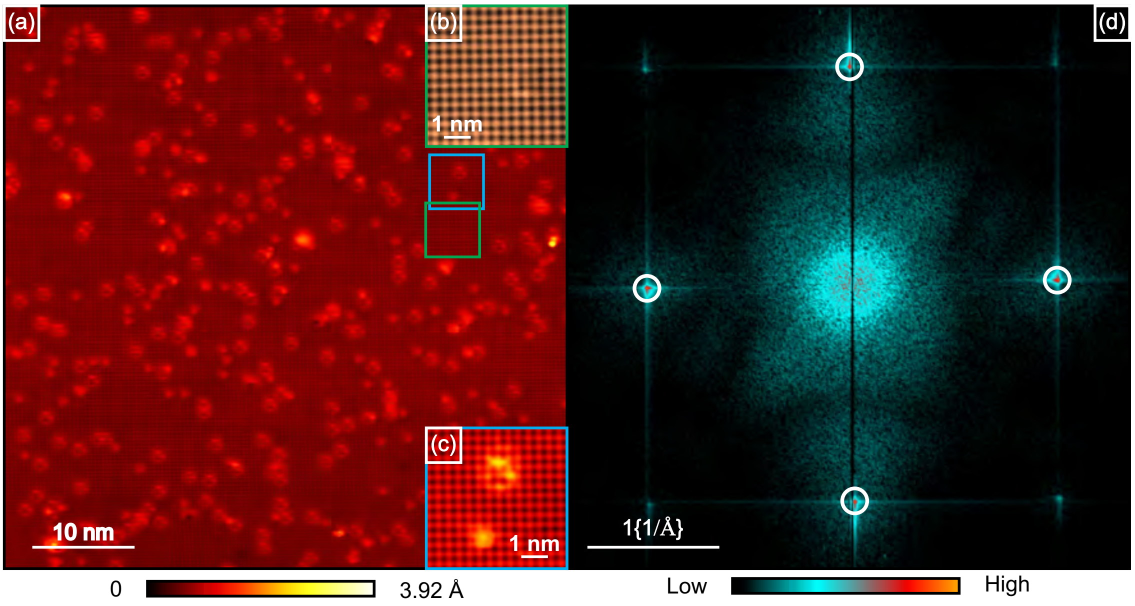

Figure 6.35.: (a) A representative high resolution (1024 × 1024 pixels^2) topography image of 55 nm × 55 nm area on off-stoichiometric LiFeAs single crystal taken at 5 K. Stabilization condition: $I_T = 1$ nA, V_{bias} = -50 mV. Inset: (b) Zoom-in of 5.3 nm × 5.3 nm area on bare surface (marked and shown also by green square in (a)). Inset: (c) Zoom-in of 5.3 nm × 5.3 nm area on donut and bright spot defects (marked and shown also by blue square in (a)). The donut defect looks asymmetric in shape. (d) The FFT of the topography where Bragg points related to Li lattice constant is marked by white circles.

probably due to extra Fe atom on the surface[31]. The concentration of donut like defects is roughly two times larger than that of bright dot defects (additional Fe atoms) in the studied sample. The bare surface spectrum (see Fig. 6.36(a)) at 7 K is comparable to the 16 K spectrum of stoichiometric LiFeAs. Such a reduction of superconducting T_c to 6.5 K[32] might be due to the appearance of around three times higher defect concentration than the stoichiometric LiFeAs. This apparently suppresses superconductivity. Here, the superconducting gap is found to be 9 mV (2Δ)[33]. Such a high superconducting gap size of 4.5 mV (Δ) and its low superconducting T_c of 6 K are very unusual phe-

---

[31] The extra atom on the surface has a lateral extension of four atomic distance (Li-Li lattice constant) over the surface. So, such extra atom cannot be originated from Li atom. Moreover, unlike additional or missing Li atom on the stoichiometric LiFeAs surface, they are also not movable during scanning by STM tip. The As atom does not consider to be its possible origin as the experimental band structure is observed very different in the QPI measurement later in this chapter. Such different electronic band structure is only possible if Fe-3d bands, which are mostly representing the band structure near the Fermi level in the compound, are influenced by such additional Fe atoms on the surface.

[32] The superconducting T_c is estimated from tunneling spectroscopic measurement. Indeed during the experiment, the Lakeshore temperature reader hanged. So below 6.6 K it always showed 6.6 K. But however in comparison to other measurement together with the spectroscopic gap structure one can estimate the superconducting T_c to be 6.5 K.

[33] We consider the coherence peak to peak value as 2Δ.

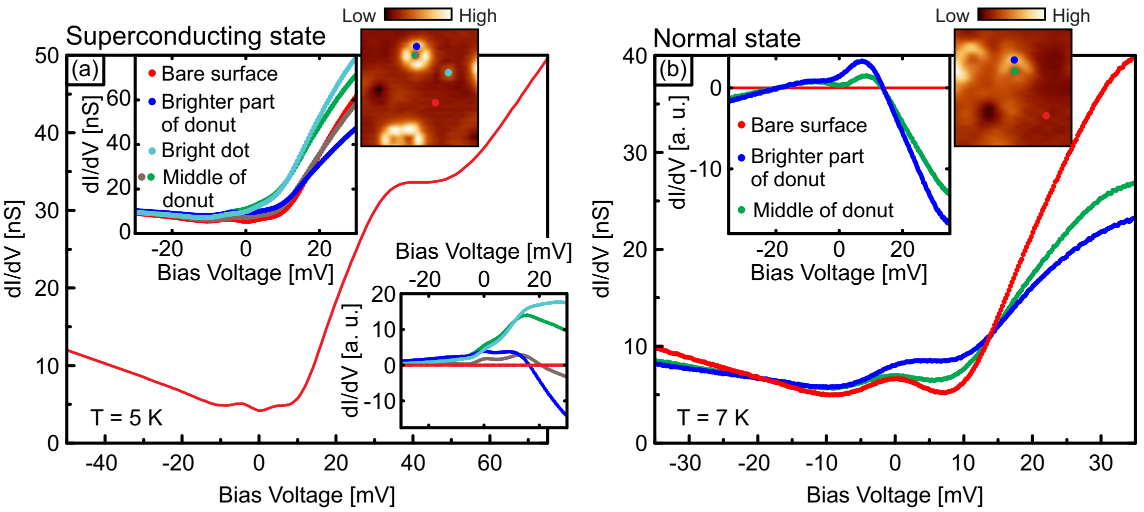

Figure 6.36.: (a) The dI/dV spectra on bare surface at 5 K between -50 mV and +75 mV. Stabilization condition: I_T = 0.6 nA, V_{bias} = -50 mV. Superconducting gap of 4.5 mV and a hump at 42 mV are distinctly visible. Upper inset: Point spectra on bare surface, brighter part of donut, bright dot defects and at the center of donut defects are shown. Lower inset: The bare surface spectra have subtracted from defects spectra. (b) The spectra at normal state (7 K) on bare surface, brighter part of the donut and at the center of the donut are shown. The bare surface spectra is comparable to the normal state spectra (20 K) on stoichiometric LiFeAs (see 6.16). Inset: The bare surface spectra have been subtracted from defects spectra to find the additional contribution of defect on differential conductance.

nomenon. This can be naively understood as the reason of excess Fe atoms found over the surface which probably acts against the formation of Cooper pairs strongly. Earlier, similar kind of surface has been reported in Danny Baumann's thesis [125] where the same qualitative gap structure at both 6 K and 0.3 K has been mentioned. The latter gap became relatively sharper but never went to zero dI/dV value within the gap even at ultra-low temperature (0.3 K). The amount of defect concentration in his study was roughly 5-6 times higher than here. But, those spectra seem very similar to our spectra. However, in the following, we perform defect study on the frequently observed defects on such surface, and QPI study to probe as well as visualize the electronic band structure in comparison to the superconducting stoichiometric LiFeAs.

6.4.3. Defect Study

A set of representative spectrum at base temperature of 5 K in superconducting state is shown in Fig. 6.36(a). Such a spectrum, which is recorded between -50 mV and +75 mV (see Fig. 6.36(a)), overall shows a very similar structure like stoichiometric LiFeAs except of the superconducting gap value (4.5 mV) and the superconducting T_c (6.5 K). The particle-hole asymmetric structure outside the gap with the presence of a hump at 42 mV, similar to stoichiometric LiFeAs, is readily visible here. In the upper inset of

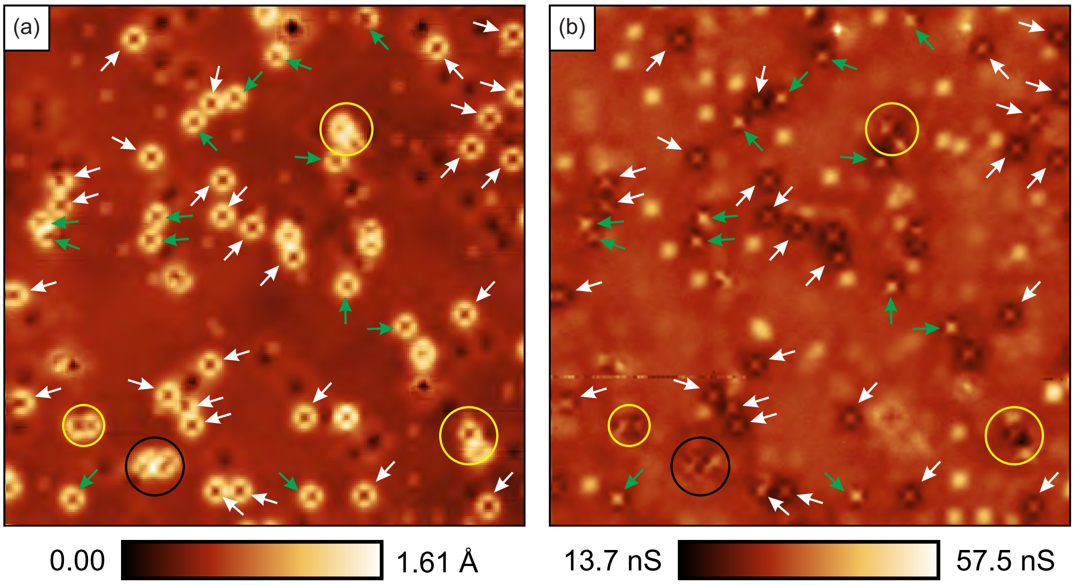

Figure 6.37.: (a) A topography image of 32.5 nm × 32.5 nm area where a full spectroscopic map is recorded. The donut and bright spot defects are mostly visible over the surface. A dI/dV energy slices at 18.5 mV is shown in (b). The centers of the donut defects have two types of electronic properties which are shown in Fig. 6.36. Such two electronically different types of the center of donut defects are pointed by green and white arrows. The donut centers which are marked by green arrows, have the spectroscopic properties shown by green color spectrum in Fig. 6.36(a). The electronic properties of the donut centers pointed by white arrows are shown by grey color spectrum in Fig. 6.36(a). The defects indicated by yellow circles have similar electronic properties. The black circle defects have different electronic properties in comparison to all the other donut defects. The properties of these both defects (yellow and black circles defects) are strongly influenced by the nearby defects and therefore its difficult to disentangle such defect's properties.

Fig. 6.36(a), the spectra that were taken on bare surface, brighter[34] part of the donut defect, bright spot defect and two different types of center of donut defects, are plotted. The superconducting gap is visible close to the Fermi level at bare surface spectra. The spectra have hardly changed for all cases at negative energies. Superconductivity is slightly influenced at the brighter part of the donut defect while it has been strongly suppressed at the bright spot defect. A slight enhancement of dI/dV value from -35 mV to 17 mV has been noticed at the brighter part of the donut while it becomes suppressed above 17 mV. The strong enhancement of dI/dV value only happens at the center of the donut defect at the unoccupied side. We have also observed two different kinds of center of donut defects depending on their electronic properties. Although the center of all the donut defects looks similar in topography image shown in Fig. 6.37(a), the selected energy slice at 18.5 mV in Fig. 6.37(b) provides a clear proof of two different types of the center of donut defects which are marked by green and white arrows. To

---

[34] The donut defect looks mostly symmetric. But sometimes, it appears little asymmetric as shown in Fig. 6.35.

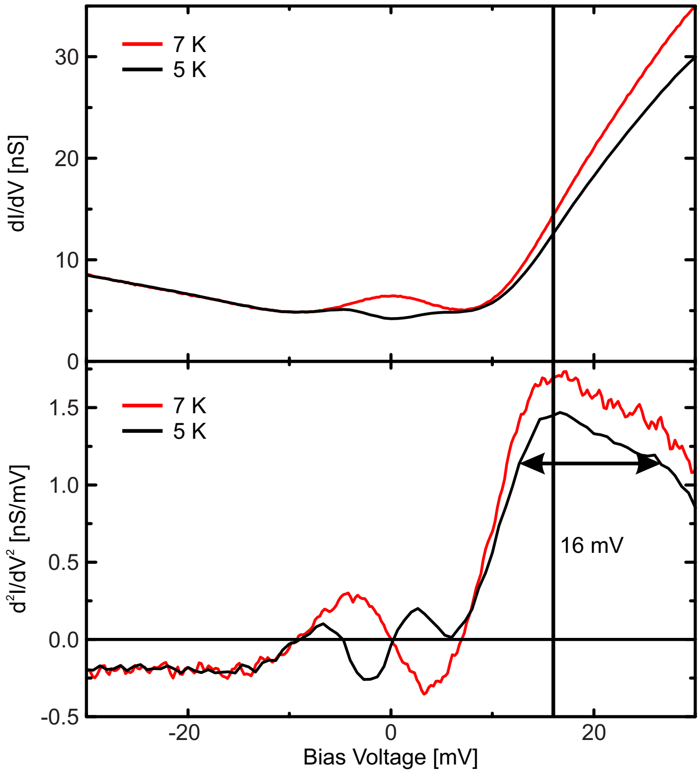

Figure 6.38.: The bare surface spectra at superconducting state (5 K) and at normal state (7 K) are shown in the upper panel while the lower panel describes the 1st derivatives of those spectra. A peak like feature at 16 mV is observed in both states. However, it is not a sharp resonance as indicated by the vertical black arrow in comparison to stoichiometric LiFeAs spectra at 6.7 K(see Fig.6.26).

get better insight about the additional effect on the dI/dV signal due to these defects, the bare surface spectra have been subtracted from spectra which are taken on defects. These are plotted in lower inset of Fig. 6.36(a). Suppression and strong enhancement in unoccupied side are easily distinct in case of the brighter part of donut and the bright spot defects, respectively. The center of the donut defects marked by green arrows has a relatively strong enhancement of dI/dV value at positive energies while the other type of center of donut defects, pointed by white arrows, is very weakly influenced.

We have also studied the normal state dI/dV on those defects. In Fig. 6.36(b), the spectra on bare surface, brighter part and center of the donut defect are shown within the energy range of ±35 mV. The normal state dI/dV spectra (7 K) on this off-stoichiometric LiFeAs are comparable to that of the stoichiometric LiFeAs spectra at 20 K (normal state). The dI/dV spectra have hardly changed in the occupied side, remaining similar to its superconducting state. The spectra on the brighter part of the donut at the unoccupied side have relatively stronger enhancement and suppression before and after 15 mV, respectively, in comparison to its value at the center of the donut.

The bare surface dI/dV spectra have been subtracted from defect spectra similar to the previous case, to find additional contribution to the dI/dV value by those defects which are plotted at the inset of Fig. 6.36(b). There is a peak at the brighter part of the donut at the unoccupied side with relatively larger dI/dV value at 7 mV while a peak position at the center of the donut is found at 9 mV. A little hump appears in both cases at the occupied side at -9 mV and -6 mV, respectively. The strong enhancement and suppression of spectra are distinct from both raw as well as subtracted spectra even at normal state. The bright spot defects show similar behaviour both in superconducting and normal state. Therefore, it is not shown here.

The representative spectra at superconducting state (5 K) and normal state (7 K) are shown in Fig. 6.38 together with their derivatives in its lower panel to compare them. In previous chapter, the similar spectra and their 1st derivatives are shown in Fig. 6.25 and in Fig. 6.26 where a peak like feature at 16 mV appears at well below superconducting T_c (in this case 6.7 K) that vanishes at normal state(25 K). Here, we have found similar 16 mV feature but it is relatively broad in shape (marked by horizontal black arrow). The measurement was performed at 5 K, close to the superconducting transition temperature which probably is the reason for not observing any sharp peak here. Except of this, the overall structure of the spectra are very similar to stoichiometric LiFeAs close to the superconducting T_c and at the normal state.

6.4.4. Quasiparticle interference

One example from several studied QPI maps at a temperature of 5 K is shown in Fig. 6.39(a)-(t) where a few selected energy slices between -30 mV and 30 mV are shown[35]. Similar like in section 6.3, it is shown in Fig. 6.41 that the energy dependent Friedel oscillations around the defects relate to the energy dependent QPI signals. In the FFT images in Fig. 6.40, a strong intensity is found near the Γ-point ($q \approx 0$) at every energy slice. A square like relatively less strong but still more than the back ground intensity with q=0.46×$2\pi/a_{Li}$ is visible at 30 mV (see Fig. 6.40(t)). The real space extension of this feature at the 30 mV energy slice is about 0.9 nm which is equivalent to the lateral extension of the defects. This remains constant until 12 mV, and below 12 mV, this feature appears as round in shape and becomes circular at the Fermi level with q=0.43×$2\pi/a_{Li}$. The white square, arc and circle are pointing those structures at 30 mV, 10 mV and the Fermi level, respectively. The intraband scattering due to the γ hole-like pocket at the Γ point is probably the origin of this feature as the q value is very similar to the reported data from ARPES [11]. Its relatively lower intensity might be due to mainly d_{xy} orbital character of the γ hole-like pocket. But in our QPI signal we do observe a square area instead of ring due to unknown reason. More interestingly at the negative energy, a ring like pattern has been noticed which is marked by pink arc at -18 mV. This pattern shows a kind of dispersive behavior which is plotted in

---

[35] The full data set is shown in appendix F.

red dots[36] and fitted well using parabolic dispersion in Fig. 6.42(a) (black curve). The tight binding fit of the ARPES data for stoichiometric LiFeAs shown in Fig. 6.42(b) for $k_z = \pi/2$ along the $\Gamma - Z$ high symmetry direction is used to compare with QPI data[37] to find the related scattering vectors [140]. The used spin-orbit coupling parameter was 10.5 mV which describes well the ARPES band structures mentioned in Ref. [87]. The interband scattering between the γ and the α_2 hole-like pockets which is pointing by the horizontal green arrows in Fig. 6.42(b) are also plotted in Fig. 6.42(a) as dashed green lines. Such scattering is shifted 10 mV down which is shown by solid green line in Fig. 6.42(a) to compare with the experimental data. The experimental QPI data and such scattering vectors have a good qualitative agreement in Fig. 6.42(a) along Fe-As direction. The similar analysis is done for the Fe-Fe high symmetry direction where our QPI data and similar interband scattering matches very well qualitatively as well as quantitatively.

However, the QPI structure is quite complex and very different in comparison to stoichiometric LiFeAs. In Fig. 6.44, the line cut along Fe-Fe and Fe-As directions in this off-stoichiometric compound (3rd column) together with the superconducting (1st column) and the normal state (2nd column) of a stoichiometric LiFeAs are compared. The off-stoichiometric LiFeAs shows a very faint particle-hole symmetric enhancement of intensity within ±1.5 mV energy near the Fermi level, very similar to the stoichiometric LiFeAs below superconducting T_c. But, it is hard to state whether it disappears above superconducting T_c as it is already subtle effect at base temperature of 5 K. The α_1 band like dispersion is not visible here. Strikingly, the strong enhancement of QPI intensity between +9 mV and +17 mV is absent here in stark contrast to stoichiometric LiFeAs where this feature exists both at the superconducting as well as the normal state. However, the rich QPI intensity is observed above +17 mV which was also seen on stoichiometric LiFeAs.

---

[36] The value of the red points are measured from each QPI energy slice manually as the line profile does not give a very strong signal (see one example in Fig. F.28). The error bar is the maximum intensity width of the ring among all the energy slices. The shown red dots are extracted from the zoom-in QPI measurement (110 nm × 110 nm) which is shown in appendix F. All the data of small area (32.5 nm × 32.5 nm) and large area (110 nm × 110 nm) maps are shown in appendix F. Such extracted data are consistent in both of these different size maps.

[37] The QPI study by real space spectroscopic imaging technique in STM does not provide any k_z resolution. However, one might argue that QPI results are sensitive to the integrated k_z value between 0 to π. It implies that naively, average k_z value i.e. $k_z = \pi/2$ will dominate in QPI results. This is, in fact, supporting from our QPI results in case of both stoichiometric and off-stoichiometric LiFeAs.

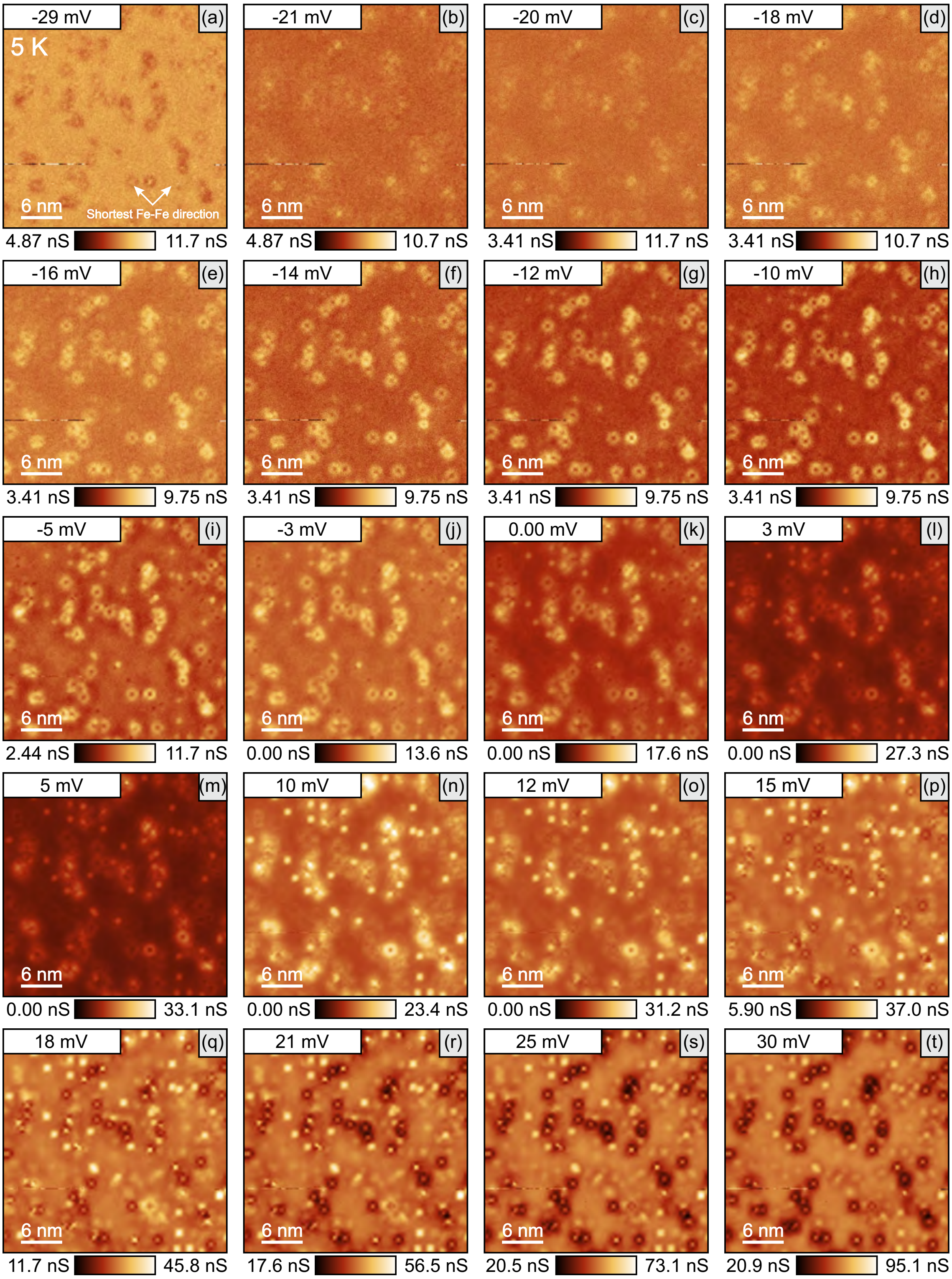

Figure 6.39.: A few selected energy slices from one spectroscopic map at 5 K are shown here. The corresponding energy of each slice is mentioned at upper left part of every image. Energy dependent Friedel oscillation can be identified distinctly in every image around defect locations. Stabilization condition: $I_T = 0.6$ nA, $V_{bias} =$ -50 mV. Size: 32.5 × 32.5 nm^2.

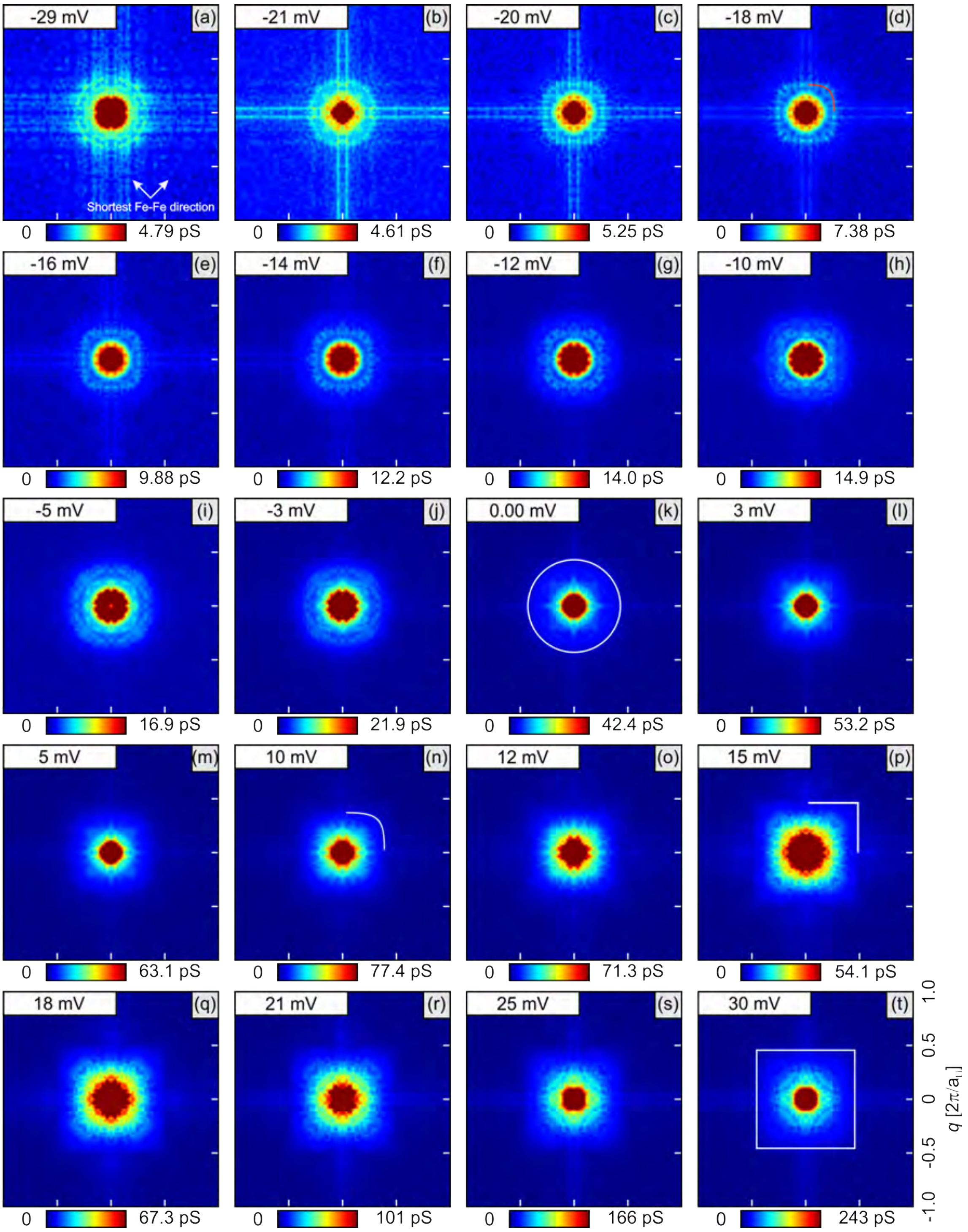

Figure 6.40.: The corresponding QPI pattern of Fig. 6.39 has shown within the first Brillouin zone. The strong QPI intensity is observed close to the Γ point. The overall structure is quite different in comparison to stoichiometric LiFeAs.

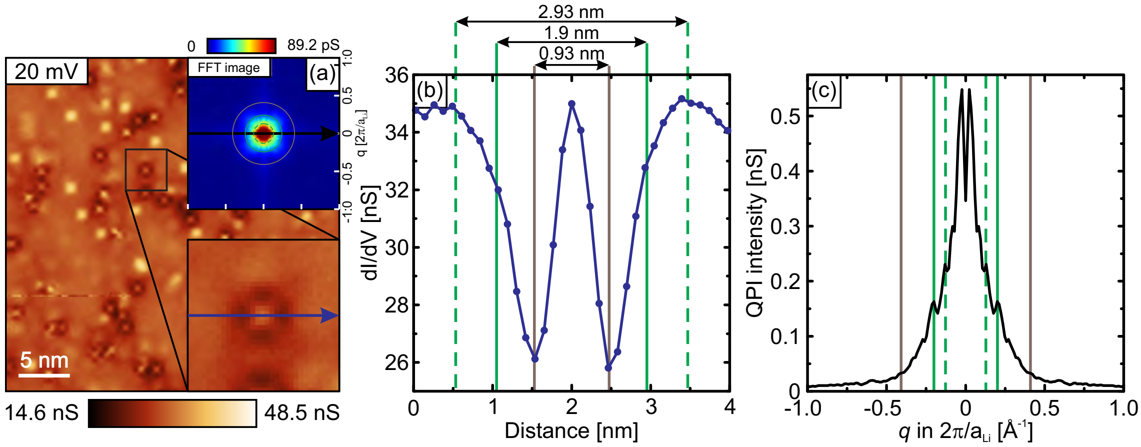

Figure 6.41.: (a) The 20 mV dI/dV energy slice from the same spectroscopic map shown in Fig. 6.39(The real space and QPI data are shown in appendix F for all energies). Oscillations around one donut (As-defect) defect with an area of 4 nm × 4 nm marked by the black square is zoomed in and shown in the lower inset of the image. The QPI intensity corresponding to the 20 mV energy slice is shown in the upper inset. The dark brown and green arrows in the QPI image are indicating dominating QPI intensities. (b) The line profile along the blue arrow on the zoomed image in (a) is plotted, whereas the line profile over the QPI intensity along black line is shown in (c). The oscillations around the zoomed in image in (a) are compared to the corresponding dominant QPI scattering which are shown using dark brown, green solid lines and green dashed line. They are also pointed by dark brown and green rings in FFT image. The real space structures of 0.92 nm, 1.9 nm and 2.93 nm corresponds to the distance of 0.41, 0.2, and 0.13 $\times 2\pi/\mathrm{a}_{Li}$, respectively in FFT image.

The 42 mV hump is a common and prominent feature in both stoichiometric and off-stoichiometric LiFeAs (see Fig. 6.36(a) and Fig. 6.6). It will therefore be worthwhile to investigate such 42 mV hump. To search for its origin, we have measured spectroscopic map between -30 mV and +75 mV. The line cut along Fe-As and Fe-Fe directions of the QPI intensity is shown in Fig. 6.45. We have found the continuation of enhanced intensity near the Γ point from +17 mV up to +75 mV. Again, the enhanced intensity between +9 mV and +17 mV is missing in the data. We did not observe any additional distinct features in QPI intensity at +42 mV.

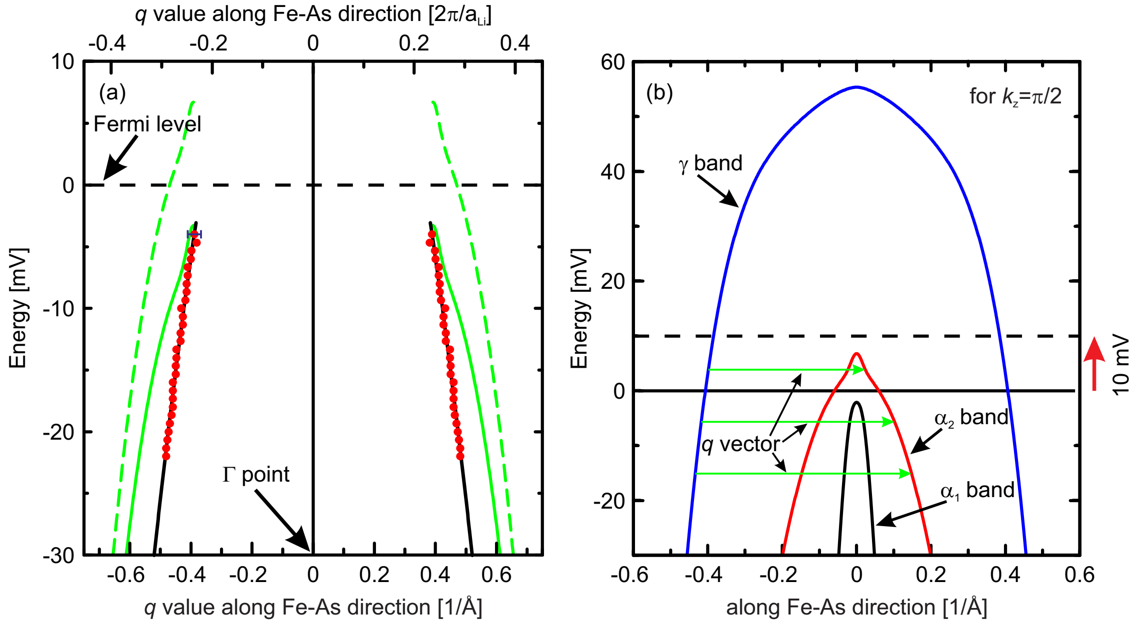

Figure 6.42.: (a) The extracted data points of ring like structure at negative energies (one of which is marked by red arc in -18 mV energy slice QPI data in Fig. 6.40(c)) shown in red dots along Fe-As high symmetry direction. The black line is the parabolic fit to the red data points which shows clear hole-like dispersive behavior. (b) The blue, red and black curves represent the γ, α_2, α_1- bands, respectively obtained by tight binding fit [140] to the ARPES data in stoichiometric LiFeAs for k_z=$\pi/2$. The top of the γ band is at 55.25 mV. The spin-orbit coupling of 10.5 mV is used for such tight binding model as it describes the ARPES data well [87]. The shown scattering vectors for interband scattering between the γ and the α_2 hole-like dispersions provide a good comparable behavior to the shown QPI scattering vectors. Such energy dependent scattering for stoichiometric LiFeAs is shown as dashed green lines in (a). To compare it with the QPI data of off-stoichiometric LiFeAs, the Fermi level of stoichiometric LiFeAs (black horizontal line in (b)) is required to shift around 10 mV towards unoccupied side (also pointing by vertical red arrow in (b)) which is shown as dashed horizontal black curve in (b). In (a), the dashed green curve is shifted 10 mV towards occupied side to compare with the QPI data which is shown as solid green curve. Such scattering matches better until -8 mV to the experimentally found dominant QPI scattering vectors while it deviates more beyond -8 mV significantly but still qualitatively matches well. The band structure calculation is taken from Ref. [140].

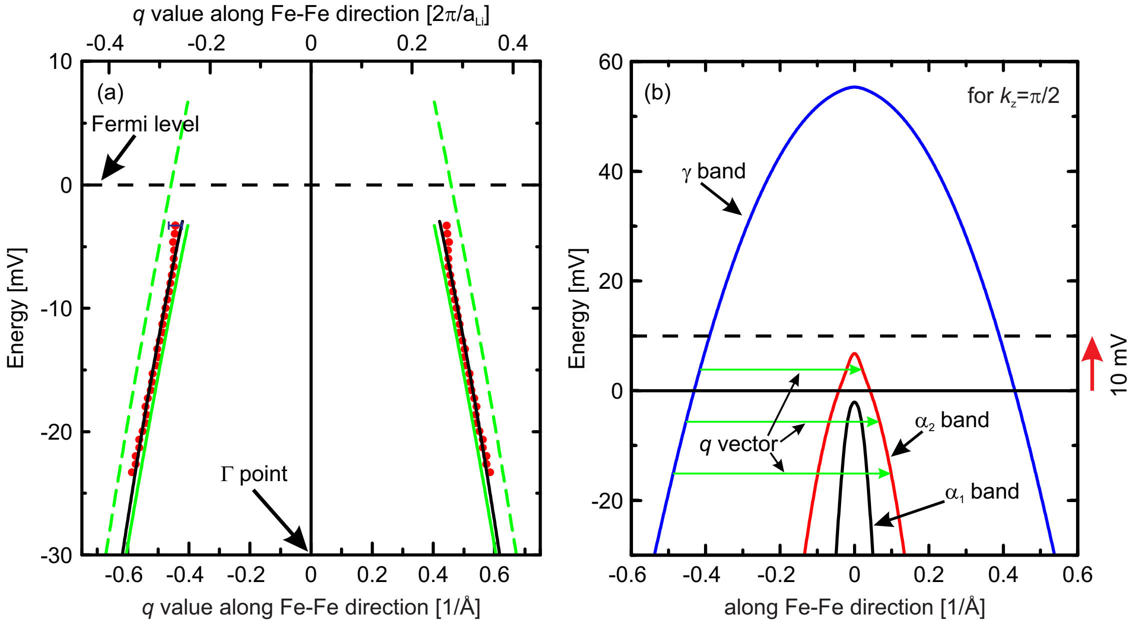

Figure 6.43.: (a) The extracted data points of the ring like structure at negative energies (one of which is marked by red arc in -18 mV energy slice QPI data in Fig. 6.40(c)) shown in red dots along Fe-Fe high symmetry direction. The black line is the parabolic fit to the red data points which shows clear hole-like dispersive behavior. (b) The blue, red and black curves represent the γ, α_2, α_1- bands, respectively obtained by tight binding fit [140] to the ARPES data in stoichiometric LiFeAs for $k_z = \pi/2$. The top of the γ band is at 55.25 mV. The spin-orbit coupling of 10.5 mV is used for such tight binding model as it describes the ARPES data well [87]. The shown scattering vectors for interband scattering between the γ and the α_2 hole-like dispersions provide the best matching to the shown QPI scattering vectors. Such energy dependent scattering for stoichiometric LiFeAs is shown as dashed green lines in (a). To compare it with the QPI data of off-stoichiometric LiFeAs, the Fermi level of stoichiometric LiFeAs (black horizontal line in (b)) is required to shift around 10 mV towards unoccupied side (also pointing by vertical red arrow in (b)) which is shown as dashed horizontal black curve in (b). In (a), the dashed green curve is shifted 10 mV towards occupied side to compare with the QPI data which is shown as solid green curve. Such scattering matches very closely to the experimentally found dominant QPI scattering vectors both qualitatively and quantitatively. The band structure calculation is taken from Ref. [140].

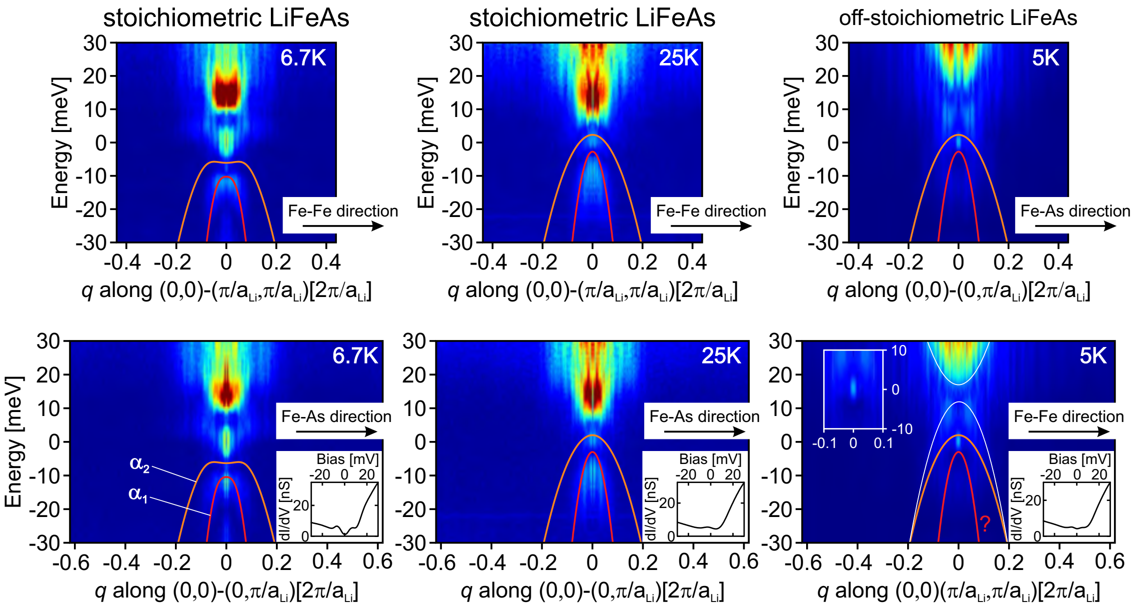

Figure 6.44.: Comparison of the band structure of off-stoichiometric LiFeAs with superconducting state as well as normal state of stoichiometric LiFeAs. The first two columns are the line cuts (Fe-Fe and Fe-As directions from up to down accordingly) at temperatures of 6.7 K and 25 K on stoichiometric LiFeAs. The last column is the line cut (Fe-As and Fe-Fe directions from up to down accordingly) on off-stoichiometric LiFeAs at 6.7 K in superconducting state. The red and orange curves are the plots of α_1 and α_2 dispersion from photoemission measurements [11]. In stoichiometric LiFeAs, the strong intensity at the Γ point near the Fermi level which basically follows an order parameter like behavior as a function of temperature (see Fig. 6.33), appears also on the off-stoichiometric LiFeAs. The inset of each lower image corresponds to the bare surface spectra to the respective surface. The size of the enhanced QPI intensity near the Fermi level for the off-stoichiometric LiFeAs sample (see the inset of lower panel) is around ±1.5 mV[38]. The hole-like white band plotted in off-stoichiometric LiFeAs indicates the probable shift of the orange band with respect to the Fermi level. The electron-like white band is pointing the structure of the enhanced intensity at positive energy. The red color band dispersion which follows α_1 band dispersion is not present in off-stoichiometric LiFeAs sample. Most importantly, the rich QPI intensity between 9 mV and 17 mV is completely absent in off-stoichiometric LiFeAs which is distinctly present in stoichiometric LiFeAs.

6.4.5. Discussion

The defect concentration in this off-stoichiometric LiFeAs is found relatively higher than the stoichiometric LiFeAs. So, the system is undoubtedly chemically doped. This may lead to the reduction of superconducting T_c to 6.5 K. The frequently observed two fold symmetric Fe-defects on stoichiometric LiFeAs surface are completely absent here, in-

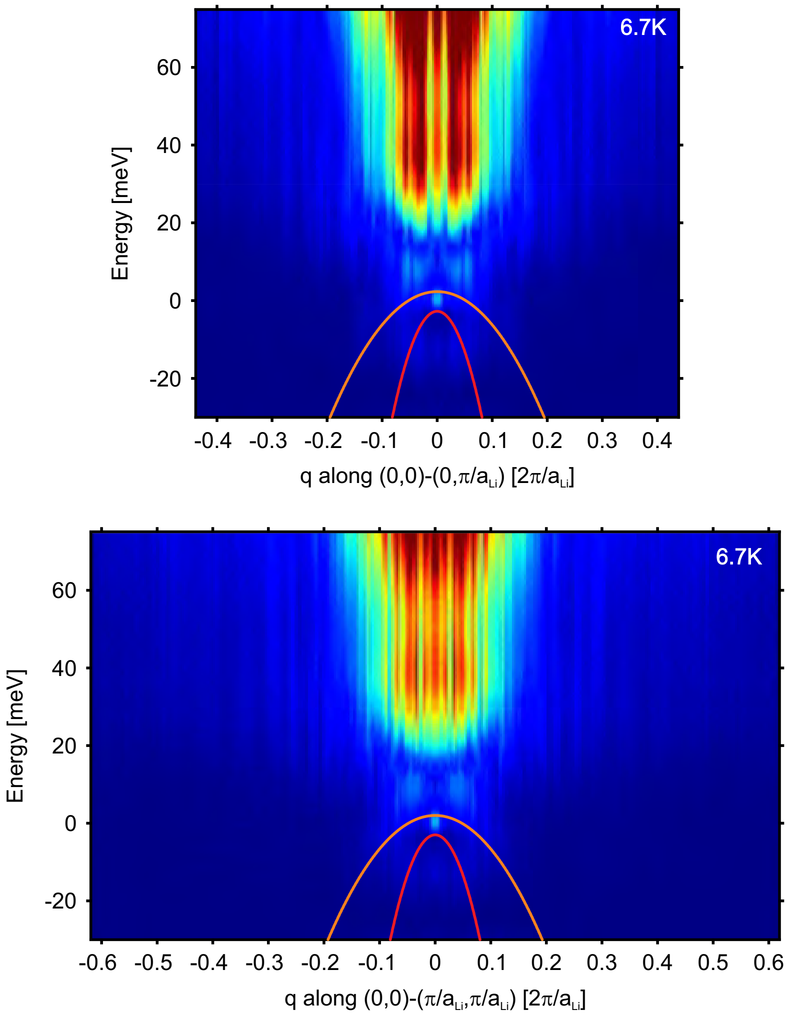

Figure 6.45.: The plot of line cuts of QPI signal along Fe-As (upper panel) and Fe-Fe (lower panel) between -30 mV to +75 mV from a spectroscopic map measurement on off-stoichiometric LiFeAs at a temperature of 6.7 K. Again the red and orange curves are the plots of α_1 and α_2 dispersion from photoemission measurements [11]. Here, the rich QPI intensity between +9 mV and +17 mV on the unoccupied side is also not present, consistent with other QPI measurements in this sample.

dicating that the Fe layers are undisturbed. But, we found the As sites to be strongly affected due to the appearance of donut like defects. Access Fe atoms on the surface are also visible as bright spot defects. All the frequently observed defects are significantly affected the dI/dV spectra at unoccupied side (positive energies) while the occupied side remains mostly unaffected. We have found two different centers of donut defects. One of which is strongly affecting the dI/dV spectra whereas the other does not change the spectral feature significantly in comparison to the bare surface spectrum. One origin of the strongly affected donut center might be due to the additional Fe-atoms sitting on the As positions but strong conclusion is difficult from our study as we are not sensitive to individual elements. On the other hand, a good theoretical model is required to compare with our experimental data and hence make a strong statement towards this direction.

Apart from the defect study, the QPI measurement on this sample provides us with very comprehensive results compared to stoichiometric LiFeAs sample. The particle-hole symmetric enhancement of QPI intensity within ±1.5 mV can be explained on the ground of Andreev scattering processes similar to stoichiometric LiFeAs. Unfortunately, our base temperature was very close to T_c. Thus, the energy extension cannot be tracked as a function of temperature. The most crucial observation is the absence of strongly enhanced QPI intensity between 9 mV and 17 mV in the unoccupied side. Such an absence of QPI intensity and the reduction of superconducting T_c to 6.5 K in comparison to stoichiometric LiFeAs where a mode around 14 mV was found both in integrated QPI intensity and in the first derivative of $\mathrm{d}I/\mathrm{d}V$ spectra in superconducting state directly support that, the 14 mV mode is relevant for superconductivity in LiFeAs. We do not observe α_1 band dispersion like stoichiometric LiFeAs. But, we have observed interband scattering between the γ and the α_2 hole-like bands centered at the Γ high symmetry point. The QPI data for the interband scattering along Fe-Fe direction matches very well with the tight binding model for $k_z = \pi/2$ along the $\Gamma - Z$ high symmetry direction where only qualitative match is found along Fe-As direction. This probably reflects that the band anisotropy [12, 86, 96] might be relatively less in this off-stoichiometric compound relative to stoichiometric LiFeAs. But the spin-orbit coupling[39] is still very similar to the stoichiometric LiFeAs as, until -8 mV, the QPI data and the interband scattering between the γ and the α_2 bands from tight binding model give a very good qualitative and quantitative agreement even along Fe-As direction. Such interband scattering has also been seen on stoichiometric LiFeAs previously in Ref. [47, 48, 96]. Their marked q_1 or h$_2$ scattering vector is comparable to our observed interband scattering. Such 10 mV shift of the Fermi level can be directly related to its three times higher defects concentration than the stoichiometric LiFeAs with additional Fe-atoms and As-defects appeared on the surface. We have also noticed that the Fermi level is shifted towards unoccupied side around 10 mV. This implies that the electron doping leads the small α bands far from the Fermi level and the reduction of the T_c also occurs at the same time. This suggests that the α bands are crucial for superconductivity in LiFeAs superconductor.

---

[39] The spin-orbit coupling affects the top of the γ and the $\alpha_{1,2}$ band mostly as a function of k_z.

7. Summary and outlook

The topic of this thesis is to investigate the electronic properties in iron-based superconductors (IBS). In this regard, the thesis is mainly focused on experimental investigation of one of the mostly debated material LiFeAs which belongs to 111 sub-class in IBS. The material LiFeAs is one of the few superconductors from IBS which superconducts without doping or external pressure with relatively high T_c of 18 K. The experimentally measured Fermi surface from ARPES yields poor nesting between the hole-like Fermi surface (γ-pocket) pocket around the Γ point and the electron-like Fermi surface pockets around M-point. While in stark contrast to this, the generic phase diagram in IBS has a Fermi-surface nested AFM ground state in the parent compounds and with doping, superconductivity emerges in the proximity of such magnetically ordered ground states. In LiFeAs, another two small hole pockets ($\alpha_{1,2}$) appear to the Fermi surface at the Γ point for $k_z = \pi$. Such small hole pockets are found to be strongly k_z-dependent and is possibly responsible to lead the system far from AFM instabilities. In fact, every try to establish canonical AFM spin-fluctuations appears to fail in this compound. The experimental INS data supports incommensurate magnetic ordering near (π,π) point instead of sharp (π,π) resonance mode. In this thesis, the low temperature scanning tunneling microscopy and spectroscopy have been used to thoroughly investigate the following electronic properties of stoichiometric and off-stoichiometric LiFeAs to understand the underlying superconducting mechanism in this compound.

The first part of the thesis concerns about a thorough surface description with two types of representative topography surfaces and a local spectroscopy of the superconducting properties. After cleaving the sample at cryogenic vacuum, we have observed mainly two different varieties of topography data where the atomic corrugation over the surface has different shape with the appearance of different types of defects. Such different topography data yield to the different matrix element effect but the spectroscopic features reveal to very similar in both cases. Of course, one cannot exclude that a minor doping during crystal growth might create such different topography data. However, the spectroscopy information remains very similar which reflects that such minor doping does not play a significant role in the electronic properties of the material. The spectroscopic features outside the superconducting gap yields a very rich spectroscopic structure at unoccupied side where a hump at 42 mV is observed very peculiarly which eventually reduces its intensity at around 60 K. The spectroscopic data of the order of eV provides a temperature independent peak at around -0.5 eV. Such a high energy peak might have a connection to the recently discussed high energy mode which is considered to explain the photoemmision band structure. Similar high energy mode features have also found on $Fe_{0.965}Se_{1.035}$ and $NaFe_{0.975}Co_{0.025}As$. This allows us to suggest that the mode with energy range of around -0.2 V to -0.4 V is a universal property among all Fe-based high temperature superconductors. The spectroscopic study on the clean surface showed the purely microscopic evidence of two distinct superconducting phases in stoichiometric LiFeAs. This has been studied between 4.8 K and 20 K within a fixed well defined place on the clean surface of about 2 nm × 2 nm area which is less than the coherence length (ξ) of the compound. One can speculate that the origin of this unexpected two distinct superconducting phases might be related to its unusual band structure where the superconductivity first sets into the shallow α-bands at 18 K, and it will be induced to all bands at the Fermi level only with sufficiently low temperature (below 16 K). Another important result from such temperature dependent spectroscopy measurements is the practically temperature independent dip positions in the tunneling spectra. This rules out the direct connection of an AFM resonance to the dip position, consistent with INS data in Ref. [14, 16, 98] where no distinct evidence of AFM spin-fluctuations have been found neither in temperature scan nor in energy scan.

In the second part, the focus is to very carefully investigate on the spatial variation of the electronic properties of the material. Friedel oscillation (so called QPI) allow here to access the momentum space electronic structure. A successful temperature dependent study of such momentum space electronic structure between 6.7 K and 25 K is used to search for the small q scattering information. A particle-hole symmetric enhancement of QPI intensity for small q scattering within ±5.5 mV has been observed which behaves like a superconducting order parameter as a function of temperature. The strong depletion of QPI intensity between 5.5 mV to 9 mV in both polarities has also been noticed. Such enhancement and depletion of QPI intensity might be related to Andreev bound state either due to multiple scattering processes or due to the usual superconductor-metal-superconductor junction occurred on the surface where the location of the defects act as the origin of normal state. The intraband scattering related to the shallow α_1 band dispersion has been tracked at 6.7 K (superconducting state) and 25 K (normal state). Its intraband scattering vectors at superconducting state (6.7 K) is compared with a band dispersion that describes the ARPES data, whereas the intraband scattering vectors at normal state (25 K) are good agreement with the tight binding fit to the ARPES band structure [140]. Furthermore, the integrated QPI intensity has a characteristic peak at 14 mV which is well consistent with the observed peak at the 1st derivative of the tunneling spectra on bare surface. Such a characteristic peak at 14 mV observed by these two different probes provides a strong argument that it is a resonance mode at $q \approx 0$ (very different from other IBS) that exists in LiFeAs. It is probably connected to shallow α pockets. The defect bound state related to frequently observed two types of Fe-defects at 4 mV has also been observed in the integrated QPI intensity.

Apart from the study on stoichiometric LiFeAs, the commonly observed defects and spatial variation of electronic properties via spectroscopic maps are also investigated successfully on off-stoichiometric LiFeAs which shows superconducting T_c of 6.5 K from our STM spectra. Here, the defect concentration is three times higher than the stoichiometric LiFeAs which might be the reason of reduction of superconducting T_c to around three times than the stoichiometric LiFeAs. The commonly observed defects have significantly influenced the tunneling spectra at unoccupied side at superconducting state (5 K), specifically on donut and bright spot defects. The origin of donut defects are most probably from As site while bright spot defects are possibly the additional Fe atoms over the surface. The two different types of donut center have been found. The one which has strongly affected the spectrum at unoccupied side in comparison to bare surface spectrum, might have an additional Fe atom sitting at the center of those donut defects. The other donut centers have a very faint effect in the tunneling spectra. The QPI data reveals a very different structure compared to stoichiometric LiFeAs sample. A dispersive ring like QPI scattering intensity is observed at negative energies. The comparison of our QPI data with the calculated band structure of the tight binding to the ARPES data suggests that its origin is most likely due to the interband scattering between the γ and α_2 bands. And in addition, the rigid band shift of 10 mV towards occupied side (relative to the Fermi level) is the second striking result. This implies that such higher doping level has shifted the Fermi level and hence, the reduction of superconductivity occurs. In this scenario, the following band structure might describe the sample electronic properties and further can help to understand the superconducting mechanism in LiFeAs superconductors. Such electron doping leads to locate the $\alpha_{1,2}$ bands far from the Fermi level where the α_1 band becomes further away from the Fermi level and the α_2 band still approaches towards the Fermi level. But, both of this bands hardly cross the Fermi level for any k_z values. The other γ hole like band and β electron like bands have a very minor changes at the Fermi level by such rigid band shift. This allows us to suggest that the small q scattering related to the α-bands are important for superconductivity in LiFeAs. In the unoccupied side intraband scattering related to the γ band is also observed but its intensity is very weak, probably due to its d_{xy} character only. It changes from its round like shape near the Fermi level to square like (high anisotropy) on far from the Fermi level at positive energies. Such anisotropy might be connected to the ordinary fluctuations between the γ and β bands which have also been suggested before by Knolle *et al.* [99]. The other striking result from the QPI measurement is the absence of strong enhanced QPI intensities between 9 mV and 17 mV. The 1st derivative of the tunneling spectra does not show any clear peak in this compound. Both the not so clear peak in the 1st derivative of the tunneling spectra and the absence of QPI intensities between 9 mV and 17 mV is related to the absence of the 14 mV mode and hence the reduction of superconducting T_c. Therefore, the 14 mV resonance mode probably is also very crucial for superconductivity in stoichiometric LiFeAs. Such a resonance mode is argued in the previous section to be connected to α bands. This is consistent with the picture of the Fermi level shift so that the absence of 14 mV mode and the location of the α bands far away from the Fermi level are connected to each other.

The essential conclusion of this thesis is as follows. The microscopic evidence of two distinct superconducting phases in stoichiometric LiFeAs from temperature dependent spectroscopy (TDS) measurements might lead to a peculiar scenario where the tiny α bands are playing a vital role on its superconducting properties. This is further supported by the QPI results from stoichiometric and off-stoichiometric LiFeAs. In the stoichiometric superconducting LiFeAs, the strong QPI intensities around $q \sim 0$ in the energy range between 8 mV to 15 mV are found whereas this feature is absent in off-stoichiometric poorly superconducting LiFeAs (putatively electron doped). The electron doping in off-stoichiometric LiFeAs results the α bands far away from the Fermi level. At the same time, the absence of QPI intensity between 9 mV and 17 mV, and the reduction of superconducting T_c occur. All of these results lead to an unusual scenario where such $q \sim 0$ fluctuations connected to α bands might fulfil Stoner criterion towards ferromagnetic instability in LiFeAs which is very different in compare to other IBS. This is further supported by recently studied off-stoichiometric LiFeAs samples where ferromagnetic phase near the superconducting dome for electron doping have been found [141].

The investigation of electronic properties in LiFeAs still remain an interesting direction to keep on study in future. Mostly, the doping dependent STM/S measurements either on a series of Fe substitute samples or on a series of off-stoichiometric LiFeAs samples would be a useful study to thoroughly investigate the band structure of LiFeAs and hence the origin of its superconductivity. Another possibility is to study the electronic properties by evaporating additional Fe atoms on the surface of LiFeAs and to check how the superconductivity affects in the presence of different concentration of Fe atoms.

Appendices

A. High energy spectra on $Fe_{0.965}Se_{1.035}$ and $NaFe_{0.975}Co_{0.025}As$

A.1. $Fe_{1-x}Se_{1+x}$:

The binary structured $Fe_{1-x}Se_{1+x}$ which belongs to the 11 subclass of Fe-HTSC, has superconducting $T_c \approx 8$ K for $x = 0 - 0.1$ [143–145]. Superconductivity here can be enhanced up to 37 K by external pressure [146–148]. Like the most of the Fe-HTSC, this material shows a structural transition (at 90 K) below which its state changes from tetragonal to orthorhombic phase [143]. Its Fermi surface consists of four pockets: two electron-like pockets at the M high symmetry point and two hole-like pockets at the Γ high symmetry point [145, 149]. However, unlike LiFeAs, the larger γ pocket at the Γ point is well below the Fermi level (see Fig. A.1(a)). The orbital-driven nematicity has been reported by Baek *et al.* [71] from a splitting of the NMR resonance line below the structural transition (see Fig. A.1(b)). This is one of the main motivation to investigate the electronic properties at the atomic scale to search for nematic fluctuations in STM/S measurements. Simultaneously, the high energy spectra will also be interesting to study due to the same reason mentioned before in the chapter 5. The results are shown below.

Topography:

The topography scan of 20 nm × 20 nm over the surface of $Fe_{0.965}Se_{1.035}$ single crystal is shown in Fig. A.2 where the used stabilization conditions are $V_{bias} = -50$ mV and set point, $I_T = 50$ pA. Commonly observed defects on such surface are dumbbell shape defects. The first order Bragg peaks in the inset refer to the Se-Se lattice constant which arise in the FFT of Fig. A.2 indicated by white arrows. Unlike LiFeAs, these Bragg peaks are forming a rectangular structure which is a clear proof of the orthorhombic phase of the crystal at 5.6 K. We found defect concentration to be roughly $3 \pm 0.5\%$, relatively much higher than the reported data on superconducting FeSe single crystal [150]. The mostly observed dumbbell defects are perhaps Fe vacancies (see Ref. [151]). The zoom-in picture of such defects and the background atomic corrugation are shown in Fig. A.3(a)-(d) which are measured on a flat part of 5 nm × 5 nm area of the sample with the stabilization condition of $V_{bias} = -50$ mV and set point of $I_T = 1$ nA. Here, donut defects can be seen in the topography, too. Those commonly observed defects are demonstrated in Fig. A.3(b) and (c), while the atomic contrast on the bare surface is

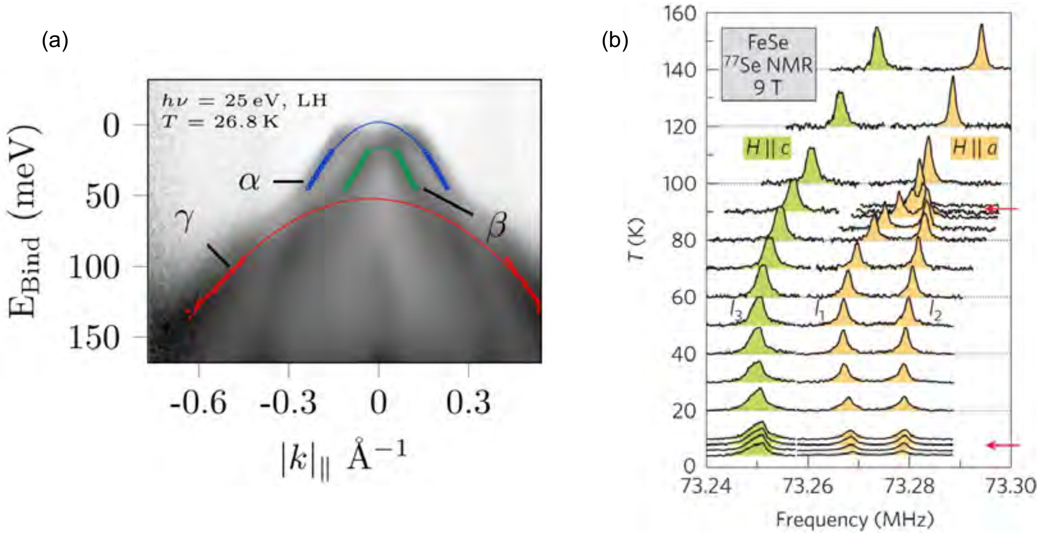

Figure A.1.: (a) ARPES spectral function reveals two hole pockets near the Fermi level at Γ high symmetry point. The large γ pocket is approaching towards the Fermi level. Note that, here the labelled β and α bands are the $\alpha_{1,2}$ bands in our notation. (b) The temperature dependent NMR study shows a splitting of the signal below 90 K due to the nematic phase when magnetic field, $H \parallel a/b$ plane is applied. The NMR signal remains unchanged for $H \parallel c$ plane below the structural transition. (a) and (b) are taken from Ref. [145] and [71], respectively.

presented in Fig. A.3(d). The topography images at 5.6 K and 120 K have shown in Fig. A.4. The defect contrast in Fig. A.4(a) and (b) has inverted probably due to the stabilization condition (see the caption of Fig. A.4).

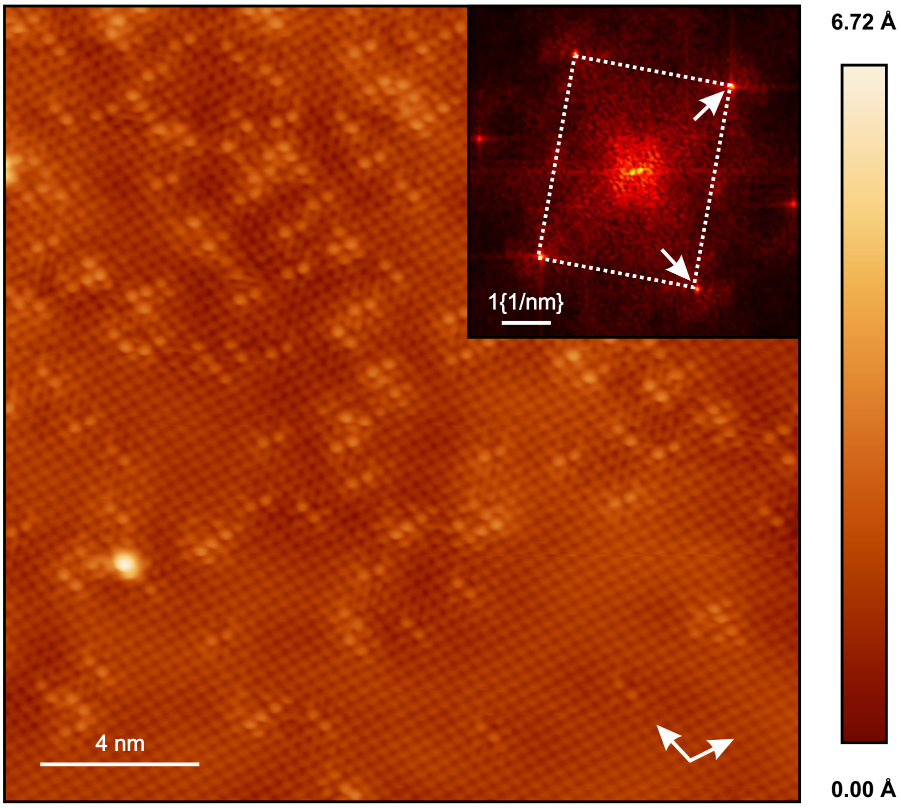

Figure A.2.: (a) Topography scan taken at constant current mode at 5.6 K on $Fe_{0.965}Se_{1.035}$ single crystal over 20 nm× 20 nm area. Stabilization condition: I_T=50 pA V_{bias}=-50 mV. Inset: The FFT image where the rectangular structure of first order Bragg point due to Se lattice constant is visible.

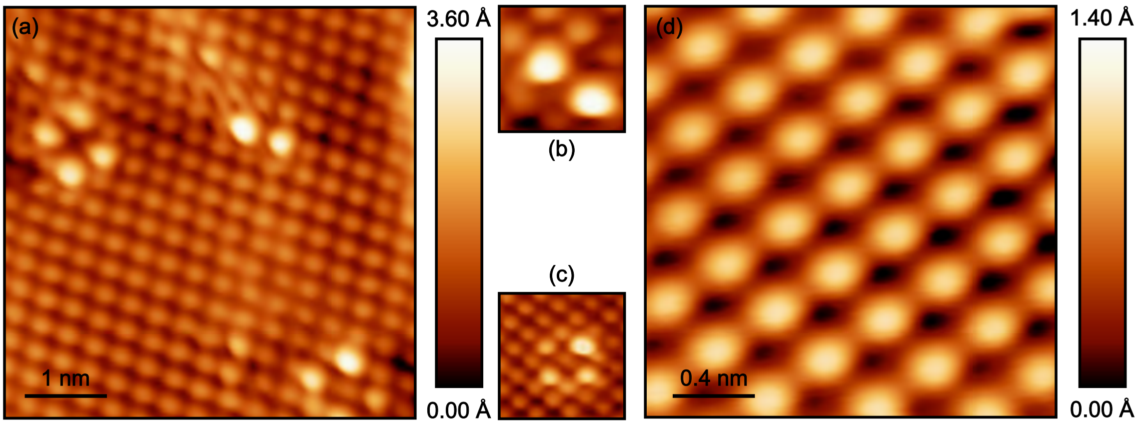

Figure A.3.: (a) Topography image of 5 nm× 5 nm scan area of $Fe_{0.965}Se_{1.035}$ crystal at 5.6 K. Stabilization condition: I_T=1 nA V_T=-50 mV. (b)-(c) The zoom-in of donut and dumble like defects that are frequently observed on the surface. (e) The clean area of 2 nm × 2 nm with atomic corrugation. Note that, (b)-(d) has rotated to have atomic corrugation along the diagonal direction.

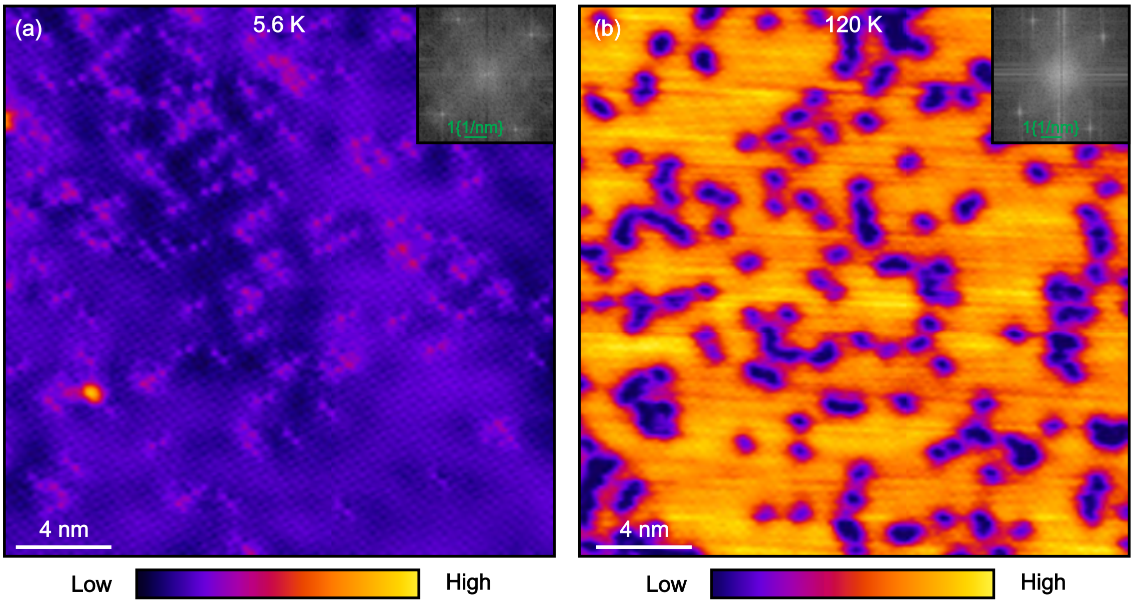

Figure A.4.: Comparison of topography of $Fe_{0.965}Se_{1.035}$ over 30 nm× 30 nm between 5.6 K (a) and 120 K (b). The atomic contrast inverted on defects. Stabilization conditions: (a) I_T=50 pA, V_T=-50 mV; (b) I_T=1 nA, V_T=-1 V

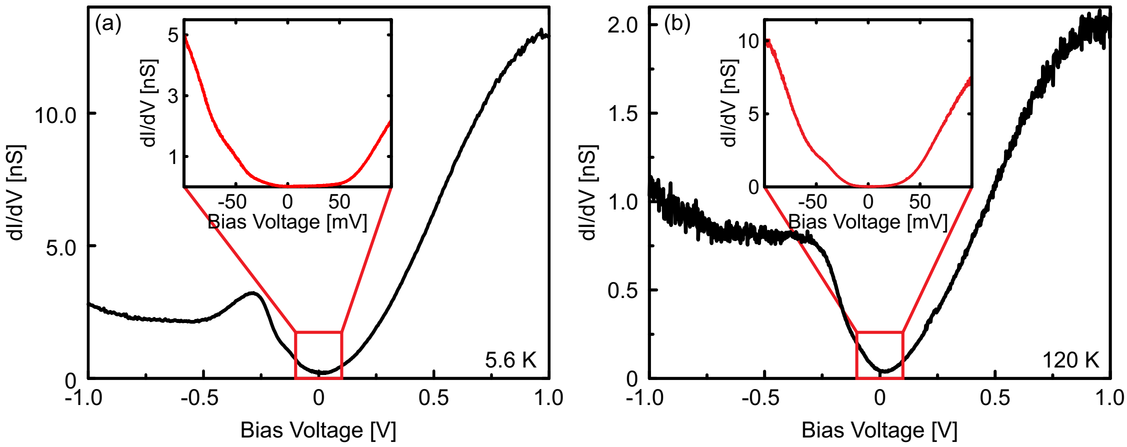

Figure A.5.: (a) Spectra over $Fe_{0.965}Se_{1.035}$ within ±1 V at 5.6 K. Inset: Zoom-in of ±0.1 V showing insulating gap of 60 mV. (b) Spectra within ±1 V at 120 K. Inset: The insulating gap reduces to 35 mV.

Spectroscopy:

The high energy spectra shown in Fig. A.5 are taken between ±1 V at 5.6 K where an insulating gap of around 60 mV at the Fermi level is found. As the defect concentration in the topography image (see Fig. A.2) is found rather higher than the reported data [150], we therefore expect that the sample was quite off from the exact or near stoichiometric samples which are superconducting [144]. Previously, Song *et al.* [144], based on their thin FeSe film data, has mentioned at 1%, 2.5%, 4.9% and 10% doping level by the defect concentration. Similar analysis is done in our result. And it turns out that our sample has a doping level of 3±0.5%. The 60 mV insulating gap that we found in spectra, is nicely consistent for such doping concentration with Song *et al.* (see supporting result of Ref. [144]). There is a sharp peak in the $\mathrm{d}I/\mathrm{d}V$ at -280 mV at base temperature which looks like a hump at 120 K with characteristic energy of -300 mV (see Fig. A.5). The insulating gap reduces to 40 mV at 120 K.

A.2. NaFeAs:

NaFeAs belongs to the 111 subclass of Fe-based superconductors. Its phase diagram resembles to the generic phase diagram (see Fig. 5.4), representing most of the Fe-HTSC (1111 and 122 subclasses) where electron or hole doping drives the system towards superconductivity from AFM or SDW parent states (see chapter 5). ARPES measurements have reported a nested Fermi surface between hole-like pockets at the Γ point and electron-like pockets at the M point which has been predicted in case of Fe-HTSC by earlier theoretical works [84, 152]. However, in case of NaFeAs, the co-existence of AFM/SDW and superconductivity occurs for parent compound where the optimally 2.5% Co-doping suppresses SDW completely and sets maximum superconducting T_c to 20 K (see Fig. A.7) with an enhancement of superconducting volume fraction to 100%. The coexistence of SDW and superconductivity has also been reported in STM measurements by Cai *et al.* [153]. The generic phase diagram of Fe-HTSC (see Fig. 5.4) indicates a nematic phase near the structural transition and has recently been reported also by a quasiparticle interference (QPI) study on NaFeAs by Rosenthal *et al.* [70]. Therefore, NaFeAs follows the generic phase diagram of Fe-based superconductors. However, a doping dependent QPI study by Cai *et al.* [154] suggests that the nematic fluctuation is not a prerequisite for strong Cooper pairing since an insignificant nematic fluctuation in optimally Co-doped NaFeAs is observed. The $s_{\pm}$-wave order parameter has been suggested by Yang *et al.* [155] from their STM/S data on non-magnetic Cu doping into the system which is expected in case of SDW parent compound and theoretically suggested previously for Fe-based superconductors [67].

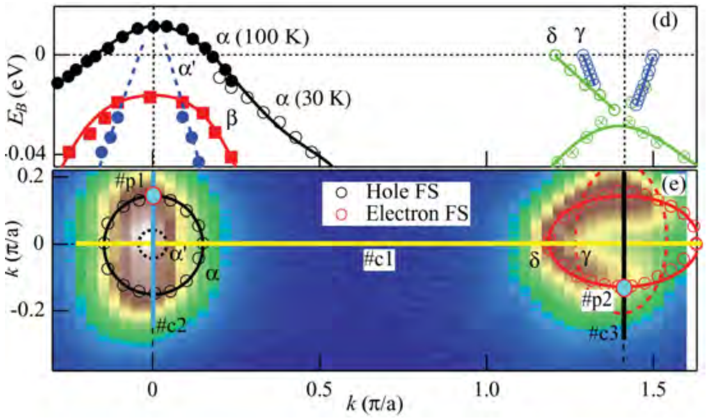

Figure A.6.: ARPES data on 0.5% Co-doped NaFeAs taken from Ref. [156]. The hole-like Fermi surfaces at the Γ point and electron-like Fermi surfaces at the M-point have similar size indicating strong nested Fermi surface.

In case of Co-doped NaFeAs, we found atomic corrugation in the topography measurement over the surface where spectroscopic measurement has been performed. But due to the electrical connection problem to one of the STM scanner electrode, the atoms were elongated in topography and therefore, is not presented here. All the shown spectra have been measured on bare surface far away from the influence of defects.

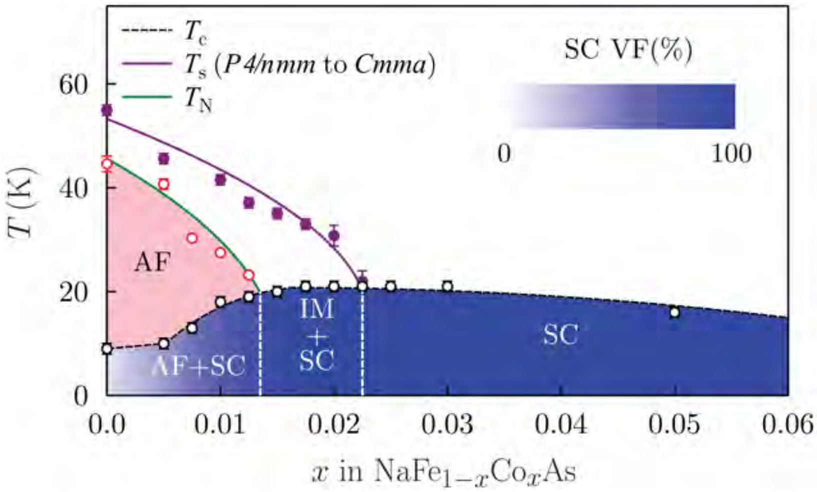

Figure A.7.: Phase diagram of NaFeAs with Co-doping. The structural transition (T_S) from tetragonal to orthorhombic phase has been measured by x-ray powder diffraction (XRPD). The magnetic transition (T_N) from paramagnetic to AFM is studied by zero-field μSR measurement. SQUID magnetometry were used to find superconducting T_c. Inhomogeneous magnetism were observed in μSR experiment. With lowering the temperature, parent state shows SDW/AFM ground state below 41 K followed by structural transition below 52 K from tetragonal to orthorhombic phase. 1.25% Co-doping suppresses AFM ordering completely and inhomogeneous magnetism with superconductivity appears in the system until 2.2% doping. Optimally 2.5% Co-doping only has homogeneous superconductivity with maximum T_c of 20 K. This is taken from Ref. [157].

Spectroscopy:

The data on optimally Co-doped (nominal value of 2.5%) NaFeAs single crystal will be presented here. A spectra within the energy range of ±0.5 V is taken at 9 K on such optimally 2.5% (nominal) Co-doped NaFeAs sample which is qualitatively similar to reported data in literature [153, 158]. The superconductivity as a function of different Co substitution has been studied previously by Zhou *et al.* [158]. According to their results, symmetric superconducting coherence peaks appear for an optimally doped sample, while over doping produces asymmetric coherence peaks. In our data, a superconducting gap of around ±15 mV (2Δ) at the Fermi level is observed but the superconducting coherence peaks become strongly asymmetric in nature as it is barely visible at unoccupied side, presumably due to the higher doping level of the sample. We have taken spectra at 19 K above the superconducting transition and found the disappearance of the superconductivity and opening of 35 mV SDW gap consistent with literature Ref. [153]. In the lower panel of Fig. A.8(a) and (b), its 1st derivative is plotted to look for the corresponding extrema. There are two hump presence at -95 mV and -283 mV which are temperature independent.

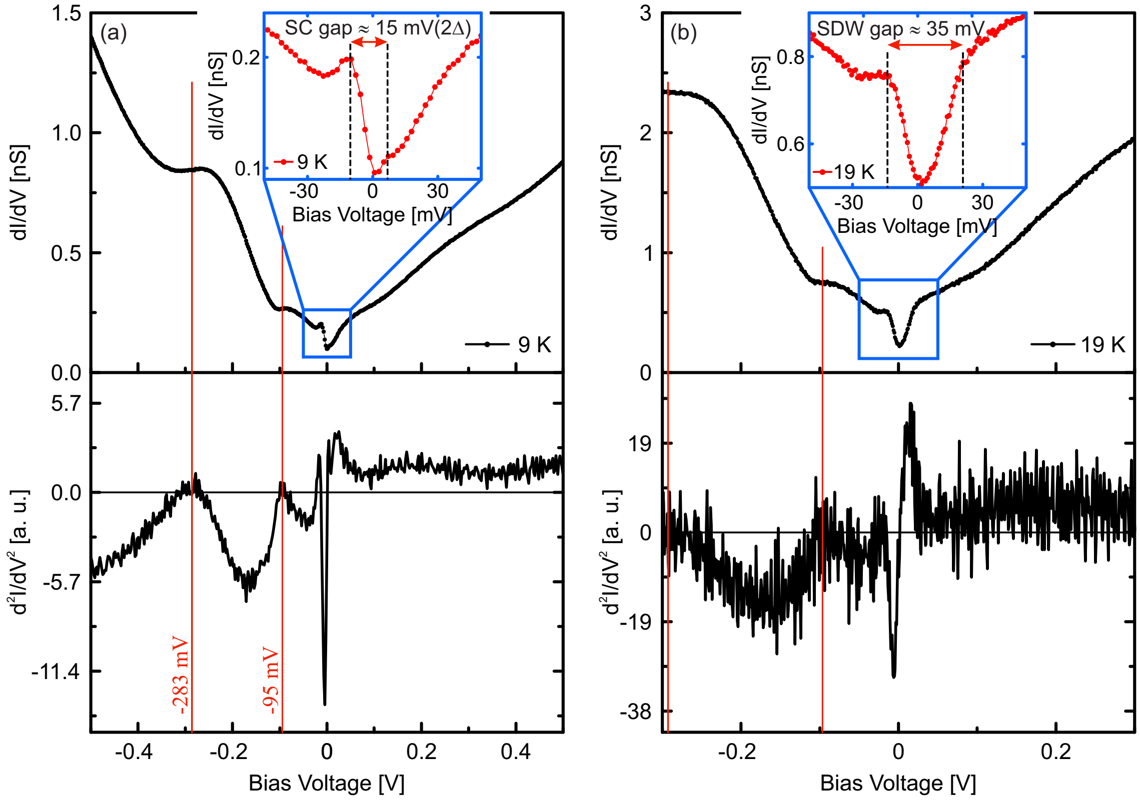

Figure A.8.: (a) Spectra of NaFe$_{0}$. 975Co$_{0}$. 025As at 9 K within ±0.5 V. Inset: The zoom-in of ±0.1 mV to show superconducting gap. Lower panel: The 1st derivative of the spectra (a). (b) Spectra at 20 K within ±0.3 V. Inset: The zoom-in of ±0.1 mV to show SDW gap opened at Fermi level. Lower panel: The 1st derivative of the spectra (b).

A.3. High energy features among three Fe-HTSC:

Similar to the subsection 6.2.1, all the high energy spectra ($\mathrm{d}I/\mathrm{d}V$) are normalized by dividing the corresponding I/V curve to remove the additional effect of matrix elements. Here, LiFeAs spectra have also been shown to compare them with these two systems. The raw spectra on three different Fe-HTSC systems have been plotted together in Fig. A.9 to compare all the high energy features. The corresponding normalized spectra are shown in Fig. A.10. LiFeAs: The normalized spectra of Fig. A.9(a) are depicted in Fig. A.10(a) where a sharp peak at -390 mV is present with two additional peaks at 85 mV and 920 mV. All the features are temperature independent except of superconducting gap at the Fermi level (see inset of Fig. A.10(a)). The normalized spectra at normal state (20 K) are quite comparable with the raw spectra near the Fermi level after normalization, indicating that such normalization is not required if the focus of interest lays close to the Fermi level. The 920 mV peak is very broad in shape compared to other peaks. NaFe$_{0.975}$Co$_{0.025}$As: Fig. A.10(b) is the normalized spectra of Fig. A.9(b) where like LiFeAs, a sharp peak appears at -200 mV. Additional peaks at -60 mV, 26 mV and 230 mV can also be noticed. Fe$_{0.965}$Se$_{1.035}$: In this case, a small peak in the normalized

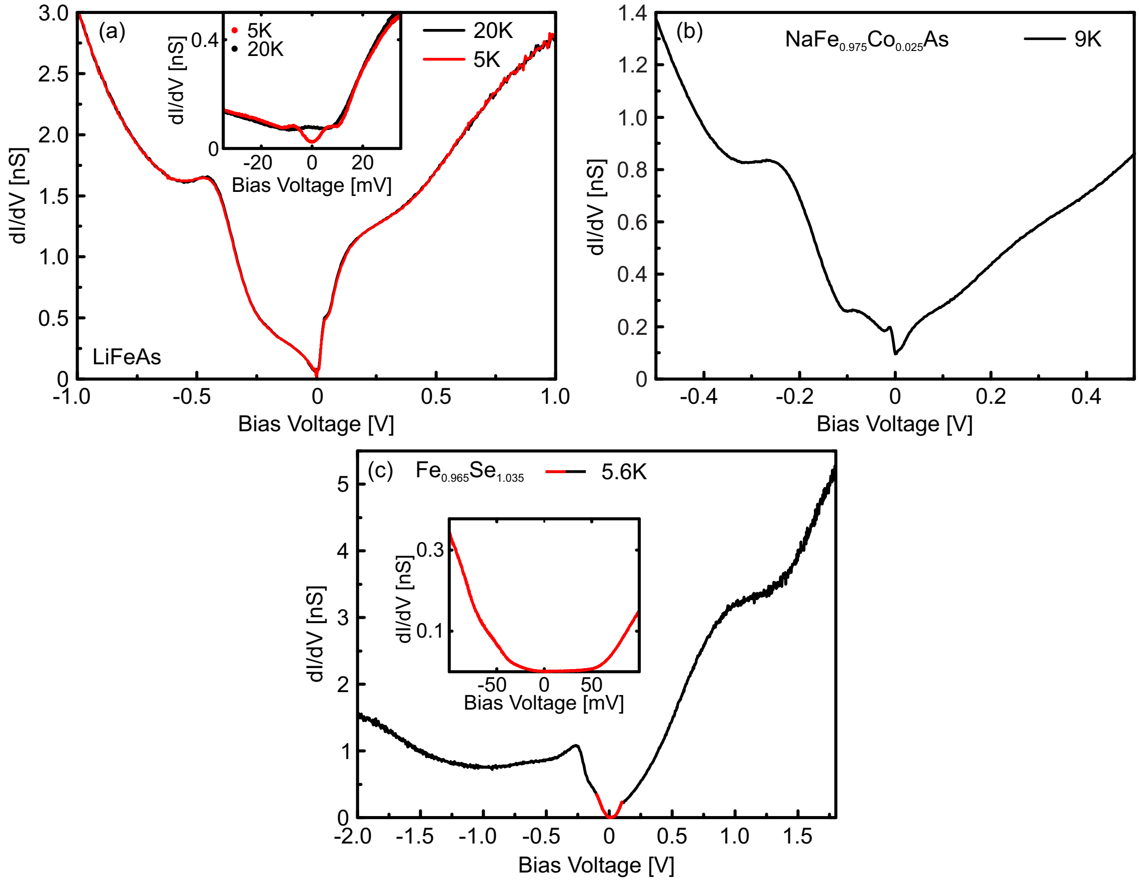

Figure A.9.: (a) LiFeAs: dI/dV spectra on defect-free area between ±1 V in LiFeAs is shown in the temperature range between 5 K and 20 K. Stabilization condition: $I_T = 3$ nA, $V_{bias} = -1$ V. Inset: Zoom-in close to the Fermi level shows superconducting state (5 K) and normal state (20 K) consistent with reported data by Nag *et al.* [49] (b) NaFe$_{0.975}$Co$_{0.025}$As: High energy spectra within ± 0.5 V in 2.5% Co-doped NaFeAs is measured at 9 K. Stabilization condition: I_T = 0.7 nA, V_{bias} = -0.5 V (c) Fe$_{0.965}$Se$_{0.035}$: spectra between -2 V to +1.8 V at 5.6 K has shown in two steps. For large energy, the stabilization condition was $I_T = 1.5$ nA, $V_{bias} = -2$ V plotted in black curve. For the better resolution close to the Fermi level, dI/dV spectra within ±0.1 V has been measured with stabilization of $I_T = 0.8$ nA, $V_{bias} = -0.1$ V plotted in red curve. Insulating gap of 55 ± 5 mV is clearly visible near the Fermi level but it is particle-hole asymmetric in energy. All the spectra shown here are average over several forward and backward sweep but stabilization was always after finishing a complete forward and backward sweep at the stabilization condition, respectively.

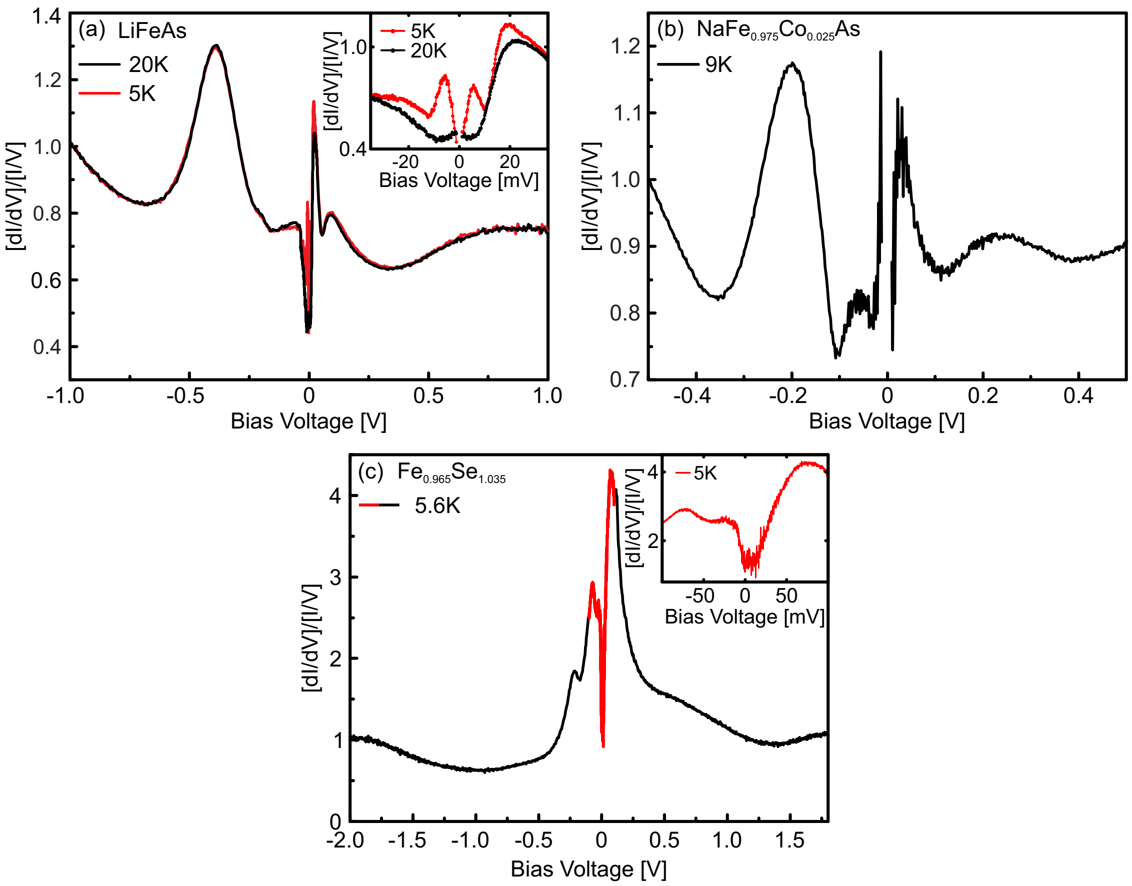

Figure A.10.: Normalized spectra of all three system discussed in Fig. A.9 are shown here. (a) LiFeAs: a peak at -390 mV appears at 5 K as well as at 20 K. At unoccupied side, there are two peak at 85 mV and 920 mV. These features are all temperature independent. The zoom-in in the inset shows the closing of the superconducting gap while the sample goes from 5 K to 20 K. Additionally, a peak at 20 mV at 5 K si noticed which interestingly becomes lower with increasing of temperature. (b) $NaFe_{0.975}Co_{0.025}As$: A similar peak at occupied side is found at -200 mV at 9 K. An additional peak at -60 mV is also present in the spectra. On the other hand, two peaks at +26 mV and +230 mV are also present at unoccupied side. The peak at +230 mV is quite broader than the other peaks. (c) $Fe_{0.965}Se_{0.035}$: In this case, observed peaks are at -210 mV and -70 mV. At unoccupied side, there is a peak at +75 mV. The other peak at +630 mV is extremely broader compared to all the spectral features shown here. The electronic temperature of the measurement is 5.6 K.

spectra (Fig. A.10(c)) appeared at -210 mV (energy range similar like the other two systems but the feature is not very sharp) with additional peaks at -70 mV, 75 mV and 630 mV. The 630 mV peak appears to be very faint. Due to the singularity problem at zero bias while normalizing by dividing I/V curve, we try to take out zero and near zero energy points from the shown spectra. Among all the observed high energy peaks, the important as well as the common features are the peak located at around -200 mV to -400 mV. This characteristic peak is comparable to the ARPES data taken on NaFeAs parent compound and other strongly correlated materials (see subsection 6.2.1).

B. Study of nematicity in $Fe_{0.965}Se_{0.035}$ single crystal:

We have tried to measure the nematic property in FeSe single crystal. The measured single crystal is not superconducting at 5.6 K. But, all the topography images shown before, have rectangular first order Bragg points in the FFT images of those topography measurements. Fig. B.1 describes a measurement at 5.6 K of two topography images at a particular location. The image (a) shows that the atoms are elongated in one particular direction. This is probably a hint that the nematicity makes unequal electronics property along different lattice direction (In this case along a and b direction.). To confirm that the measurement does not depend on the strange tip-state configuration, the image (b)

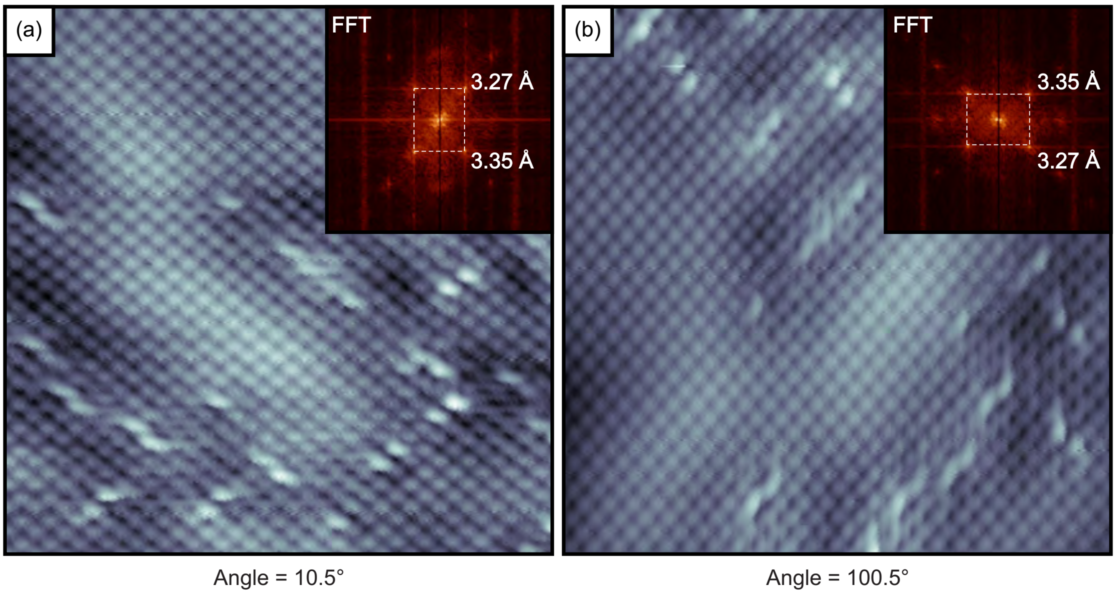

Figure B.1.: (a) A topography on $Fe_{0.965}Se_{0.035}$ single crystal at 5.6 K with stabilization condition of $I_T = 100$ pA, $V_{bias} = -50$ mV. The FFT image in the inset has a rectangular shape of the first order Bragg points due to the elongated atomic structure in the image. (b) The topography at the same place with same stabilization conditions but the scan size is rotated 90° with respected to the image (a). In fact, the structure is also rotated in the topography. The inset FFT image confirms that the rectangular shape has rotated by 90°, too.

is measured by 90° rotated to the image taken at (a). And in fact, the structure has also rotated. This provides the confirmation that the measured unequal electronic properties are intrinsic properties of the sample.

To check whether this feature is related to nematicity, a topography measurement at 95 K above the structural transition (90 K) is recorded which is shown in Fig. B.2. If this phenomenon is related to nematicity, one would expect that above the structural transition, when the system goes from orthorhombic to tetragonal phase, this electronic information will change from unequal (rectangular) to equal (square)[1]. Howeevr, the topography image shows the similar unequal behavior. This is also confirmed from the line cut of the FFT image in the right side of the Fig. B.2. Thus, it does not give us clear proof that this is connected to nematic phase of the sample. In fact, the composition of the studied sample is quite off from the superconducting FeSe single crystal. This is probably the reason that we do not observe clear hint of nematicity here.

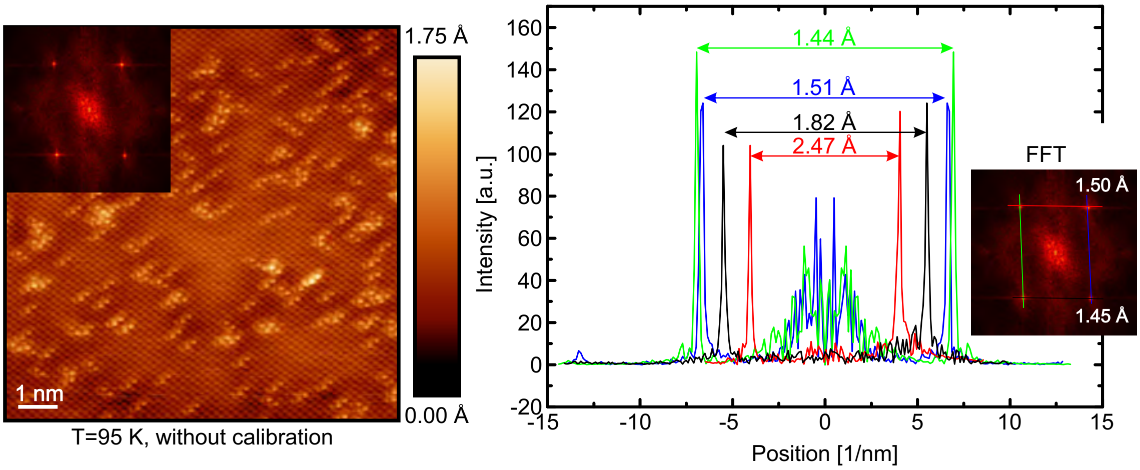

Figure B.2.: Another topography image measured at 95 K with the stabilization condition of $I_T = 50$ pA, $V_{bias} = -50$ mV. The inset image in topography is the FFT image where rectangular shape remains in the system. The right side plot is the line profile along the shown linear direction in the inset image to show that the Bragg peaks are far away from square shape.

---

[1] One example of the square lattice pattern is shown in Fig. 6.1 on LiFeAs sample.

C. Additional results and analysis of temperature dependent spectroscopy study on LiFeAs:

The discussed temperature dependent measurements in the subsection 6.2.2 are challenging as the stability of the system at elevated temperature and the influence of the tip state on the measured data are crucial and can strongly interfere the spectral features. Therefore, we will provide a few more experimental data to proof that practically, we are proving the sample's electronic properties only. Fig. C.1 depicts topography images which are taken before (a) and after (b) the temperature dependent spectroscopic measurement. The atoms over the surface appear similar in both of the images. The defects are seen similar in both images. The shaded 2nd layer defects also appear to be the same in both cases. This has confirmed that we have the same tip-state probing the electronic properties at various measured temperatures between 5 K and 20 K.

One could think a further complicated situation that the tip might be changed during the heating as well as during the measurement of the sample. And afterwards, it can be again changed in this process to the initial tip-state at 20 K. To rule out such scenario, the topography measurement at every temperature stabilized at +35 mV and -35 mV energy is plotted in Fig. C.2. It is distinct from such plot that the shape of the atoms are the same for all the images scanned with same energy[1]. The appearance of atoms is different between positive and negative energy scan. This is due to the asymmetric measured $\mathrm{d}I/\mathrm{d}V$ spectroscopic structure, not due to the change of tip states. This confirms again that the tip-state does not change at all during the entire temperature dependent spectroscopy measurement.

The drift of the system has been discussed in Fig. C.3 at elevated temperature (20 K). The topography images of (a) and (b) at 20 K are measured within the time interval of 3.5 hours. Two black ovals which marked a few defect locations, are pointed in (a). This has changed their location to shaded position in (b). This leads to the conclusion that at 20 K, the drift of the system is around 1 atom/hour. Such high stability of the system allows to perform such highly accurate spectroscopic measurement described in subsection 6.2.2. Such high stability is also useful for long term spectroscopic measurement for example, FT-SI-STM measurement.

---

[1] One example of different tip-states' effect on topography scan is shown in appendix D.

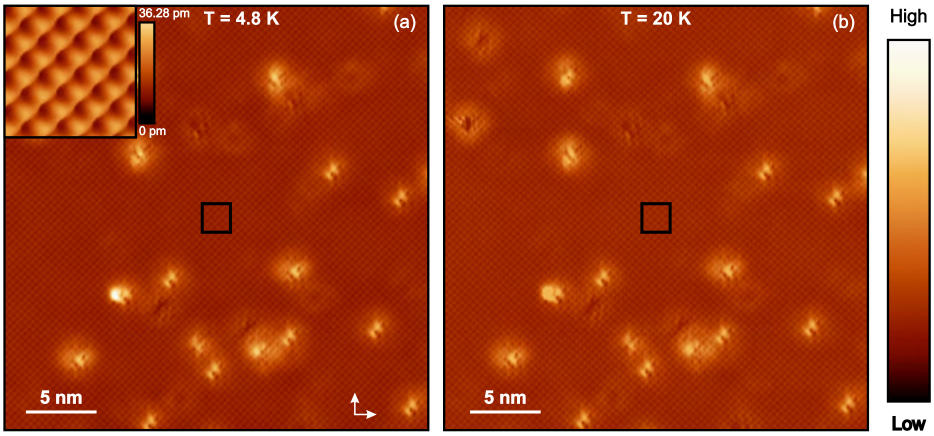

Figure C.1.: Overview topography before (a) and after (b) performing temperature dependent spectroscopic measurement ensure the same tip-state during the full experiment data set. (a) 30 nm × 30 nm area of atomically resolved constant current mode topography image of LiFeAs (I_T = 300 pA, V_{bias} = +35 mV) measured at $T = 4.8$ K. White arrows indicate the in-plane shortest Fe-Fe directions. The atomic corrugation on the surface corresponds to the Li-Li (As-As) lattice spacing of 3.77 Å. Temperature dependent spectroscopy has been measured within the black square of 2 nm × 2 nm area (see the inset image). (b) Same area of a) measured with the same experimental conditions except $T = 20$ K.

The spectroscopic features are discussed within ±35 mV in subsection 6.2.2. Fig. C.4 shows the topography images i.e. the integrated LDOS from the Fermi level until the stabilized energies at +35 mV (a) and -35 mV (b). Again the atomic contrasts are different in these images. We expect this as the bare surface dI/dV spectra have an asymmetric shape. And, the color scale value also proofs that the topography image (at +35 mV) at the unoccupied side in (a) has relatively higher integrated LDOS than the topography image (at -35 mV) at the occupied side in (b). This is also consistent with bare surface dI/dV spectra value.

The spectra in Fig. C.5 are a proof for the reproducibility of all the shown spectra. For example, the green and orange spectra of 20 K-data-1 at 20 K were taken before the blue and red spectra measured at 5 K. After that, again the black and magenta spectra of 20 K-data-2 at 20 K were measured. During the full process of cooling down from 20 K to 5 K and heating back to 20 K again, all the 20 K spectra lay on top of each other, indicating that the same tip-state was used for the measurement of all the spectra at both of these temperatures. The used stabilization condition for the green, black and blue spectra were V_{bias}=-100 mV and I_T=600 pA while the orange, magenta and red spectra were measured with the stabilization voltage (V_{bias}) of -35 mV and setpoint (I_T) of 300 pA. After normalization, all the 20 K spectra (also for 5 K spectra) also lay on each other. This conforms no additional effect due to z-point effect i.e. spectra does

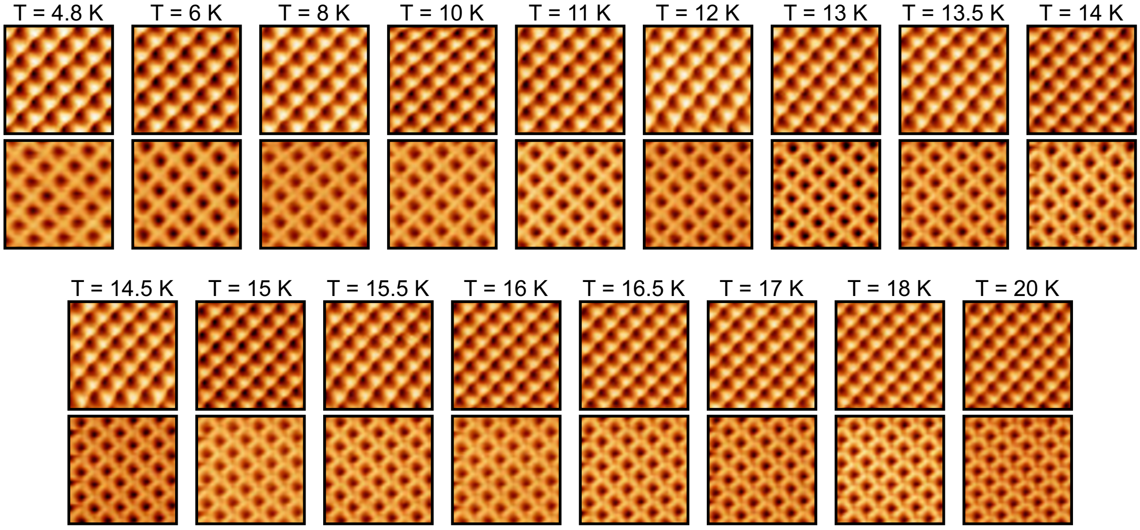

Figure C.2.: The topography images at each temperature sweep where the temperature dependent spectroscopic measurement has been performed to proof unchanged tip-state. Upper and lower panel of each temperature have been measured with same conditions as mentioned in Fig. 6.8 except $V_{bias} = +35$ mV and -35 mV, respectively.

not depend on tip-sample separation due to different stabilization conditions.

Here, temperature dependent dI/dV spectra are treated differently to show that all the features that have been discussed in subsection 6.2.2, can be reproduced. To remove the matrix element effect, the temperature dependent dI/dV spectra in subsection 6.2.2 are divided by I/V even at very small energy scale (see Fig. C.6(a)). Later, we normalise them by dividing 20 K spectra to show the only superconducting DOS, which is shown in Fig. C.6(b). The very systematic closing of the superconducting gap of $\Delta \approx 4.8$ mV is observed with increasing of temperature. The dip-hump structures in both polarities remain clearly visible. In Fig. C.7(a), the zoom-in of Fig. C.6(b) is plotted to show that hump positions are temperature independent until 18 K. The dip positions are marked by down (low temperature) and up (above 16 K) arrows. The waterfall plots of spectra between 16 K and 18 K are shown in Fig. C.7(b). The jump of superconducting coherence peaks and dip positions are visible at 16 K and 18 K. Thus, the observed two distinct superconducting phases in subsection 6.2.2 are consistent with this type of analysis, too.

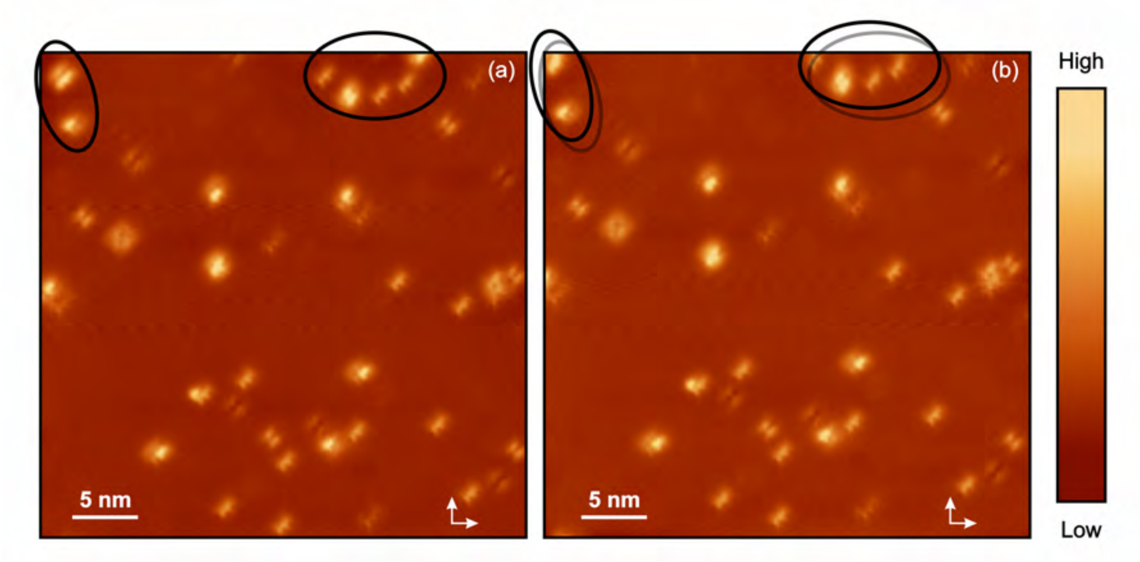

Figure C.3.: (a) and (b) have been measured at 20 K with same stabilization condition(I_T=50 pA and V_{bias} =-35 mV) at same location within the interval of 3.5 hours. The stability of the system is remarkable at such elevated temperature with thermal drift of 1 atom/hour which is important for temperature dependent spectroscopic measurement.

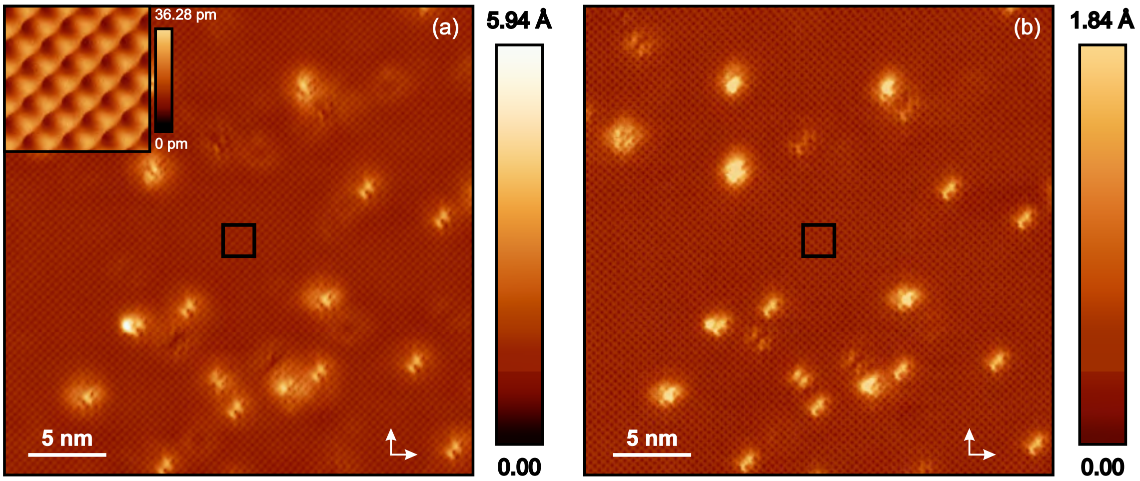

Figure C.4.: Different atomic contrast appeared at topography scan in (a) and (b) presumably due to asymmetric LDOS (see Fig. 6.10) background. All the experimental conditions are the same (mentioned in Fig. 6.8) except (a) with V_{bias} = +35 mV and (b) with V_{bias} = -35 mV. The second layer defects are more sensitive to the positive energy. The measurement was done at 4.8 K. Inset of Fig. (a): Zoom in of black area of 2 nm × 2 nm.

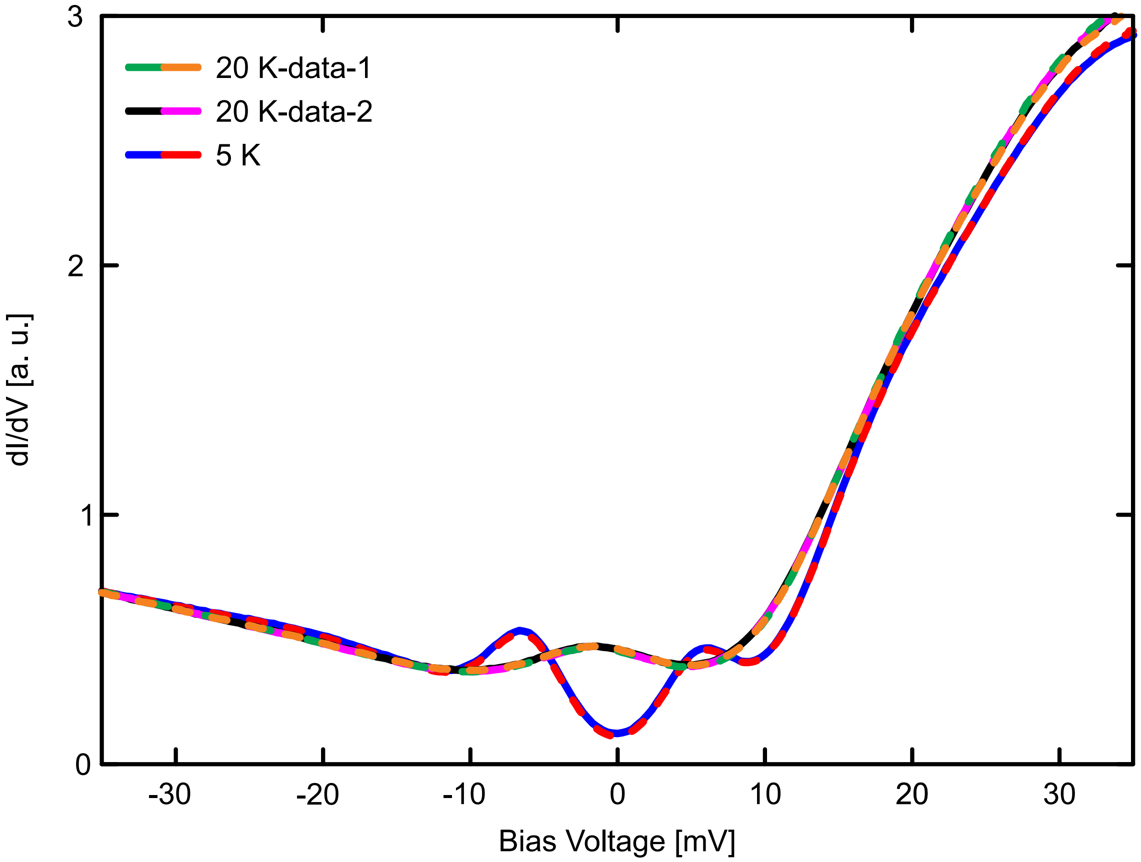

Figure C.5.: The thermal stability as well as reproducibility of spectroscopic data are shown here. Several spectra taken at different stabilization conditions are plotted by different colors at their respective temperatures. 20 K spectra labelled by 20 K-data-1 was taken first and then 5 K data was recorded and at the end, 20 K-data-2 was again measured to confirm unaffected tip-state during such measurements. The stability conditions are: The blue, black and green are taken with I_T=600 pA and V_{bias} =-100 mV while the red, orange and magenta are I_T=300 pA and V_{bias} =-35 mV. This is taken on surface-B of stoichiometric LiFeAs.

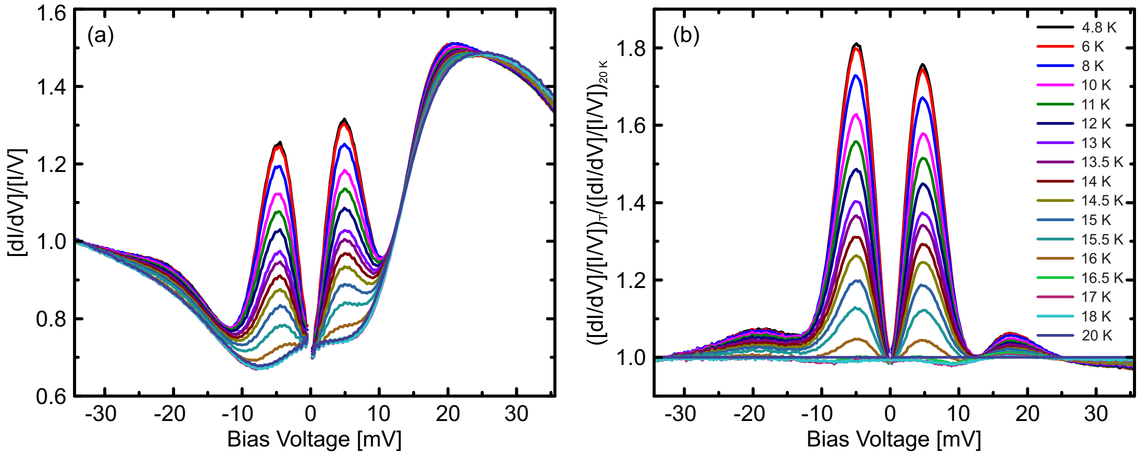

Figure C.6.: Different way to normalize temperature dependent spectroscopy data discussed in subsection 6.2.2. (a) A plot of dI/dV as a function of temperature after normalized by I/V to remove matrix element effect if there are any. (b) The spectra in (a) is again normalized by dividing the 20 K spectra to extract only the superconducting DOS.

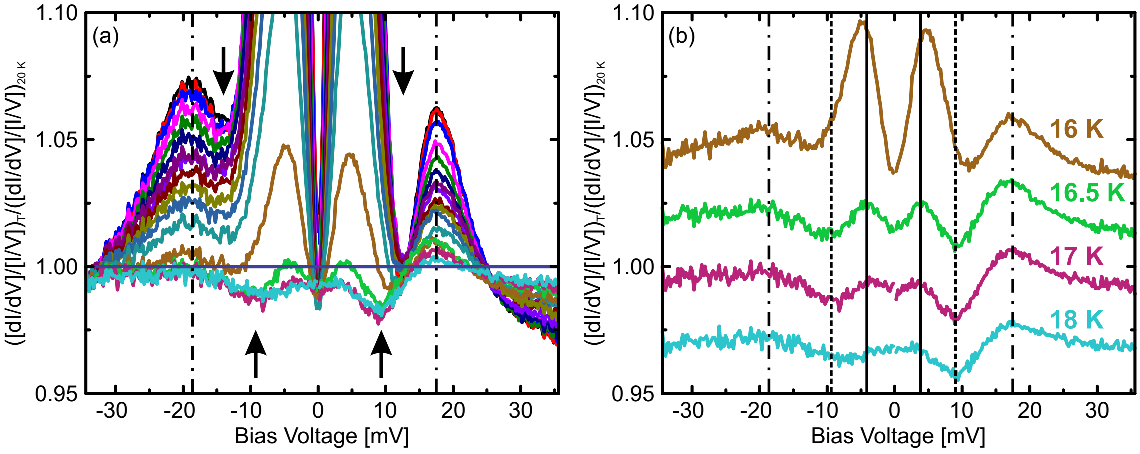

Figure C.7.: (a) The zoom-in part of Fig. C.6(b) to show the evolution of dip-hump structure with temperature. The down arrows indicate dip positions which remain almost constant until 16 K and then jump and remain at lower value at 16.5 K (up arrows). (b) The waterfall representation of spectral features between 16 K to 18 K. The jump of dip and superconducting coherence peak positions from 16 K to 16.5 K can be noticed while the hump position stays in the same position.

D. Effect of different tip-states on topography image

Here, I will provide one example of the appearance of different topography informations because of different tip state. Fig. D.1 shows two topography images which have been recorded with the same conditions. The only difference is the change of tip-state while scanning over the surface. The topography images look completely different unambiguously. The observed changes between them are the following. The first and very easily noticeable changes are the atomic contrasts over the surface. In Fig. D.1(a) atomic contrast is relatively stronger than the Fig. D.1(b). The atomic corrugations over the donut shape defects in (a) have disappeared in image (b). These donut shape defects which are looking asymmetric shape in (a), are turned into a symmetric shape on image (b). One example of this is marked by light blue arrow in both images. The bright spot

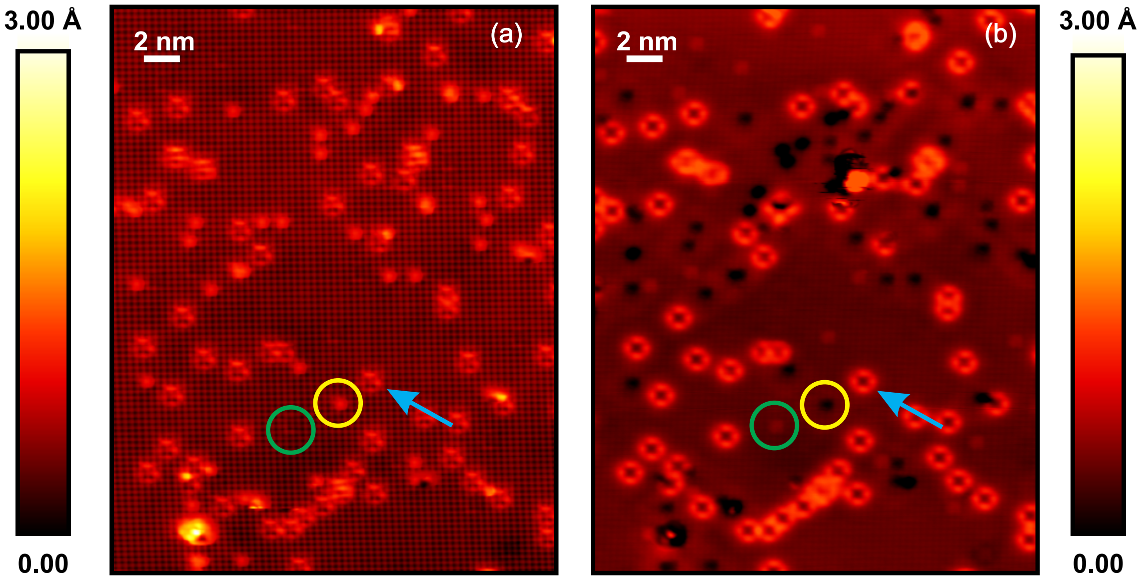

Figure D.1.: Two topography images are shown which are reordered with two different tip-states on a specific location of a off-stoichiometric LiFeAs sample. The marked green, red circles and light blue arrow are pointing three defects which appear differently on the surface during the recording of topography informations. The used stabilization conditions for both of the images are: $I_T = 1$ nA, $V_{bias} =$ -50 mV.

defects in Fig. D.1(a) changed to missing atom defects in Fig. D.1(b). The green circles are pointing one example of this. The bright spot defects in Fig. D.1(b) are hardly visible in Fig. D.1(a). This can clearly proof that the change of tip state can be identified by measuring the topography images and hence can modify spectroscopic features. This supports that the thorough and accurate temperature dependent spectroscopic measurements in subsection C with similar atomic contrast at each temperature measurement confirm no additional effect of tip-state in the discussed spectroscopic features.

E. Additional data of temperature dependent QPI measurements

Here I will provide some additional information on the temperature dependent QPI measurements. The line profiles of the line cut of the QPI signal at 6.7 K along Fe-As direction are shown in Fig. E.1. All the temperature dependent QPI data set is difficult to put in the thesis due to large data size. But, I will show in the following three selected temperatures all the real space and their corresponding QPI signals. These three temperatures are 6.7 K, 14 K and 25 K, respectively. The rest of the measurements at 8 K, 11 K, 15 K, 16 K, 17 K, 18 K, 20 K are shown in the electronic version and in the additional DVD.

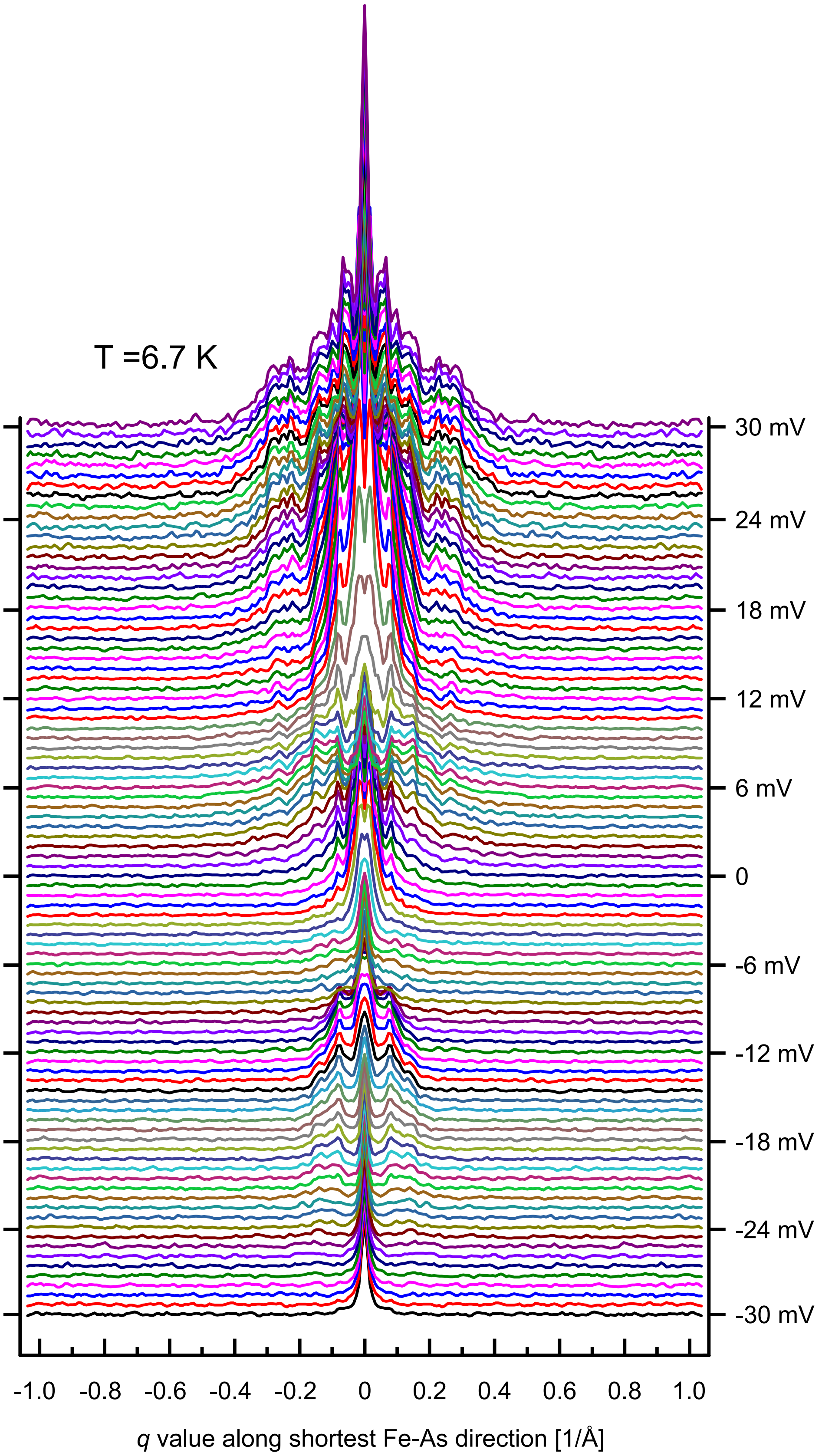

Figure E.1.: The waterfall presentation of the all line profiles along Fe-As direction from the shown spectroscopic map in Fig. 6.21 at 6.7 K.

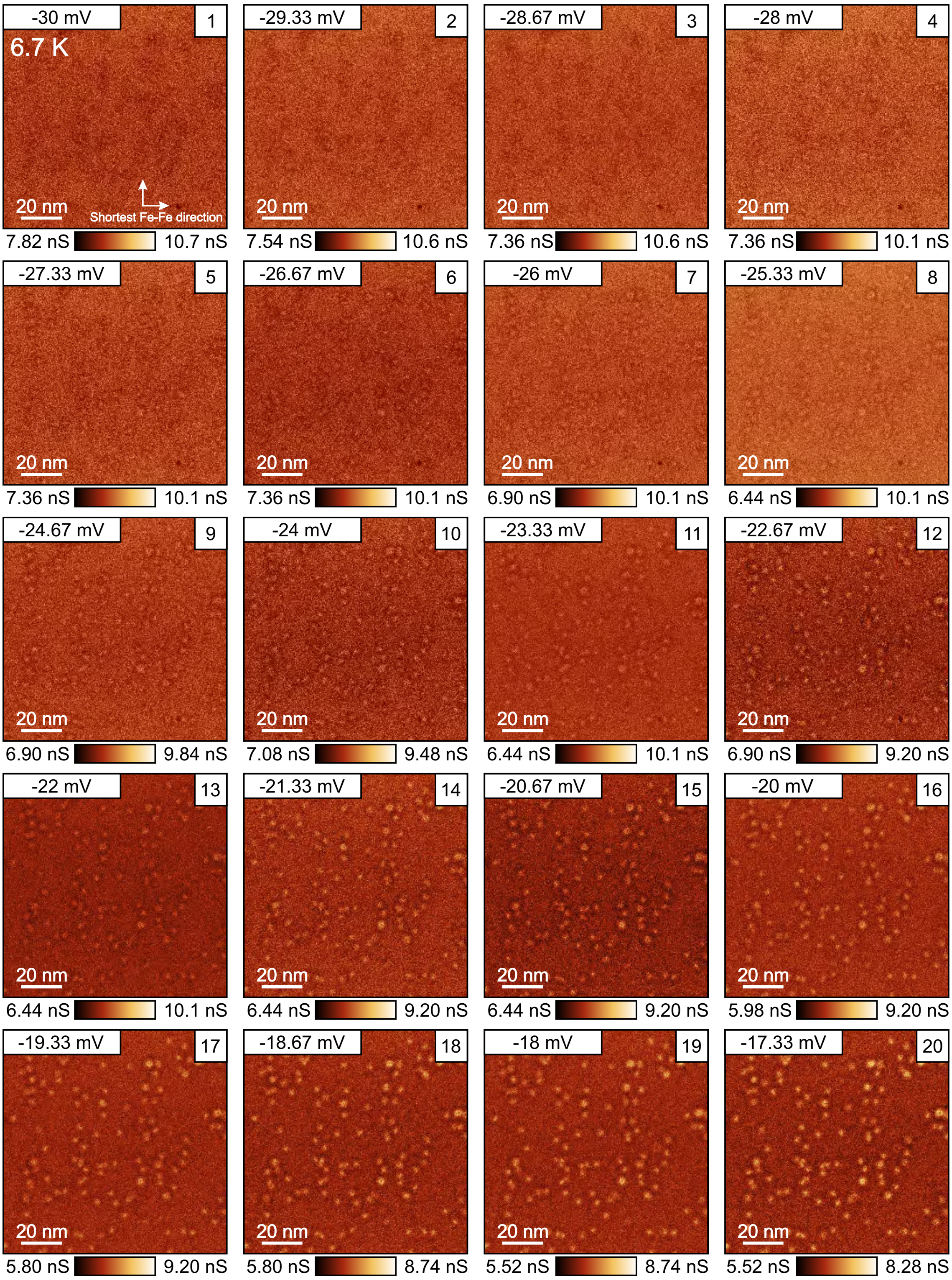

Figure E.2.: The constant energy dI/dV slices from spectroscopic map taken at the same place of Fig. 6.18. The corresponding energies of those images ((1)-(20)) are shown in the left upper corner of each image which are from -30 mV to -17.33 mV. Total size of each image is 110 nm × 110 nm. This is measured at 6.7 K.

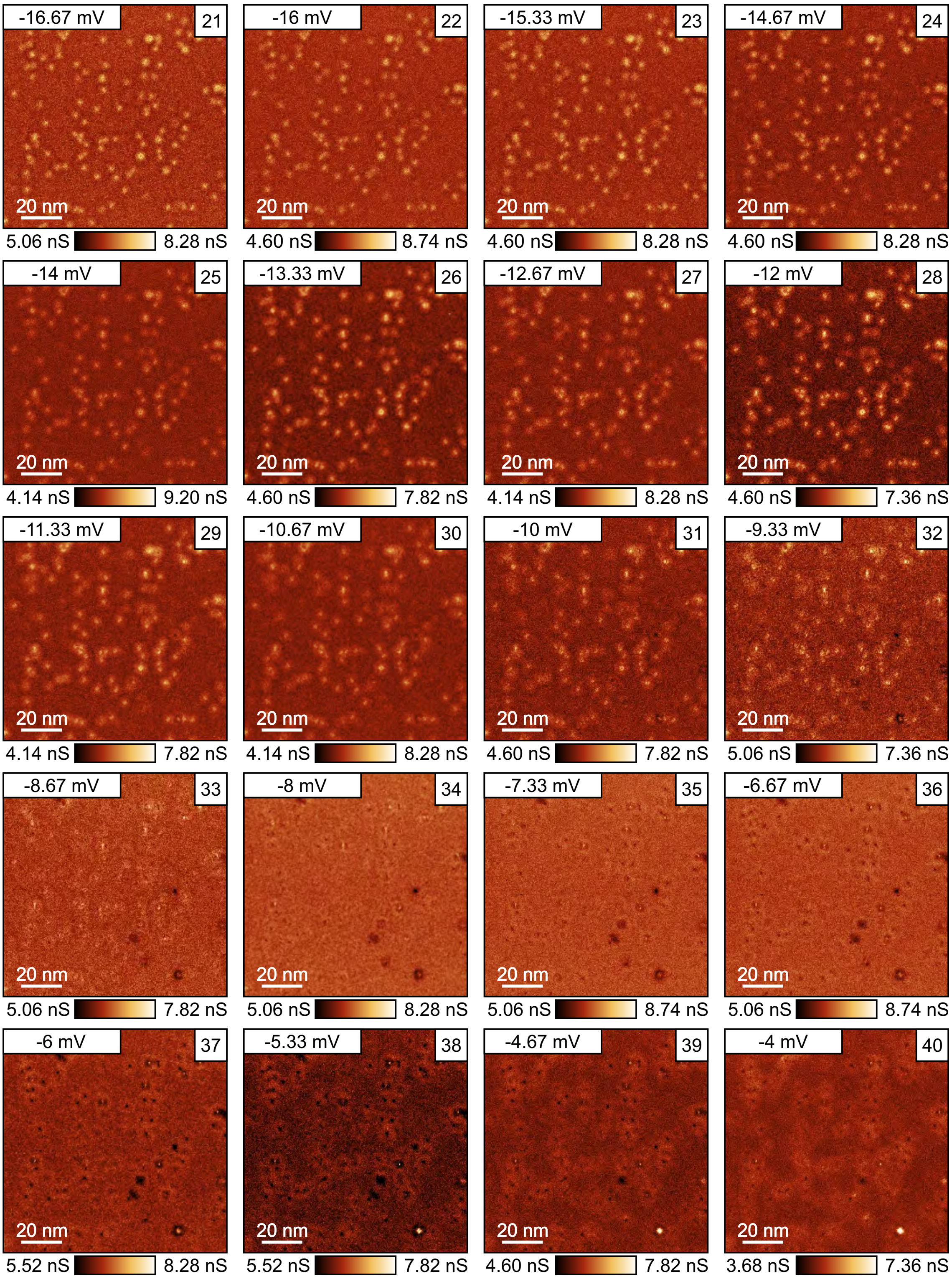

Figure E.3.: The constant energy $\mathrm{d}I/\mathrm{d}V$ slices from spectroscopic map taken at the same place of Fig. 6.18. The corresponding energies of those images ((21)-(40)) are shown in the left upper corner of each image which are from -16.67 mV to -4 mV. Total size of each image is 110 nm × 110 nm. This is measured at 6.7 K.

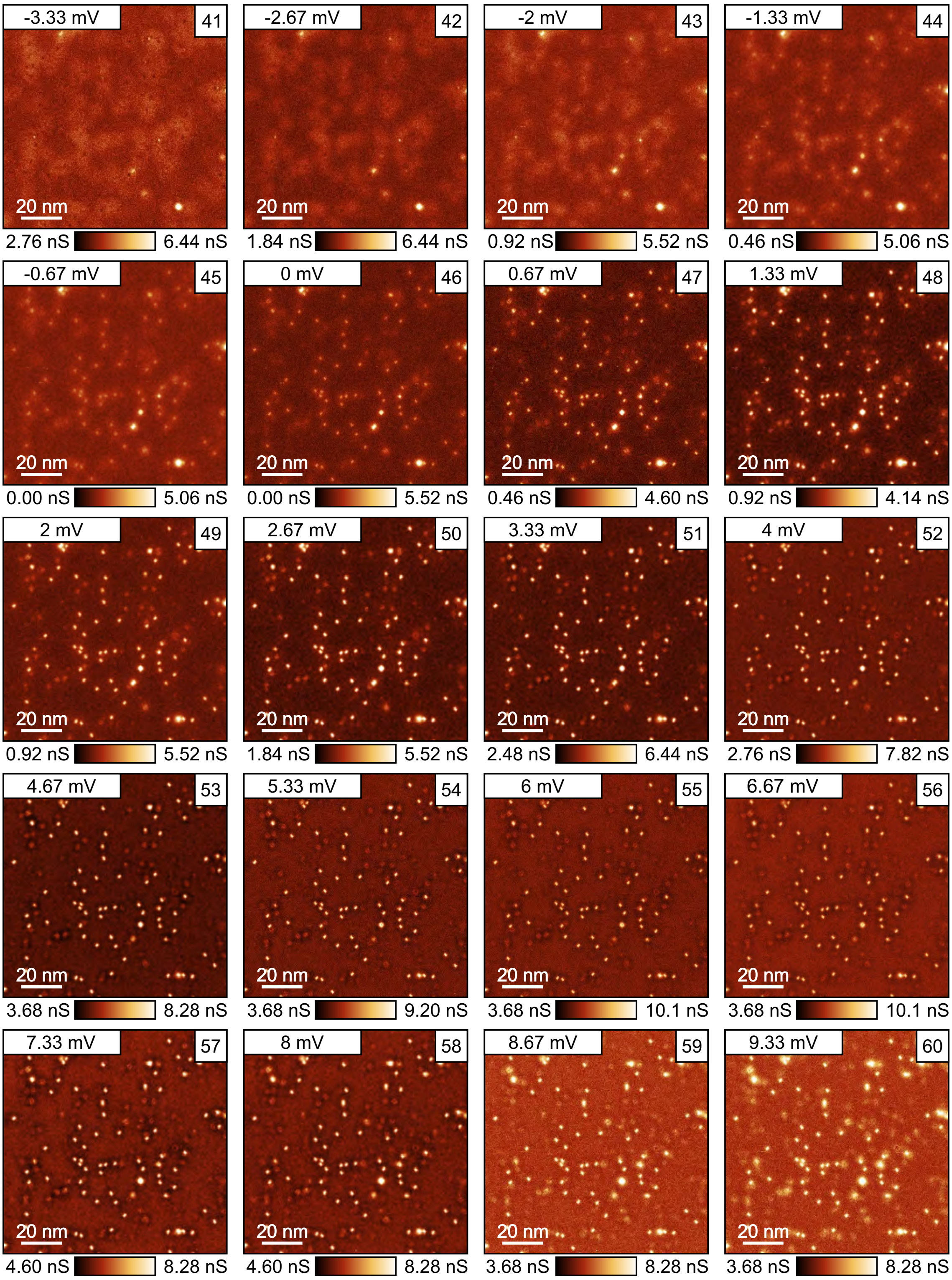

Figure E.4.: The constant energy dI/dV slices from spectroscopic map taken at the same place of Fig. 6.18. The corresponding energies of those images ((41)-(60)) are shown in the left upper corner of each image which are from -3.33 mV to 9.33 mV. Total size of each image is 110 nm × 110 nm. This is measured at 6.7 K.

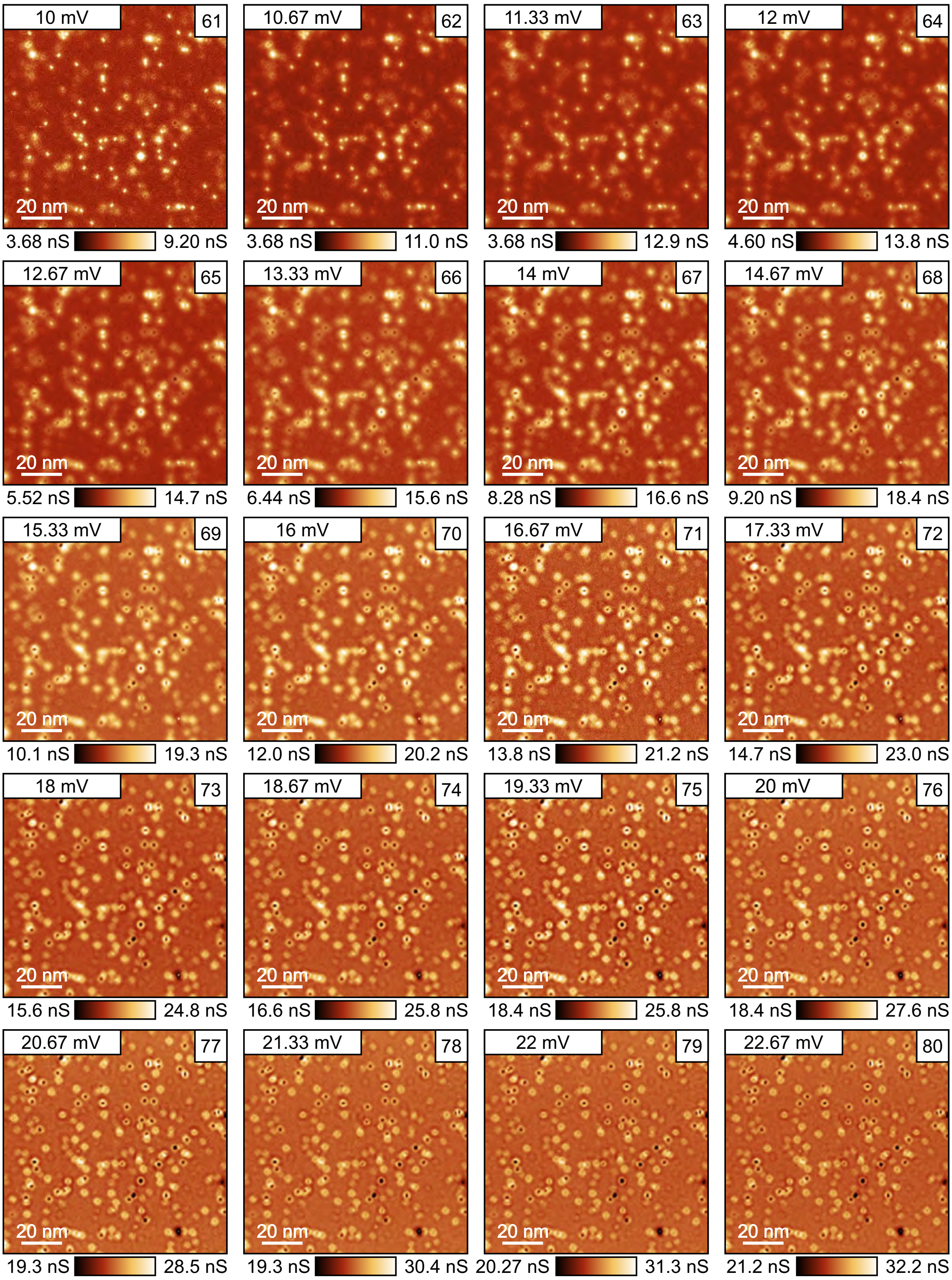

Figure E.5.: The constant energy $\mathrm{d}I/\mathrm{d}V$ slices from spectroscopic map taken at the same place of Fig. 6.18. The corresponding energies of those images ((61)-(80)) are shown in the left upper corner of each image which are from 10 mV to 22.67 mV. Total size of each image is 110 nm × 110 nm. This is measured at 6.7 K.

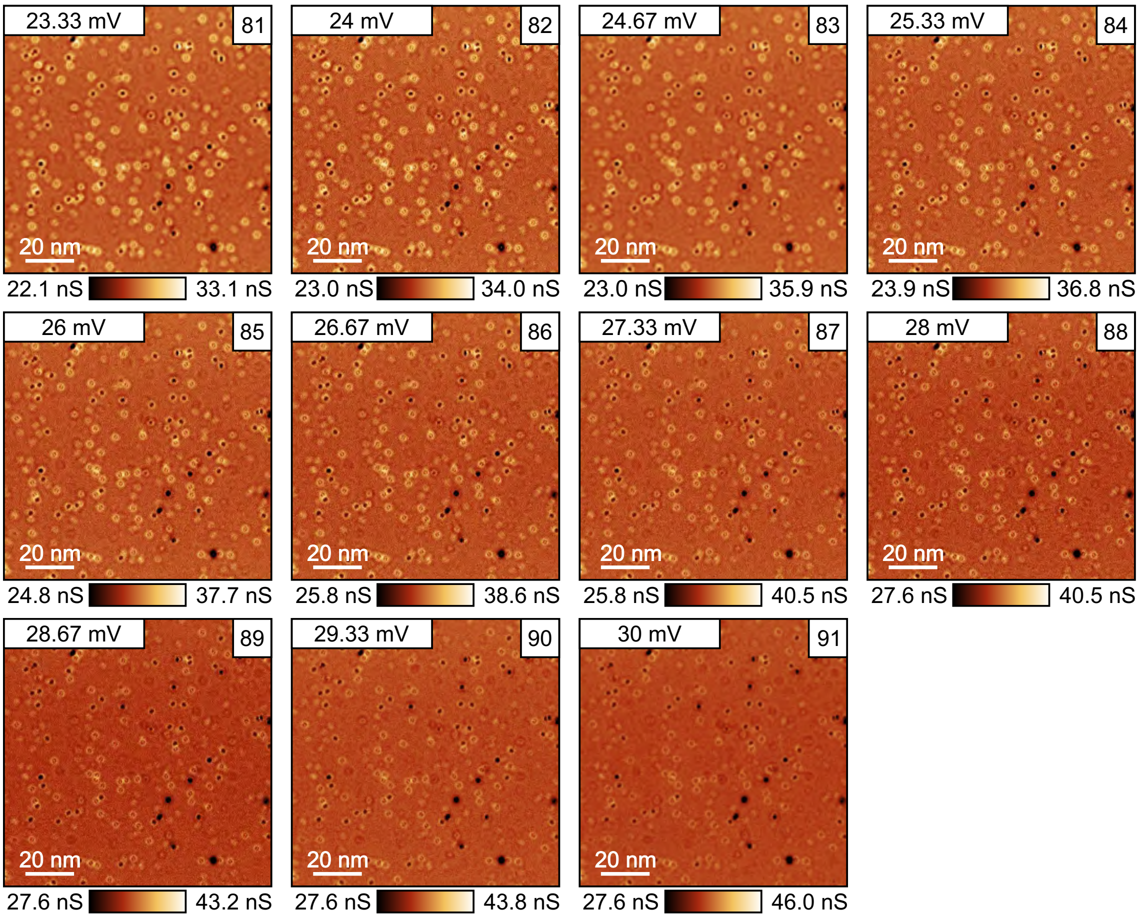

Figure E.6.: The constant energy dI/dV slices from spectroscopic map taken at the same place of Fig. 6.18. The corresponding energies of those images ((81)-(91)) are shown in the left upper corner of each image which are from 33.33 mV to 30 mV. Total size of each image is 110 nm × 110 nm. This is measured at 6.7 K.

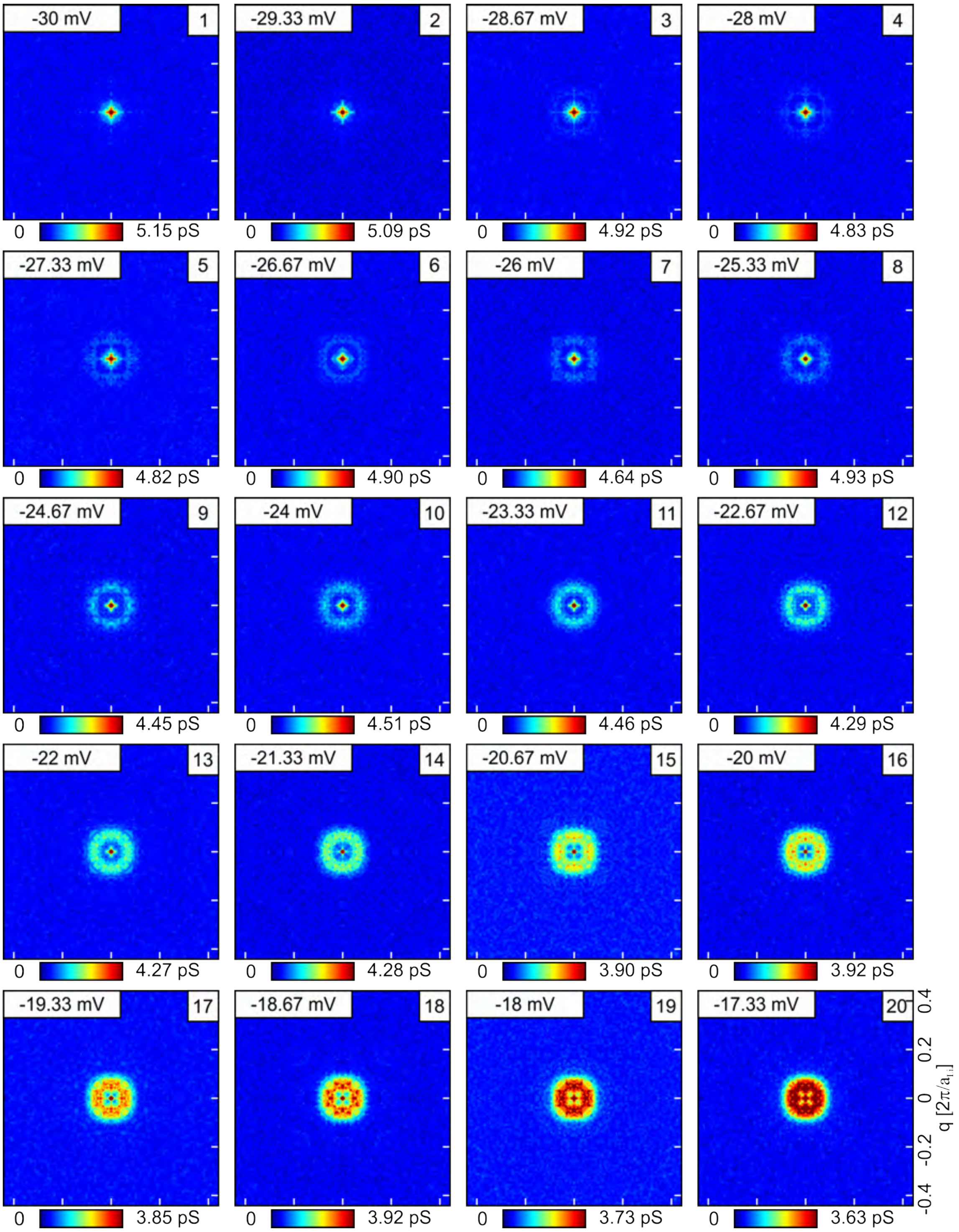

Figure E.7.: The QPI signals related to the constant dI/dV energy slices in Fig. E.2. The corresponding energies of those images ((1)-(20)) are shown in the left upper corner of each image which are from -30 mV to -17.33 mV. Total size of each image is $\pm 0.44 \times 2\pi/\mathrm{a}_{Li}$. This is measured at 6.7 K.

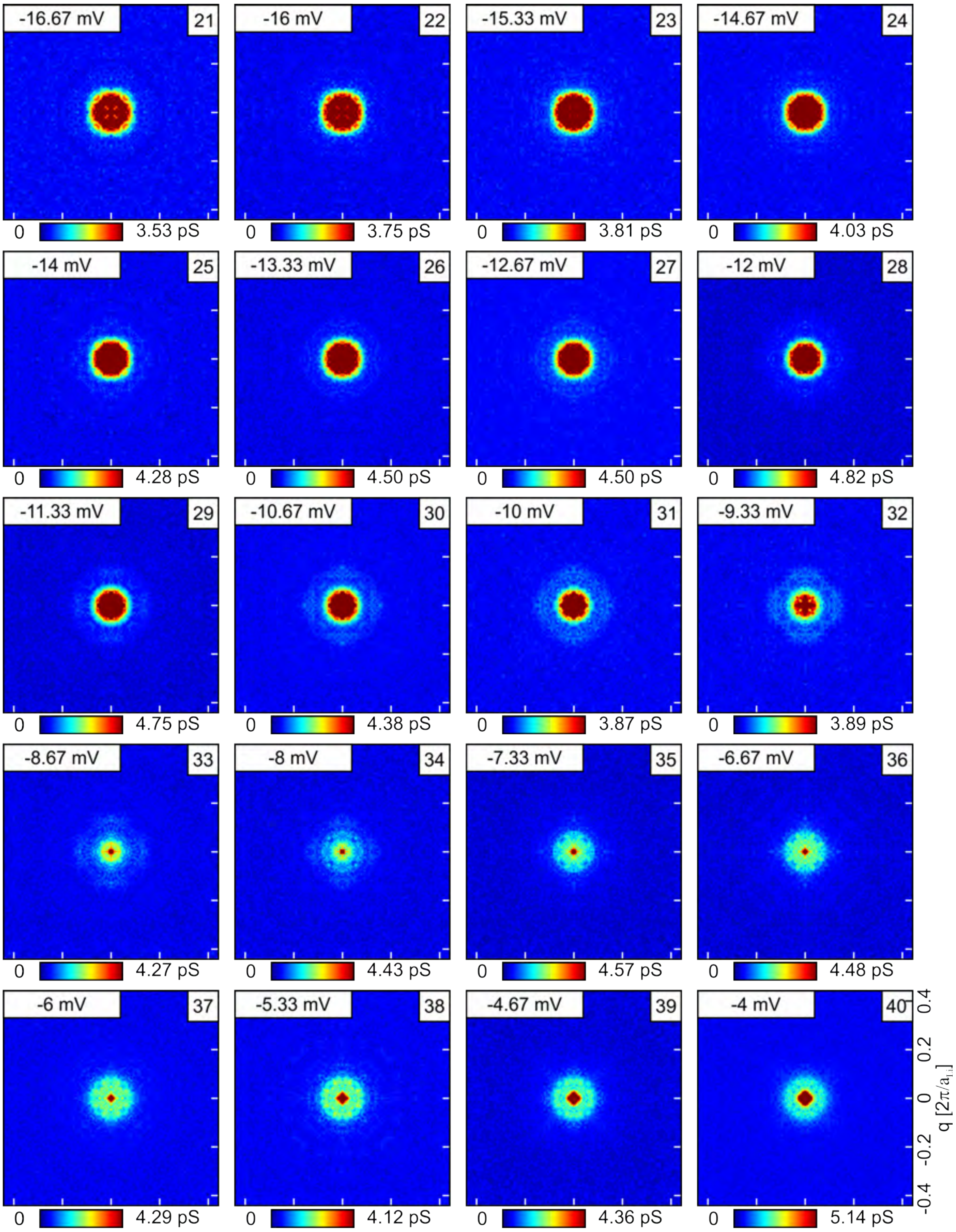

Figure E.8.: The QPI signals related to the constant dI/dV energy slices in Fig. E.3. The corresponding energies of those images ((21)-(40)) are shown in the left upper corner of each image which are from -16.67 mV to -4 mV. Total size of each image is $\pm 0.44 \times 2\pi/\mathrm{a}_{Li}$. This is measured at 6.7 K.

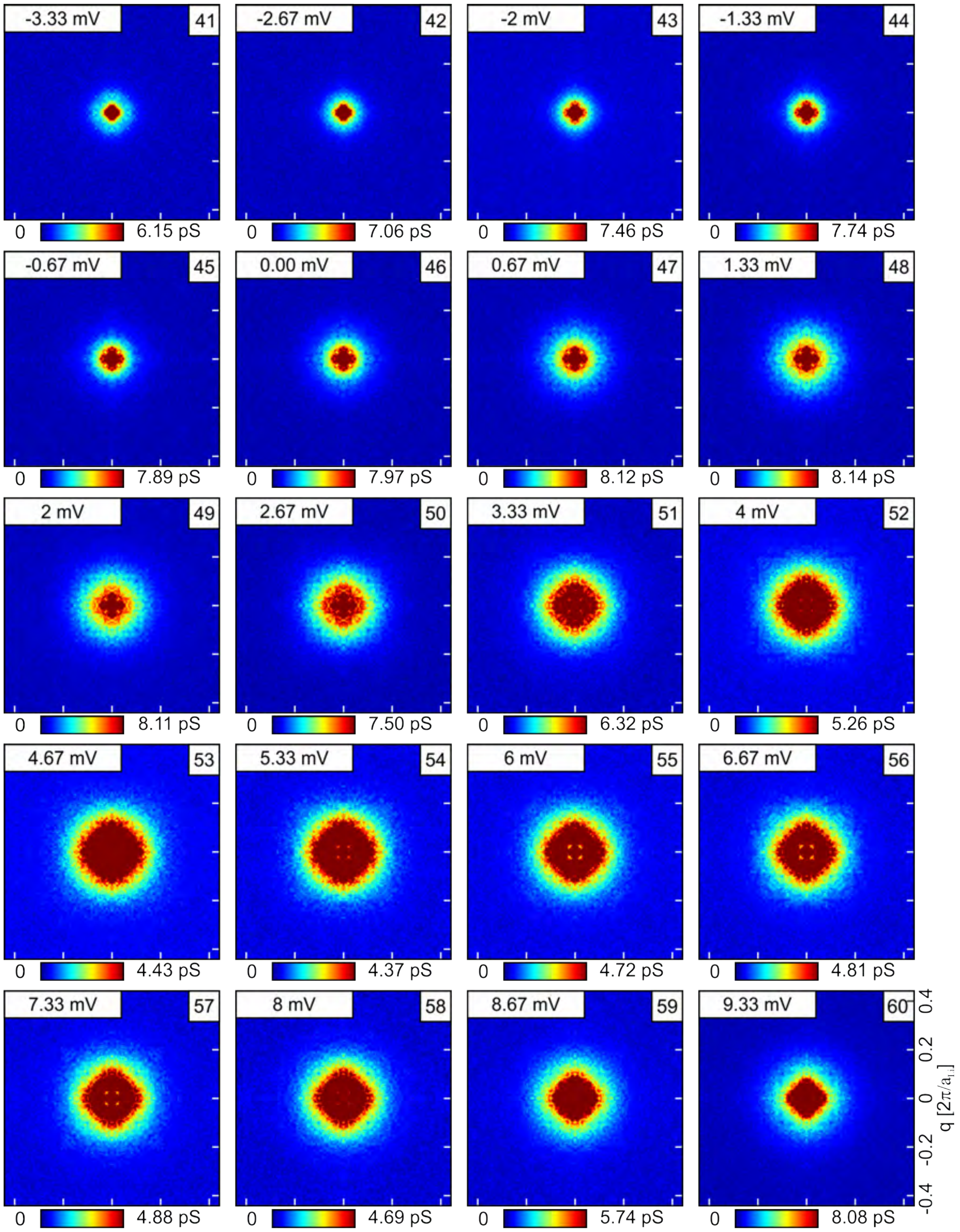

Figure E.9.: The QPI signals related to the constant dI/dV energy slices in Fig. E.4. The corresponding energies of those images ((41)-(60)) are shown in the left upper corner of each image which are from -3.33 mV to 9.33 mV. Total size of each image is $\pm 0.44 \times 2\pi/\mathrm{a}_{Li}$. This is measured at 6.7 K.

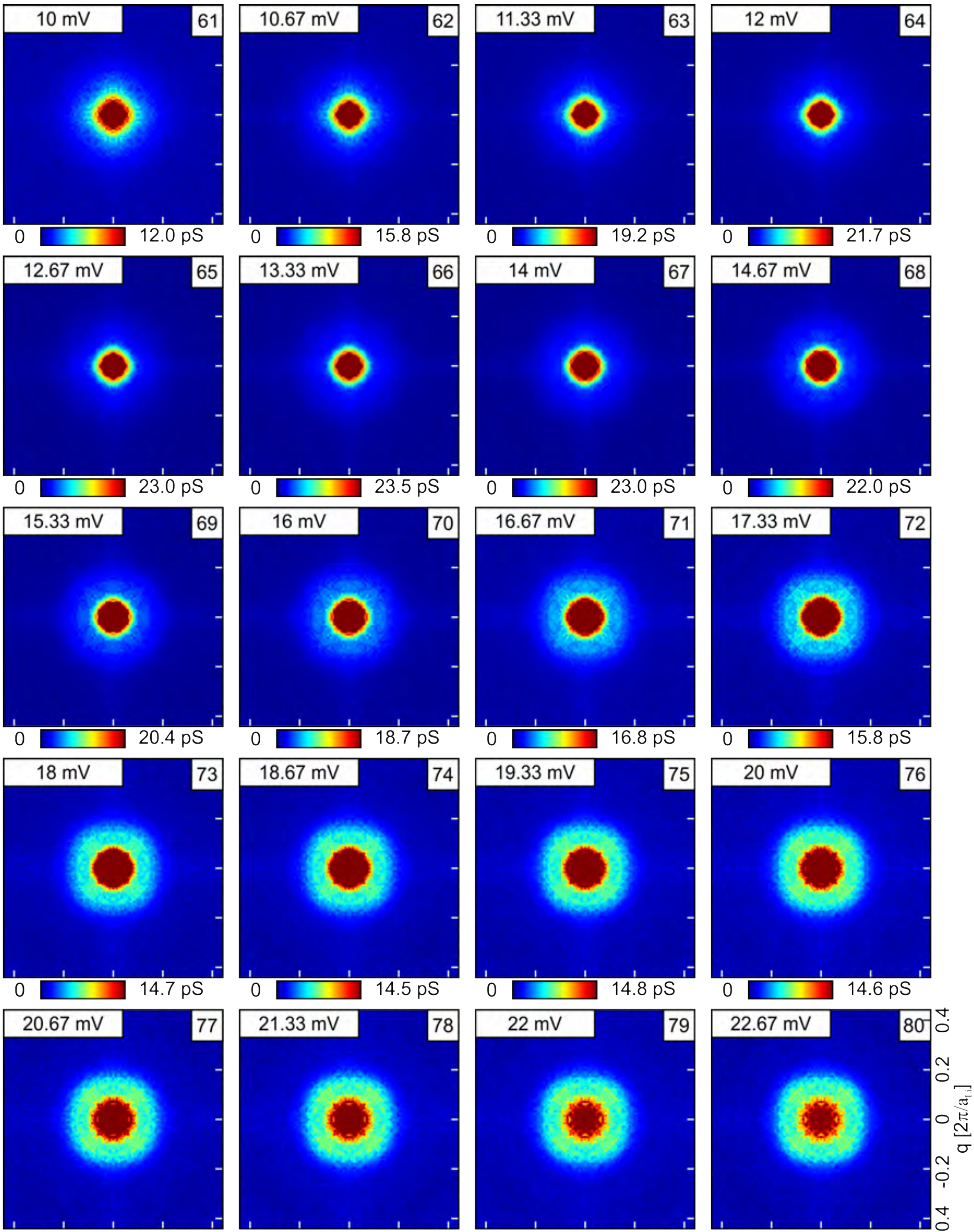

Figure E.10.: The QPI signals related to the constant dI/dV energy slices in Fig. E.5. The corresponding energies of those images ((61)-(80)) are shown in the left upper corner of each image which are from 10 mV to 22.67 mV. Total size of each image is $\pm 0.44\times 2\pi/\mathrm{a}_{Li}$. This is measured at 6.7 K.

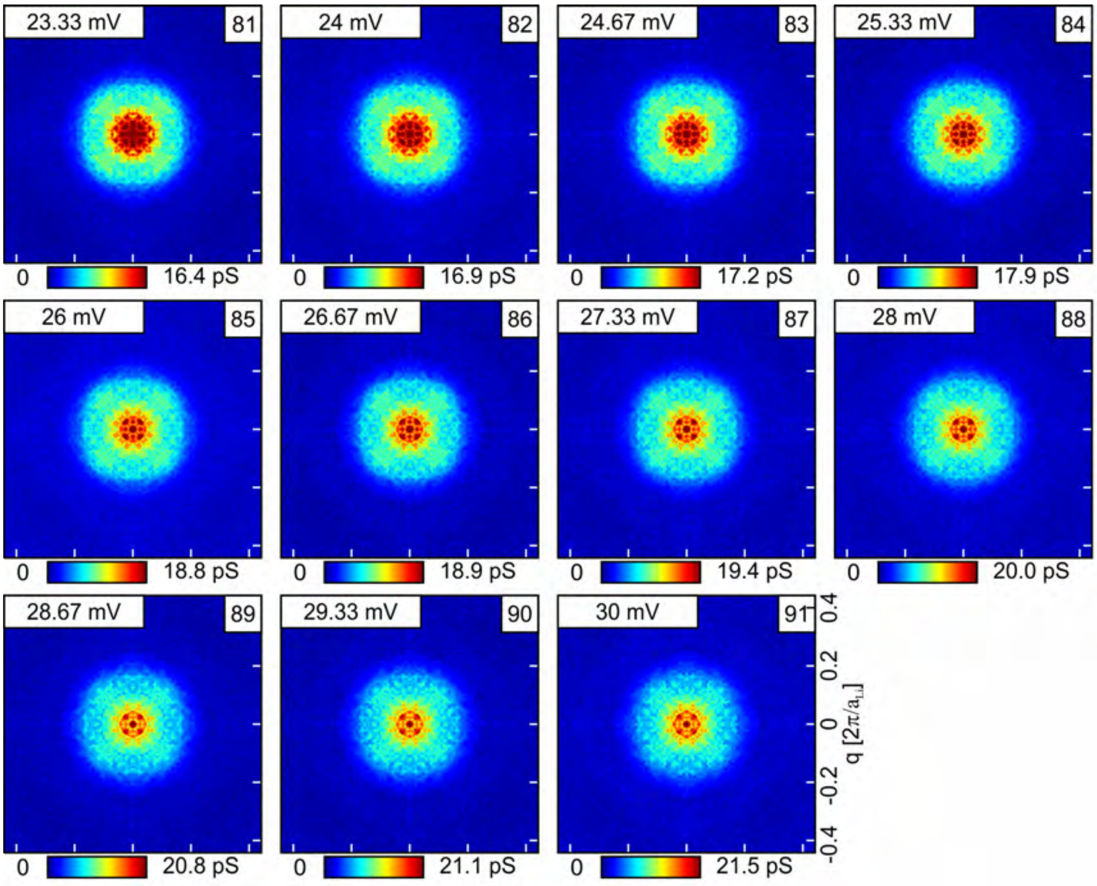

Figure E.11.: The QPI signals related to the constant dI/dV energy slices in Fig. E.6. The corresponding energies of those images ((81)-(91)) are shown in the left upper corner of each image which are from 23.33 mV to 30 mV. Total size of each image is $\pm 0.44 \times 2\pi/\mathrm{a}_{Li}$. This is measured at 6.7 K.

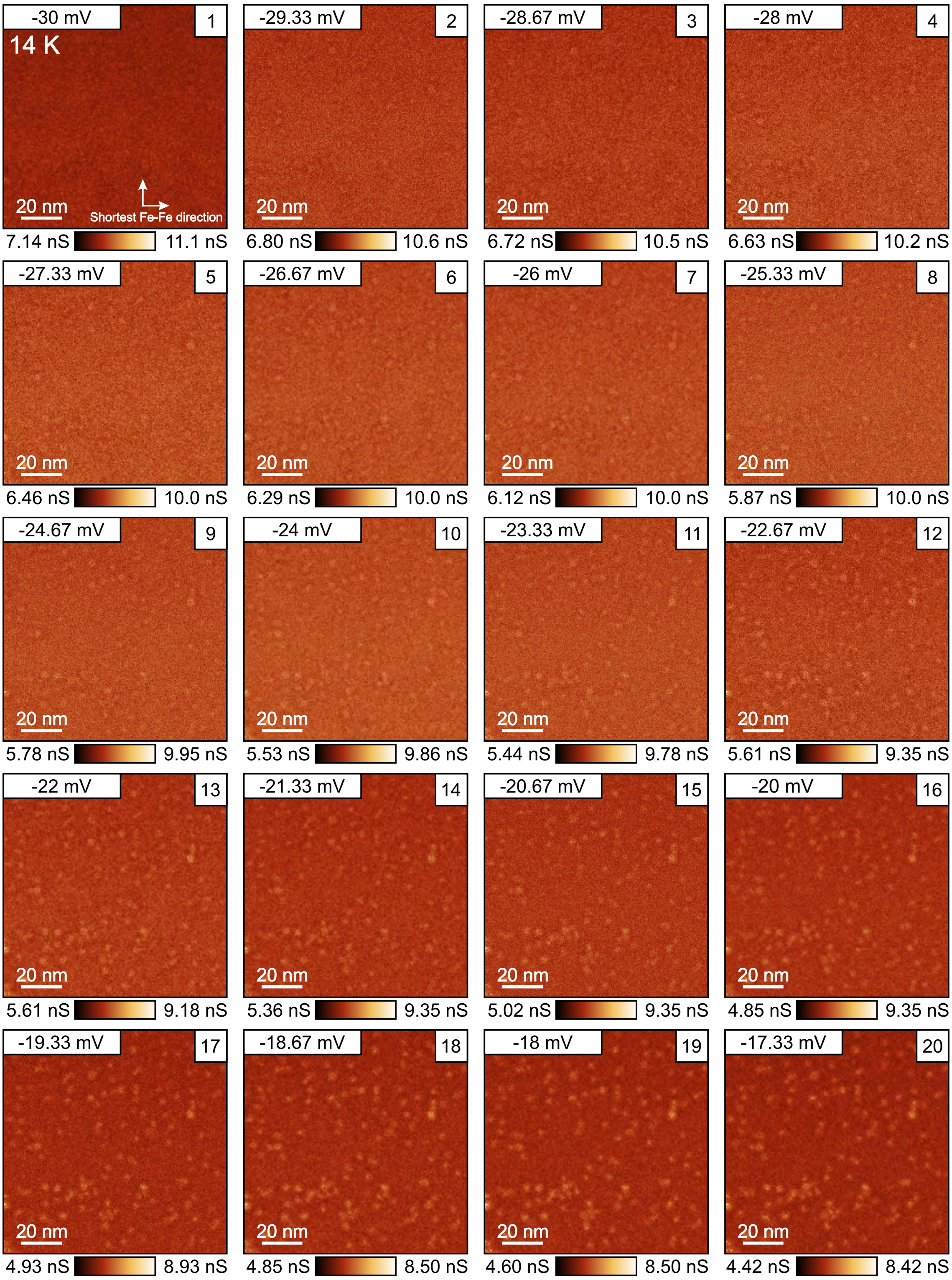

Figure E.12.: The constant energy $\mathrm{d}I/\mathrm{d}V$ slices from spectroscopic map taken at the place of Fig. 6.24(c). The corresponding energies of those images ((1)-(20)) are shown in the left upper corner of each image which are from -30 mV to -17.33 mV. Total size of each image is 110 nm × 110 nm. This is measured at 14 K.

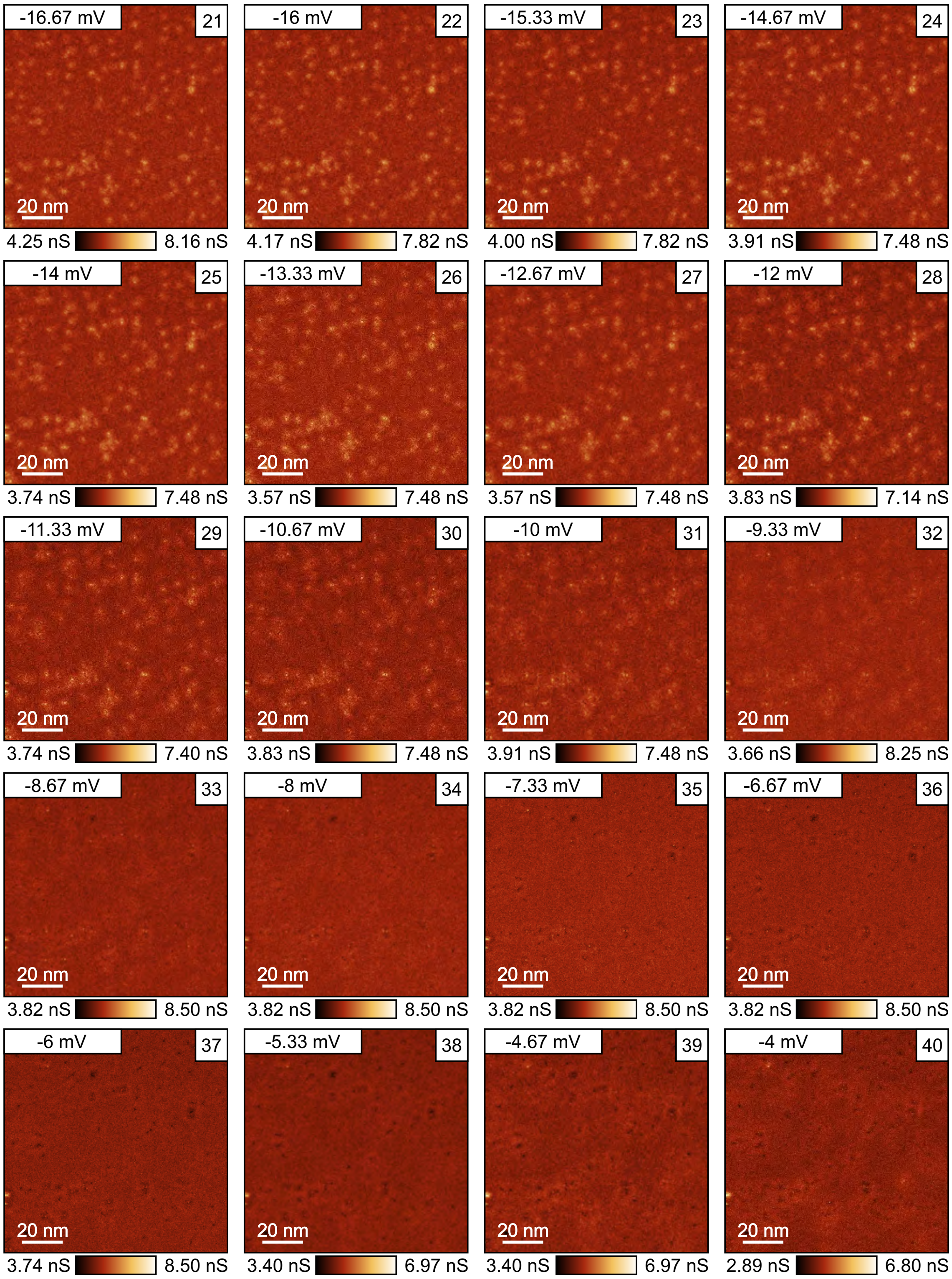

Figure E.13.: The constant energy dI/dV slices from spectroscopic map taken at the place of Fig. 6.24(c). The corresponding energies of those images ((21)-(40)) are shown in the left upper corner of each image which are from -16.67 mV to -4 mV. Total size of each image is 110 nm × 110 nm. This is measured at 14 K.

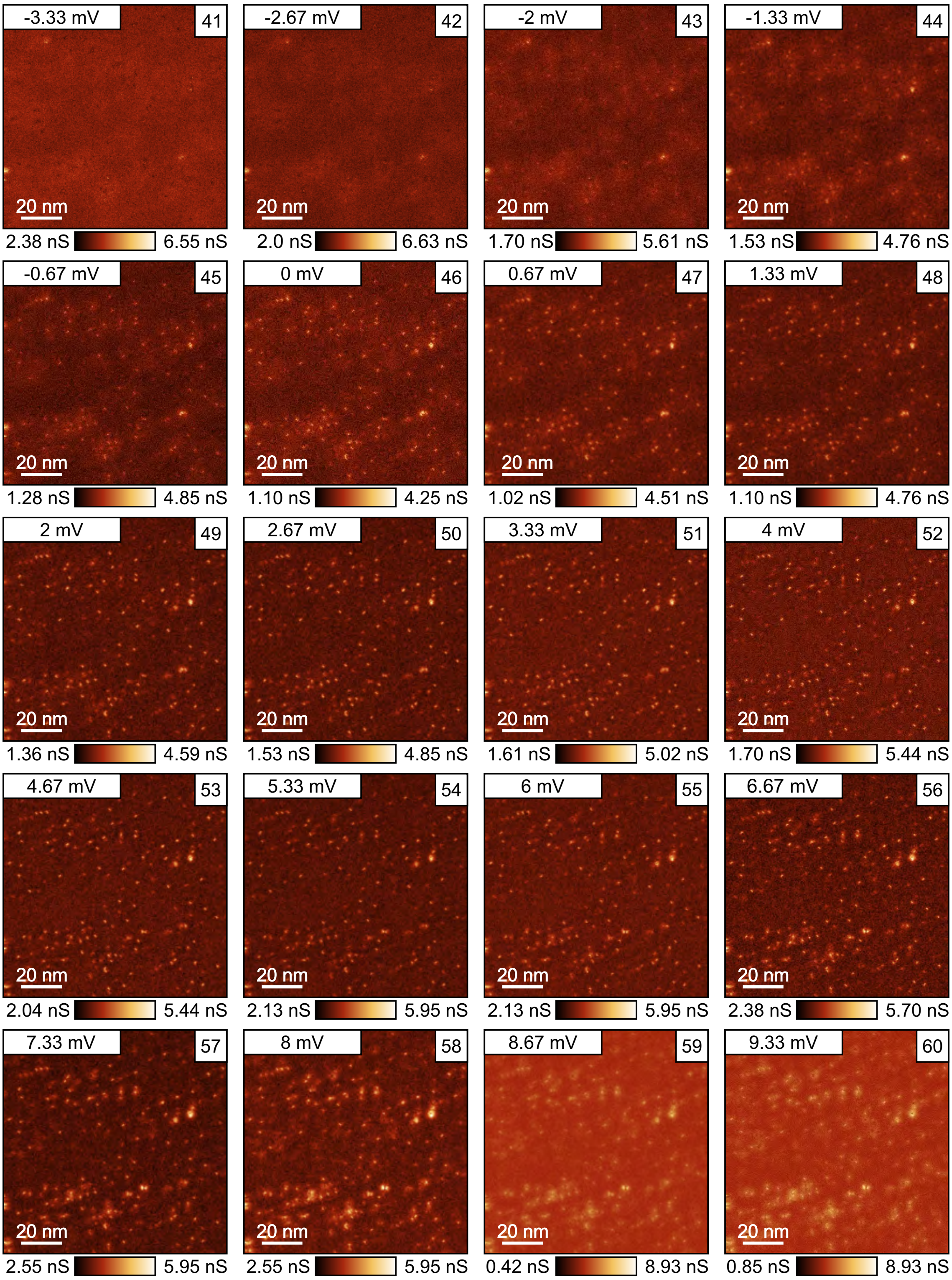

Figure E.14.: The constant energy dI/dV slices from spectroscopic map taken at the place of Fig. 6.24(c). The corresponding energies of those images ((41)-(60)) are shown in the left upper corner of each image which are from -3.33 mV to 9.33 mV. Total size of each image is 110 nm × 110 nm. This is measured at 14 K.

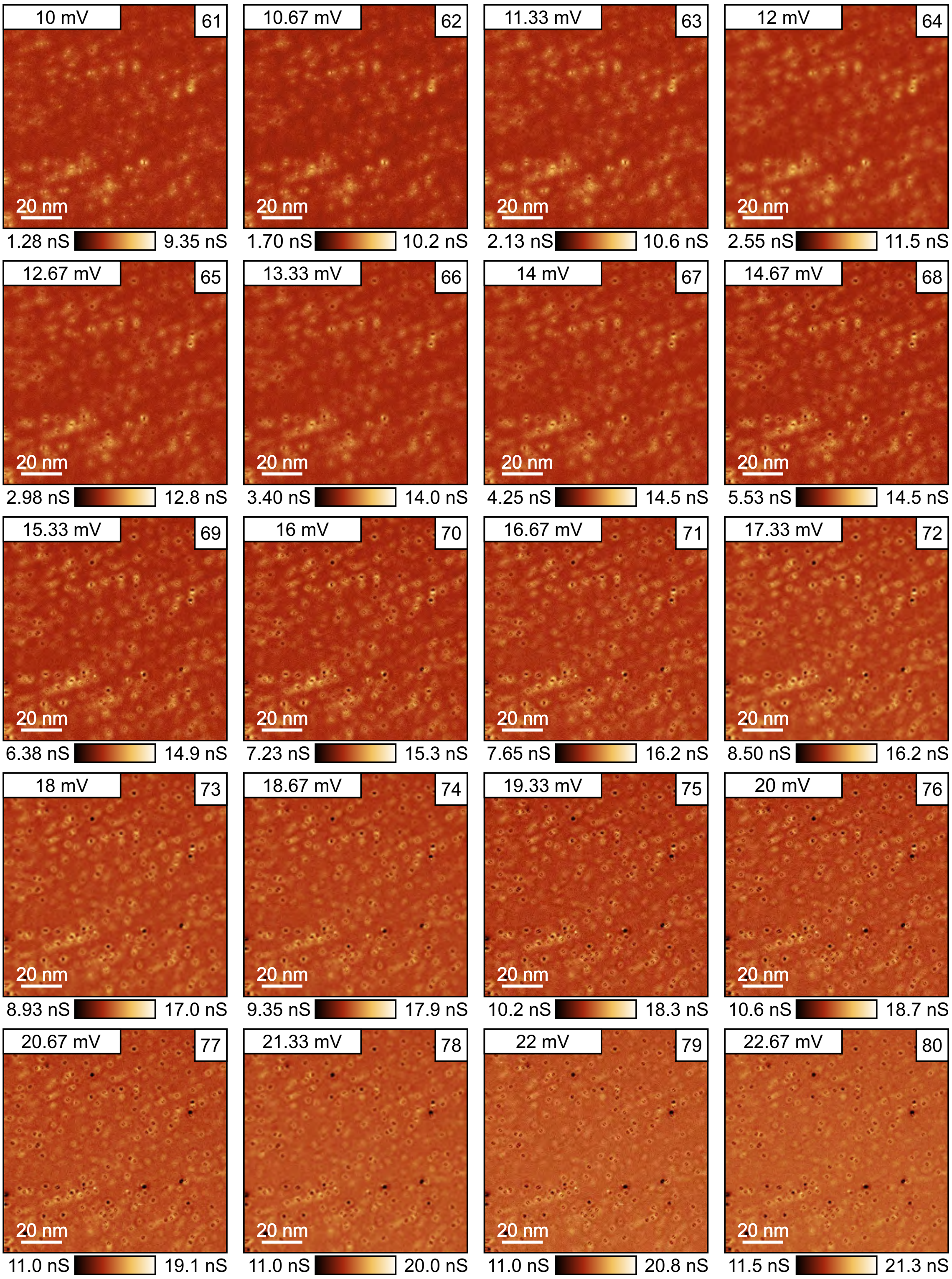

Figure E.15.: The constant energy dI/dV slices from spectroscopic map taken at the place of Fig. 6.24(c). The corresponding energies of those images ((61)-(80)) are shown in the left upper corner of each image which are from 10 mV to 22.67 mV. Total size of each image is 110 nm × 110 nm. This is measured at 14 K.

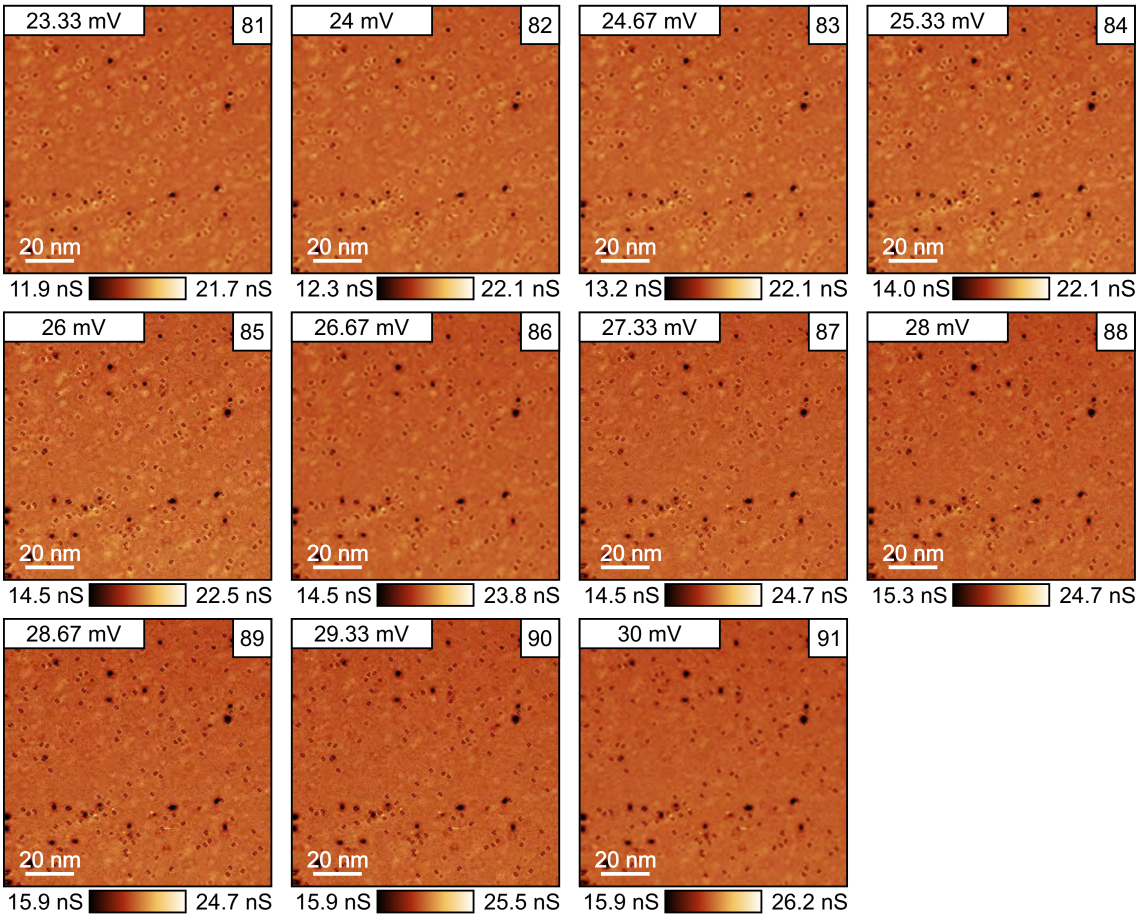

Figure E.16.: The constant energy $\mathrm{d}I/\mathrm{d}V$ slices from spectroscopic map taken at the place of Fig. 6.24(c). The corresponding energies of those images ((81)-(91)) are shown in the left upper corner of each image which are from 23.33 mV to 30 mV. Total size of each image is 110 nm × 110 nm. This is measured at 14 K.

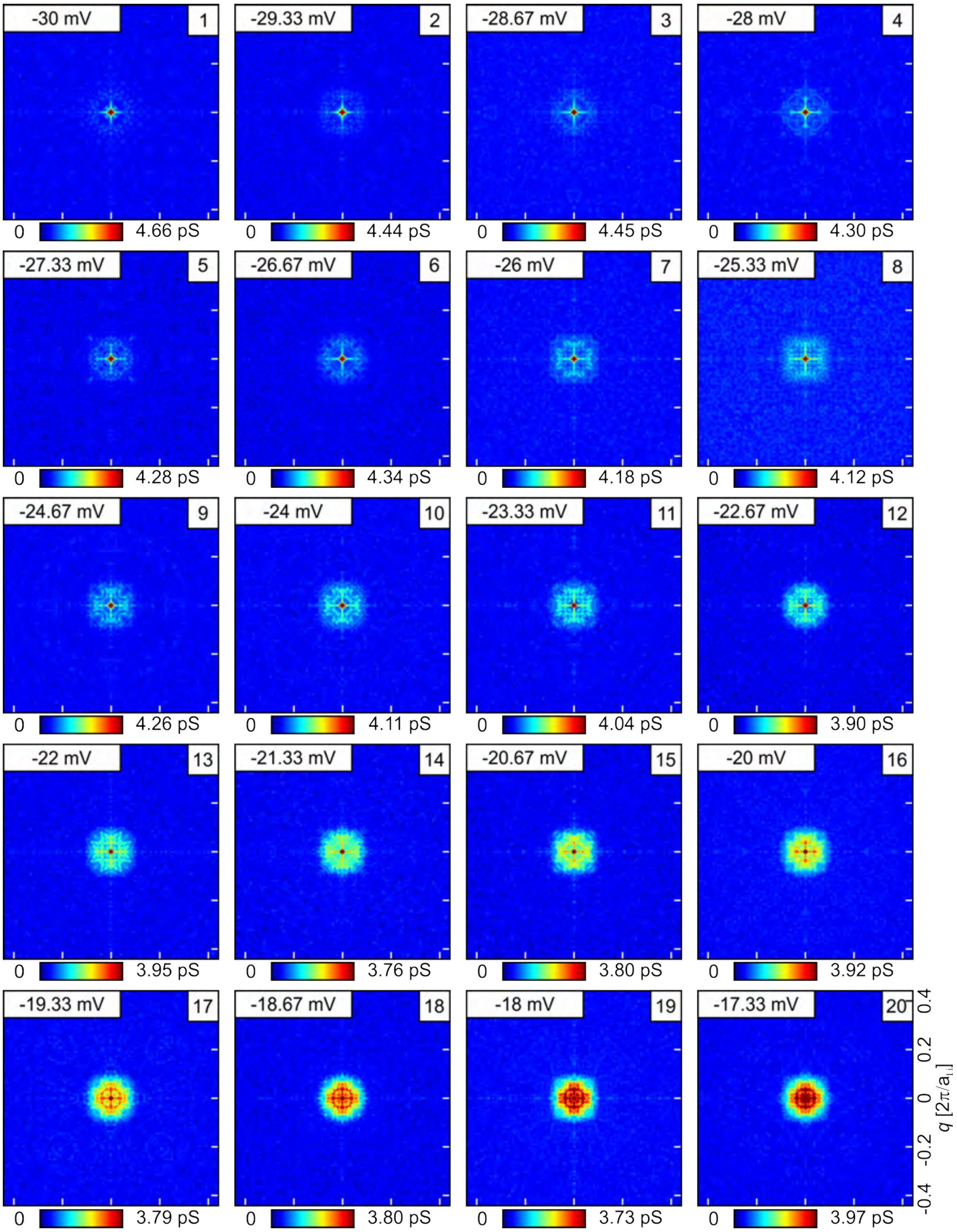

Figure E.17.: The QPI signals related to the constant $\mathrm{d}I/\mathrm{d}V$ energy slices in Fig. E.12. The corresponding energies of those images ((1)-(20)) are shown in the left upper corner of each image which are from -30 mV to -17.33 mV. Total size of each image is $\pm 0.44\times 2\pi/\mathrm{a}_{Li}$. This is measured at 14 K.

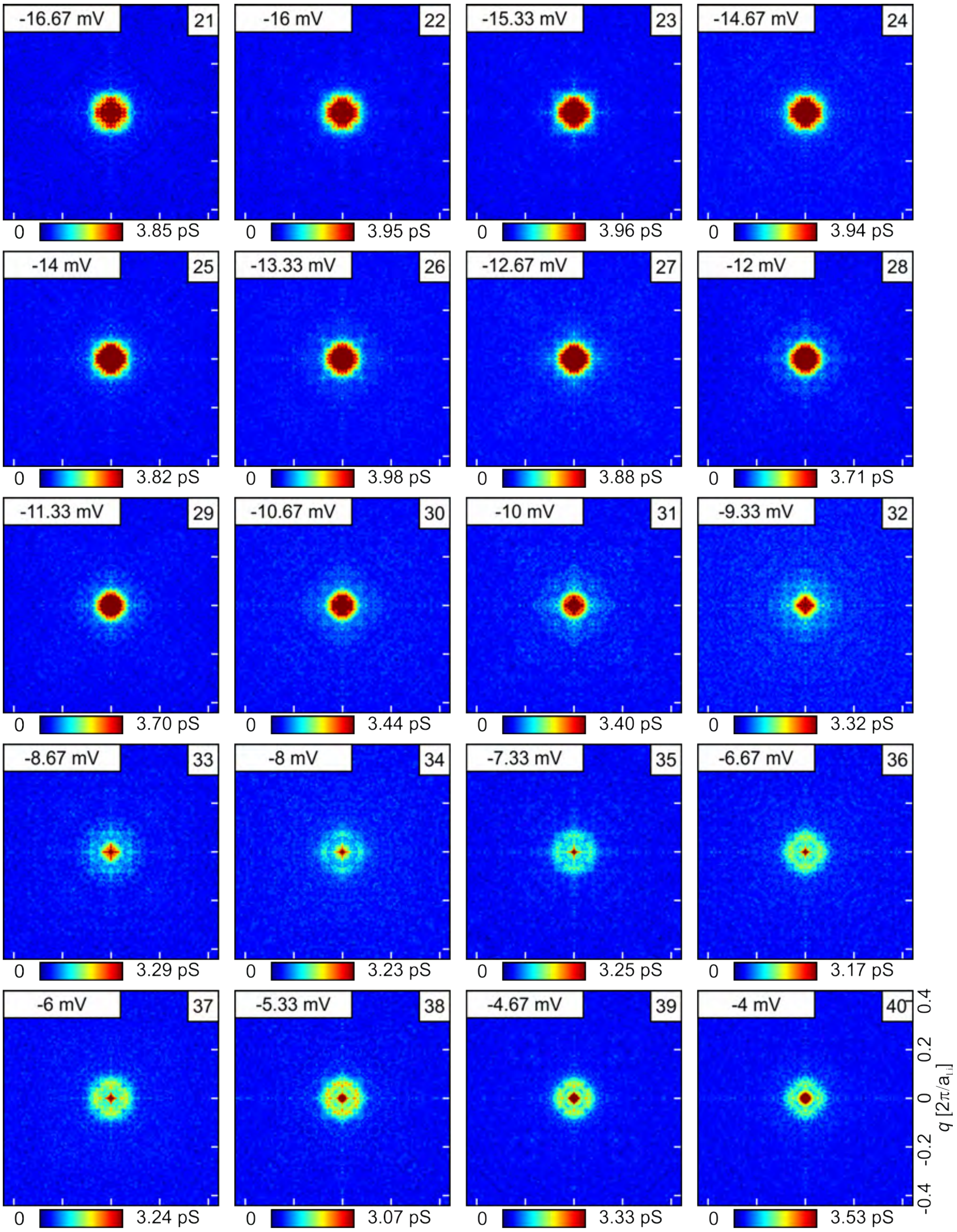

Figure E.18.: The QPI signals related to the constant dI/dV energy slices in Fig. E.13. The corresponding energies of those images ((21)-(40)) are shown in the left upper corner of each image which are from -16.67 mV to -4 mV. Total size of each image is $\pm 0.44 \times 2\pi/\mathrm{a}_{Li}$. This is measured at 14 K.

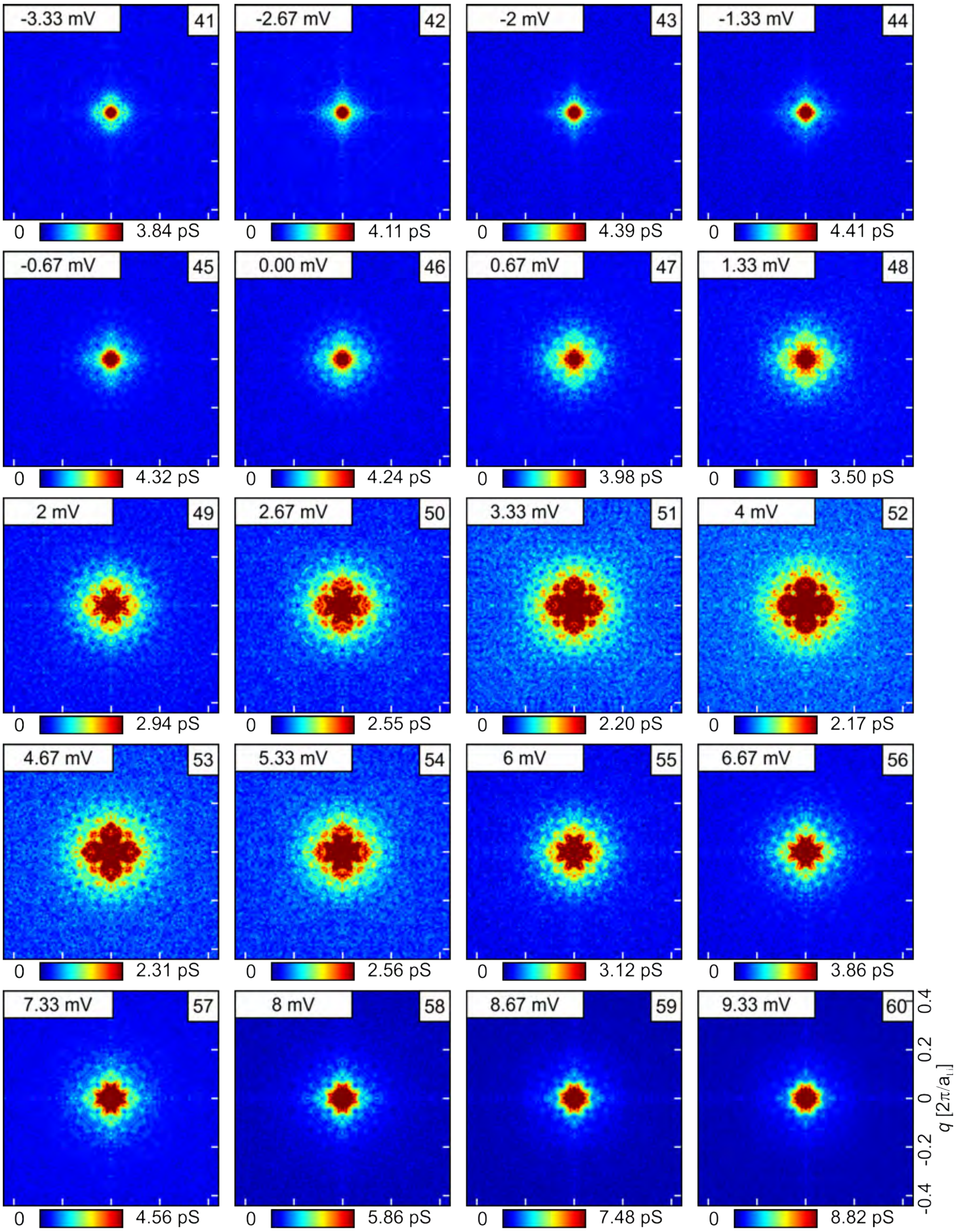

Figure E.19.: The QPI signals related to the constant dI/dV energy slices in Fig. E.14. The corresponding energies of those images ((41)-(60)) are shown in the left upper corner of each image which are from -3.33 mV to 9.33 mV. Total size of each image is $\pm 0.44 \times 2\pi/\mathrm{a}_{Li}$. This is measured at 14 K.

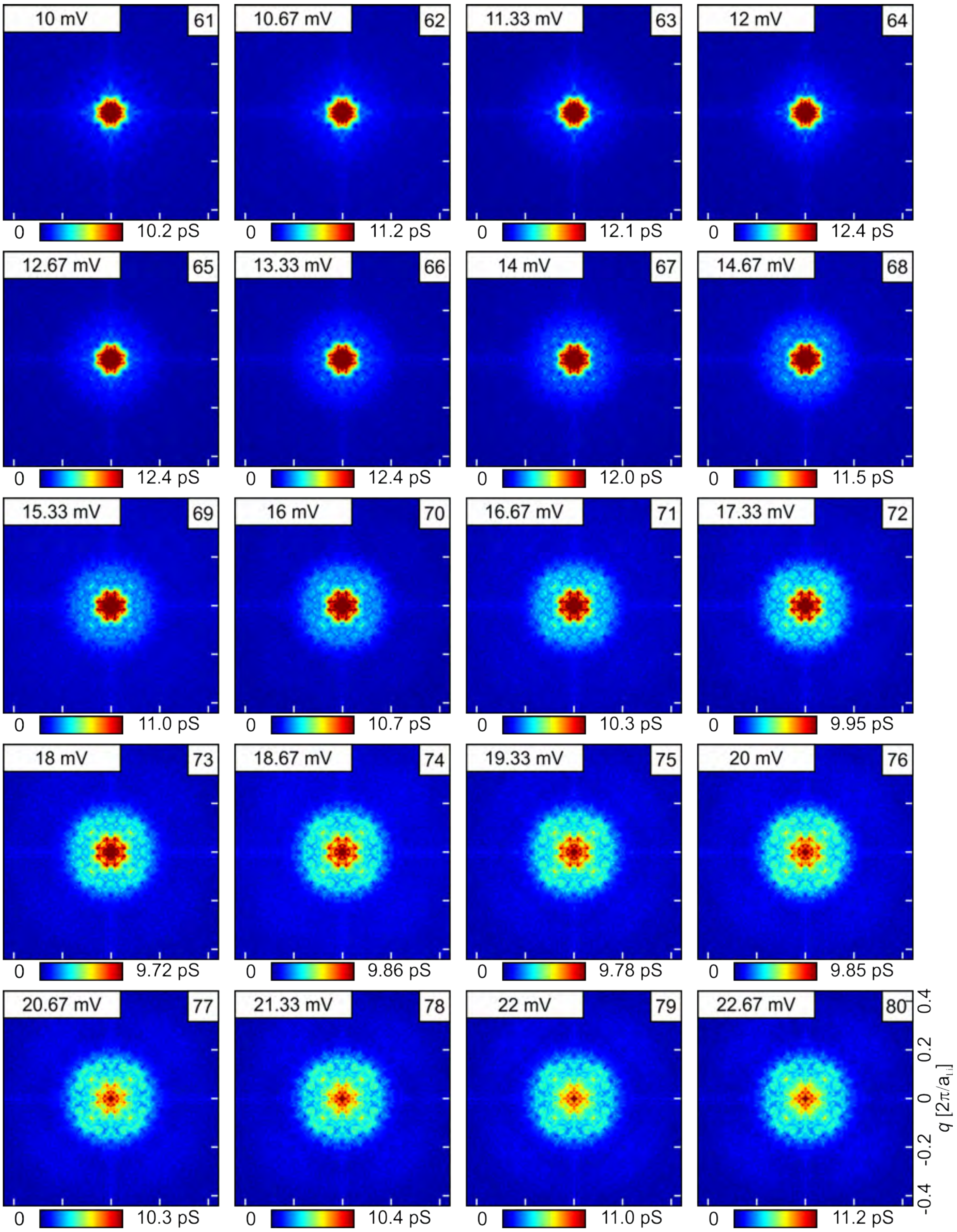

Figure E.20.: The QPI signals related to the constant dI/dV energy slices in Fig. E.15. The corresponding energies of those images ((61)-(80)) are shown in the left upper corner of each image which are from 10 mV to 22.67 mV. Total size of each image is $\pm 0.44 \times 2\pi/\mathrm{a}_{Li}$. This is measured at 14 K.

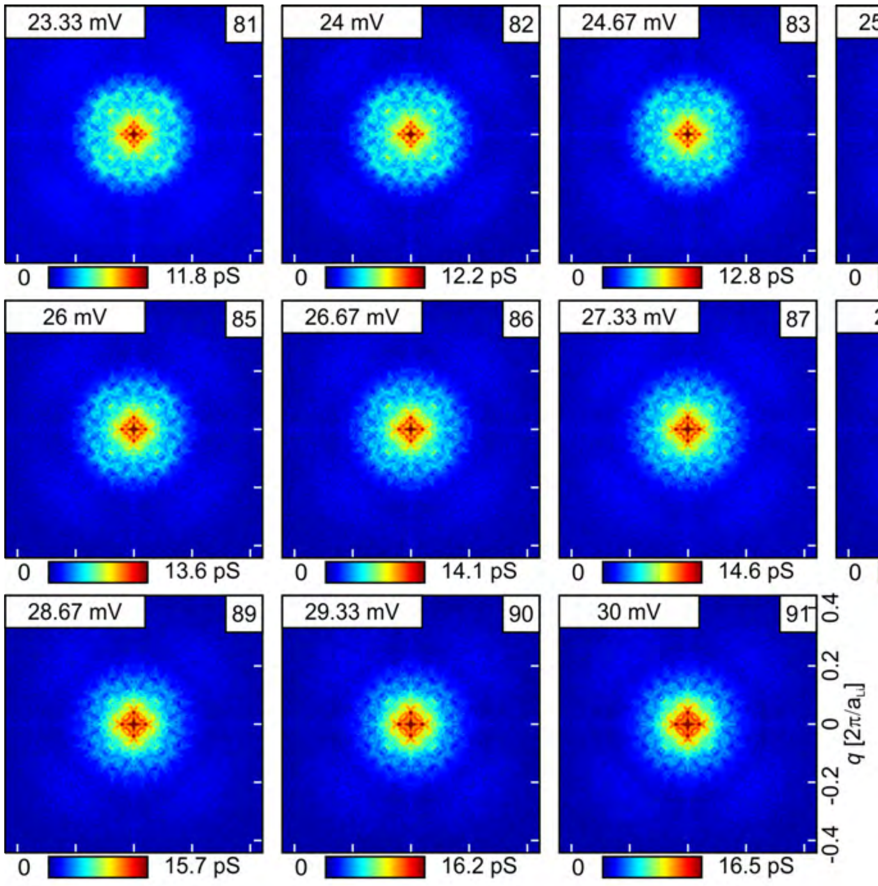

Figure E.21.: The QPI signals related to the constant $\mathrm{d}I/\mathrm{d}V$ energy slices in Fig. E.16. The corresponding energies of those images ((81)-(91)) are shown in the left upper corner of each image which are from 23.33 mV to 30 mV. Total size of each image is $\pm 0.44\times 2\pi/\mathrm{a}_{Li}$. This is measured at 14 K.

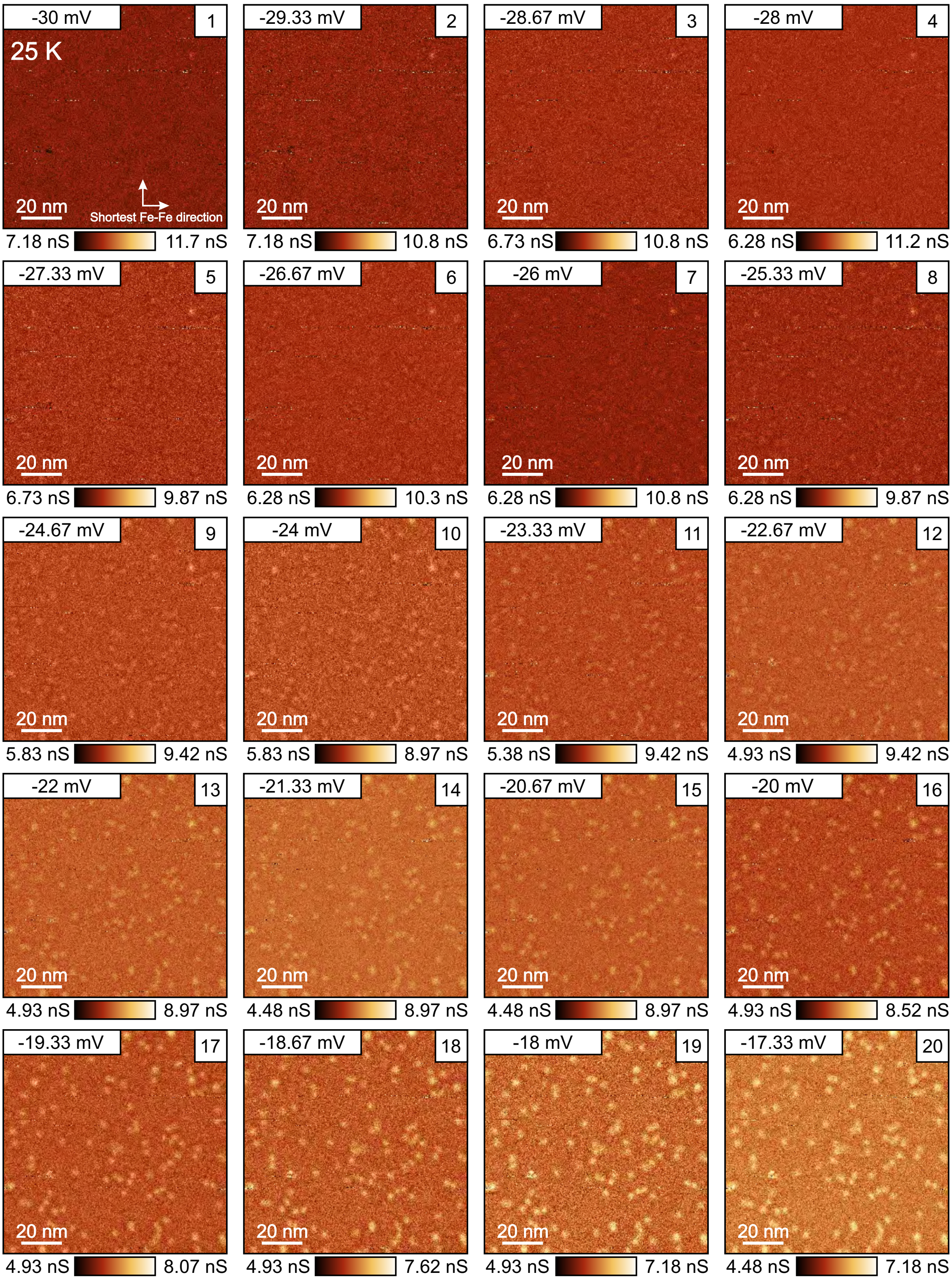

Figure E.22.: The constant energy dI/dV slices from spectroscopic map taken at the place of Fig. 6.24(i). The corresponding energies of those images ((1)-(20)) are shown in the left upper corner of each image which are from -30 mV to -17.33 mV. Total size of each image is 110 nm × 110 nm. This is measured at 25 K.

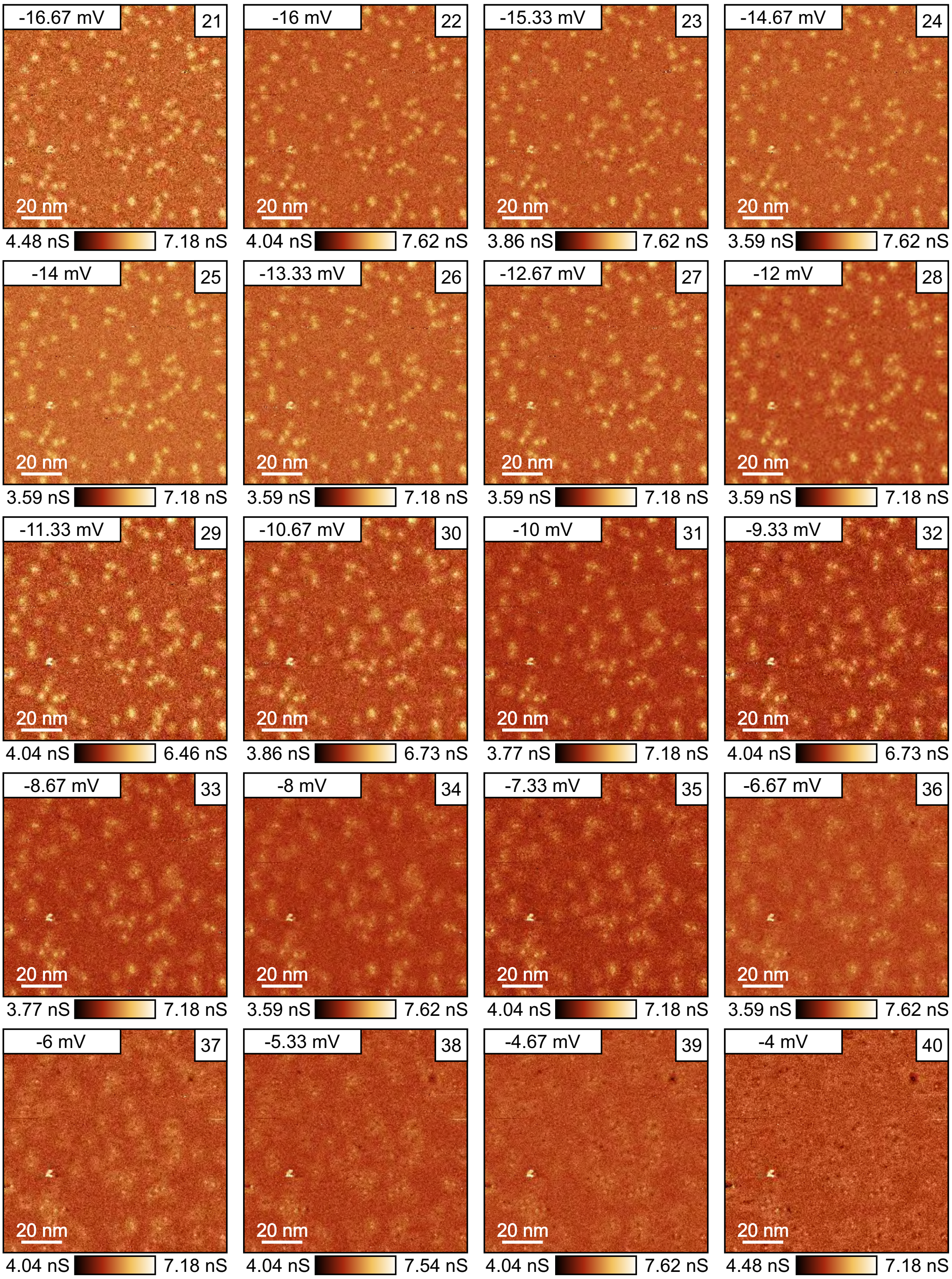

Figure E.23.: The constant energy dI/dV slices from spectroscopic map taken at the place of Fig. 6.24(i). The corresponding energies of those images ((21)-(40)) are shown in the left upper corner of each image which are from -16.67 mV to -4 mV. Total size of each image is 110 nm × 110 nm. This is measured at 25 K.

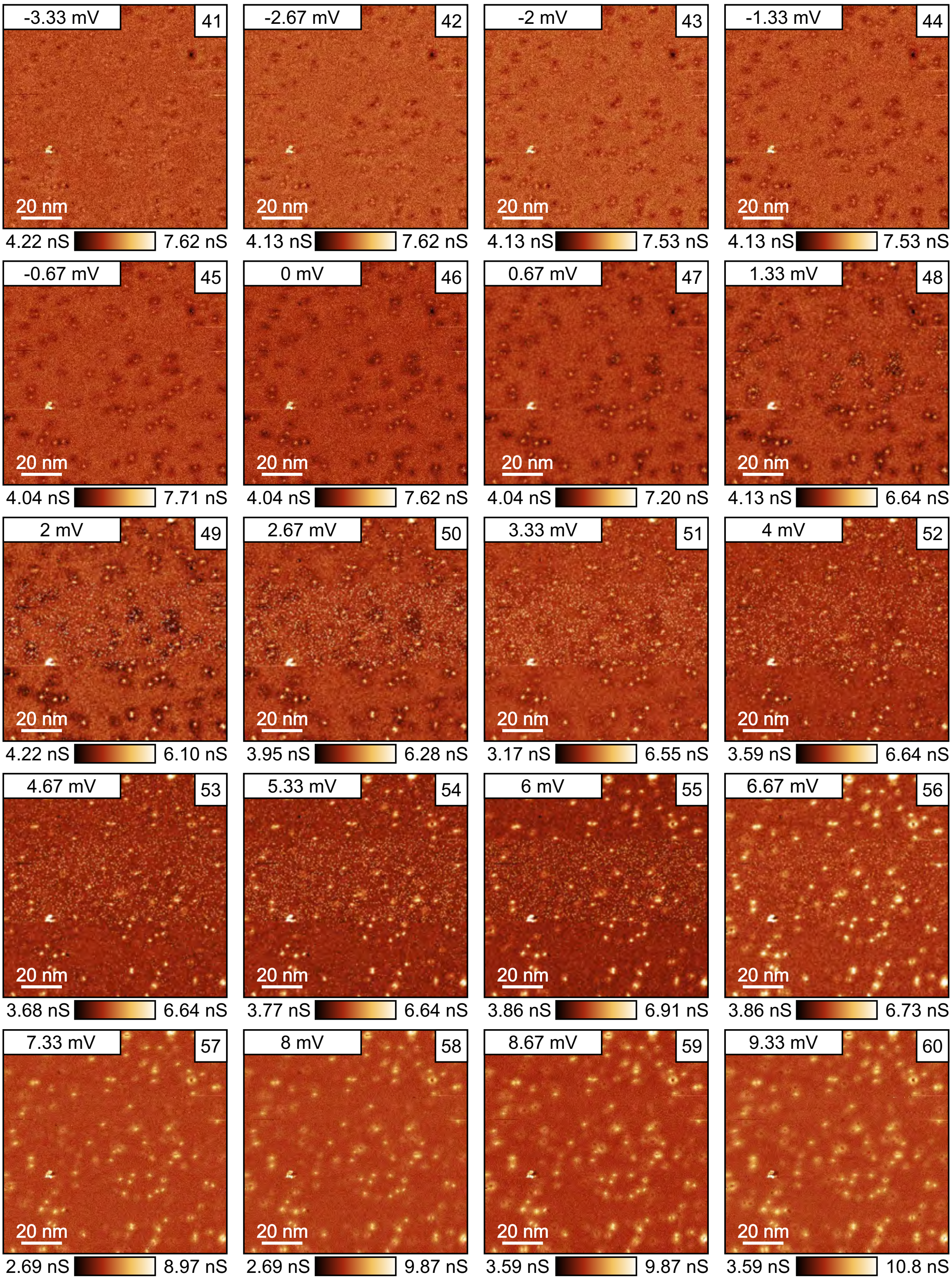

Figure E.24.: The constant energy dI/dV slices from spectroscopic map taken at the place of Fig. 6.24(i). The corresponding energies of those images ((41)-(60)) are shown in the left upper corner of each image which are from -3.33 mV to 9.33 mV. Total size of each image is 110 nm × 110 nm. This is measured at 25 K.

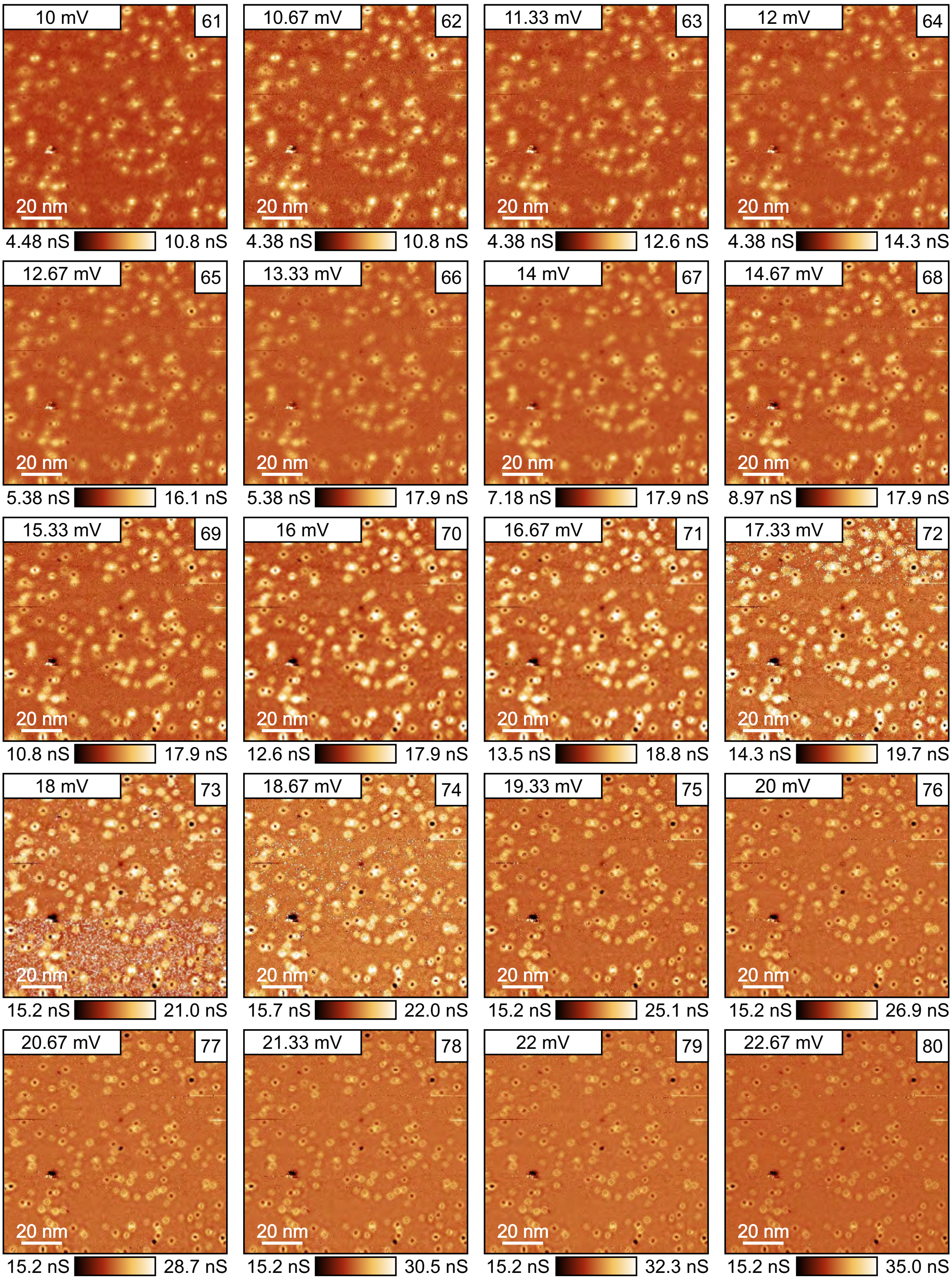

Figure E.25.: The constant energy $\mathrm{d}I/\mathrm{d}V$ slices from spectroscopic map taken at the place of Fig. 6.24(i). The corresponding energies of those images ((61)-(80)) are shown in the left upper corner of each image which are from 10 mV to 22.67 mV. Total size of each image is 110 nm × 110 nm. This is measured at 25 K.

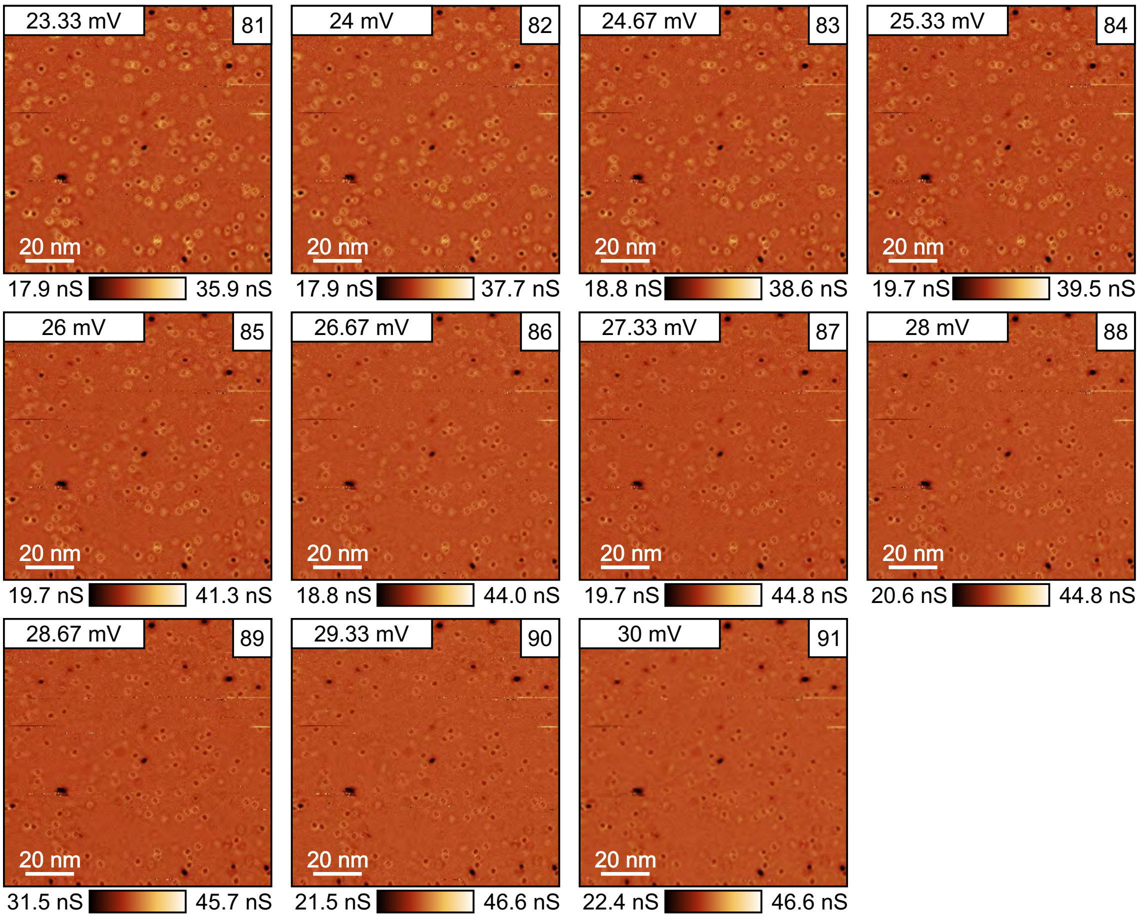

Figure E.26.: The constant energy dI/dV slices from spectroscopic map taken at the place of Fig. 6.24(i). The corresponding energies of those images ((81)-(91)) are shown in the left upper corner of each image which are from 23.33 mV to 30 mV. Total size of each image is 110 nm × 110 nm. This is measured at 25 K.

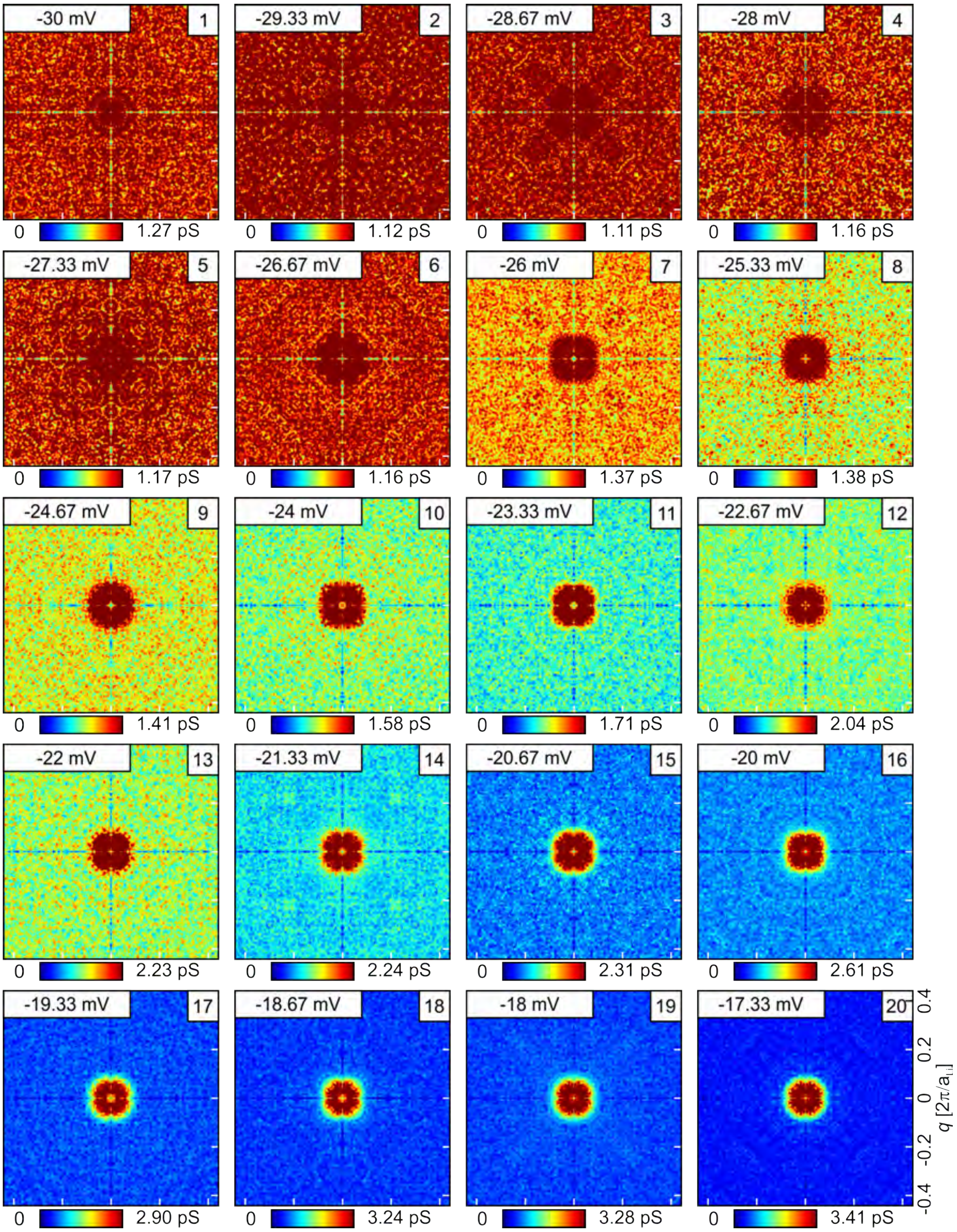

Figure E.27.: The QPI signals related to the constant dI/dV energy slices in Fig. E.22. The corresponding energies of those images ((1)-(20)) are shown in the left upper corner of each image which are from -30 mV to -17.33 mV. Total size of each image is $\pm 0.44\times 2\pi/\mathrm{a}_{Li}$. This is measured at 25 K.

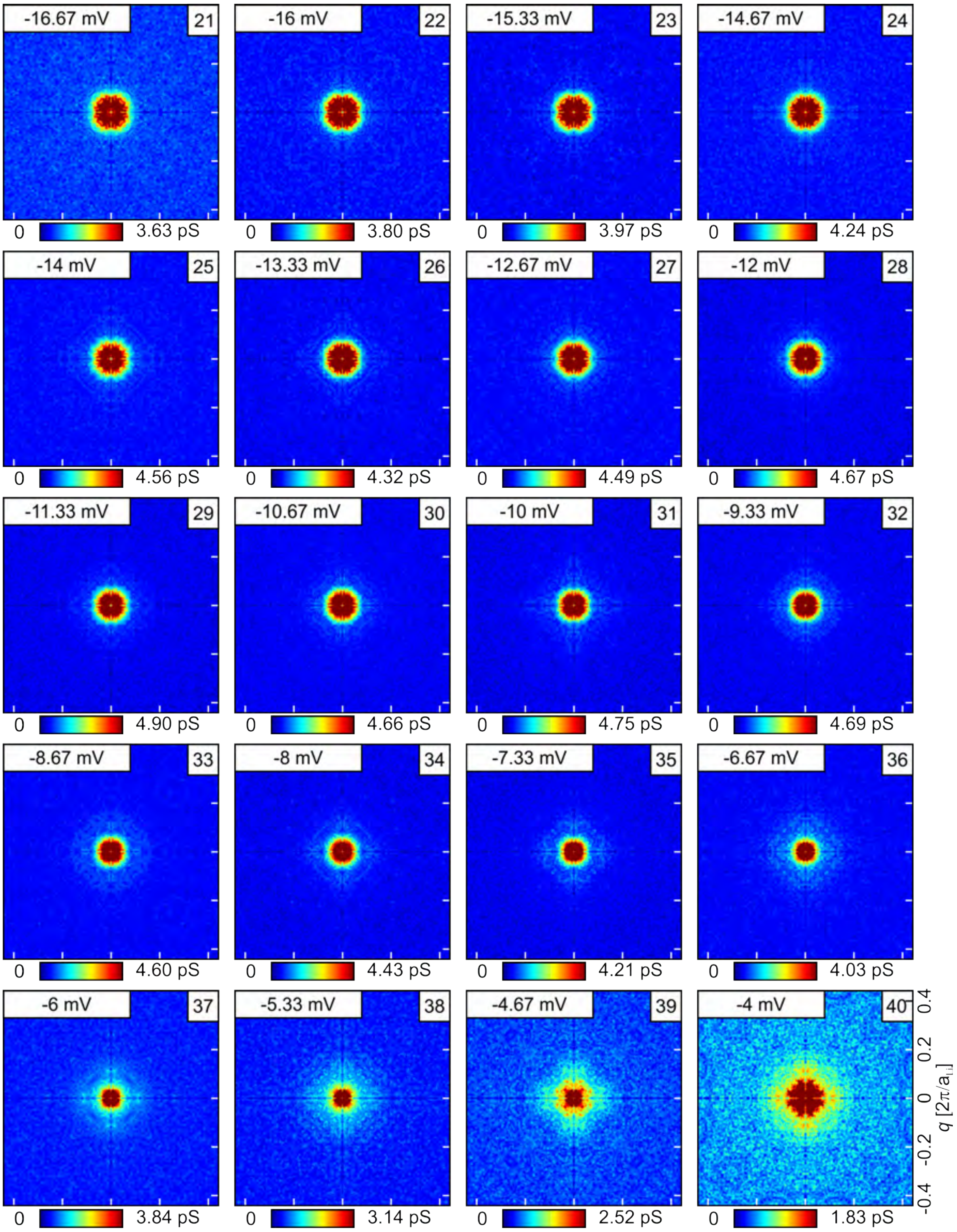

Figure E.28.: The QPI signals related to the constant dI/dV energy slices in Fig. E.23. The corresponding energies of those images ((21)-(40)) are shown in the left upper corner of each image which are from -16.67 mV to -4 mV. Total size of each image is $\pm 0.44\times 2\pi/\mathrm{a}_{Li}$. This is measured at 25 K.

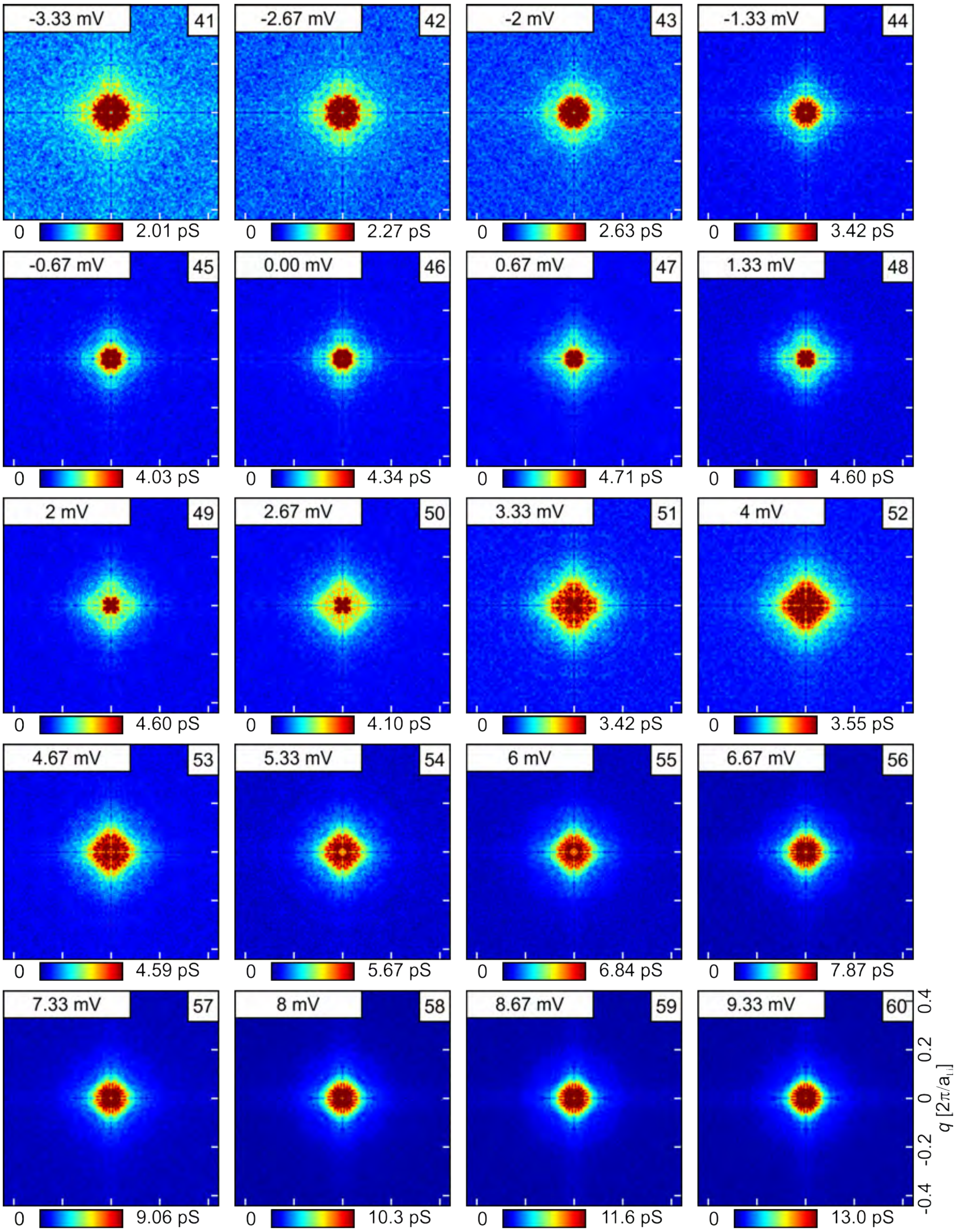

Figure E.29.: The QPI signals related to the constant dI/dV energy slices in Fig. E.24. The corresponding energies of those images ((41)-(60)) are shown in the left upper corner of each image which are from -3.33 mV to 9.33 mV. Total size of each image is $\pm 0.44 \times 2\pi/\mathrm{a}_{Li}$. This is measured at 25 K.

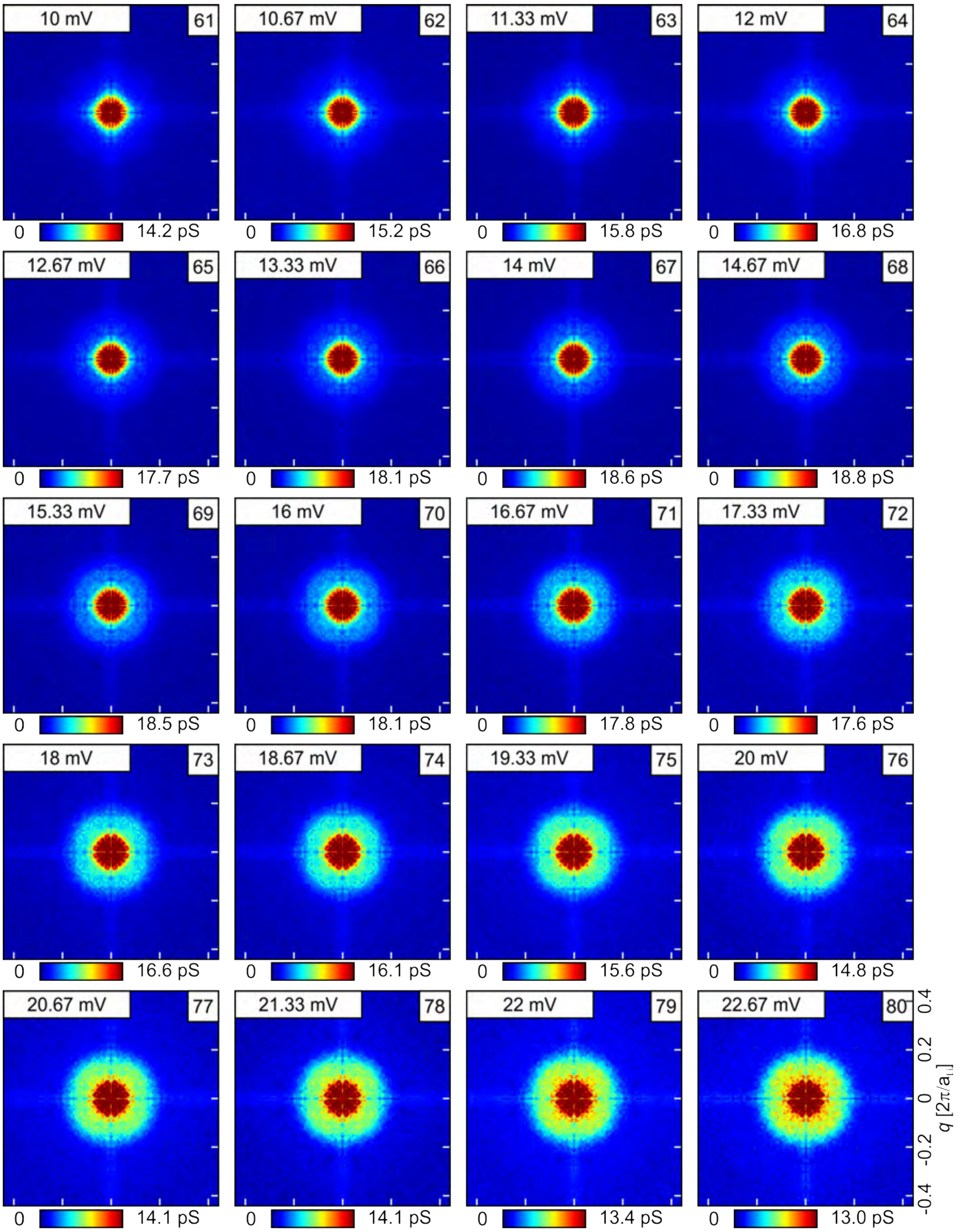

Figure E.30.: The QPI signals related to the constant dI/dV energy slices in Fig. E.25. The corresponding energies of those images ((61)-(80)) are shown in the left upper corner of each image which are from 10 mV to 22.67 mV. Total size of each image is $\pm 0.44\times 2\pi/\mathrm{a}_{Li}$. This is measured at 25 K.

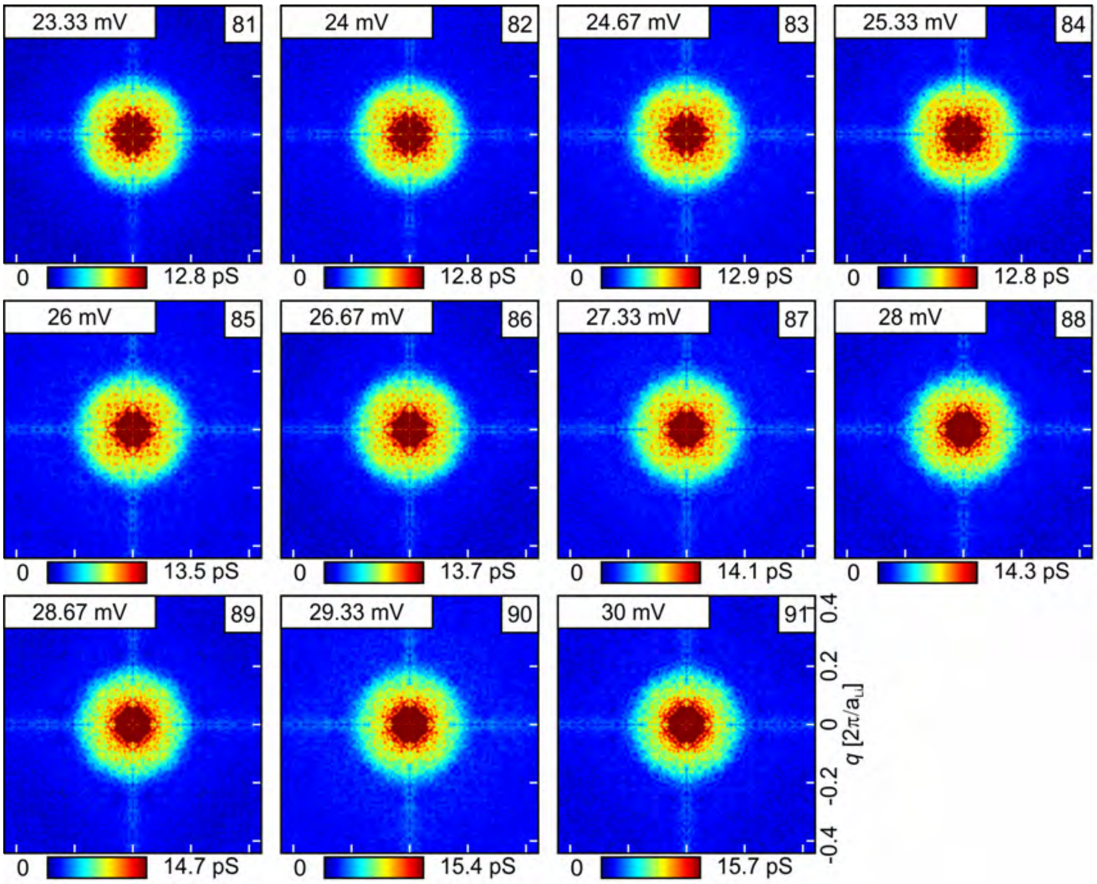

Figure E.31.: The QPI signals related to the constant dI/dV energy slices in Fig. E.26. The corresponding energies of those images ((81)-(91)) are shown in the left upper corner of each image which are from 23.33 mV to 30 mV. Total size of each image is $\pm 0.44 \times 2\pi/\mathrm{a}_{Li}$. This is measured at 25 K.

E.1. The procedure of extracting the intraband scattering vectors

Here I will discuss the process of data treatment to extract the intraband scattering vectors from QPI data measured at 6.7 K (superconducting state) and 25 K (normal state). The waterfall representation of all the line cuts along Fe-Fe high symmetry direction are shown in Fig. 6.29(a). The all line cuts between -24.67 mV and -9.33 mV are fitted using Gaussian function after subtracting the Gaussian background. Such data treatment for three selected energies at -24.67 mV, -14 mV and -9.33 mV is shown in Fig. E.32. The line cuts at 25 K are shown in Fig. E.33. To extract the observed scattering between -24.67 mV and -4.67 mV, a Gaussian fit to the raw data is performed. Such Gaussian fit to the three selective energies at -24.67 mV, -14 mV and -4.67 mV are shown in Fig. E.34.

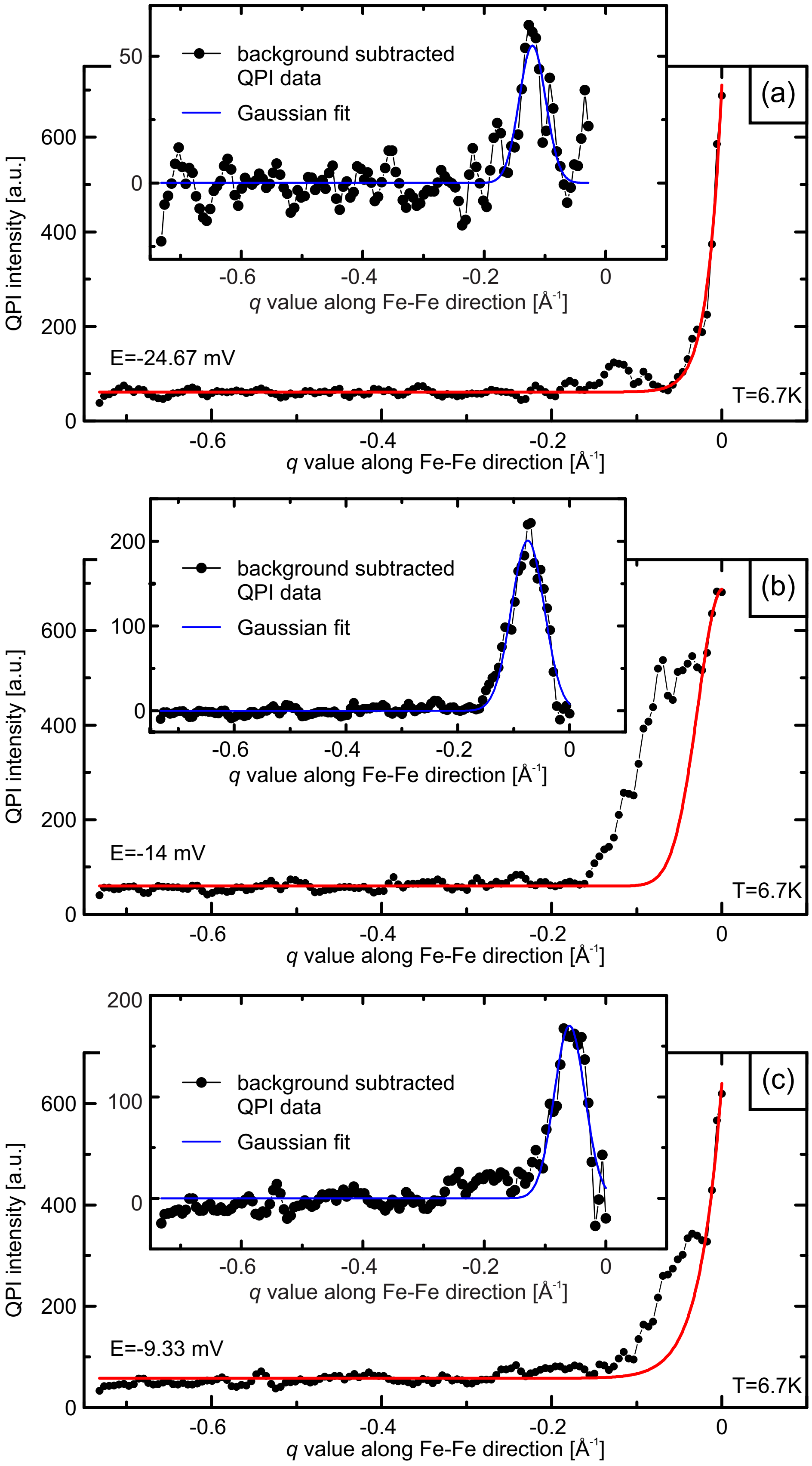

Figure E.32.: Three representative data points at -24.67 mV (a), -14 mV (b) and -9.33 mV (c) where after subtracting the Gaussian background, a Gaussian fit to the data is executed.

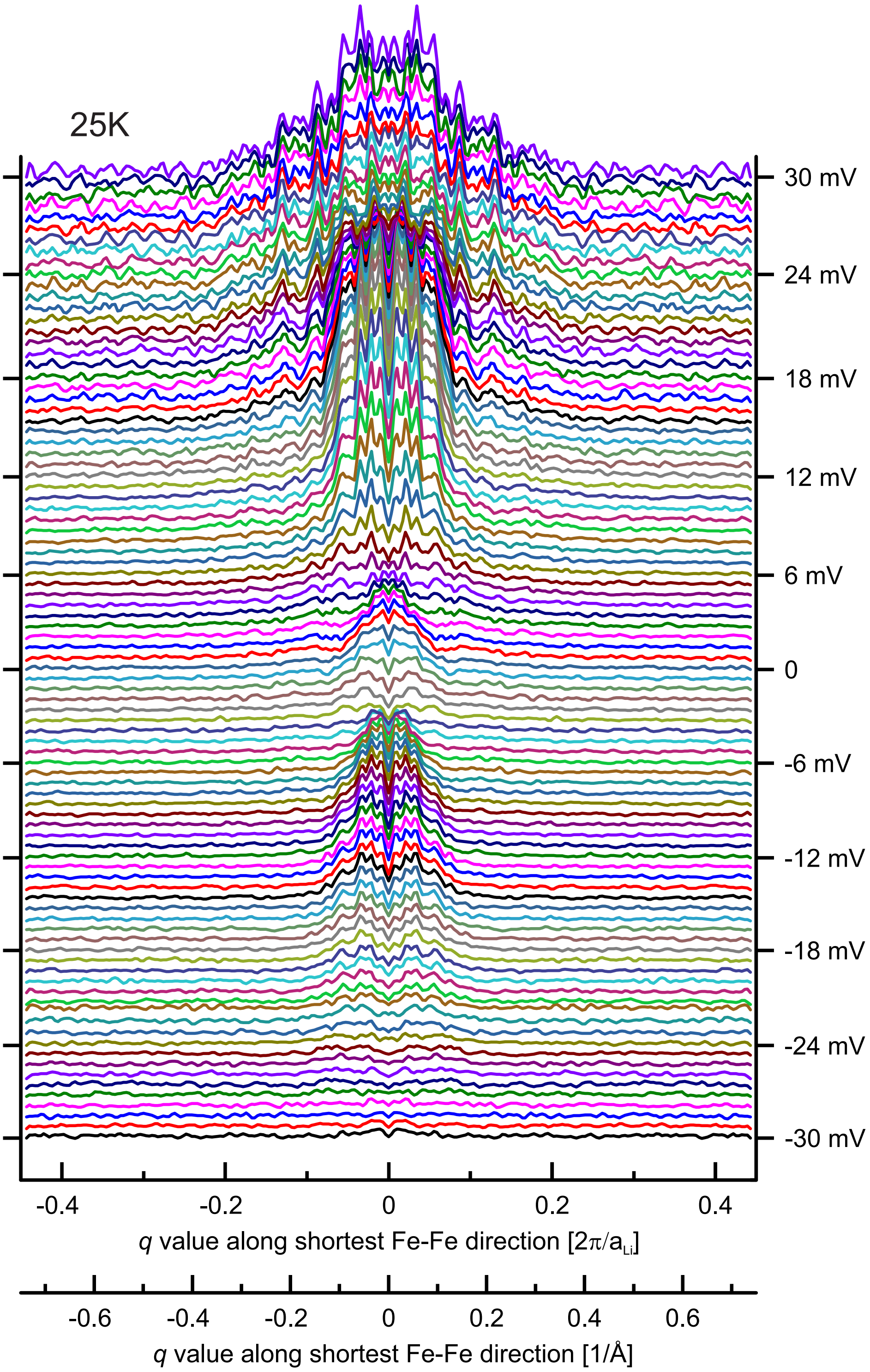

Figure E.33.: The line cuts along Fe-Fe direction for energy range between -30 mV to 30 mV at 25 K.

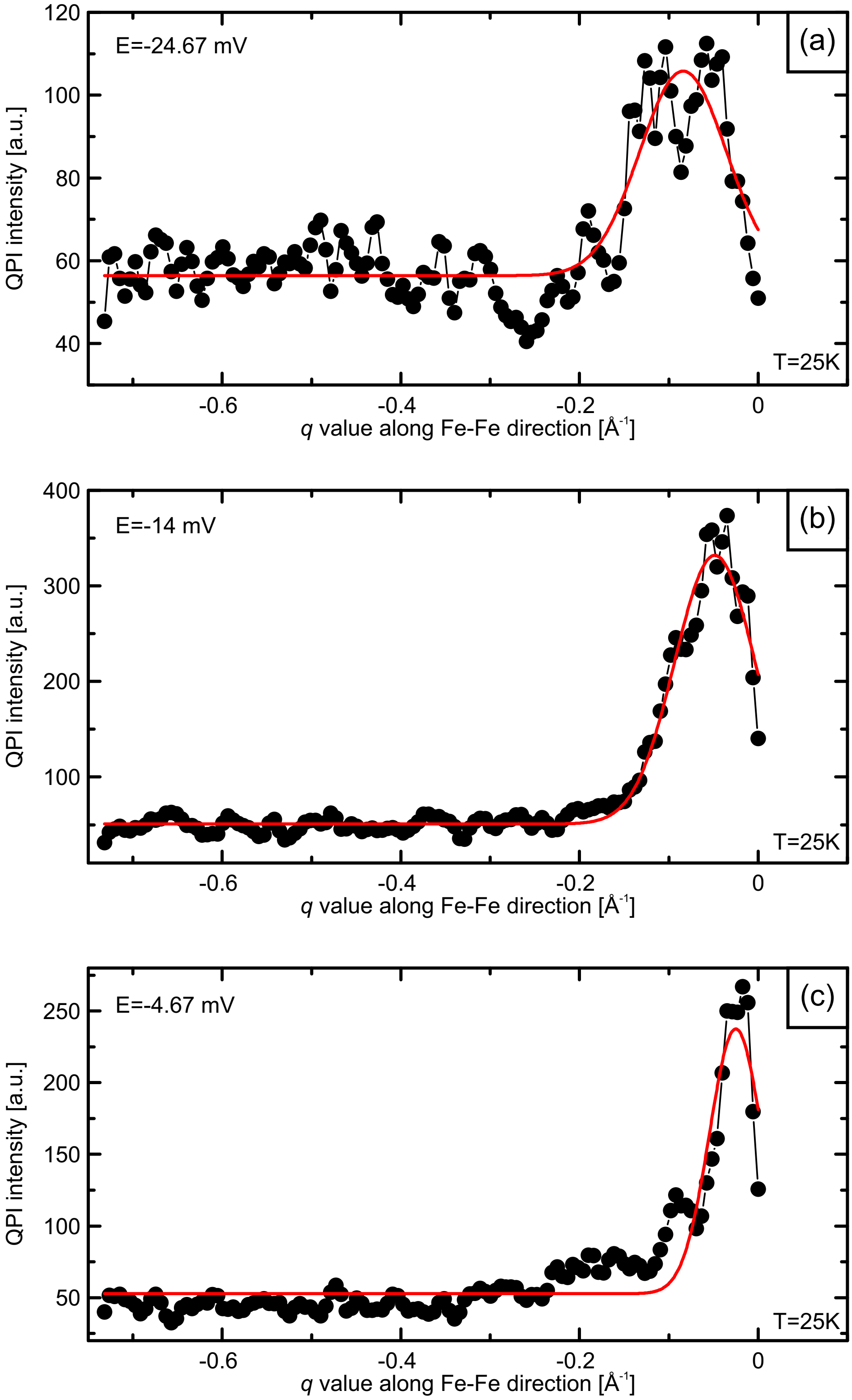

Figure E.34.: Three representative data points at -24.67 mV (a), -14 mV (b) and -9.33 mV (c) where a Gaussian fit to the raw data is executed.

F. Additional data of QPI measurements on off-stoichiometric LiFeAs

Large area topography images at three different temperatures of 7 K, 6 K and 5 K are shown on Fig. F.1. The number of donut defects appeared on the surface are counted and mentioned in each image. The defects concentration of around 0.9±0.1% is consistent for three different temperatures on three different places over the surface. The intraband scattering of the γ and α_2 bands is compared and discussed in Fig. F.2. The k_z dependency of those γ and α_2 bands are shown in Fig. F.3. The comparison of the tight binding model for zero spin-orbit coupling with QPI scattering vectors are discussed in Fig. F.4 and Fig. F.5. A full spectroscopic maps at 5 K with all the energy slices and there corresponding QPI signal are shown below. The first set of the QPI data are shown within the full Brillouin zone where the second set of QPI data are taken in a large area in real space which is comparable to the size of $\pm$ 0.44 $\times$ $(2\pi/\mathrm{a}_{Li})$.

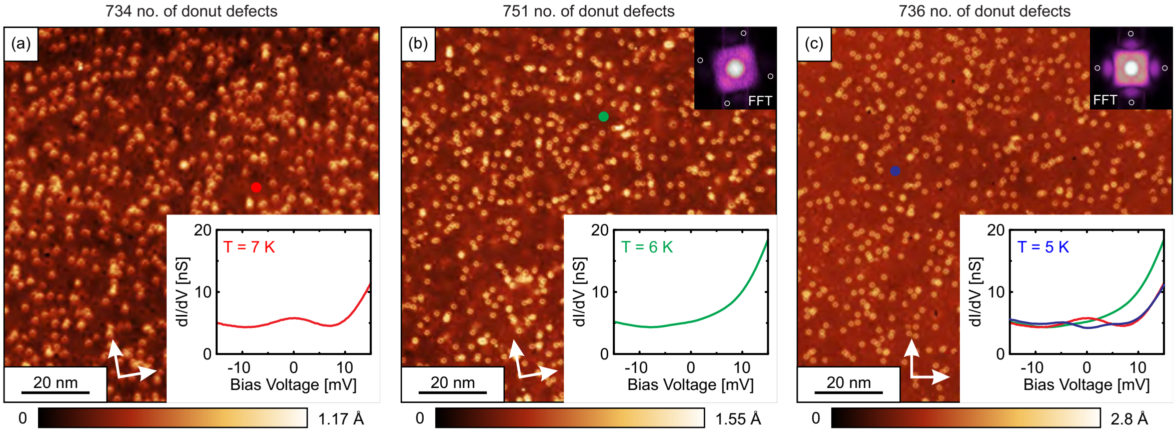

Figure F.1.: The representative topography on off-stoichiometric LiFeAs at 7 K, 6 K and 5 K. The spectrum at clean surface for each topography is shown at the inset of each image. The measurement conditions are: (a) $I_T = 0.3$ nA, $V_{bias} =$ -35 mV with 512 pixels × 512 pixels resolution; (b) $I_T = 0.6$ nA, $V_{bias} =$ -50 mV with 512 pixels × 512 pixels resolution; and (c) $I_T = 0.3$ nA, $V_{bias} =$ -50 mV with 2048 pixels × 2048 pixels resolution. The white arrows are indicating the Li-Li lattice direction.

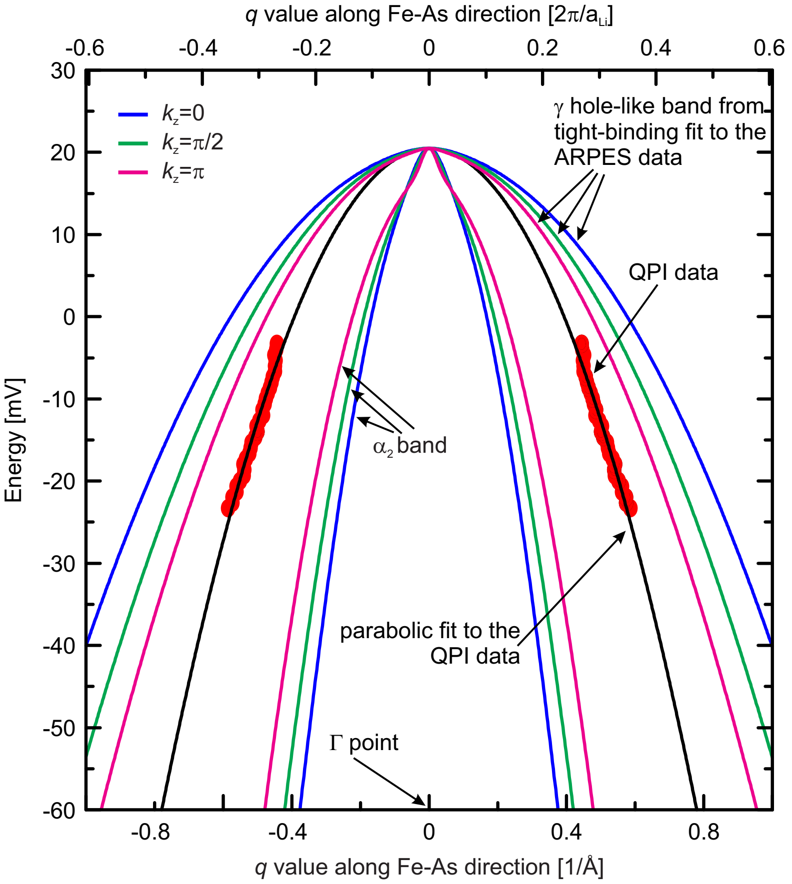

Figure F.2.: The α_2 bands and γ band are plotted with QPI data to compare for intraband scattering. The top of all bands are shifted to 20.44214 mV and the momentum values for all the bands are doubled to compare easily with QPI data. The intraband scattering related to either α_2 band and γ band cannot be related to the QPI data. The k_z dependency of both these bands are also plotted. The used spin-orbit coupling was 10.5 mV.

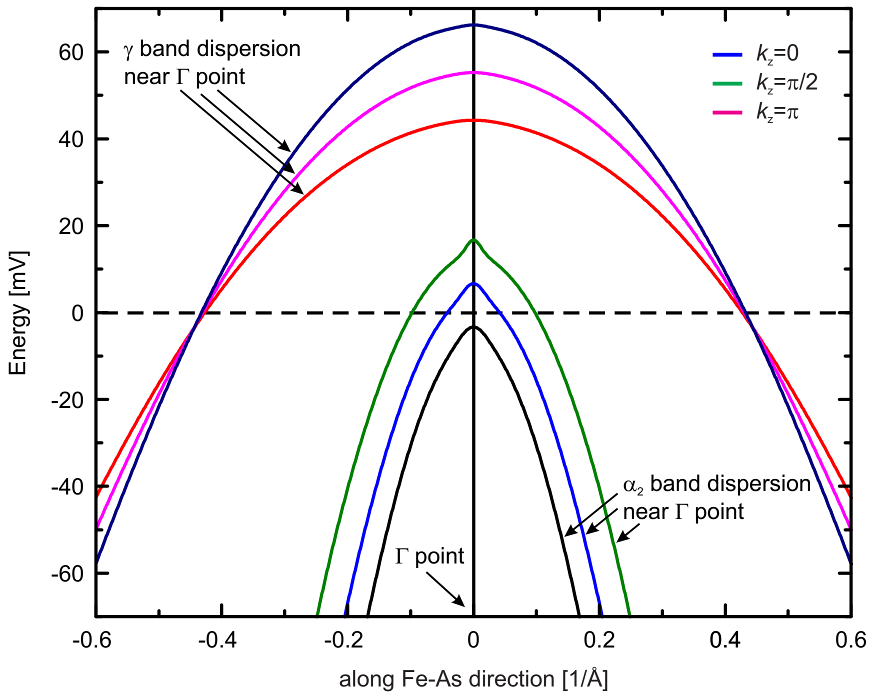

Figure F.3.: The α_2 bands and γ bands are plotted with their real dispersive behavior for three selected k_z values. The used spin-orbit coupling was 10.5 mV.

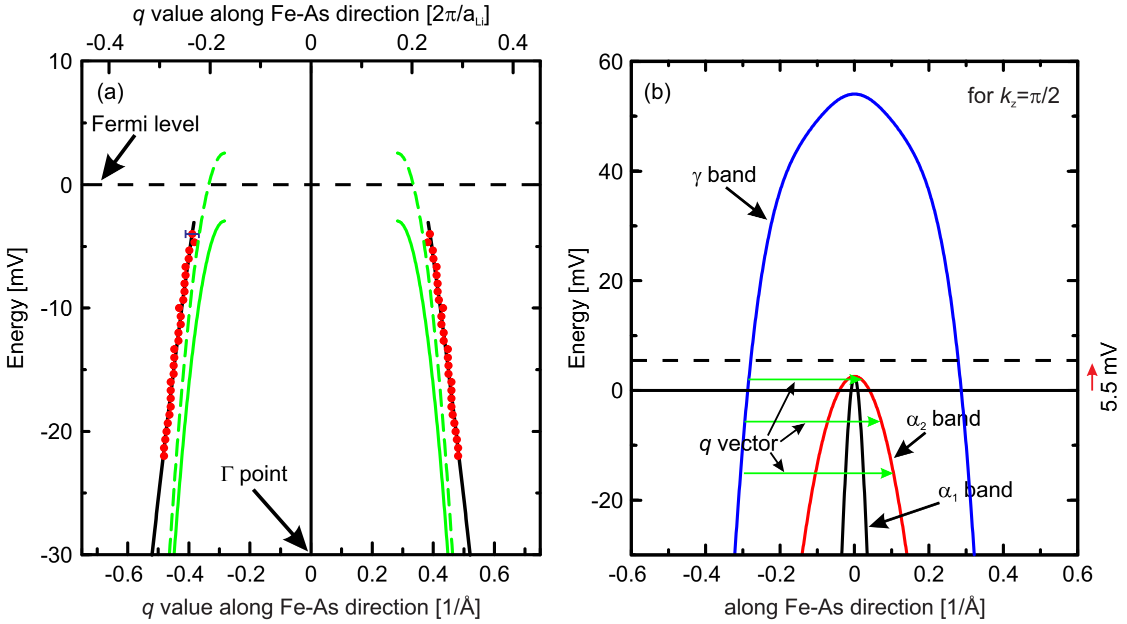

Figure F.4.: The similar analysis is done like Fig. 6.42 for zero spin-orbit coupling along Fe-As direction. The Fermi level is required to shift 5.5 mV in this case but still the interband scattering does not describe well the QPI data.

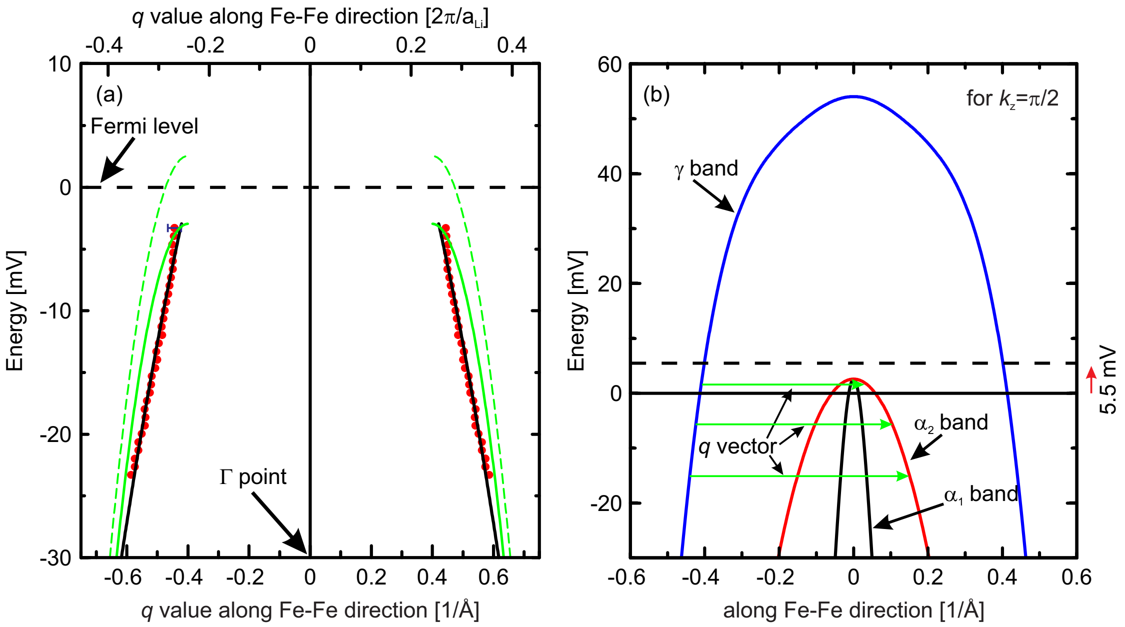

Figure F.5.: The similar interband scattering is compared with QPI data for zero spin-orbit coupling along Fe-Fe direction. The Fermi level is shifted around 5.5 mV but still it does not provide better match with QPI data like Fig 6.43.

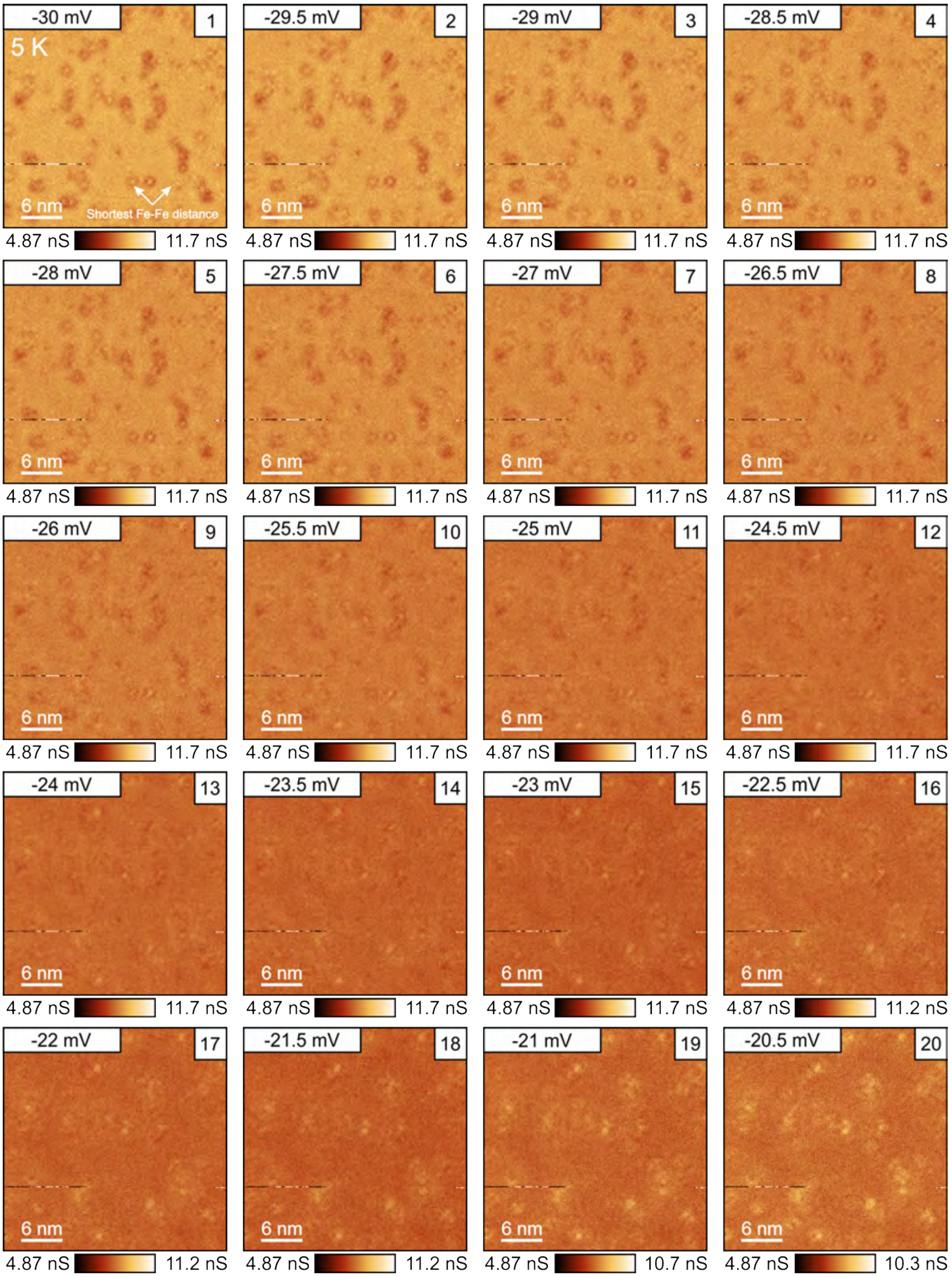

Figure F.6.: The constant energy $\mathrm{d}I/\mathrm{d}V$ slices from spectroscopic map taken at the place of Fig. 6.37(a). The corresponding energies of those images ((1)-(20)) are shown in the left upper corner of each image which are from -30 mV to -20.5 mV. Total size of each image is 32.5 nm × 32.5 nm. This is measured at 5 K.

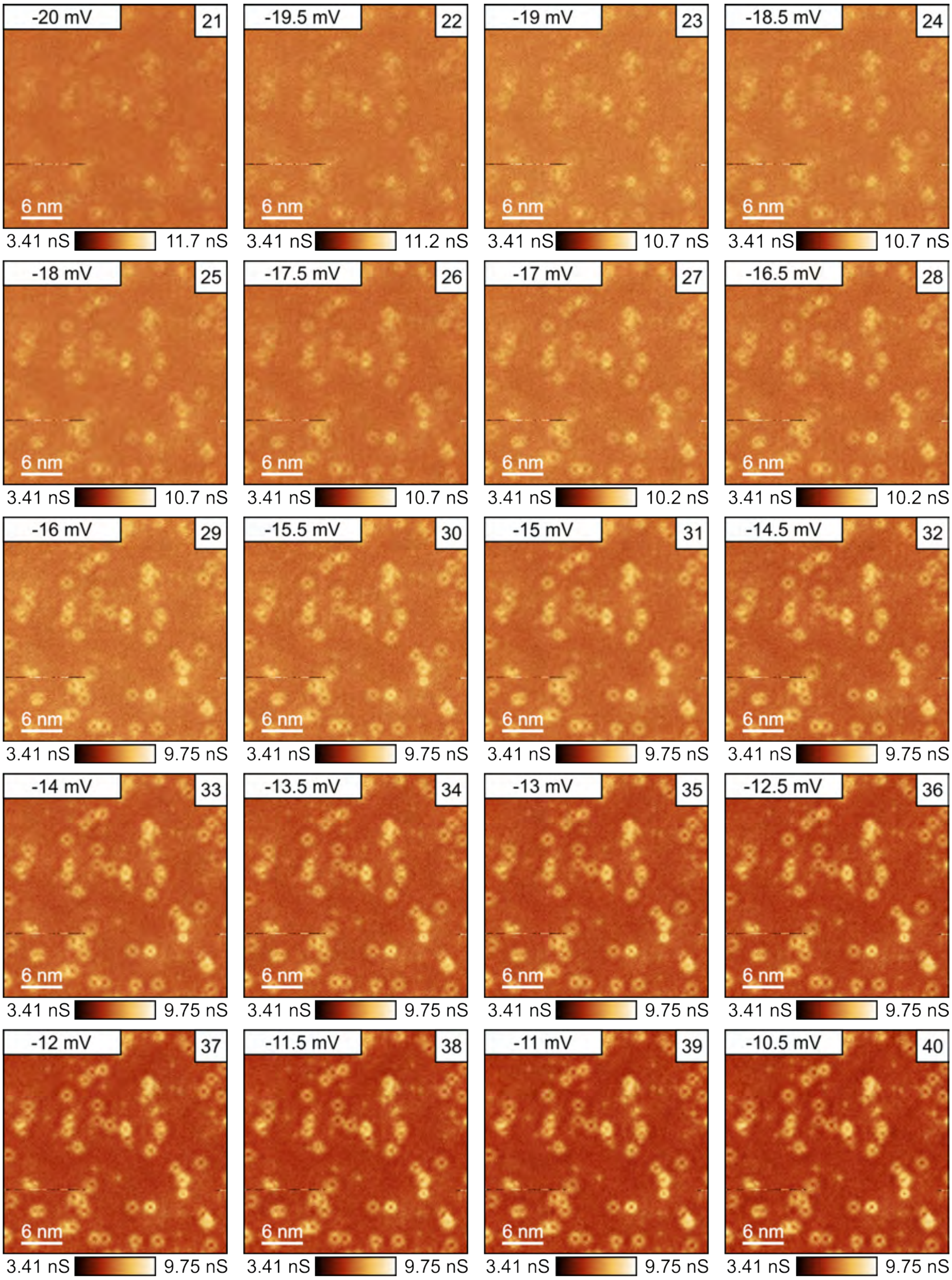

Figure F.7.: The constant energy dI/dV slices from spectroscopic map taken at the place of Fig. 6.37(a). The corresponding energies of those images ((21)-(40)) are shown in the left upper corner of each image which are from -20 mV to -10.5 mV. Total size of each image is 32.5 nm × 32.5 nm. This is measured at 5 K.

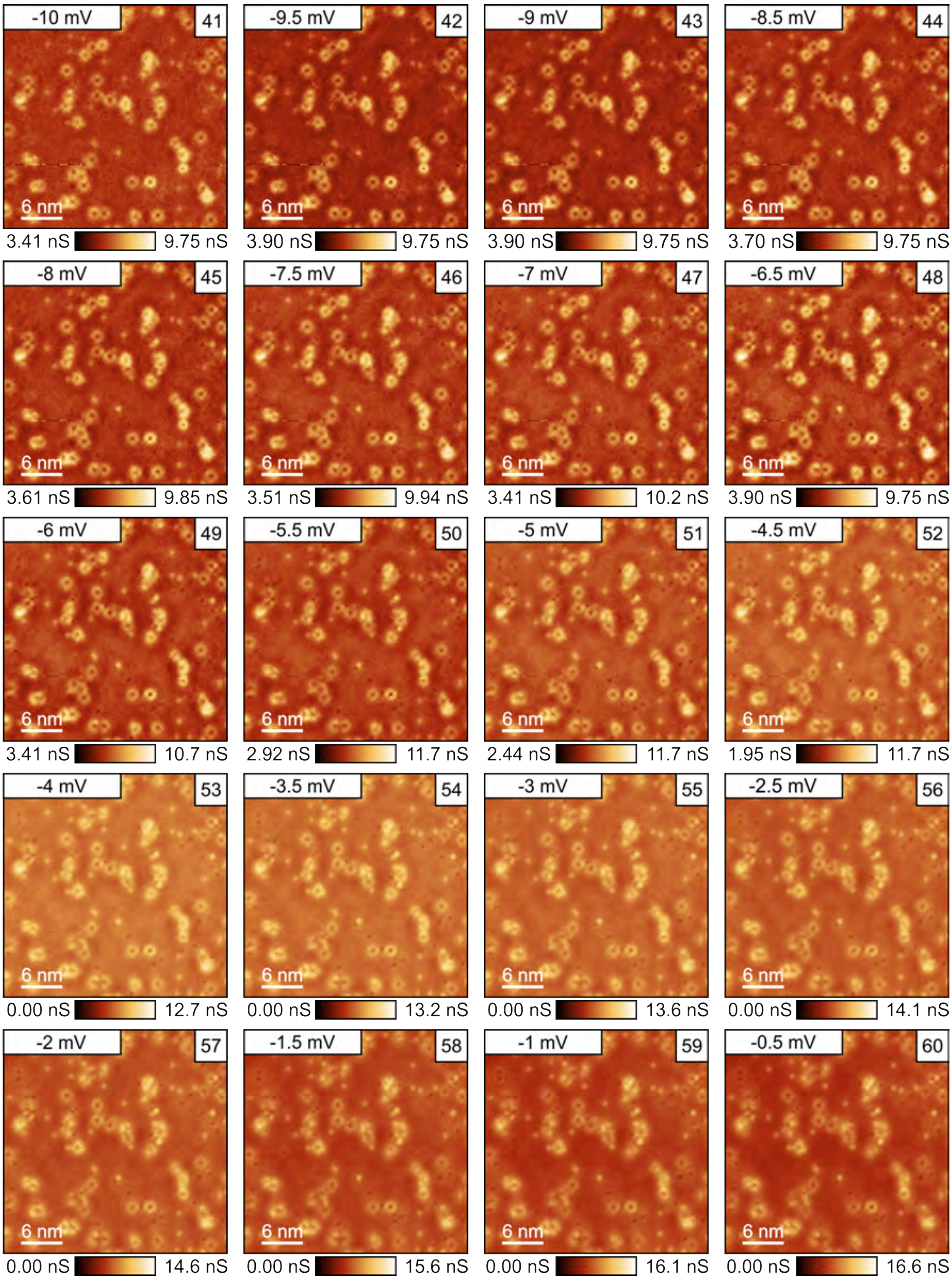

Figure F.8.: The constant energy $\mathrm{d}I/\mathrm{d}V$ slices from spectroscopic map taken at the place of Fig. 6.37(a). The corresponding energies of those images ((41)-(60)) are shown in the left upper corner of each image which are from -10 mV to -0.5 mV. Total size of each image is 32.5 nm × 32.5 nm. This is measured at 5 K.

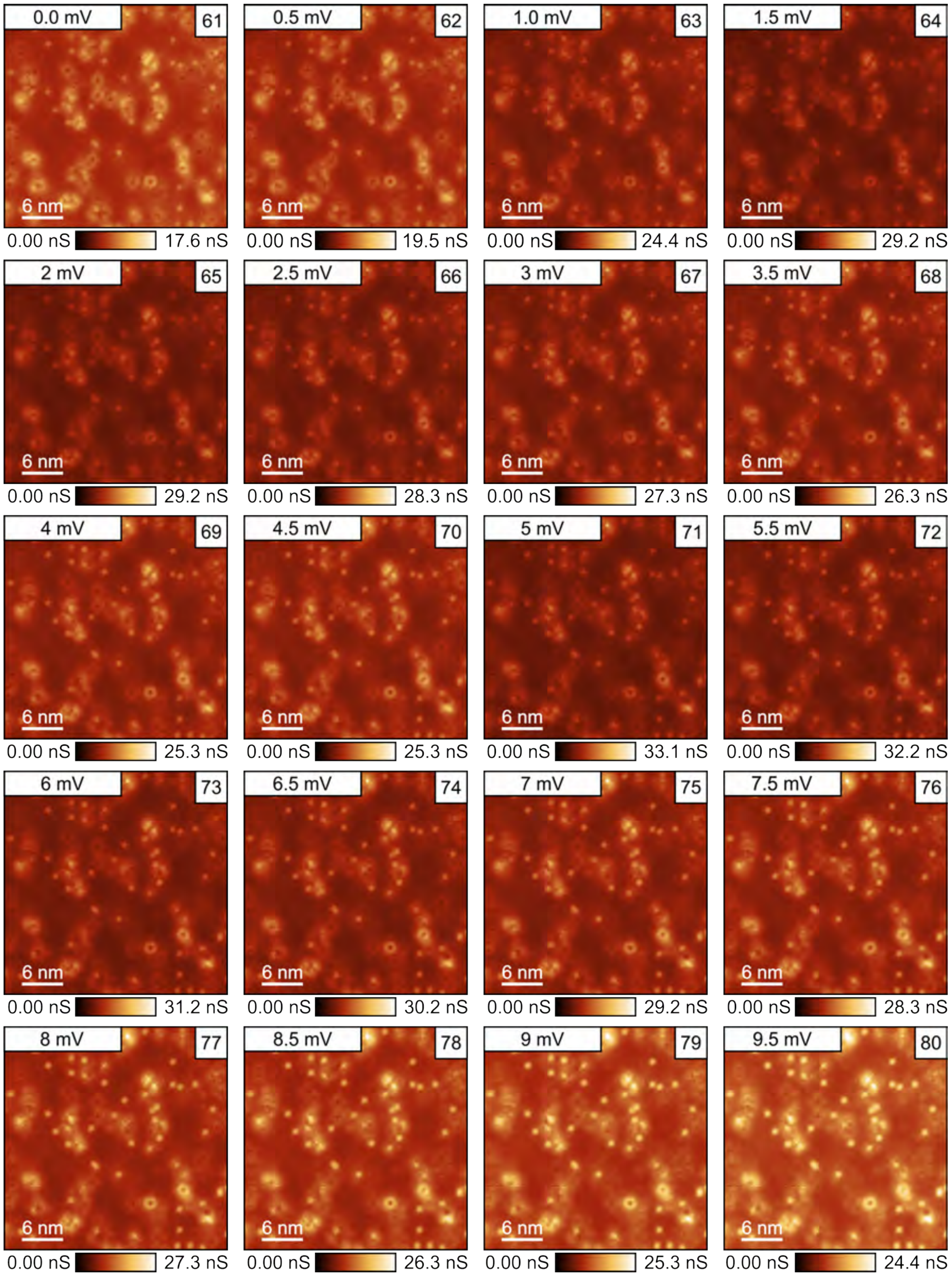

Figure F.9.: The constant energy dI/dV slices from spectroscopic map taken at the place of Fig. 6.37(a). The corresponding energies of those images ((61)-(80)) are shown in the left upper corner of each image which are from 0 mV to 9.5 mV. Total size of each image is 32.5 nm × 32.5 nm. This is measured at 5 K.

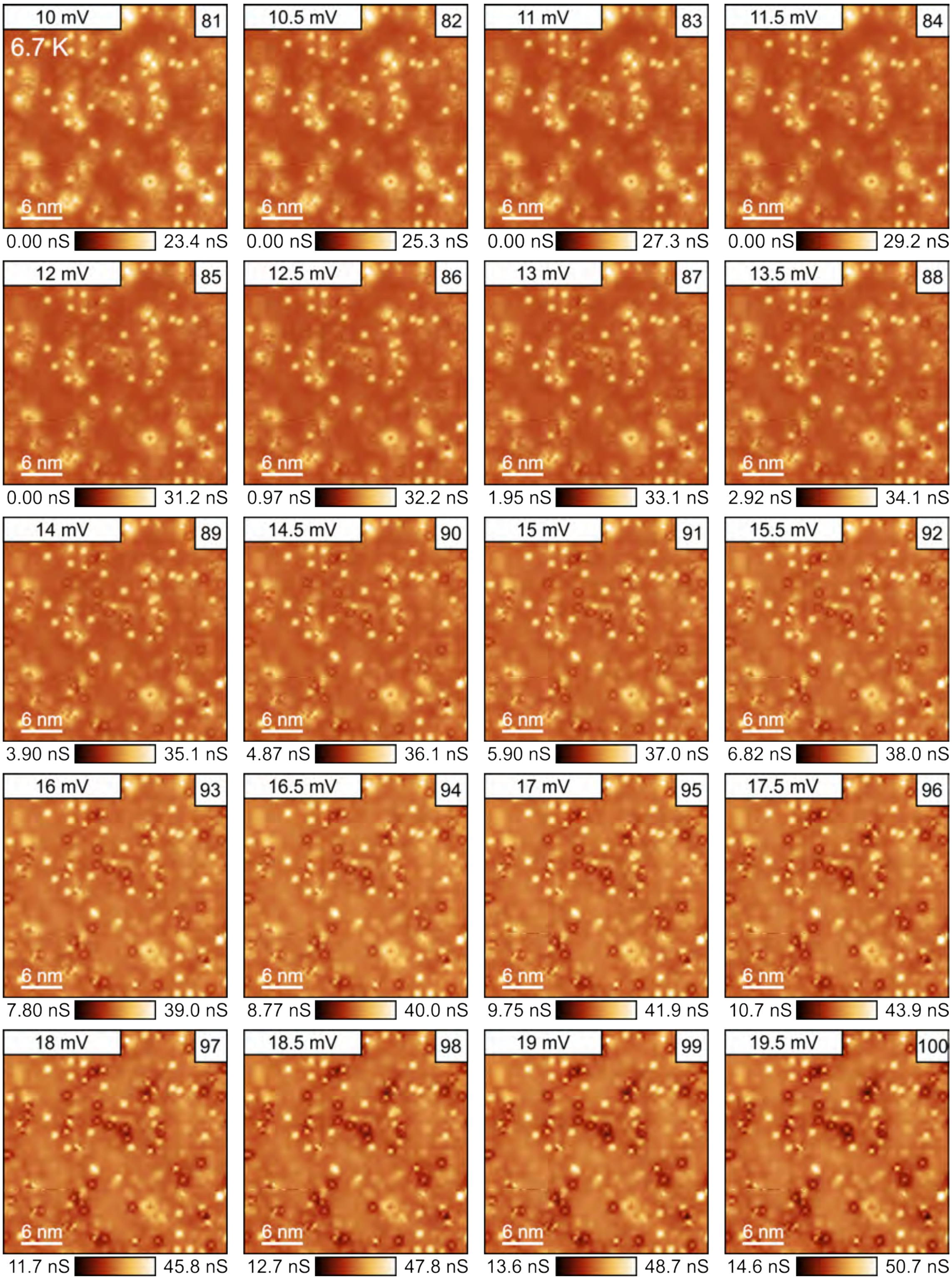

Figure F.10.: The constant energy dI/dV slices from spectroscopic map taken at the place of Fig. 6.37(a). The corresponding energies of those images ((81)-(100)) are shown in the left upper corner of each image which are from 10 mV to 19.5 mV. Total size of each image is 32.5 nm × 32.5 nm. This is measured at 5 K.

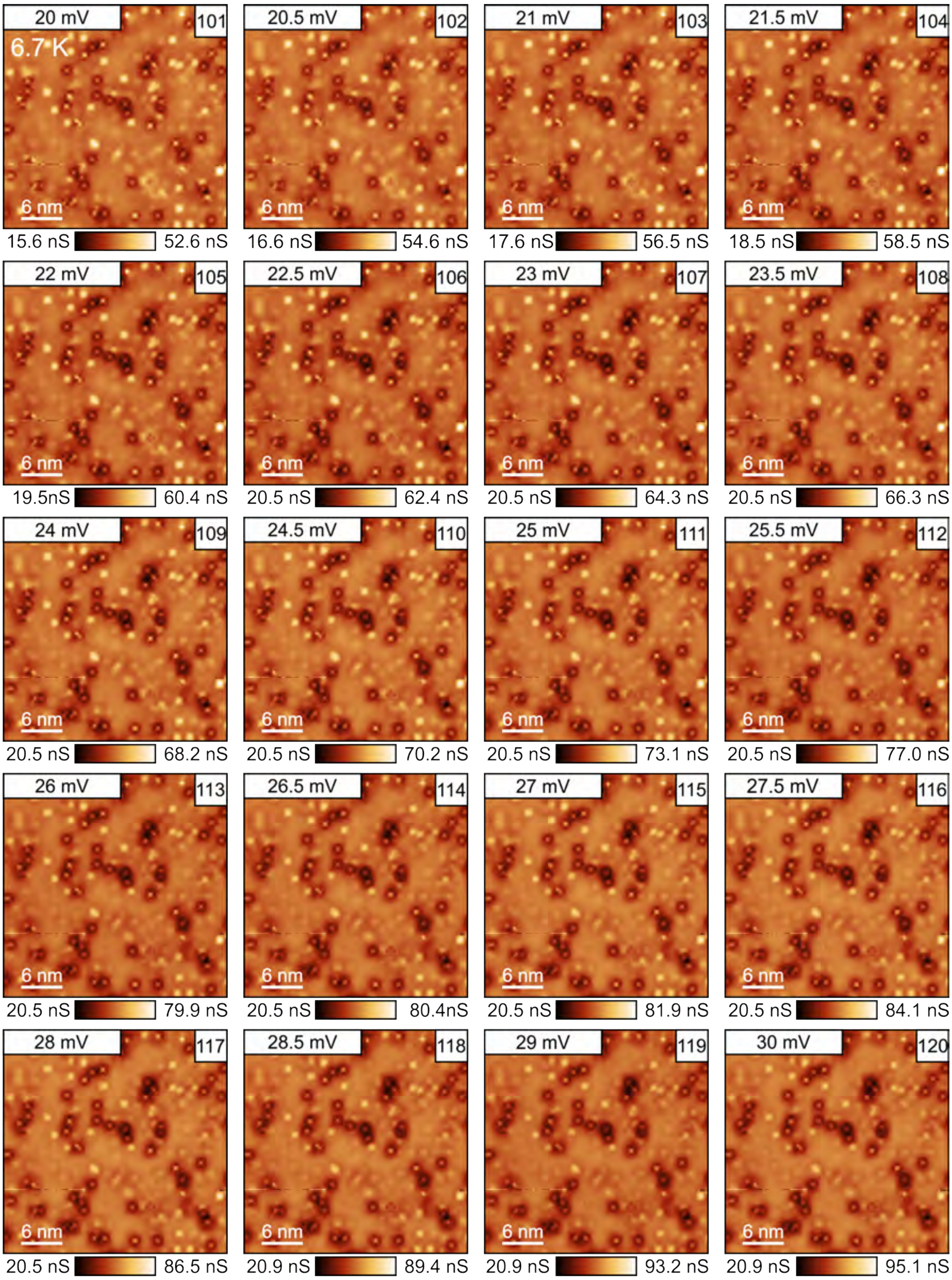

Figure F.11.: The constant energy dI/dV slices from spectroscopic map taken at the place of Fig. 6.37(a). The corresponding energies of those images ((101)-(120)) are shown in the left upper corner of each image which are from 20 mV to 30 mV. Total size of each image is 32.5 nm × 32.5 nm. This is measured at 5 K.

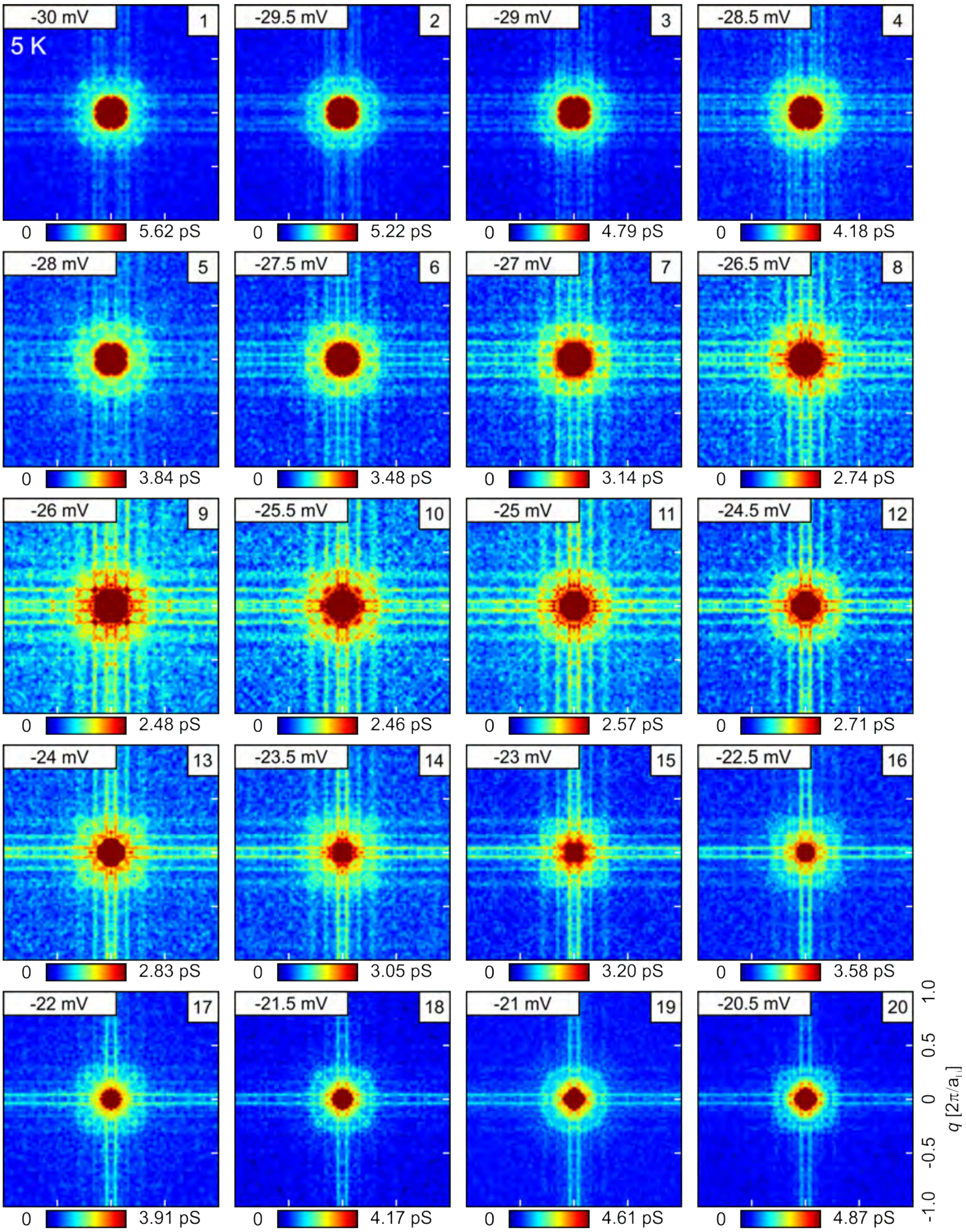

Figure F.12.: The QPI signals related to the constant dI/dV energy slices in Fig. F.6. The corresponding energies of those images ((1)-(20)) are shown in the left upper corner of each image which are from -30 mV to -20.5 mV. Total size of each image is $\pm 1.0 \times 2\pi/\mathrm{a}_{Li}$. This is measured at 5 K.

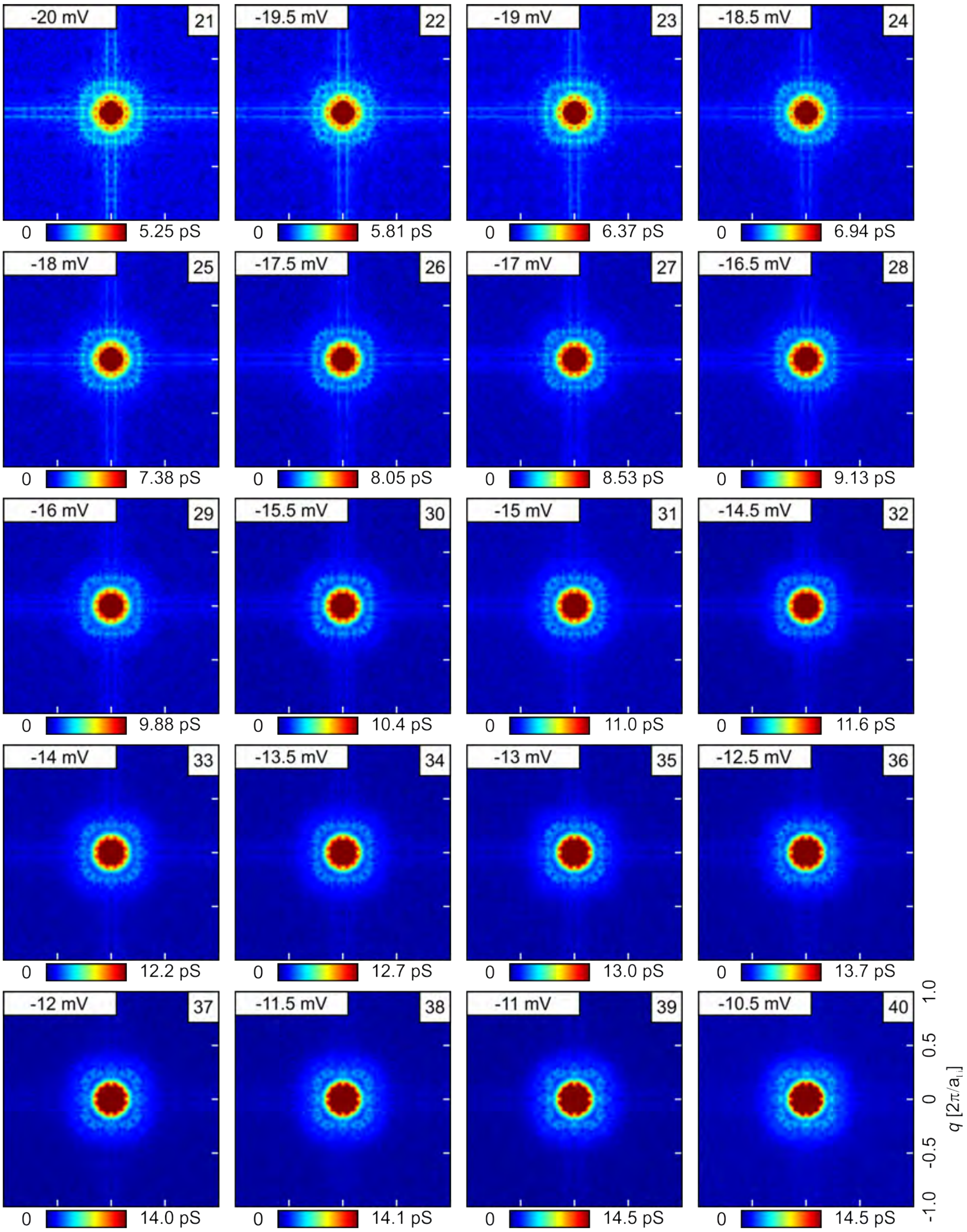

Figure F.13.: The QPI signals related to the constant dI/dV energy slices in Fig. F.7. The corresponding energies of those images ((21)-(40)) are shown in the left upper corner of each image which are from -20 mV to -10.5 mV. Total size of each image is $\pm 1.0 \times 2\pi/\mathrm{a}_{Li}$. This is measured at 5 K.

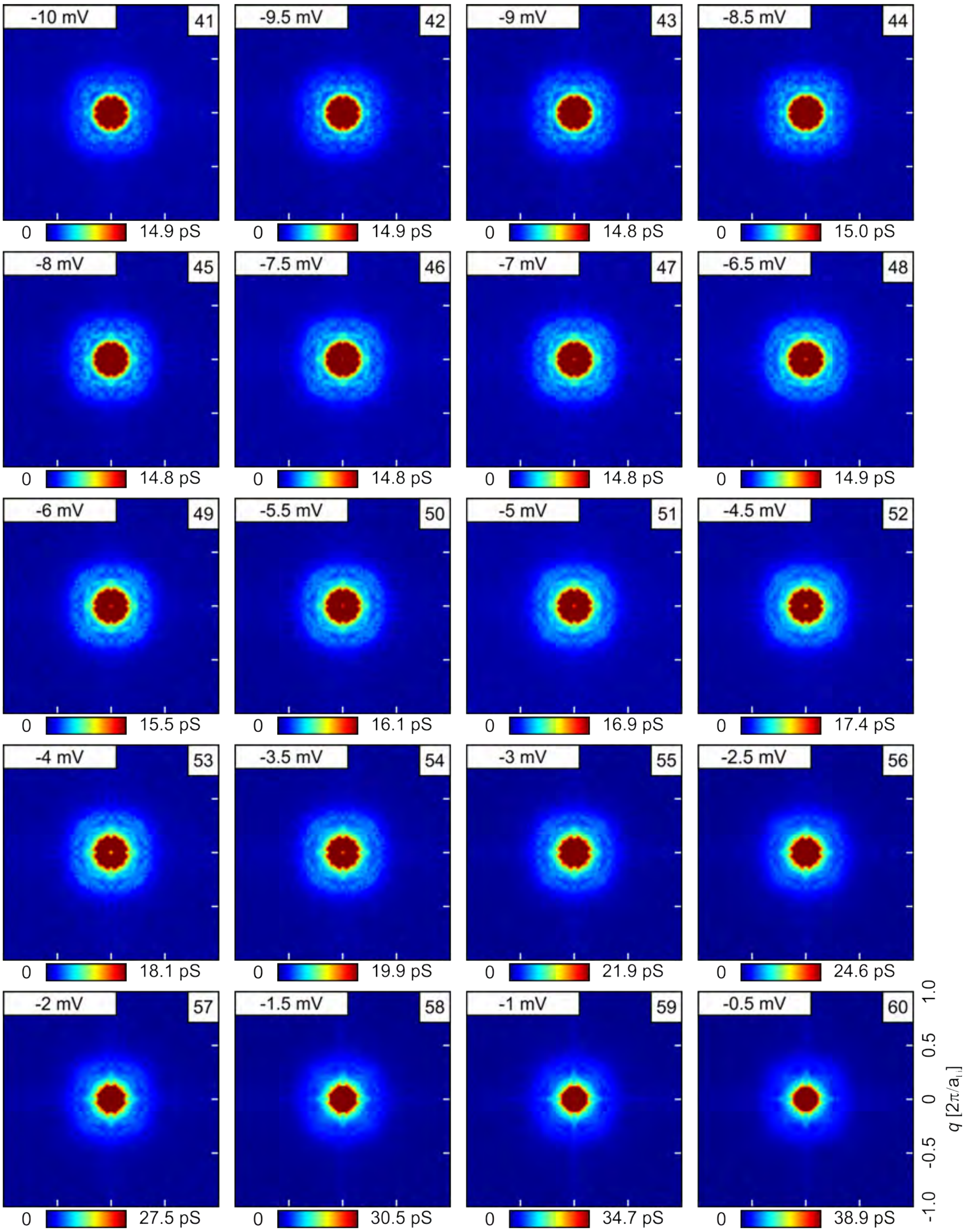

Figure F.14.: The QPI signals related to the constant dI/dV energy slices in Fig. F.8. The corresponding energies of those images ((41)-(60)) are shown in the left upper corner of each image which are from -10 mV to -0.5 mV. Total size of each image is $\pm1.0\times2\pi/\mathrm{a}_{Li}$. This is measured at 5 K.

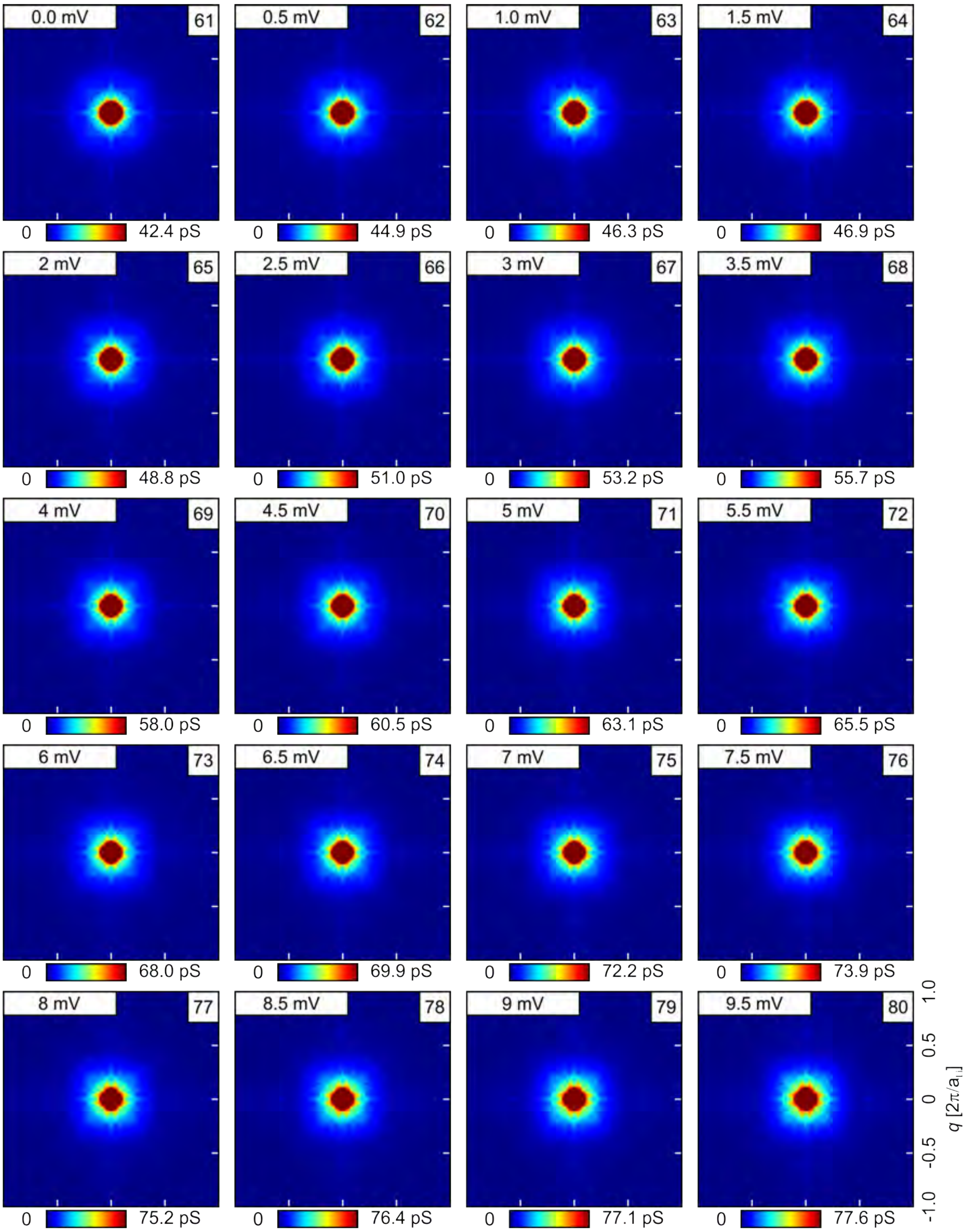

Figure F.15.: The QPI signals related to the constant $\mathrm{d}I/\mathrm{d}V$ energy slices in Fig. F.9. The corresponding energies of those images ((61)-(80)) are shown in the left upper corner of each image which are from 0 mV to 9.5 mV. Total size of each image is $\pm 1.0 \times 2\pi/\mathrm{a}_{Li}$. This is measured at 5 K.

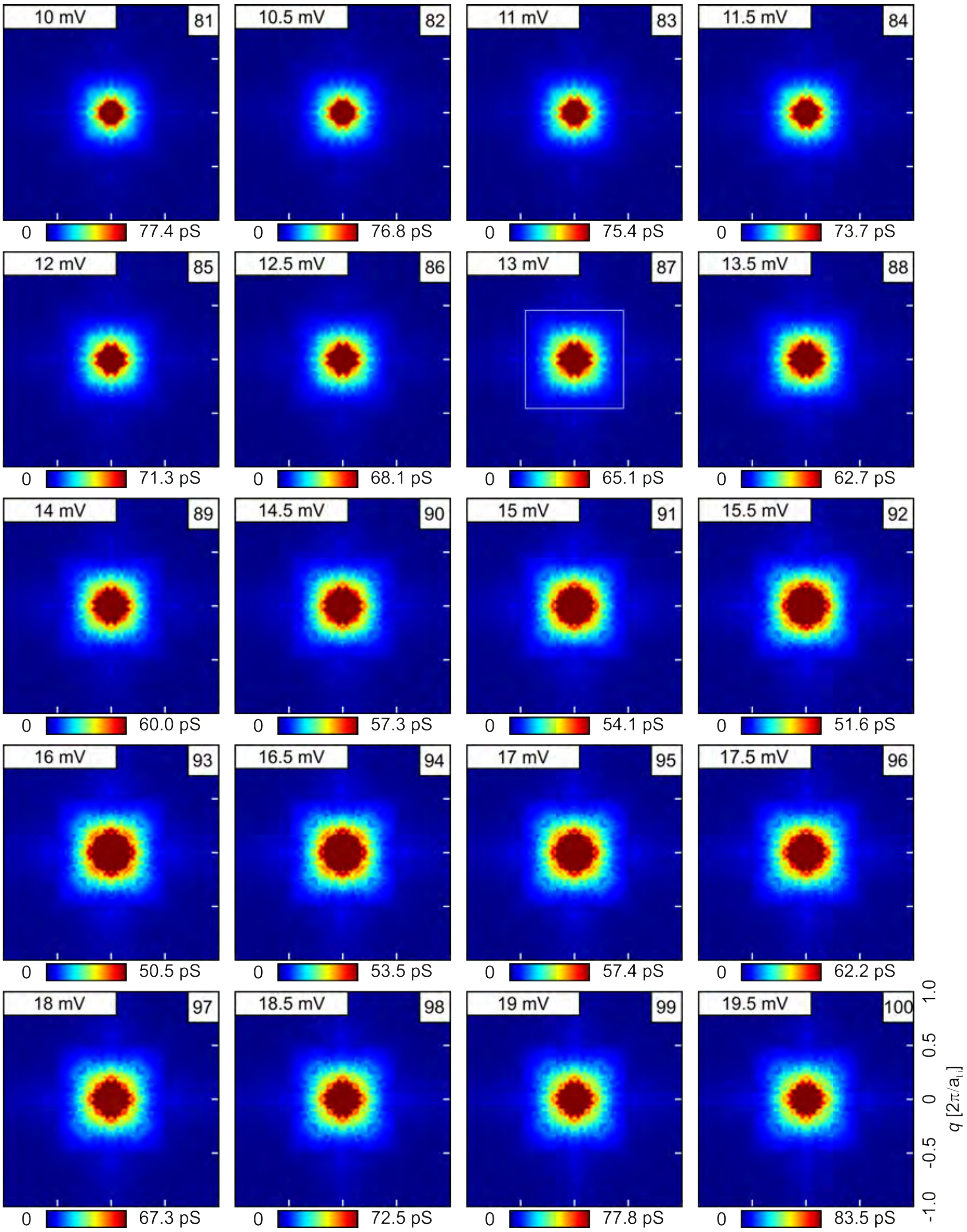

Figure F.16.: The QPI signals related to the constant dI/dV energy slices in Fig. F.10. The corresponding energies of those images ((81)-(100)) are shown in the left upper corner of each image which are from 10 mV to 19.5 mV. Total size of each image is $\pm 1.0 \times 2\pi/\mathrm{a}_{Li}$. This is measured at 5 K.

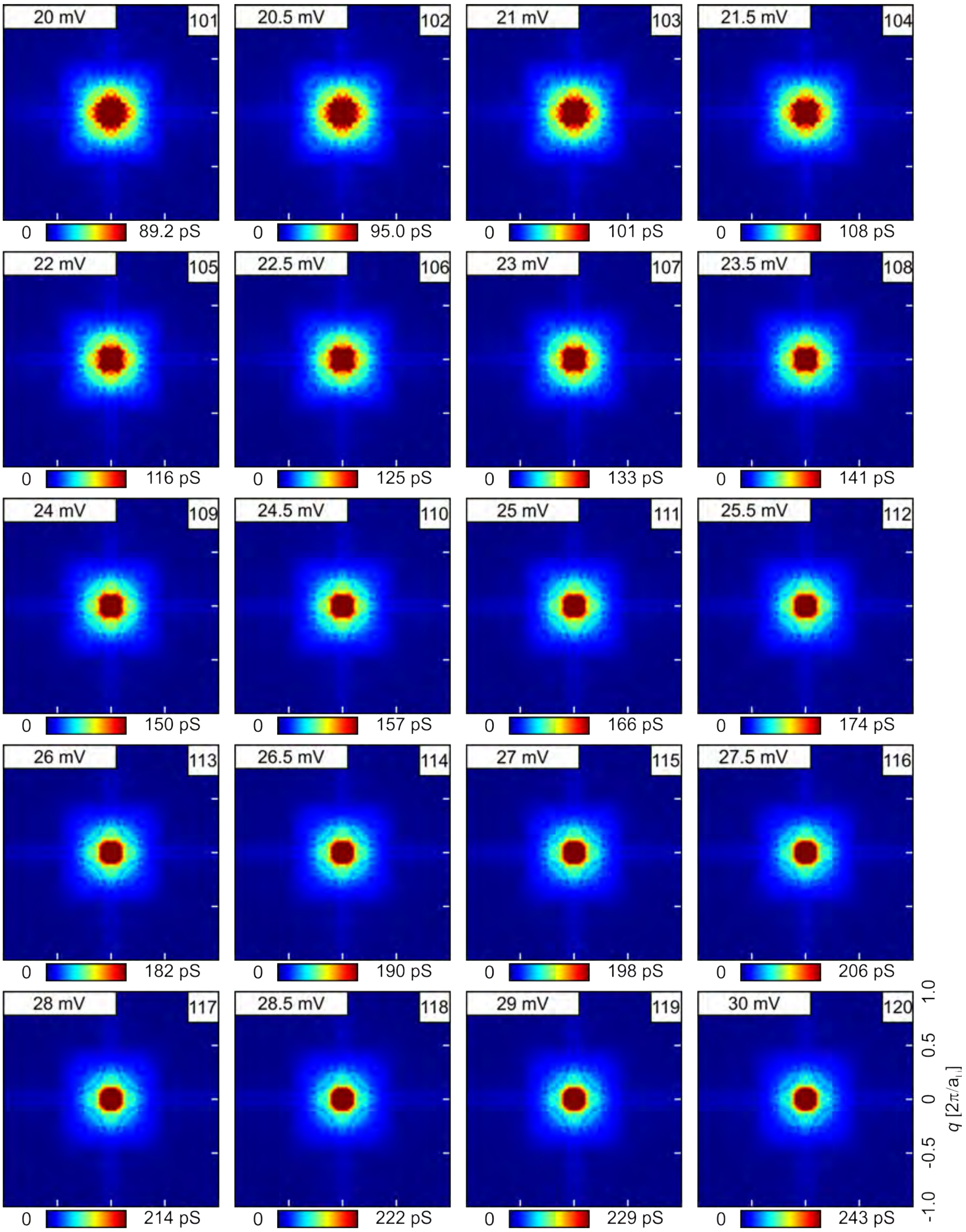

Figure F.17.: The QPI signals related to the constant $\mathrm{d}I/\mathrm{d}V$ energy slices in Fig. F.11. The corresponding energies of those images ((101)-(120)) are shown in the left upper corner of each image which are from 20 mV to 30 mV. Total size of each image is $\pm 1.0 \times 2\pi/a_{Li}$. This is measured at 5 K.

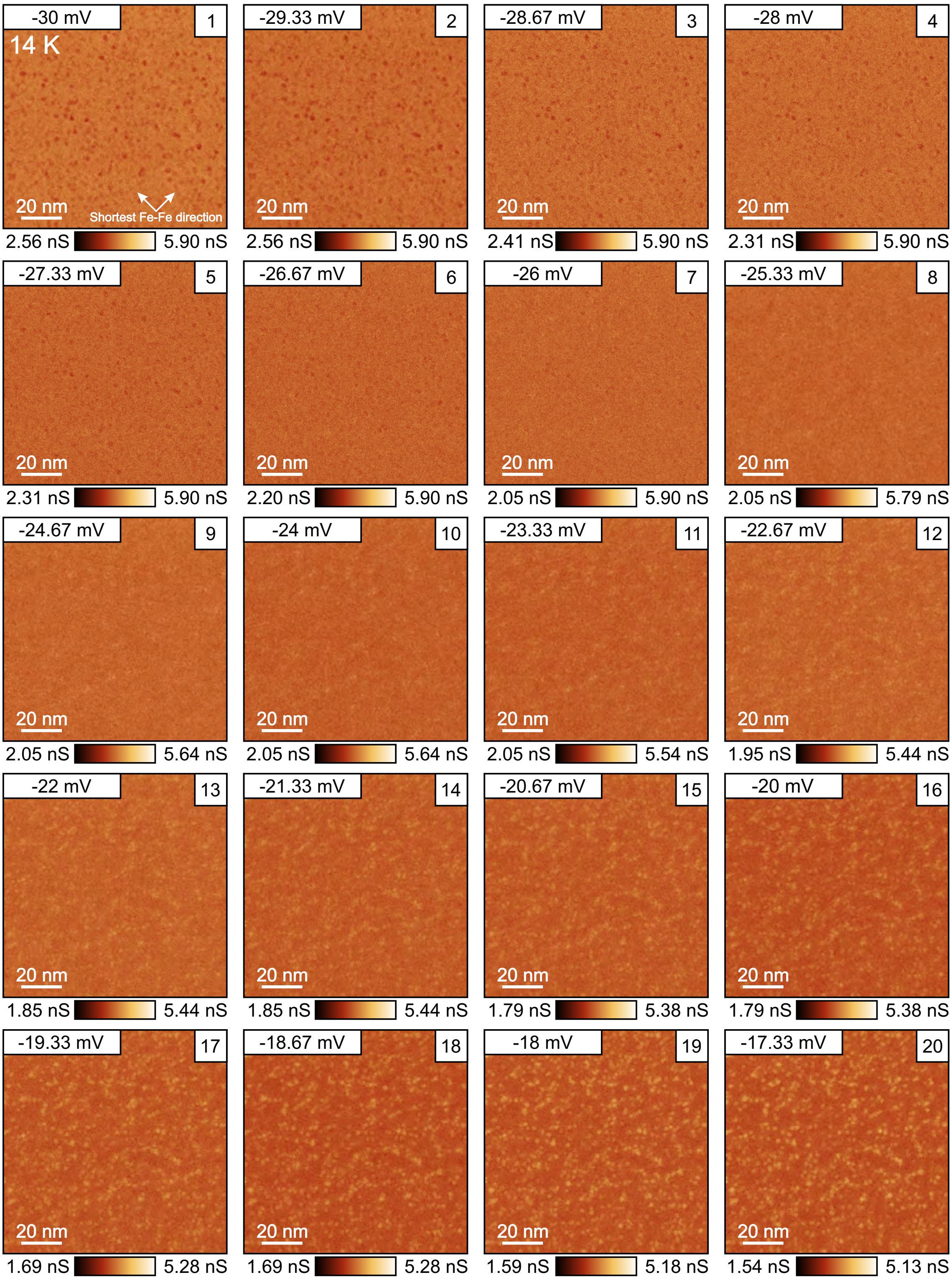

Figure F.18.: The constant energy dI/dV slices from spectroscopic map taken at the place of Fig. F.1(c). The corresponding energies of those images ((1)-(20)) are shown in the left upper corner of each image which are from -30 mV to -17.33 mV. Total size of each image is 110 nm × 110 nm. This is measured at 5 K.

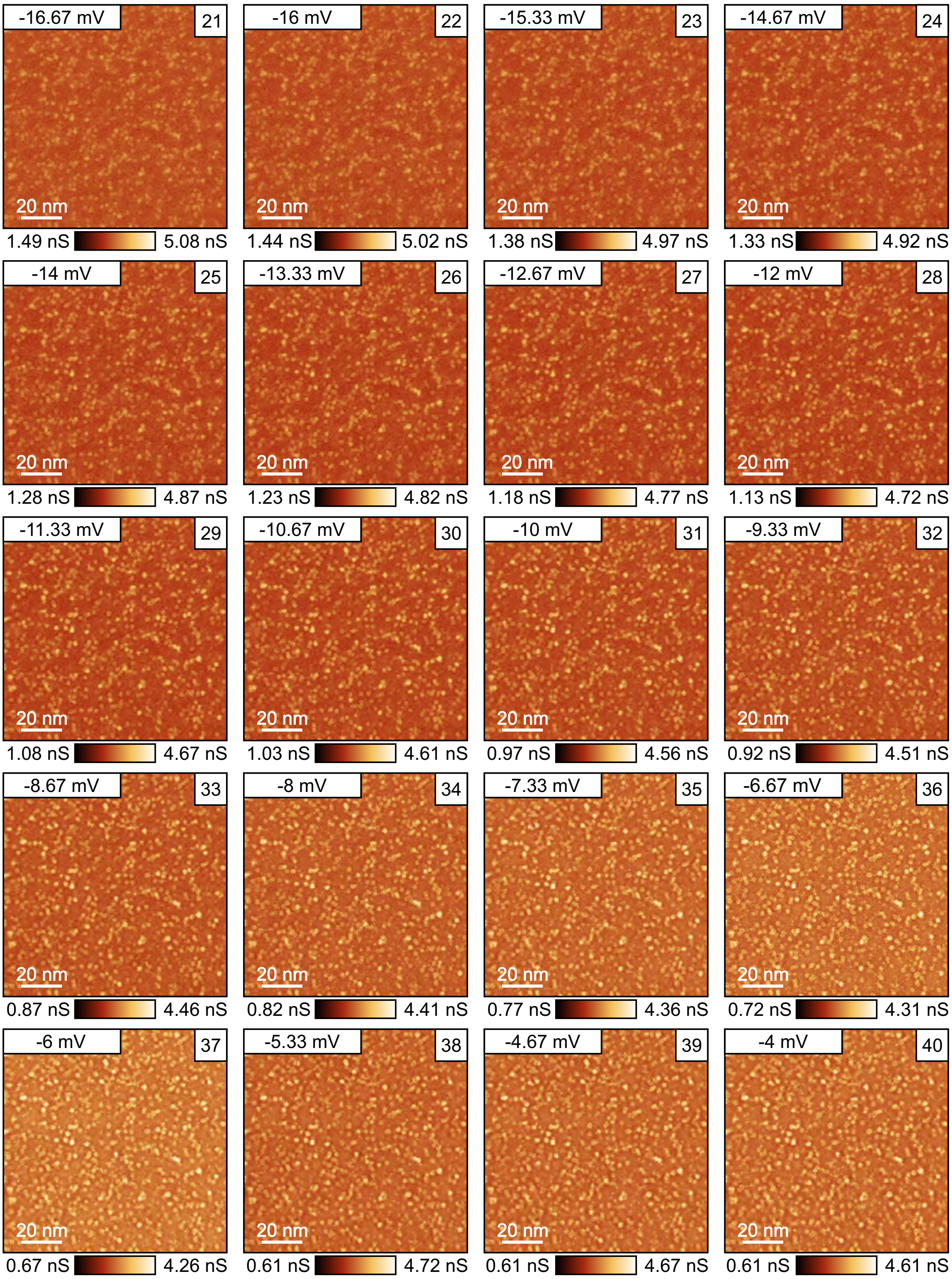

Figure F.19.: The constant energy dI/dV slices from spectroscopic map taken at the place of Fig. F.1(c). The corresponding energies of those images ((21)-(40)) are shown in the left upper corner of each image which are from -16.67 mV to -4 mV. Total size of each image is 110 nm × 110 nm. This is measured at 5 K.

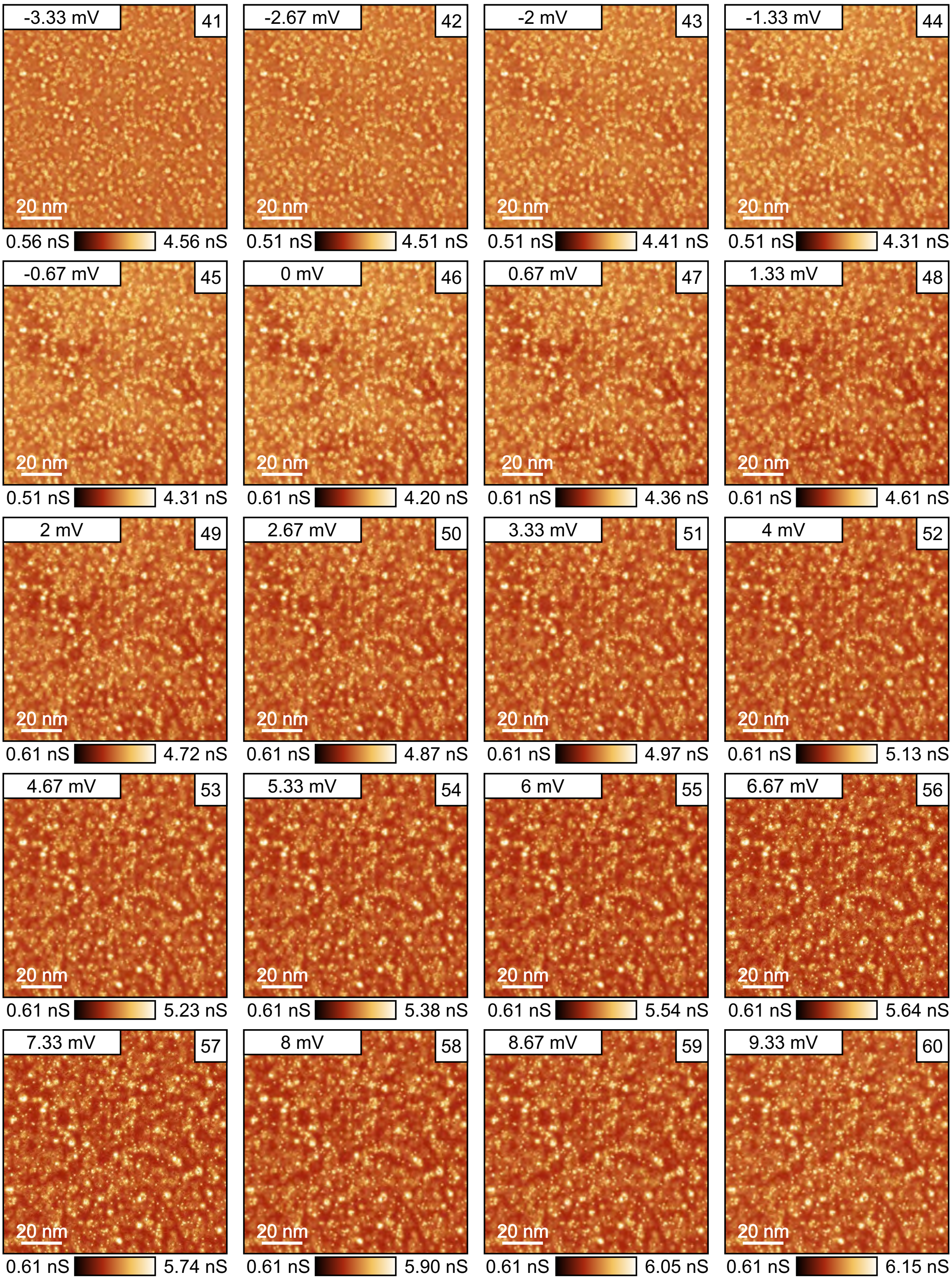

Figure F.20.: The constant energy dI/dV slices from spectroscopic map taken at the place of Fig. F.1(c). The corresponding energies of those images ((41)-(60)) are shown in the left upper corner of each image which are from -3.33 mV to 9.33 mV. Total size of each image is 110 nm × 110 nm. This is measured at 5 K.

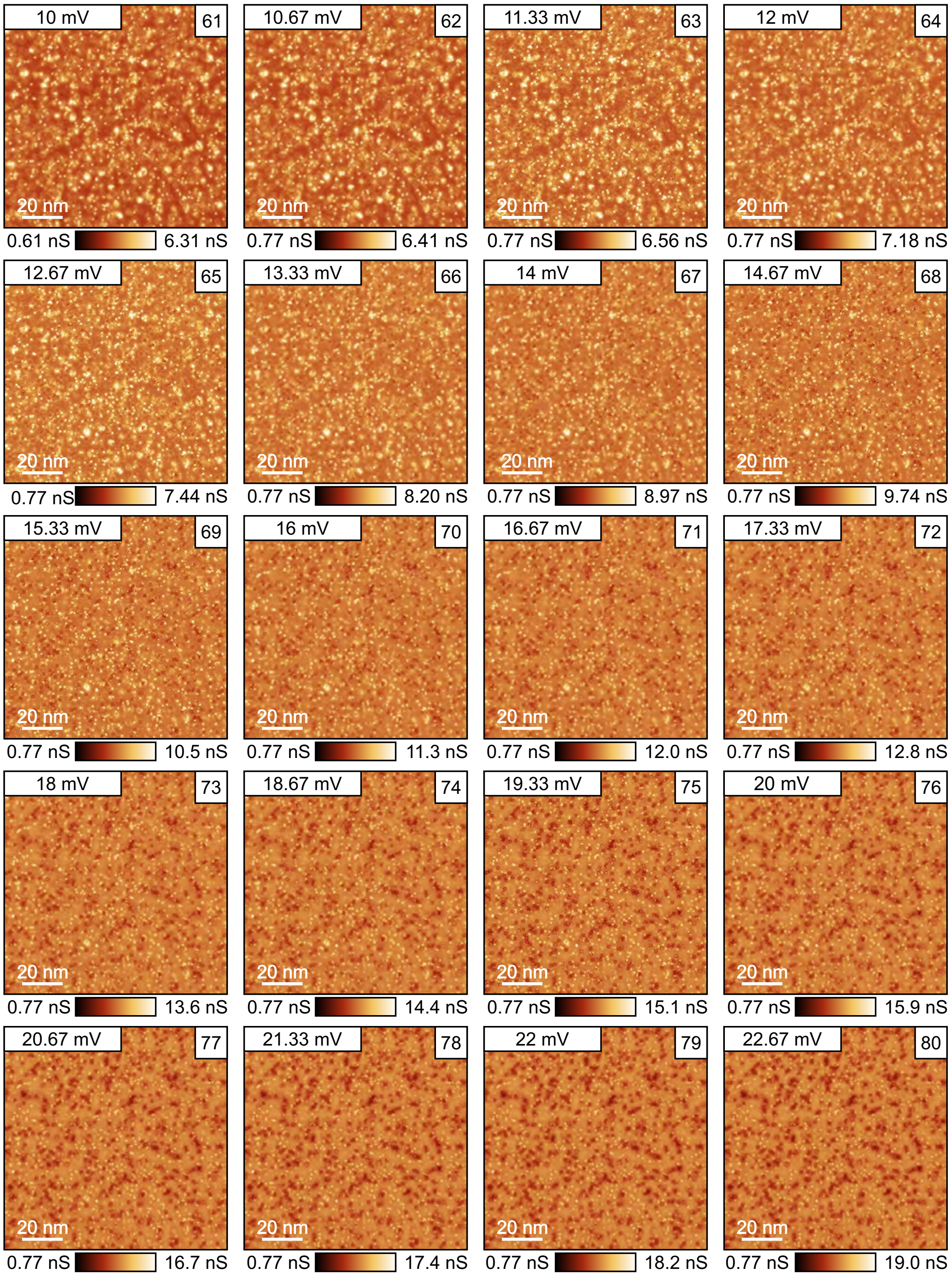

Figure F.21.: The constant energy dI/dV slices from spectroscopic map taken at the place of Fig. F.1(c). The corresponding energies of those images ((61)-(80)) are shown in the left upper corner of each image which are from 10 mV to 22.67 mV. Total size of each image is 110 nm × 110 nm. This is measured at 5 K.

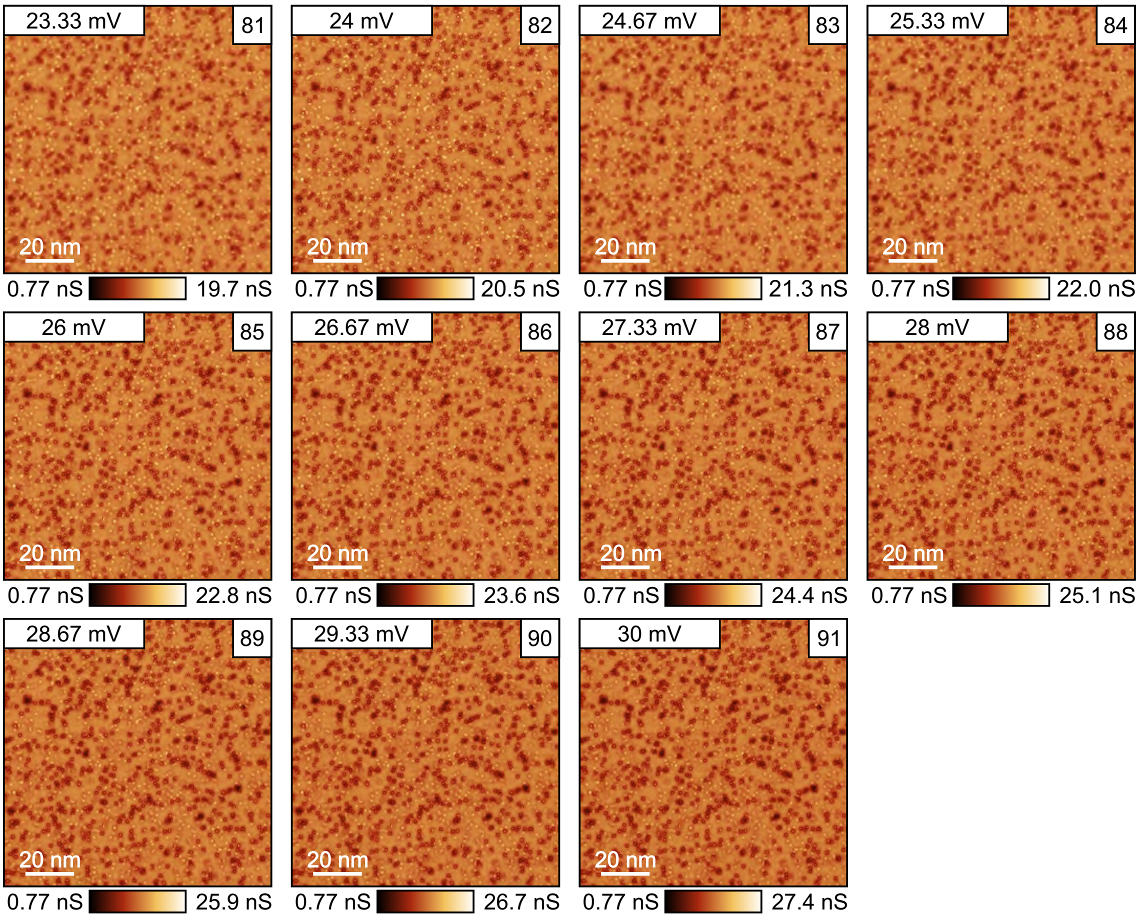

Figure F.22.: The constant energy dI/dV slices from spectroscopic map taken at the place of Fig. F.1(c). The corresponding energies of those images ((81)-(91)) are shown in the left upper corner of each image which are from 23.33 mV to 30 mV. Total size of each image is 110 nm × 110 nm. This is measured at 5 K.

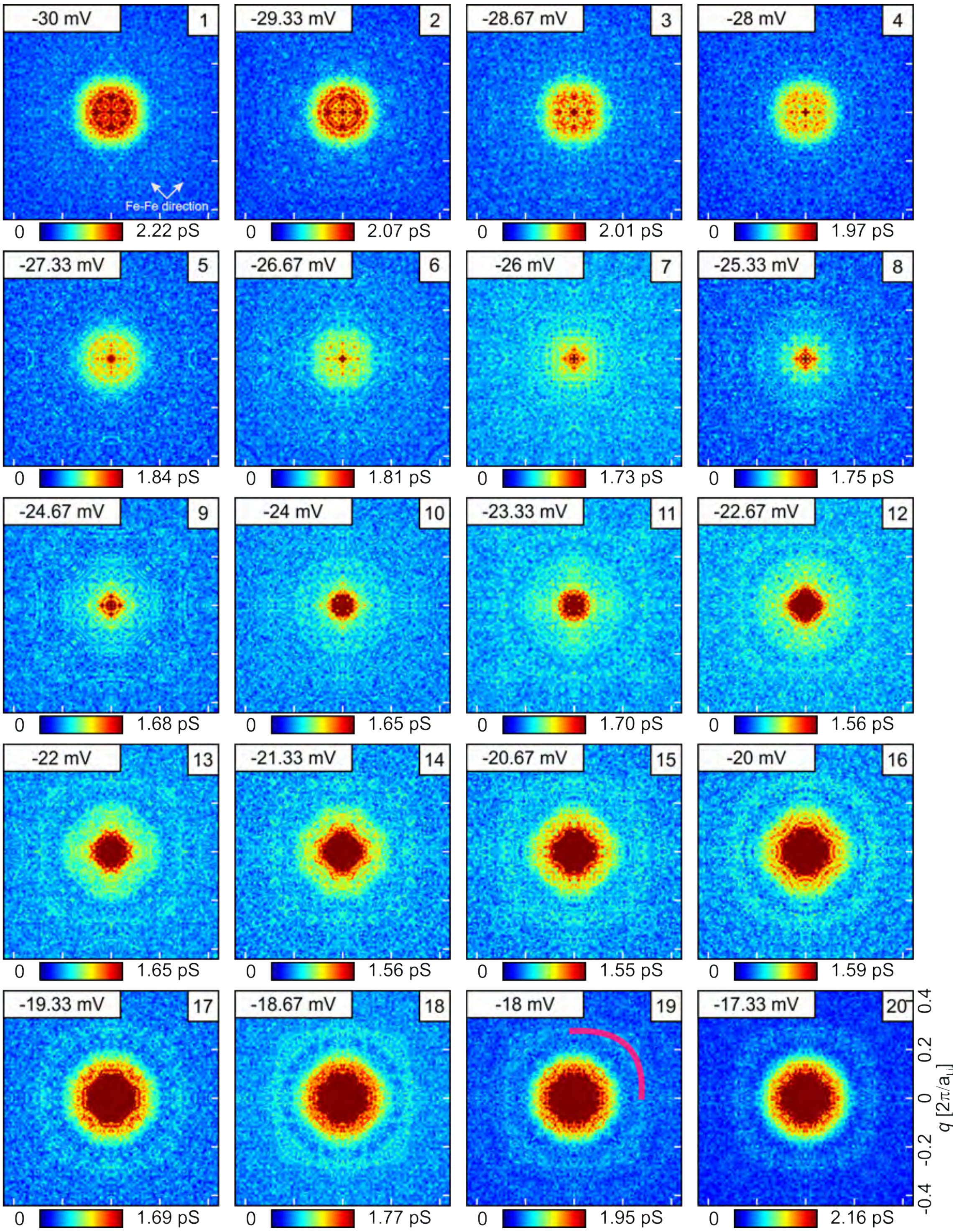

Figure F.23.: The QPI signals related to the constant $\mathrm{d}I/\mathrm{d}V$ energy slices in Fig. F.18. The corresponding energies of those images ((1)-(20)) are shown in the left upper corner of each image which are from -30 mV to -17.33 mV. Total size of each image is $\pm 0.44 \times 2\pi/\mathrm{a}_{Li}$. This is measured at 5 K.

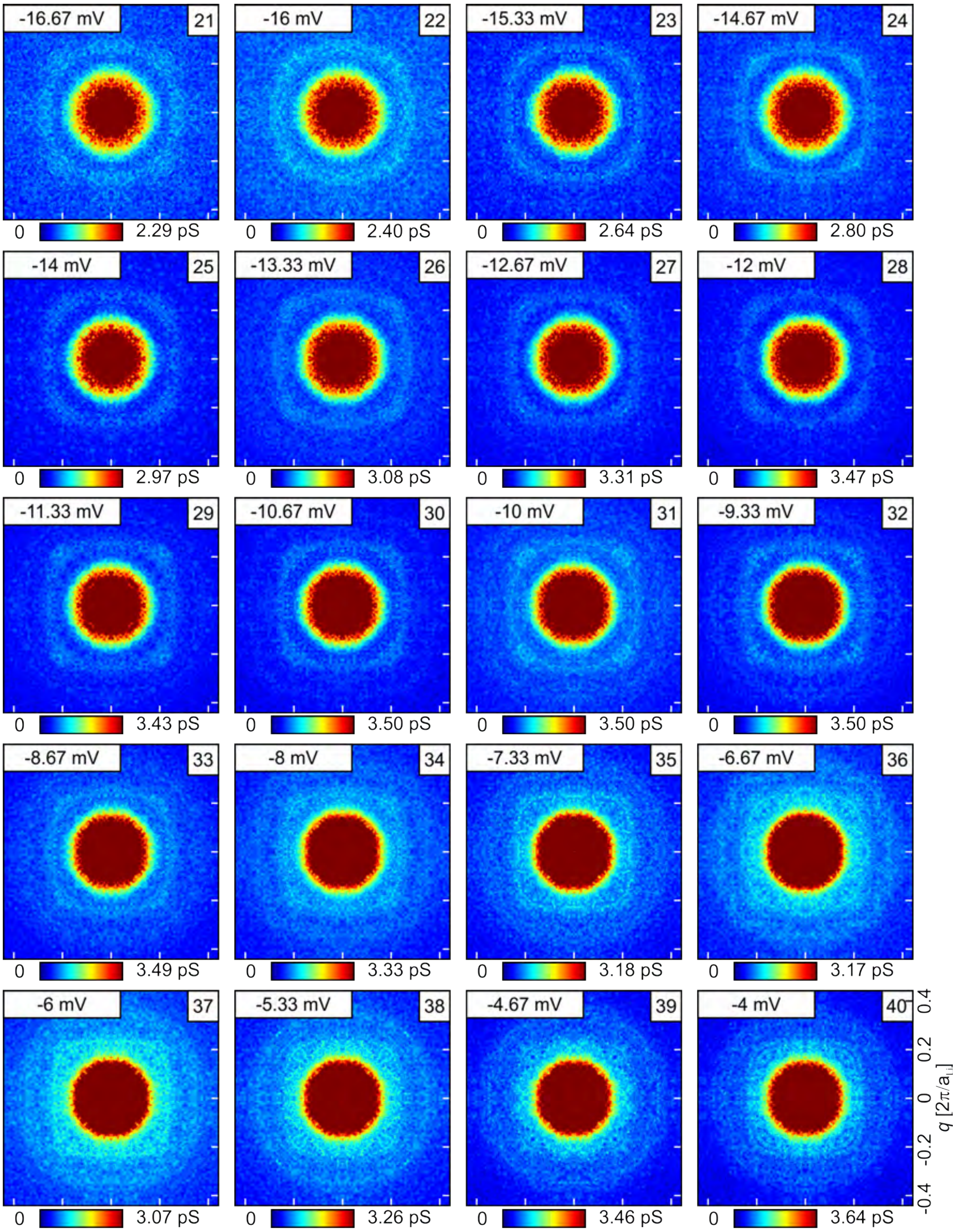

Figure F.24.: The QPI signals related to the constant dI/dV energy slices in Fig. F.19. The corresponding energies of those images ((21)-(40)) are shown in the left upper corner of each image which are from -16.67 mV to -4 mV. Total size of each image is $\pm 0.44 \times 2\pi/\mathrm{a}_{Li}$. This is measured at 5 K.

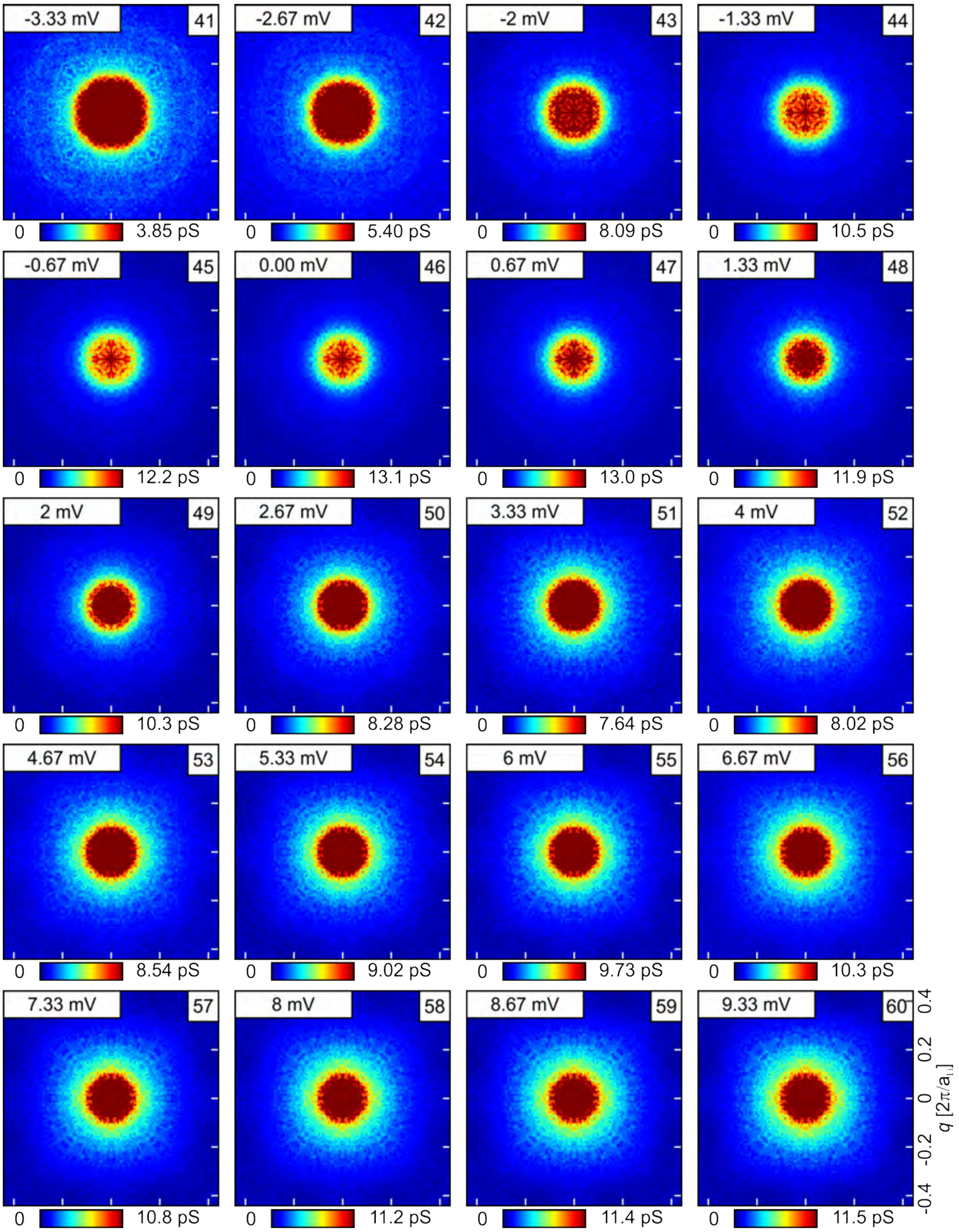

Figure F.25.: The QPI signals related to the constant dI/dV energy slices in Fig. F.20. The corresponding energies of those images ((41)-(60)) are shown in the left upper corner of each image which are from -3.33 mV to 9.33 mV. Total size of each image is $\pm0.44\times2\pi/\mathrm{a}_{Li}$. This is measured at 5 K.

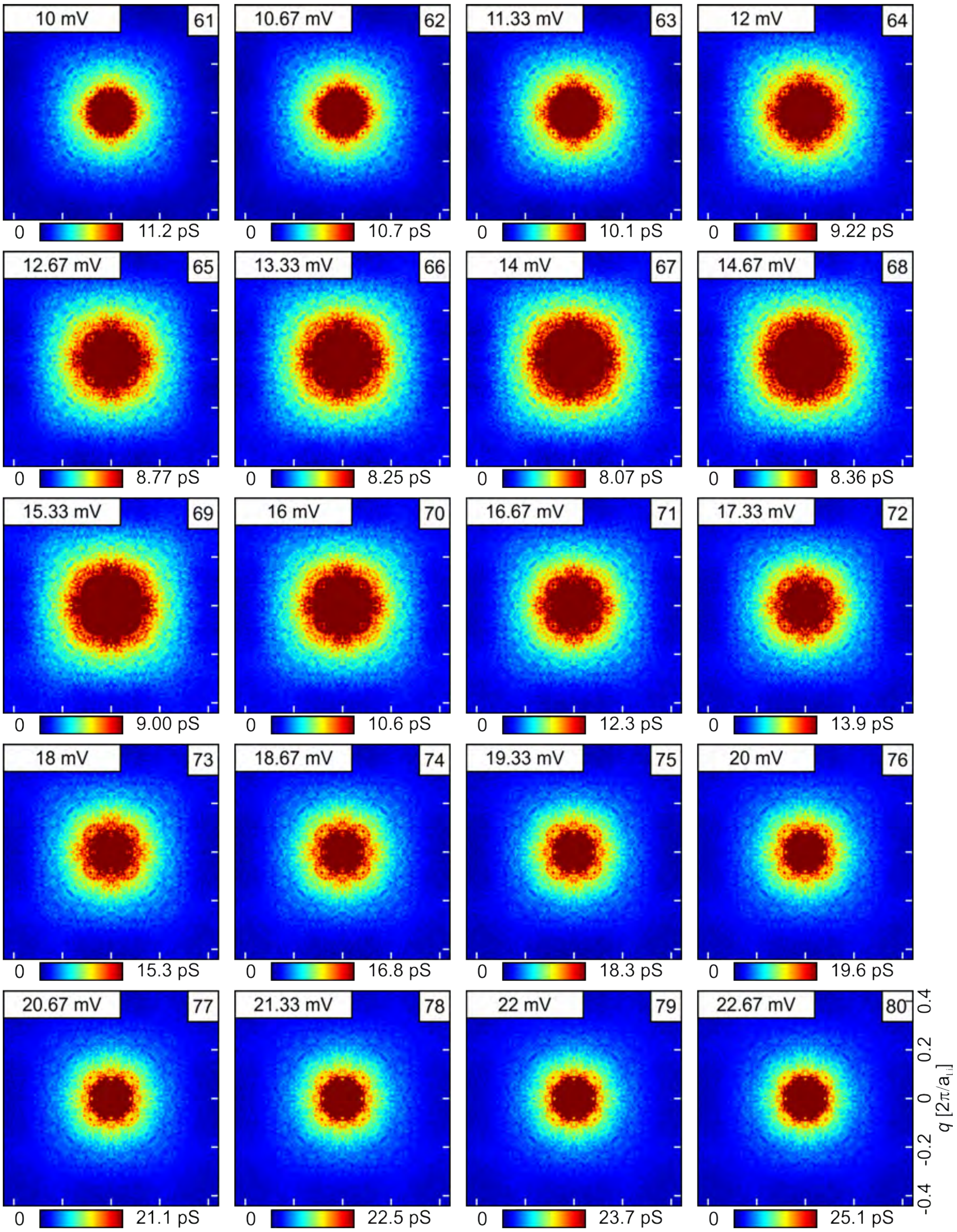

Figure F.26.: The QPI signals related to the constant dI/dV energy slices in Fig. F.21. The corresponding energies of those images ((61)-(80)) are shown in the left upper corner of each image which are from 10 mV to 22.67 mV. Total size of each image is $\pm 0.44 \times 2\pi/\mathrm{a}_{Li}$. This is measured at 5 K.

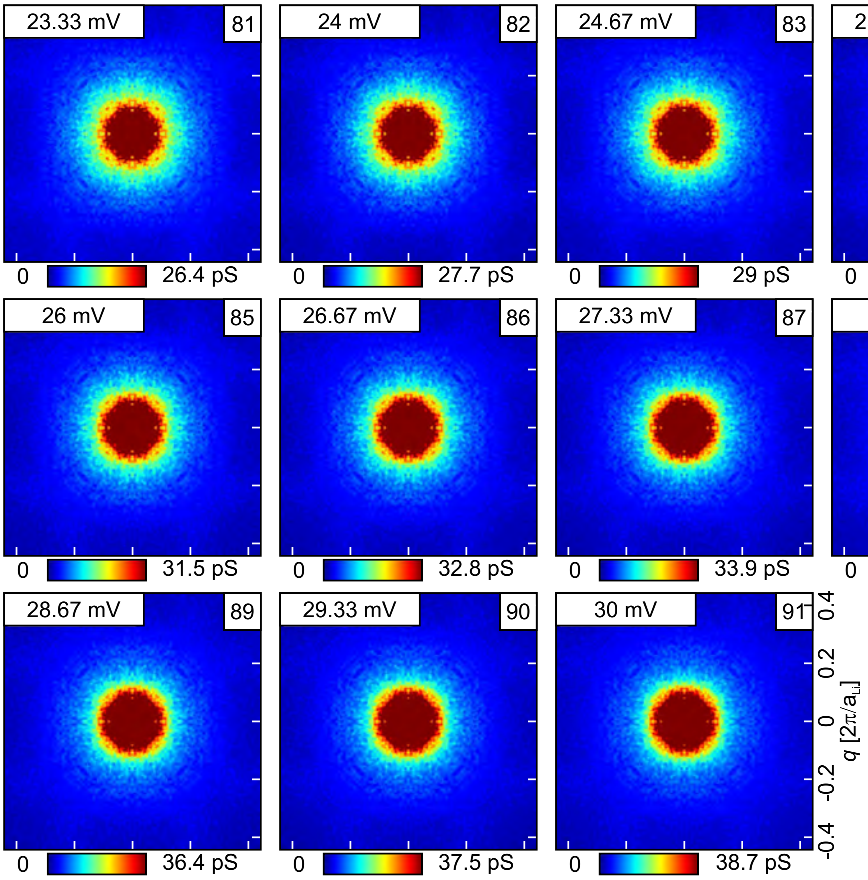

Figure F.27.: The QPI signals related to the constant dI/dV energy slices in Fig. F.22. The corresponding energies of those images ((81)-(91)) are shown in the left upper corner of each image which are from 23.33 mV to 30 mV. Total size of each image is $\pm 0.44 \times 2\pi/\mathrm{a}_{Li}$. This is measured at 5 K.

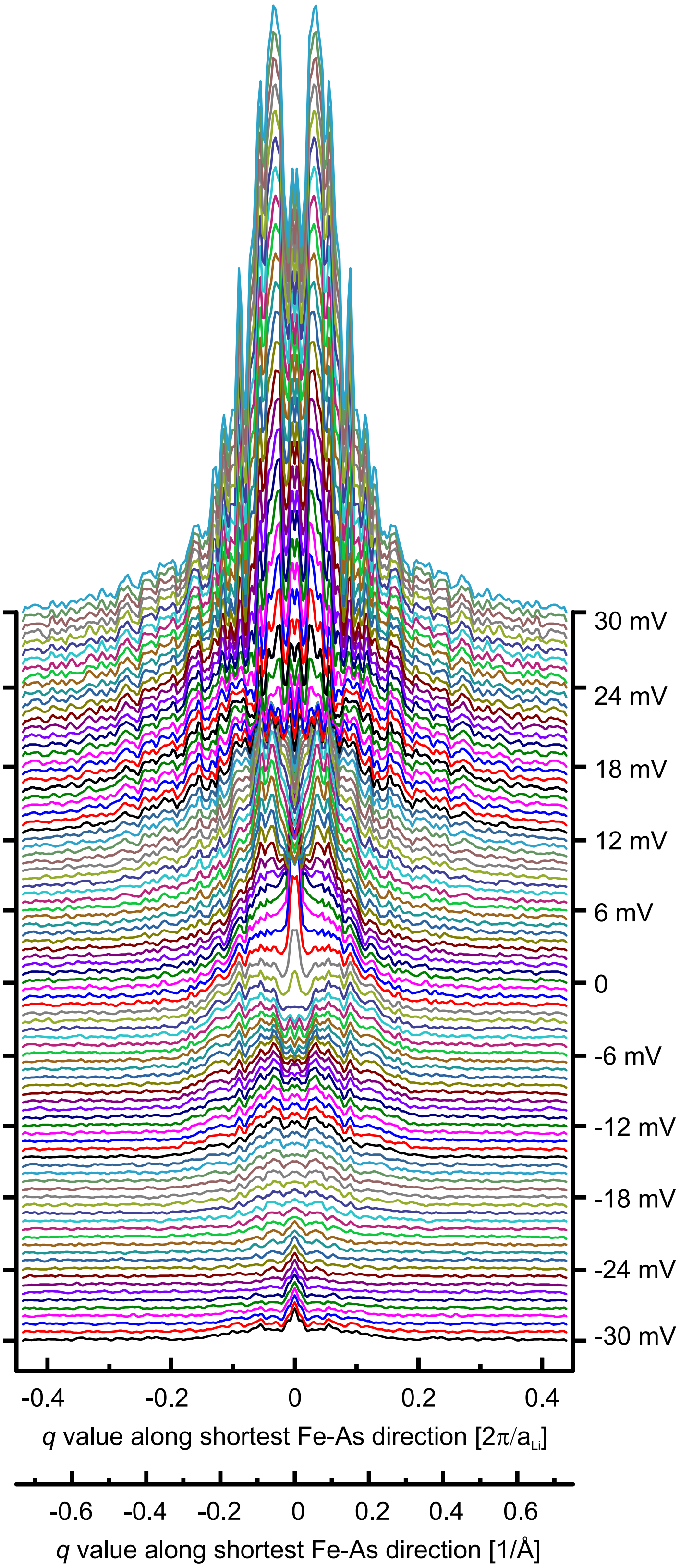

Figure F.28.: This is the line profile along Fe-As direction corresponding to all the QPI data taken at 5 K between Fig. F.23 to Fig. F.27. The ring like structure related to interband scattering is hard to distinguish from this waterfall presentation due to its low intensity.

List of Publications:

1. R. Schlegel, T. Hänke, D. Baumann, M. Kaiser, **P. K. Nag**, R. Voigtländer, D. Lindackers, B. Büchner and C. Hess. *Design and properties of a cryogenic dip-stick scanning tunneling microscope with capacitive coarse approach control.* **Review of Scientific Instruments 85, (2014)**.

2. **P. K. Nag**, R. Schlegel, D. Baumann, H. -J. Grafe, R. Beck, S. Wurmehl, B. Büchner and C. Hess. *Two distinct superconducting phases in LiFeAs.* **Scientific Reports 6, 27926 (2016)**.

3. R. Schlegel, **P. K. Nag**, D. Baumann, R. Beck, S. Wurmehl, B. Büchner and C. Hess. *Defect states in LiFeAs as seen by low-temperature scanning tunneling microscopy and spectroscopy.* **physica status solidi (b) 254, 1600159 (2017)**.

4. Z. Sun, **P. K. Nag**, D. Baumann, R. Kappenberger, S. Wurmehl, B. Büchner and C. Hess. *Temperature dependent quasiparticle interference study to visualize the band structure in LiFeAs* (in preparation).

Conferences:

- P. K. Nag, D. Baumann, R. Schlegel, R. Pohle, M. Scheffler, T. Hänke, R. Beck, S. Aswartham, S. Wurmehl, B. Büchner and C. Hess. ***STM/STS Study on Co-doped NaFeAs superconductor***, Frühjahrstagung der Deutschen Physikalischen Gesellschaft, Dresden, Germany, 11.03.2013 (Poster).

- P. K. Nag, D. Baumann, R. Schlegel, R. Beck, S. Aswartham, S. Wurmehl, B. Büchner and C. Hess. ***Temperature dependent density of states study in stoichiometric LiFeAs***, Frühjahrstagung der Deutschen Physikalischen Gesellschaft, Dresden, Germany, 31.03.2014 (Poster).

- R. Schlegel, P. K. Nag, D. Baumann, R. Beck, S. Wurmehl, B. Büchner and C. Hess. ***Magnetic Vortices in LiFeAs as seen by Scanning Tunneling Spectroscopy***, Frühjahrstagung der Deutschen Physikalischen Gesellschaft, Dresden, Germany, 1.04.2014 (Talk).

- P. K. Nag, D. Baumann, R. Schlegel, R. Beck, U. Gräfe, S. Wurmehl, B. Büchner and C. Hess. ***Temperature dependent density of states study in stoichiometric LiFeAs***, Workshop “Quantum Critical Matter - from Atoms to Bulk”, Obergurgl University Center, Obergurgl, Austria, 22.08.2014 (Poster).

- P. K. Nag, D. Baumann, R. Schlegel, R. Beck, S. Wurmehl, T. Wolf, B. Büchner and C. Hess. ***High energy spectra on Fe-based unconventional superconductors***, Frühjahrstagung der Deutschen Physikalischen Gesellschaft, Dresden, Germany, 16.03.2015 (Poster).

- P. K. Nag, D. Baumann, R. Schlegel, U. Gräfe, R. Beck, S. Wurmehl, T. Wolf, B. Büchner and C. Hess. ***Unusual temperature evolution of superconductivity in LiFeAs***, Workshop on the “two-dimensional chalcogenides: exotic electronic orders, superconductivity and magnetism”, IFW Dresden, Germany, 31.08.2015 (Poster).

- P. K. Nag, R. Schlegel, D. Baumann, H. J. Grafe, R. Beck, S. Wurmehl, B. Büchner and C. Hess. ***Unusual temperature evolution of superconductivity in LiFeAs***, Frühjahrstagung der Deutschen Physikalischen Gesellschaft, Dresden, Germany, 8.03.2016 (Talk).

- Z. Sun, P. K. Nag, D. Baumann, R. Kappenberger, S. Wurmehl, B. Büchner and C. Hess. ***Superconductivity in LiFeAs probed with quasiparticle interference***, Frühjahrstagung der Deutschen Physikalischen Gesellschaft, Dresden, Germany, 8.03.2016 (Talk).

Acknowledgements:

- In this point, I would like to express a humble attitude as well as special thanks to my PhD thesis advisor Prof. Bernd Büchner to give me an opportunity to pursue my doctoral work under his guidance and support me throughout my doctoral studies.

- I would like to give special thanks to Christian Hess to allow me to work in his "Tunneling" group and giving me the excellent facilities and supportive atmosphere during my PhD time at IFW Dresden. In addition, I would like to express my sincere gratitude to him for fruitful discussions and suggestions on my doctoral work.

- I would like to thank to S. Borisenko for fruitful discussion to explain LiFeAs band structure. I would like to thank Piers Coleman and Chandra Verma for fruitful discussions during a conference in Obergurgl, Austria.

- Many thanks goes to my lab-mates e.g. Danny Baumann, Ronny Schlegel, Christian David Salazar Enriquez, Uwe Gräfe, Rico Pohle, Martha Scheffler, Tim Kühne, Sebastian Schimmel, Mostafa Enayat, Jose Maria Guevara Parra, H. - J. Grafe, etc. to have nice lab atmosphere and their assistantships when it was necessary.

- I would like to thank Danny Baumann for his technical support and fruitful discussions, also for sharing his experiences on Dip-Stick STM. Additional thanks goes to him for suggestions on my private life during my stay in Dresden.

- Special acknowledgement goes to Zhixiang Sun for helping me to analyse QPI data and other useful discussions. Special thanks also goes to Steffen Sykora for several useful discussions, especially for theoretical understanding of the QPI data.

- I would like to acknowledge Richard Heinrich and Steffen Sykora for giving their valuable time to voluntary proofreading of this thesis partially. I also would like to give a special thanks to Marie Petersilie for her voluntary work on proofreading the whole thesis and her important suggestions and remarks towards this direction.

- At the end, I would like to thank my parents and my elder sister for their enormous mental support during my stay in Dresden.

List of Figures

ïż£

Bibliography

[1] D. N. Basov and A. V. Chubukov, Nat. Phys. **7**, 272 (2011). [Cited on pages: 1 and 36.]

[2] D. C. Johnston, Advances in Physics **59**, 803 (2010). [Cited on pages: 1, 33, and 37.]

[3] G. R. Stewart, Rev. Mod. Phys. **83**, 1589 (2011). [Cited on pages: 1 and 33.]

[4] P. Dai, Rev. Mod. Phys. **87**, 855 (2015). [Cited on pages: 1, 33, and 43.]

[5] J. D. Wright, M. J. Pitcher, W. Trevelyan-Thomas, T. Lancaster, P. J. Baker, F. L. Pratt, S. J. Clarke and S. J. Blundell, Phys. Rev. B. **88**, 060401 (2013). [Cited on pages: 1 and 41.]

[6] Y. Kamihara, T. Watanabe, M. Hirano and H. Hosono, J. Am. Chem. Soc. **130**, 3296 (2008). [Cited on pages: 1, 33, 34, 35, 40, and 46.]

[7] H. Luetkens, H.-H. Klauss, M. Kraken, F. J. Litterst, T. Dellmann, R. Klingeler, C. Hess, R. Khasanov, A. Amato, C. Baines, M. Kosmala, O. J. Schumann, M. Braden, J. Hamann-Borrero, N. Leps, A. Kondrat, G. Behr, J. Werner and B. Büchner, Nat. Mater. **8**, 305 (2009). [Cited on pages: 1, 35, 37, and 40.]

[8] M. Rotter, M. Tegel, D. Johrendt, I. Schellenberg, W. Hermes and R. Pottgen, Phys. Rev. B **78**, 020503 (2008). [Cited on pages: 1, 35, and 40.]

[9] A. S. Sefat, M. A. McGuire, B. C. Sales, R. Jin, J. Y. Howe and D. Mandrus, Phys. Rev. B **77**, 174503 (2008). [Cited on pages: 1, 35, and 40.]

[10] J. H. Tapp, Z. Tang, B. Lv, K. Sasmal, B. Lorenz, P. C. W. Chu and A. M. Guloy, Phys. Rev. B **78**, 060505 (2008). [Cited on pages: 1 and 59.]

[11] S. V. Borisenko, V. B. Zabolotnyy, D. V. Evtushinsky, T. K. Kim, I. V. Morozov, A. N. Yaresko, A. A. Kordyuk, G. Behr, A. Vasiliev, R. Follath and B. Büchner, Phys. Rev. Lett. **105**, 067002 (2010). [Cited on pages: 1, 40, 41, 42, 65, 89, 99, 106, and 107.]

[12] K. Umezawa, Y. Li, H. Miao, K. Nakayama, Z.-H. Liu, P. Richard, T. Sato, J. B. He, D.-M. Wang, G. F. Chen, H. Ding, T. Takahashi and S.-C. Wang, Phys. Rev. Lett. **108**, 037002 (2012). [Cited on pages: 1, 40, 41, 42, 64, and 108.]

[13] S. Aswartham, G. Behr, L. Harnagea, D. Bombor, A. Bachmann, I. V. Morozov, V. B. Zabolotnyy, A. A. Kordyuk, T. K. Kim, D. V. Evtushinsky, S. V. Borisenko, A. U. B. Wolter, C. Hess, S. Wurmehl and B. Büchner, Phys. Rev. B **84**, 054534 (2011). [Cited on pages: 1 and 42.]

[14] N. Qureshi, P. Steffens, Y. Drees, A. C. Komarek, D. Lamago, Y. Sidis, L. Harnagea, H.-J. Grafe, S. Wurmehl, B. Büchner and M. Braden, Phys. Rev. Lett. **108**, 117001 (2012). [Cited on pages: 1, 43, 44, 66, 69, and 110.]

[15] D. S. Inosov, J. S. White, D. V. Evtushinsky, I. V. Morozov, A. Cameron, U. Stockert, V. B. Zabolotnyy, T. K. Kim, A. A. Kordyuk, S. V. Borisenko, E. M. Forgan, R. Klingeler, J. T. Park, S. Wurmehl, A. N. Vasiliev, G. Behr, C. D. Dewhurst and V. Hinkov, Phys. Rev. Lett. **104**, 187001 (2010). [Cited on pages: 1 and 36.]

[16] N. Qureshi, P. Steffens, D. Lamago, Y. Sidis, O. Sobolev, R. A. Ewings, L. Harnagea, S. Wurmehl, B. Büchner and M. Braden, Phys. Rev. B **90**, 144503 (2014). [Cited on pages: 1, 43, 44, 66, 69, and 110.]

[17] R. Wiesendanger, Rev. Mod. Phys. **81**, 1495 (2009). [Cited on page: 1.]

[18] R. Wiesendanger, *Scanning Probe Microscopy and Spectroscopy*, Cambridge University Press, 2001. [Cited on pages: 1, 5, and 19.]

[19] A. V. Balatsky, I. Vekhter and J.-X. Zhu, Rev. Mod. Phys. **78**, 373 (2006). [Cited on page: 1.]

[20] Y. Zhang, V. W. Brar, C. Girit, A. Zettl and M. F. Crommie, Nat. Phys. **5**, 722 (2009). [Cited on page: 1.]

[21] O. Fischer, M. Kugler, I. Maggio-Aprile, C. Berthod and C. Renner, Rev. Mod. Phys. **79**, 353 (2007). [Cited on pages: 1 and 17.]

[22] D. V. Evtushinsky, A. N. Yaresko, V. B. Zabolotnyy, J. Maletz, T. K. Kim, A. A. Kordyuk, M. S. Viazovska, M. Roslova, I. Morozov, R. Beck, S. Wurmehl, H. Berger, B. Büchner and S. V. Borisenko, arXiv:1409.1537 (2014). [Cited on pages: 2, 48, and 56.]

[23] D. J. Scalapino, J. R. Schrieffer and J. W. Wilkins, Phys. Rev. **148**, 263 (1966). [Cited on pages: 2, 46, 47, 62, 67, and 69.]

[24] G. Binnig, H. Rohrer, C. Gerber and E. Weibel, Applied Physics Letters **40**, 178 (1982). [Cited on page: 5.]

[25] C. J. Chen, *Introduction to Scanning Tunneling Microscopy (second edition)*, Oxford University Press, 2008. [Cited on pages: 5, 6, 11, and 12.]

[26] R. Feenstra, J. A. Stroscio and A. Fein, Surface Science **181**, 295 (1987). [Cited on pages: 5, 11, 12, and 13.]

[27] D. J. Griffiths, *Introduction to Quantum Mechanics*, Prentice Hall, 1995. [Cited on pages: 6, 7, and 23.]

[28] J. Bardeen, Phys. Rev. Lett. **6**, 57 (1961). [Cited on pages: 8, 9, and 11.]

[29] J. Tersoff and D. R. Hamann, Phys. Rev. Lett. **50**, 1998 (1983). [Cited on page: 8.]

[30] J. E. Hoffman, Reports on Progress in Physics **74**, 124513 (2011). [Cited on page: 17.]

[31] R. Schlegel, P. K. Nag, D. Baumann, R. Beck, S. Wurmehl, B. Büchner and C. Hess, physica status solidi (b) **254**, 1600159 (2017). [Cited on pages: 18, 25, 49, 50, 51, 52, 53, 55, 58, 59, 74, 75, 83, 87, and 94.]

[32] S. Grothe, S. Chi, P. Dosanjh, R. Liang, W. N. Hardy, S. A. Burke, D. A. Bonn and Y. Pennec, Phys. Rev. B **86**, 174503 (2012). [Cited on pages: 18, 49, 50, 53, 59, 74, 75, and 94.]

[33] S. H. Pan, E. W. Hudson, K. M. Lang, H. Eisaki, S. Uchida and J. C. Davis, Nature **403**, 746 (2000). [Cited on page: 18.]

[34] J. M. Ziman, *Principles of the theory of solids*, Cambridge University Press, 1964. [Cited on page: 21.]

[35] A. C. Hewson, *The Kondo problem to Heavy Fermions*, Cambridge University Press, 1997. [Cited on page: 21.]

[36] M. F. Crommie, C. P. Lutz and D. M. Eigler, Nature **363**, 524 (1993). [Cited on pages: 21, 22, and 24.]

[37] Y. Hasegawa and P. Avouris, Phys. Rev. Lett. **71**, 1071 (1993). [Cited on page: 21.]

[38] L. Petersen, P. T. Sprunger, P. Hofmann, E. Lægsgaard, B. G. Briner, M. Doering, H.-P. Rust, A. M. Bradshaw, F. Besenbacher and E. W. Plummer, Phys. Rev. B **57**, R6858 (1998). [Cited on pages: 22, 23, and 24.]

[39] M. F. Crommie, C. P. Lutz and D. M. Eigler, Science **262**, 218 (1993). [Cited on page: 24.]

[40] M. Maltseva and P. Coleman, Phys. Rev. B **80**, 144514 (2009). [Cited on pages: 24 and 89.]

[41] R. Schlegel, *Aufbau and Inbetriebnahme eines Eintauch - Rastertunnelmikroskopes*, 2010. [Cited on page: 25.]

[42] R. Schlegel, T. Hänke, D. Baumann, M. Kaiser, P. K. Nag, R. Voigtländer, D. Lindackers, B. Büchner and C. Hess, Review of Scientific Instruments **85**, (2014). [Cited on pages: 26 and 27.]

[43] *Macor, Corning Incorporated, One Riverfront Plaza Corning, New York 14831, USA*. [Cited on page: 27.]

[44] *Lake Shore Cryotronics, Cernox Sensor, Lake Shore Cryotronics, Inc., 575 McCorkle Blvd, Westerville, Ohio 43082-8699, USA*. [Cited on page: 27.]

[45] *S. H. Pan, "Piezo-electric motor", International Patent Publication Number WO 93/19494 (International Bureau, World Intellectual Property Organization, 1993).* [Cited on page: 25.]

[46] G. Mariotto, M. D'Angelo and I. V. Shvets, Review of Scientific Instruments **70**, 3651 (1999). [Cited on page: 27.]

[47] T. Hänke, S. Sykora, R. Schlegel, D. Baumann, L. Harnagea, S. Wurmehl, M. Daghofer, B. Büchner, J. van den Brink and C. Hess, Phys. Rev. Lett. **108**, 127001 (2012). [Cited on pages: 28, 42, 44, 49, 59, 74, 92, and 108.]

[48] C. Hess, S. Sykora, T. Hänke, R. Schlegel, D. Baumann, V. B. Zabolotnyy, L. Harnagea, S. Wurmehl, J. van den Brink and B. Büchner, Phys. Rev. Lett. **110**, 017006 (2013). [Cited on pages: 28, 42, 49, 74, 92, and 108.]

[49] P. K. Nag, R. Schlegel, D. Baumann, H.-J. Grafe, R. Beck, S. Wurmehl, B. Büchner and C. Hess, Scientific Reports **6**, 27926 (2016). [Cited on pages: 28, 49, 52, 94, and 123.]

[50] E. O. Brigham, *The Fast Fourier Transform And Its Applications*, Prentic Hall, 1996. [Cited on pages: 29, 31, and 32.]

[51] J. Bardeen, L. N. Cooper and J. R. Schrieffer, Phys. Rev. **108**, 1175 (1957). [Cited on page: 33.]

[52] J. G. Bednorz and K. A. Müller, Zeitschrift für Physik B Condensed Matter **64**, 189 (1986). [Cited on page: 33.]

[53] M. K. Wu, J. R. Ashburn, C. J. Torng, P. H. Hor, R. L. Meng, L. Gao, Z. J. Huang, Y. Q. Wang and C. W. Chu, Phys. Rev. Lett. **58**, 908 (1987). [Cited on page: 33.]

[54] U. Onbasli, Y. T. Wang, A. Naziripour, R. Tello, W. Kiehl and A. M. Hermann, physica status solidi (b) **194**, 371 (1996). [Cited on page: 33.]

[55] H. K. Onnes, Commun. Phys. Lab. Univ. Leiden; No. 120b (1911). [Cited on page: 34.]

[56] R. E. Hummel, *Electronic Properties of Materials*, Springer, 2005. [Cited on page: 34.]

[57] A. M. Omar, *Elementary Solid State Physics*, Pearson Education, 1999. [Cited on page: 34.]

[58] M. J. Pitcher, D. R. Parker, P. Adamson, S. J. C. Herkelrath, A. T. Boothroyd, R. M. Ibberson, M. Brunelli and S. J. Clarke, Chem. Commun., 5918-5920 (2008). [Cited on pages: 35, 40, 46, and 64.]

[59] D. R. Parker, M. J. Pitcher, P. J. Baker, I. Franke, T. Lancaster, S. J. Blundell and S. J. Clarke, Chem. Commun., 2189-2191 (2009). [Cited on page: 35.]

[60] F.-C. Hsu, J.-Y. Luo, K.-W. Yeh, T.-K. Chen, T.-W. Huang, P. M. Wu, Y.-C. Lee, Y.-L. Huang, Y.-Y. Chu, D.-C. Yan and M.-K. Wu, Proc. Natl. Acad. Sci. **105**, 14262 (2008). [Cited on page: 35.]

[61] J.-H. Chu, J. G. Analytis, C. Kucharczyk and I. R. Fisher, Phys. Rev. B **79**, 014506 (2009). [Cited on page: 37.]

[62] C. Liu, G. D. Samolyuk, Y. Lee, N. Ni, T. Kondo, A. F. Santander-Syro, S. L. Bud'ko, J. L. McChesney, E. Rotenberg, T. Valla, A. V. Fedorov, P. C. Canfield, B. N. Harmon and A. Kaminski, Phys. Rev. Lett. **101**, 177005 (2008). [Cited on pages: 36 and 38.]

[63] J. Paglione and R. L. Greene, Nat. Phys. **6**, 645 (2010). [Cited on page: 33.]

[64] A. Chubukov, Annual Review of Condensed Matter Physics **3**, 57 (2012). [Cited on pages: 33, 38, and 64.]

[65] P. Dai, J. Hu and E. Dagotto, Nat. Phys. **8**, 709 (2012). [Cited on page: 33.]

[66] I. I. Mazin, D. J. Singh, M. D. Johannes and M. H. Du, Phys. Rev. Lett. **101**, 057003 (2008). [Cited on pages: 35, 36, 37, and 38.]

[67] I. I. Mazin, Nature **464**, 183 (2010). [Cited on pages: 35, 38, 39, 40, and 120.]

[68] R. M. Fernandes, A. V. Chubukov and J. Schmalian, Nat. Phys. **10**, 97 (2014). [Cited on pages: 36 and 38.]

[69] J.-H. Chu, J. G. Analytis, K. De Greve, P. L. McMahon, Z. Islam, Y. Yamamoto and I. R. Fisher, Science **329**, 824 (2010). [Cited on page: 36.]

[70] E. P. Rosenthal, E. F. Andrade, C. J. Arguello, R. M. Fernandes, L. Y. Xing, X. C. Wang, C. Q. Jin, A. J. Millis and A. N. Pasupathy, Nat. Phys. **10**, 225 (2014). [Cited on pages: 36, 40, 73, and 120.]

[71] S.-H. Baek, D. V. Efremov, J. M. Ok, J. S. Kim, J. van den Brink and B. Büchner, Nat. Mater. **14**, 210 (2015). [Cited on pages: 36, 115, and 116.]

[72] A. Dusza, A. Lucarelli, F. Pfuner, J.-H. Chu, I. R. Fisher and L. Degiorgi, EPL (Europhysics Letters) **93**, 37002 (2011). [Cited on page: 36.]

[73] Y. Gallais, R. M. Fernandes, I. Paul, L. Chauvière, Y.-X. Yang, M.-A. Méasson, M. Cazayous, A. Sacuto, D. Colson and A. Forget, Phys. Rev. Lett. **111**, 267001 (2013). [Cited on page: 36.]

[74] S. Onari and H. Kontani, Phys. Rev. Lett. **109**, 137001 (2012). [Cited on page: 36.]

[75] M. Nakajima, T. Liang, S. Ishida, Y. Tomioka, K. Kihou, C. H. Lee, A. Iyo, H. Eisaki, T. Kakeshita, T. Ito and S. Uchida, Proceedings of the National Academy of Sciences **108**, 12238 (2011). [Cited on page: 36.]

[76] S. Kasahara, H. J. Shi, K. Hashimoto, S. Tonegawa, Y. Mizukami, T. Shibauchi, K. Sugimoto, T. Fukuda, T. Terashima, A. H. Nevidomskyy and Y. Matsuda, Nature **486**, 382 (2012). [Cited on page: 36.]

[77] C. Dhital, Z. Yamani, W. Tian, J. Zeretsky, A. S. Sefat, Z. Wang, R. J. Birgeneau and S. D. Wilson, Phys. Rev. Lett. **108**, 087001 (2012). [Cited on page: 36.]

[78] M. Yi, D. Lu, J.-H. Chu, J. G. Analytis, A. P. Sorini, A. F. Kemper, B. Moritz, S.-K. Mo, R. G. Moore, M. Hashimoto, W.-S. Lee, Z. Hussain, T. P. Devereaux, I. R. Fisher and Z.-X. Shen, Proceedings of the National Academy of Sciences **108**, 6878 (2011). [Cited on page: 36.]

[79] C. de la Cruz, Q. Huang, J. W. Lynn, J. Li, W. R. II, J. L. Zarestky, H. A. Mook, G. F. Chen, J. L. Luo, N. L. Wang and P. Dai, Nature **453**, 899 (2008). [Cited on page: 36.]

[80] T. Nomura, S. W. Kim, Y. Kamihara, M. Hirano, P. V. Sushko, K. Kato, M. Takata, A. L. Shluger and H. Hosono, Supercond. Sci. Technol. **21**, 125028 (2008). [Cited on page: 36.]

[81] L. Wang, Z. Gao, Y. Qi, X. Zhang, D. Wang and Y. Ma, Supercond. Sci. Technol. **22**, 015019 (2009). [Cited on page: 36.]

[82] F. Ma and Z.-Y. Lu, Phys. Rev. B **78**, 033111 (2008). [Cited on page: 36.]

[83] D. J. Singh and M.-H. Du, Phys. Rev. Lett. **100**, 237003 (2008). [Cited on page: 36.]

[84] M. M. Korshunov and I. Eremin, Physical Review B **78**, 140509 (2008). [Cited on pages: 36, 37, 39, and 120.]

[85] V. B. Zabolotnyy, D. S. Inosov, D. V. Evtushinsky, A. Koitzsch, A. A. Kordyuk, G. L. Sun, J. T. Park, D. Haug, V. Hinkov, A. V. Boris, C. T. Lin, M. Knupfer, A. N. Yaresko, B. Büchner, A. Varykhalov, R. Follath and S. V. Borisenko, Nature **457**, 569 (2009). [Cited on page: 36.]

[86] S. V. Borisenko, V. B. Zabolotnyy, A. A. Kordyuk, D. V. Evtushinsky, T. K. Kim, I. V. Morozov, R. Follath and B. Büchner, Symmetry **4**, 251 (2012). [Cited on pages: 40, 41, 42, 44, 64, 86, 90, and 108.]

[87] S. V. Borisenko, D. V. Evtushinsky, Z.-H. Liu, I. Morozov, R. Kappenberger, S. Wurmehl, B. Büchner, A. N. Yaresko, T. K. Kim, M. Hoesch, T. Wolf and N. D. Zhigadlo, Nat. Phys. **12**, 311 (2016). [Cited on pages: 40, 76, 86, 100, 104, and 105.]

[88] Y. Wang, A. Kreisel, V. B. Zabolotnyy, S. V. Borisenko, B. Büchner, T. A. Maier, P. J. Hirschfeld and D. J. Scalapino, Phys. Rev. B **88**, 174516 (2013). [Cited on pages: 40, 44, 64, and 70.]

[89] F. Ahn, I. Eremin, J. Knolle, V. B. Zabolotnyy, S. V. Borisenko, B. Büchner and A. V. Chubukov, Phys. Rev. B **89**, 144513 (2014). [Cited on pages: 40, 44, 65, and 69.]

[90] S. Aswartham, C. Nacke, G. Friemel, N. Leps, S. Wurmehl, N. Wizent, C. Hess, R. Klingeler, G. Behr, S. Singh and B. Büchner, Journal of Crystal Growth **314**, 341 (2011). [Cited on pages: 40, 46, and 64.]

[91] M. Gooch, B. Lv, J. H. Tapp, Z. Tang, B. Lorenz, A. M. Guloy and P. C. W. Chu, EPL **85,**, 27005 (2009). [Cited on page: 40.]

[92] C. Putzke, A. I. Coldea, I. Guillamón, D. Vignolles, A. McCollam, D. LeBoeuf, M. D. Watson, I. I. Mazin, S. Kasahara, T. Terashima, T. Shibauchi, Y. Matsuda and A. Carrington, Phys. Rev. Lett. **108**, 047002 (2012). [Cited on pages: 41 and 46.]

[93] B. Zeng, D. Watanabe, Q. R. Zhang, G. Li, T. Besara, T. Siegrist, L. Y. Xing, X. C. Wang, C. Q. Jin, P. Goswami, M. D. Johannes and L. Balicas, Phys. Rev. B **88**, 144518 (2013). [Cited on pages: 41 and 42.]

[94] P. Fazekas, *Lecture Notes on Electron Correlation and Magnetism*, Uto-Print, 1999. [Cited on page: 41.]

[95] P. M. R. Brydon, M. Daghofer, C. Timm and J. van den Brink, Phys. Rev. B **83**, 060501 (2011). [Cited on pages: 41 and 44.]

[96] M. P. Allan, A. W. Rost, A. P. Mackenzie, Y. Xie, J. C. Davis, K. Kihou, C. H. Lee, A. Iyo, H. Eisaki and T.-M. Chuang, Science **336**, 563 (2012). [Cited on pages: 42, 49, 66, 74, and 108.]

[97] M. P. Allan, K. Lee, A. W. Rost, M. H. Fischer, F. Massee, K. Kihou, C.-H. Lee, A. Iyo, H. Eisaki, T.-M. Chuang, J. C. Davis and E.-A. Kim, Nat. Phys. **11**, 177 (2015). [Cited on pages: 43, 60, 66, and 74.]

[98] Y. Li, Z. Yin, X. Wang, D. W. Tam, D. L. Abernathy, A. Podlesnyak, C. Zhang, M. Wang, L. Xing, C. Jin, K. Haule, G. Kotliar, T. A. Maier and P. Dai, Phys. Rev. Lett. **116**, 247001 (2016). [Cited on pages: 43, 69, and 110.]

[99] J. Knolle, V. B. Zabolotnyy, I. Eremin, S. V. Borisenko, N. Qureshi, M. Braden, D. V. Evtushinsky, T. K. Kim, A. A. Kordyuk, S. Sykora, C. Hess, I. V. Morozov, S. Wurmehl, R. Moessner and B. Büchner, Phys. Rev. B **86**, 174519 (2012). [Cited on pages: 43, 66, and 111.]

[100] D. S. Inosov, J. T. Park, P. Bourges, D. L. Sun, Y. Sidis, A. Schneidewind, K. Hradil, D. Haug, C. T. Lin, B. Keimer and V. Hinkov, Nat. Phys. **6**, 178 (2010). [Cited on page: 44.]

[101] S. Baek, H. Grafe, F. Hammerath, M. Fuchs, C. Rudisch, L. Harnagea, S. Aswartham, S. Wurmehl, J. van den Brink and B. Büchner, Eur. Phys. J. B **85**, 1 (2012). [Cited on pages: 44 and 59.]

[102] C. Platt, R. Thomale and W. Hanke, Phys. Rev. B **84**, 235121 (2011). [Cited on page: 44.]

[103] S. Chi, S. Johnston, G. Levy, S. Grothe, R. Szedlak, B. Ludbrook, R. Liang, P. Dosanjh, S. A. Burke, A. Damascelli, D. A. Bonn, W. N. Hardy and Y. Pennec, Phys. Rev. B **89**, 104522 (2014). [Cited on pages: 44 and 74.]

[104] Z. P. Yin, K. Haule and G. Kotliar, Nat. Phys. **10**, 845 (2014). [Cited on page: 44.]

[105] S.-H. Baek, L. Harnagea, S. Wurmehl, B. Büchner and H.-J. Grafe, Journal of Physics: Condensed Matter **25**, 162204 (2013). [Cited on pages: 45, 46, 58, and 64.]

[106] M. J. Pitcher, T. Lancaster, J. D. Wright, I. Franke, A. J. Steele, P. J. Baker, F. L. Pratt, W. T. Thomas, D. R. Parker, S. J. Blundell and S. J. Clarke, J. Am. Chem. Soc. **132**, 10467 (2010). [Cited on pages: 46 and 64.]

[107] S. Khim, B. Lee, J. W. Kim, E. S. Choi, G. R. Stewart and K. H. Kim, Phys. Rev. B **84**, 104502 (2011). [Cited on pages: 46 and 64.]

[108] G. Li, R. R. Urbano, P. Goswami, C. Tarantini, B. Lv, P. Kuhns, A. P. Reyes, C. W. Chu and L. Balicas, Phys. Rev. B **87**, 024512 (2013). [Cited on pages: 46 and 64.]

[109] U. Stockert, M. Abdel-Hafiez, D. V. Evtushinsky, V. B. Zabolotnyy, A. U. B. Wolter, S. Wurmehl, I. Morozov, R. Klingeler, S. V. Borisenko and B. Büchner, Phys. Rev. B **83**, 224512 (2011). [Cited on pages: 46 and 64.]

[110] X. Wang, Q. Liu, Y. Lv, W. Gao, L. Yang, R. Yu, F. Li and C. Jin, Solid State Communications **148**, 538 (2008). [Cited on pages: 46 and 64.]

[111] O. Heyer, T. Lorenz, V. B. Zabolotnyy, D. V. Evtushinsky, S. V. Borisenko, I. Morozov, L. Harnagea, S. Wurmehl, C. Hess and B. Büchner, Phys. Rev. B **84**, 064512 (2011). [Cited on pages: 46 and 64.]

[112] S. Chi, S. Grothe, R. Liang, P. Dosanjh, W. N. Hardy, S. A. Burke, D. A. Bonn and Y. Pennec, Phys. Rev. Lett. **109**, 087002 (2012). [Cited on pages: 46, 49, 60, 63, 64, 65, 66, 70, and 94.]

[113] T. Hanaguri, K. Kitagawa, K. Matsubayashi, Y. Mazaki, Y. Uwatoko and H. Takagi, Phys. Rev. B **85**, 214505 (2012). [Cited on pages: 46, 49, 60, 63, 64, and 66.]

[114] W. L. McMillan and J. M. Rowell, Phys. Rev. Lett. **14**, 108 (1965). [Cited on page: 46.]

[115] F. Ronning, K. M. Shen, N. P. Armitage, A. Damascelli, D. H. Lu, Z.-X. Shen, L. L. Miller and C. Kim, Phys. Rev. B **71**, 094518 (2005). [Cited on pages: 46, 48, and 56.]

[116] R. D. Parks, *Superconductivity Volume 1*, Marcel Dekker, INC., New York, 1969. [Cited on page: 47.]

[117] D. S. Inosov, J. Fink, A. A. Kordyuk, S. V. Borisenko, V. B. Zabolotnyy, R. Schuster, M. Knupfer, B. Büchner, R. Follath, H. A. Dürr, W. Eberhardt, V. Hinkov, B. Keimer and H. Berger, Phys. Rev. Lett. **99**, 237002 (2007). [Cited on pages: 48 and 56.]

[118] W. Meevasana, X. J. Zhou, S. Sahrakorpi, W. S. Lee, W. L. Yang, K. Tanaka, N. Mannella, T. Yoshida, D. H. Lu, Y. L. Chen, R. H. He, H. Lin, S. Komiya, Y. Ando, F. Zhou, W. X. Ti, J. W. Xiong, Z. X. Zhao, T. Sasagawa, T. Kakeshita, K. Fujita, S. Uchida, H. Eisaki, A. Fujimori, Z. Hussain, R. S. Markiewicz, A. Bansil, N. Nagaosa, J. Zaanen, T. P. Devereaux and Z.-X. Shen, Phys. Rev. B **75**, 174506 (2007). [Cited on pages: 48 and 56.]

[119] J. Graf, G.-H. Gweon, K. McElroy, S. Y. Zhou, C. Jozwiak, E. Rotenberg, A. Bill, T. Sasagawa, H. Eisaki, S. Uchida, H. Takagi, D.-H. Lee and A. Lanzara, Phys. Rev. Lett. **98**, 067004 (2007). [Cited on pages: 48 and 56.]

[120] T. Valla, T. E. Kidd, W.-G. Yin, G. D. Gu, P. D. Johnson, Z.-H. Pan and A. V. Fedorov, Phys. Rev. Lett. **98**, 167003 (2007). [Cited on pages: 48 and 56.]

[121] B. P. Xie, K. Yang, D. W. Shen, J. F. Zhao, H. W. Ou, J. Wei, S. Y. Gu, M. Arita, S. Qiao, H. Namatame, M. Taniguchi, N. Kaneko, H. Eisaki, K. D. Tsuei, C. M. Cheng, I. Vobornik, J. Fujii, G. Rossi, Z. Q. Yang and D. L. Feng, Phys. Rev. Lett. **98**, 147001 (2007). [Cited on pages: 48 and 56.]

[122] D. S. Inosov, R. Schuster, A. A. Kordyuk, J. Fink, S. V. Borisenko, V. B. Zabolotnyy, D. V. Evtushinsky, M. Knupfer, B. Büchner, R. Follath and H. Berger, Phys. Rev. B **77**, 212504 (2008). [Cited on pages: 48 and 56.]

[123] M. Ikeda, T. Yoshida, A. Fujimori, M. Kubota, K. Ono, Y. Kaga, T. Sasagawa and H. Takagi, Phys. Rev. B **80**, 184506 (2009). [Cited on pages: 48 and 56.]

[124] F. Schmitt, B. Moritz, S. Johnston, S.-K. Mo, M. Hashimoto, R. G. Moore, D.-H. Lu, E. Motoyama, M. Greven, T. P. Devereaux and Z.-X. Shen, Phys. Rev. B **83**, 195123 (2011). [Cited on pages: 48 and 56.]

[125] D. Baumann, *Aufbau eines ultrahochauflösenden Tieftemperatur- Rastertunnelmikroskops*, Die Spiegel-Bestseller, 2012. [Cited on pages: 49 and 96.]

[126] J. L. Zhang, L. Jiao, F. F. Balakirev, X. C. Wang, C. Q. Jin and H. Q. Yuan, Phys. Rev. B **83**, 174506 (2011). [Cited on page: 58.]

[127] N. Kurita, K. Kitagawa, K. Matsubayashi, A. Kismarahardja, E.-S. Choi, J. S. Brooks, Y. Uwatoko, S. Uji and T. Terashima, Journal of the Physical Society of Japan **80**, 013706 (2011). [Cited on page: 58.]

[128] I. Morozov, A. Boltalin, O. Volkova, A. Vasiliev, O. Kataeva, U. Stockert, M. Abdel-Hafiez, D. Bombor, A. Bachmann, L. Harnagea, M. Fuchs, H.-J. Grafe, G. Behr, R. Klingeler, S. Borisenko, C. Hess, S. Wurmehl and B. Büchner, Crystal Growth & Design **10**, 4428 (2010). [Cited on pages: 59 and 93.]

[129] Z. Li, Y. Ooe, X.-C. Wang, Q.-Q. Liu, C.-Q. Jin, M. Ichioka and G. qing Zheng, Journal of the Physical Society of Japan **79**, 083702 (2010). [Cited on page: 59.]

[130] M. Tinkham, *Introduction to Superconductivity*, Dover Publications, 2004. [Cited on pages: 63 and 89.]

[131] D. F. Agterberg, V. Barzykin and L. P. Gor'kov, Phys. Rev. B **60**, 14868 (1999). [Cited on page: 64.]

[132] J. W. Alldredge, J. Lee, K. McElroy, M. Wang, K. Fujita, Y. Kohsaka, C. Taylor, H. Eisaki, S. Uchida, P. J. Hirschfeld and J. C. Davis, Nat. Phys. **4**, 319 (2008). [Cited on pages: 65 and 66.]

[133] R. C. Dynes, V. Narayanamurti and J. P. Garno, Phys. Rev. Lett. **41**, 1509 (1978). [Cited on pages: 65 and 66.]

[134] P. Hlobil, J. Jandke, W. Wulfhekel and J. Schmalian, arXiv:1603.05288v2 (2016). [Cited on pages: 67, 68, and 69.]

[135] J. Jandke, P. Hlobil, M. Schackert, W. Wulfhekel and J. Schmalian, Phys. Rev. B **93**, 060505 (2016). [Cited on page: 68.]

[136] C. Platt, R. Thomale, C. Honerkamp, S.-C. Zhang and W. Hanke, Phys. Rev. B **85**, 180502 (2012). [Cited on page: 69.]

[137] L. Shan, J. Gong, Y.-L. Wang, B. Shen, X. Hou, C. Ren, C. Li, H. Yang, H.-H. Wen, S. Li and P. Dai, Phys. Rev. Lett. **108**, 227002 (2012). [Cited on page: 70.]

[138] C.-L. Song, Y.-L. Wang, Y.-P. Jiang, Z. Li, L. Wang, K. He, X. Chen, J. E. Hoffman, X.-C. Ma and Q.-K. Xue, Phys. Rev. Lett. **112**, 057002 (2014). [Cited on page: 70.]

[139] K.-H. Lin, K.-J. Wang, C.-C. Chang, Y.-C. Wen, D.-H. Tsai, Y.-R. Wu, Y.-T. Hsieh, M.-J. Wang, B. Lv, P. C.-W. Chu and M.-K. Wu, Phys. Rev. B **90**, 174502 (2014). [Cited on page: 73.]

[140] *The tight binding fit to the ARPES data in stoichiometric LiFeAs is done by Jose Maria Guevara Parra, Steffen Sykora and Zhixiang Sun at IFW Dresden.* [Cited on pages: 86, 89, 100, 104, 105, and 110.]

[141] *"Investigation of the Superconducting and Magnetic Phase Diagram of Off-Stoichiometric LiFeAs" by Uwe Gräfe.* [Cited on pages: 93 and 112.]

[142] *The NQR data is measured by U. Gräfe while the susceptibility data is taken by R. Kappenberger at IFW Dresden.* [Cited on page: 94.]

[143] A. E. Böhmer, F. Hardy, F. Eilers, D. Ernst, P. Adelmann, P. Schweiss, T. Wolf and C. Meingast, Phys. Rev. B **87**, 180505 (2013). [Cited on page: 115.]

[144] C.-L. Song, Y.-L. Wang, P. Cheng, Y.-P. Jiang, W. Li, T. Zhang, Z. Li, K. He, L. Wang, J.-F. Jia, H.-H. Hung, C. Wu, X. Ma, X. Chen and Q.-K. Xue, Science **332**, 1410 (2011). [Cited on pages: 115 and 119.]

[145] J. Maletz, V. B. Zabolotnyy, D. V. Evtushinsky, S. Thirupathaiah, A. U. B. Wolter, L. Harnagea, A. N. Yaresko, A. N. Vasiliev, D. A. Chareev, A. E. Böhmer, F. Hardy, T. Wolf, C. Meingast, E. D. L. Rienks, B. Büchner and S. V. Borisenko, Phys. Rev. B **89**, 220506 (2014). [Cited on pages: 115 and 116.]

[146] M. Bendele, A. Amato, K. Conder, M. Elender, H. Keller, H.-H. Klauss, H. Luetkens, E. Pomjakushina, A. Raselli and R. Khasanov, Phys. Rev. Lett. **104**, 087003 (2010). [Cited on page: 115.]

[147] S. Medvedev, T. M. McQueen, I. A. Troyan, T. Palasyuk, M. I. Eremets, R. J. Cava, S. Naghavi, F. Casper, V. Ksenofontov, G. Wortmann and C. Felser, Nat. Mater. **8**, 630 (2009). [Cited on page: 115.]

[148] S. Masaki, H. Kotegawa, Y. Hara, H. Tou, K. Murata, Y. Mizuguchi and Y. Takano, Journal of the Physical Society of Japan **78**, 063704 (2009). [Cited on page: 115.]

[149] K. Nakayama, Y. Miyata, G. N. Phan, T. Sato, Y. Tanabe, T. Urata, K. Tanigaki and T. Takahashi, Phys. Rev. Lett. **113**, 237001 (2014). [Cited on page: 115.]

[150] T. Watashige, Y. Tsutsumi, T. Hanaguri, Y. Kohsaka, S. Kasahara, A. Furusaki, M. Sigrist, C. Meingast, T. Wolf, H. v. Löhneysen, T. Shibauchi and Y. Matsuda, Phys. Rev. X **5**, 031022 (2015). [Cited on pages: 115 and 119.]

[151] D. Huang, T. A. Webb, C.-L. Song, C.-Z. Chang, J. S. Moodera, E. Kaxiras and J. E. Hoffman, Nano Letters **16**, 4224 (2016). [Cited on page: 115.]

[152] A. V. Chubukov, D. Efremov and I. Eremin, Phys. Rev. B **78**, 134512 (2008). [Cited on page: 120.]

[153] P. Cai, X. Zhou, W. Ruan, A. Wang, X. Chen, D.-H. Lee and Y. Wang, Nat. Commun. **4**, 1596 (2013). [Cited on pages: 120 and 121.]

[154] P. Cai, W. Ruan, X. Zhou, C. Ye, A. Wang, X. Chen, D.-H. Lee and Y. Wang, Phys. Rev. Lett. **112**, 127001 (2014). [Cited on page: 120.]

[155] H. Yang, Z. Wang, D. Fang, Q. Deng, Q.-H. Wang, Y.-Y. Xiang, Y. Yang and H.-H. Wen, Nat. Commun. **4**, (2013). [Cited on page: 120.]

[156] Z.-H. Liu, P. Richard, K. Nakayama, G.-F. Chen, S. Dong, J.-B. He, D.-M. Wang, T.-L. Xia, K. Umezawa, T. Kawahara, S. Souma, T. Sato, T. Takahashi, T. Qian, Y. Huang, N. Xu, Y. Shi, H. Ding and S.-C. Wang, Phys. Rev. B **84**, 064519 (2011). [Cited on page: 120.]

[157] J. D. Wright, T. Lancaster, I. Franke, A. J. Steele, J. S. Möller, M. J. Pitcher, A. J. Corkett, D. R. Parker, D. G. Free, F. L. Pratt, P. J. Baker, S. J. Clarke and S. J. Blundell, Phys. Rev. B **85**, 054503 (2012). [Cited on page: 121.]

[158] X. Zhou, P. Cai, A. Wang, W. Ruan, C. Ye, X. Chen, Y. You, Z.-Y. Weng und Y. Wang, Phys. Rev. Lett. **109**, 037002 (2012). [Cited on page: 121.]

Eigenständigkeitserklärung:

Hiermit versichere ich, dass ich die vorliegende Arbeit ohne unzulässige Hilfe Dritter und ohne Benutzung anderer als der angegebenen Hilfsmittel angefertigt habe; die aus fremden Quellen direkt oder indirekt übernommenen Gedanken sind als solche kenntlich gemacht. Die Arbeit wurde bisher weder im Inland noch im Ausland in gleicher oder ähnlicher Form einer anderen Prüfungsbehörde vorgelegt.

Die vorliegende Arbeit wurde unter Betreuung von Prof. Dr. B. Büchner am IFW Dresden angefertigt. Es haben keine früheren erfolglosen Promotionsverfahren stattgefunden. Ich erkenne die Promotionsordnung der Fakultät Mathematik und Naturwissenschaften der Technischen Universität Dresden an.

Dresden, 20. März 2017

Pranab Kumar Nag

short curriculum vita

Pranab Kumar Nag	Nationality: Indian;
06.05.1989	born in Khirpai Hat-Tala (West Midnapur, West Bengal, India), Parents: Sukumar Nag, Sabita Nag;
1998 to 2004	West Bengal Board of Secondary Education (Marh Gopalpur Sindhubala High School, West Midnapur);
05.2004 to 06.2006	West Bengal Council of Higher Secondary Education (Khirpai H.S. Multipurpose School, West Midnapur);
06.2006 to 07.2009	Bachelor of Science (B.Sc.(Hons.)): Honours in Physics from Vidyasagar University (Panskura Banamali College);
07.2009 to 06.2011	Master of Science (M.Sc.) in Physics from IIT Kanpur;
04.2011	Master thesis title: "Low Temperature Scanning Tunneling Microscopy(STM) and Spectroscopy Study of Defects in Few Layers Graphene and Graphite";
06.2011 to 03.2012	Research Associate in DST unit of Nanoscience, IIT Kanpur;
04.2012 to 07.2012	Guest Scientist at IFW Dresden, Germany;
08.2012 to 03.2017	PhD student at TU Dresden and Employee at IFW, Dresden.